

RAPORT STIINTIFIC SI TEHNIC
Asupra rezultatelor cercetarilor angajate
prin temele din Contractul Nr. 1EU/ 8.08.2008
pe perioada 4 ianuarie – 30 iunie 2010

Forma extinsa

Florin Spineanu

Sef al Unitatii de Cercetare al Asociatiei EURATOM – MEdC Romania

INTERPRETATION AND CONTROL OF HELICAL PERTURBATIONS IN TOKAMAKS

C.V. Atanasiu, A. Moraru

National Institute for Lasers, Plasma and Radiation Physics, Bucharest, Romania

During the period January-June 2010, the common research between the **Mathematical Modelling for Fusion Plasmas Group of the National Institute for Lasers, Plasma and Radiation Physics (NILPRP)**, Magurele - Bucharest, Romania with the **Max-Planck - Institut für Plasmaphysik (IPP)**, Garching, Germany has been focalized on the following objective:

1 Provision of support to the advancement of the ITER Physics Basis

1.3 MHD stability and plasma control

Specific Objective: Resistive wall modes (RWMs) stabilization

The target of this research, made in common with IPP Garching, Tokamakphysics Department, is to advance the physics understanding of RWMs stability, including the dependence on plasma rotation, wall/plasma distance, and active feedback control, with the ultimate goal of achieving sustained operation at beta values close to the ideal-wall beta limit through passive and active stabilization of the RWMs. Such objective has its justification in the fact that the stabilization of RWM in ITER, where it is probably not possible to maintain a very fast plasma rotation is still an open problem.

We have continued our research on RWMs made in 2009, in the frame of the following *milestone*:

- **M1 Application of our numerical model in the calculation of the wall response (for a real 3D geometry with holes) to the external kink mode perturbations of ITER. TF-ITM (IMP#2-T4)**

We have continued our approach of calculating the wall response to an external kink mode perturbation with the help of a scalar potential (current stream function) [1, 2, 3]. The EURATOM FP7 Specific Programme stipulates that, after the review of the facilities in the fusion programme has been carried out, ASDEX Upgrade plays the best “step-ladder” role for RWMs control in ITER. Indeed, ASDEX Upgrade will have 3x8 internal coils to support ITER proposal (3x9 coils), while JET has 4 coils only and DIII-D 2x6 coils. We have applied our approach to the ASDEX Upgrade wall configuration.

In our previous research we investigated the non-rotating plasma case, where the distribution of the eddy currents induced in the wall by an external kink mode has been determined from the equation

$$\nabla^2 U = \sigma w \frac{\partial B_{\perp}}{\partial t}; B_{\perp} = B_{\perp}^{pl} + B_{\perp}^{eddy}; B_{\perp}^{pl} = B_0 e^{i(n\theta - n\zeta)}$$

$$\nabla^2 U = \gamma \sigma w (B_{\perp}^{pl} + B_{\perp}^{eddy})$$

where σ is the electrical conductivity, γ is the growth rate of the mode and W is the wall thickness.

For a plasma column rotating with a poloidal and toroidal angular rotations

$$\begin{aligned}
B_{\perp}^{pl}(t, \theta, \zeta) &= B_0^{pl} e^{\gamma + i(m\theta - n\zeta) + i(m\Omega_{\theta} - n\Omega_{\zeta})t} = B_0^{pl} e^{\gamma t + i\alpha + i\omega t} \\
B_{\perp}^{eddy}(t, \theta, \zeta) &= B_0^{eddy} e^{\gamma t + i(m\theta - n\zeta) + i(m\Omega_{\theta} - n\Omega_{\zeta})t} = B_0^{eddy} e^{\gamma t + i\alpha + i\beta + i\omega t} \\
U_{\perp}^{eddy}(t, \theta, \zeta) &= U_0^{eddy} e^{\gamma t + i(m\theta - n\zeta) + i(m\Omega_{\theta} - n\Omega_{\zeta})t} = U_0^{eddy} e^{\gamma t + i\alpha + i\beta + i\omega t} \\
\alpha &= m\theta - n\zeta, \omega = m\Omega_{\theta} - n\Omega_{\zeta}, \Omega_{\theta} = \frac{d\theta}{dt}, \Omega_{\zeta} = \frac{d\zeta}{dt} \\
\omega &= \text{angular frequency, } \Omega_{\theta}, \Omega_{\zeta} = \text{poloidal, toroidal plasma rotation} \\
\beta &= \beta(\theta, \zeta) \text{ phase du to the RL character of the circuit}
\end{aligned}$$

and the diffusion equation in the frequency-domain formulation looks like

$$\nabla [U_0 e^{i(\alpha+\beta)}] = w\sigma [\gamma + i\omega] [b_0^{pl} e^{i\alpha} + b_0^{eddy} e^{i(\alpha+\beta)}]$$

Our new solving approach has been tested on the following test problem

$$\Delta V = f(x, y),$$

$$f(x, y) = -\exp(x+y)(xy(6-2x-2xy-2y) + 10xy(x^2-y^2))$$

with Dirichlet boundary conditions on the wall and hole contours. Five holes and 764 interior meshpoints have been considered. Different numerical approaches have been used:

I) SOR: $\omega_k = 1.726$, $N_{iter} = 3001$, $\varepsilon_{max}^r = 0.495E-12$, $\varepsilon_{max}^a = 0.128E-12$, at a CPU-time of 48.4776 seconds;

II) Factorization: 2 vectors: Real(361090), Integer(108327) and some smaller vectors; at a CPU-time of factorization: 9.6124 seconds, (IMSL – DLFTXG; NAG - F01BRF or F01BSF) and at a CPU-time of system solving (IMSL – DLFSXG, NAG – F04AXF) (after performed factorization): 0.01155 seconds

To verify our approach for the rotating plasma case, we developed an alternative approach by considering a fixed plasma with a moving wall. With the assumption that the plasma cross-section perpendicular to the moving direction is constant, by using the Minkowski formulation for the Maxwell equations and Ohm's law, the following diffusion like equation has been obtained

$$\frac{\partial(\vec{B}^{eddy})}{\partial t} = \frac{1}{\mu\sigma} \nabla^2 \vec{B}^{eddy} + [(\vec{B}^{pl} + \vec{B}^{eddy}) \bullet \nabla] \vec{v} - (\vec{v} \bullet \nabla)(\vec{B}^{pl} + \vec{B}^{eddy}) - \frac{\partial \vec{B}^{pl}}{\partial t}.$$

where

$$\frac{\vec{v}}{r^{pl}} = m\Omega_{\theta} - n\Omega_{\zeta}, \Omega_{\theta} = \frac{d\theta}{dt}, \Omega_{\zeta} = \frac{d\zeta}{dt}$$

with r^{pl} is some plasma minor radius, and θ and ζ are the poloidal and toroidal angles, m and n are the poloidal and toroidal wave numbers, respectively.

Special attention has been given to extend our previous method to remove the singularity at the re-entry corner applied to a Laplace type problem to a Poisson one.

Next steps:

- to include in our model the interaction of the plasma and wall with the feedback and error coils, by using our concept of surface current [6, 7].

This work has been carried out in close collaboration with our colleagues from the Tokamak Physics Department of the Max-Planck-Institut für Plasmaphysik, Garching, Germany, during the mobility 27.03.10-26.06.10 [8].

References :

- [1] C.V. Atanasiu, [S. Günter](#), [A. Moraru](#), [L. E. Zakharov](#), *Resistive wall modes stabilization in the presence of 3D wall structures*, EPS34 (P4.086), Warsaw, Poland, 2-6 July 2007.
- [2] C.V. Atanasiu, [A. Moraru](#), [L. E. Zakharov](#), *The investigation of resistive wall modes in a diverted tokamak configuration*, 35th EPS Conference on Plasma Physics and Fusion, 9-11 July, Hersonissos, Crete, Greece.
- [3] C.V. Atanasiu, A. Moraru, L.E. Zakharov, “*Response of a resistive wall with holes to an external kink mode in a tokamak*”, 21st International Conference on Numerical Simulation of Plasmas, Lisbon, Portugal, 6-9 October 2009.
- [4] C.V. Atanasiu, A. Moraru, L.E. Zakharov, “*Influence of a Nonuniform Resistive Wall on the RWM Stability in a Tokamak*”, APS Plasma Meeting, Atlanta, USA, 2-6 November 2009.
- [5] O. Gruber, “*Status and Experimental Opportunities of ASDEX Upgrade in 2009*”, Ringberg Meeting, 2008.
- [6] [C. V. Atanasiu](#), [S. Günter](#), [K. Lackner](#), [A. Moraru](#), [L. E. Zakharov](#), and [A. A. Subbotin](#), Phys. Plasmas **11**, 5580 (2004).
- [7] C.V. Atanasiu, A.H. Boozer, L.E. Zakharov, A.A. Subbotin, Phys. Plasmas **6**, 2781 (1999).
- [8] J. [Adamek](#), C. [Angioni](#), G. [Antar](#), C.V. Atanasiu, M. [Balden](#), W. [Becker](#), REVIEW OF SCIENTIFIC INSTRUMENTS, **81**, 3, 033507 (2010).

Dr. C.V. Atanasiu

**Universitatea din Craiova
Tema BS-3A**

Scientific Report

**To the Contract 1EU-2/11.08.2008
For January - June 2010**

Project BS-3A: *Anomalous Transport in Plasma:
Integrated Tokamak Modeling*

**Integrated Tokamak Modeling
WP10 –ITM-IMP5-ACT4-T1-01/MedC**

Plasma Theory Group: Gy. Steinbrecher

- **General Objectives**

The aim of this project is to make progress in understanding the transport in fusion plasma from devices like ITER, by numerical simulations. The results obtained in this project can be applied to existing large plasma devices but are oriented specially to be applied to plasma in ITER device.

For the year 2010 the general objective is:

1. Integrated Tokamak Modeling.

- **Specific Objective**

In this stage of the project, January-June 2010 we have attained the following specific objective from the previously mentioned general objective:

1. Development of an advanced 3D ion Fokker Planck solver for ions.

- **Resume of the stage**

1. *Development of an advanced 3D ion Fokker Planck solver for ions.*

The mathematical aspects required for the efficient numerical solution of the stochastic differential equations related to Fokker Planck solver from [1] were elaborated in [4], by generalizing the results from [2, 3]. The dependence of the convergence from the quality of random number generator was studied, by using results from [3, 8]. The convergence rate of the stochastic Euler integrator from [1] was studied, by using different random number generators. A C code for general second order stochastic Runge-Kutta integrator was elaborated.

- **Scientific description**

Specific Objective 1

1. *Development of an advanced 3D ion Fokker Planck solver for ions.*

Co-operations: C.E.A. Cadarache, France

Milestone: *Study of the numerical methods for the stochastic differential equations associated to the Monte-Carlo method.*

The problem of numerical stability and speed up of the orbit-following numerical method used in [1] was studied. In the small time step-size limit the stochastic process from [1] is equivalent to Ito stochastic differential equation.

For the numerical stability studies the results from [2,3] were generalized in [4] by new category of topological vector space methods. The problem of correct numerical approximation of the large amplitude fluctuations, due to instabilities, was studied.

This type of fluctuations appears due to the instability inherited from the complex deterministic process, e.g. wave- particle interaction, approximated by Monte-Carlo operators. At the level of the Fokker-Planck equation the instability is disguised in coordinate dependence of the second order coefficients. In the stochastic differential equations it appears as a multiplicative noise, studied in [2-4].

Another motivation of this study is the occurrence of the singularities in the stationary solution of the Fokker-Planck equation containing coordinate dependent second order derivative term. This singularity is related to the noise-driven on-off intermittency [5, 6]. In the case of the stochastic extension of the Hamiltonian dynamical systems, in the linear approximation, the multiplicative noise always destabilizes the dynamical system. This destabilization is manifest by the exponential blow-up of the second order moments for large time [7].

A solvable discrete time stochastic process [8] of the large deviations in the stationary probability distribution function was studied, in the small discretization time limit. By comparing these discrete time results with the continuum time exact results from [2-4], the effect of various approximation of the Gaussian random number generator was studied. The error was estimated by computing the exact and approximate value of the power law exponent of the stationary probability density function.

The numerical method used in the work [1] is stochastic Euler method having robust first order convergence of the expectation values. In the following studies the weak convergence is sufficient. It is possible to speed-up the numerical method by adapting higher order Runge-Kutta integrators. In contradistinction to the deterministic equations, in the stochastic framework it is difficult to obtain general higher order algorithm without analytic differentiation of the r.h.s. of the stochastic differential equation. In order to balance between convergence speed and coding difficulty, a version the second order stochastic Runge-Kutta integrator from [9] was adapted.

This integrator solves the following system of stochastic differential equations

$$dx_i(t) = a_i(\mathbf{x}(t))dt + \sum_{a=1}^m b_{i,a}(\mathbf{x}(t))dw_a(t); 1 \leq i \leq d$$

Here d is the dimension of the system and $w_m(t)$ are standard mutually independent Wiener processes [9]. Boldface denote the vector with suitable components

The algorithm is the following.

Denote by Δt the time step and by $y_i(t) := y_i, y_i(t + \Delta t)$ its approximants. We use the notations and recurrences:

$$a_i := a_i(\mathbf{y}(t)); b_{i,a} := b_{i,a}(\mathbf{y}(t)); 1 \leq i \leq d, 1 \leq a \leq m$$

$$u_{\pm,i,a} = y_i \pm b_{i,a} \sqrt{\Delta t}$$

$$R_{\pm,i,a} = u_{\pm,i,a} + a_i \Delta t$$

We use also the condensed notation

$$u_{\pm,i,a} = (\mathbf{u}_{\pm,a})_i$$

$$R_{\pm,i,a} = (\mathbf{R}_{\pm,a})_i$$

$$z_i = y_i + a_i \Delta t + \sum_{a=1}^m b_{i,a} \Delta w_a$$

$$z_i = (\mathbf{z})_i$$

In the last formula by Δw_a we denoted random variables with mean zero and variance Δt . Their approximation by exact Gaussian or some more rapid discrete distribution is the one of the subject of the study.

In the following we denote

$$\begin{aligned}
c_{1,i} &= \frac{1}{2}(a_i(\mathbf{z}) + a_i)\Delta t \\
c_{2,i} &= \frac{1}{4} \sum_{a=1}^m (b_{i,a}(\mathbf{R}_{+,a}) + b_{i,a}(\mathbf{R}_{-,a}) + 2b_{i,a})\Delta w_a \\
c_{3,i} &= \frac{1}{4} \sum_{a=1}^m \sum_{\substack{r=1 \\ r \neq j}}^m (b_{i,a}(\mathbf{u}_{+,r}) + b_{i,a}(\mathbf{u}_{-,r}) - 2b_{i,a})\Delta w_a \\
c_{4,i} &= \frac{1}{4} \sum_{a=1}^m (b_{i,a}(\mathbf{R}_{+,a}) - b_{i,a}(\mathbf{R}_{-,a}) + 2b_{i,a})[(\Delta w_a)^2 - (\Delta t)]\Delta w_a
\end{aligned}$$

Define the random matrix $V_{a,b}$ as follows.

If $b < a$ then $P(V_{a,b} = \pm \Delta t) = 1/2$

If $b = a$ then $V_{a,a} = \Delta t$

If $b > a$ then $V_{a,b} = -V_{b,a}$

In the continuation we define

$$c_{5,i} = \frac{1}{4} \sum_{a=1}^m \sum_{\substack{r=1 \\ r \neq j}}^m (b_{i,a}(\mathbf{u}_{+,r}) - b_{i,a}(\mathbf{u}_{-,r}))[\Delta w_a \Delta w_r - V_{r,a}]\Delta w_a$$

The recurrence relation is given by

$$y_i(t + \Delta t) = y_i(t) + \sum_{k=1}^5 c_{k,i}$$

A maximally portable C program was elaborated, and used to solve a system of stochastic differential equations studied in [3]. The language C was chosen due to its portability and possibility to manipulate bits, necessary for the coding of the random number generators. The exact result from [3] and the numerical result obtained were compared in order to verify the correctness of the code and the effect of the random number generators.

• Conclusions

1. Development of an advanced 3D ion Fokker Planck solver for ions.

The numerical stability of Monte-Carlo method used in the solution of the Fokker-Planck equations for ions was studied. The first problem was the correct numerical description of the large amplitude fluctuations in the stationary distribution function, due to various approximations. By using exact results on continuous and discrete time models conditions on the random number generators were obtained. For the physical applications an improved stochastic Runge-Kutta method was studied and efficient C program was elaborated.

The results will be used to speed-up the existing Fokker-Planck codes for optimal use of ICRF and NBI for large tokamaks, like ITER.

- **Project for August-December**

1. The previous C code will be rewritten in a suitable FORTRAN version and transferred to Gateway.
2. Because our code has second order precision only for autonomous systems, will be studied the decrease of the precision due to time dependence.
3. Extrapolation methods will be elaborated.

- **References**

- [1]. L.-G. Ericson, M. Schneider, “*Monte-Carlo operators for ions interactiong with radio frequency waves*”. Physics of Plasmas **12**, 072524, (2005).
- [2] Steinbrecher, W. T. Shaw. “*Quantile Mechanics*”, European Journal of Applied Mathematics, **19**, 87, (2008).
- [3] Steinbrecher G., Weyssow B., “*Generalized Randomly Amplified Linear System Driven by Gaussian Noise. Extreme Heavy Tail and Algebraic Correlation Decay in Plasma Turbulence*”, Physical Review Letters **92**, 125003 (2004).
- [4]. G. Steinbrecher, X. Garbet, B. Weyssow, “*Large time behavior in random multiplicative processes*”, arXiv:1007.0952v1 [math.PR].
- [5] S. Aumaître, F. Pétrélis, K. Mallick, “*Low frequency noise control on-off intermittency in bifurcation systems*”, Phys. Rev. Lett. **95**, 064101, (2005).
- [6]. X. Garbet, G. Steinbrecher, “*On-off intermittency. Exact results*”. Presented at the “Solvay Workshop <A Tribute to Radu Balescu>”, Brussels, 6-8 March 2008.
- [7] G. Steinbrecher, X. Garbet, “*Stochastic Linear Instability Analysis*”, International Workshop on “Hamiltonian Approaches to ITER Physics”, CIRM, Marseille, 2-6 November 2009.
- http://www.cirm.univmrs.fr/web.ang/liste_rencontre/programmes/AbstractsProgRenc395.pdf
- [8]. H. Takayasu, A-H. Sato, M. Takayasu, “*Stable infinite variance fluctuations in randomly amplified Langevin systems.*” Phys. Rev. Lett. 1997, **79**, 966-969.
- [9]. P. E. Kloeden, E. Platen, “*Numerical Solutions of Stochastic Differential Equations*”. Springer, (1995), page 486-487.

Universitatea din Craiova
Tema BS-3B

Scientific Report

To the Contract 1EU-2/11.08.2008
For the period January - June 2010

Project BS-3B: *Anomalous Transport in Plasma. Stochastic processes and transport in turbulent plasma*

Plasma Theory Group: D. Constantinescu, M. Negrea, I. Petrisor

- **General Objectives**

The scope of the project is to explain some features of the anomalous transport and to develop the analytical and numerical skills to evaluate correctly the transport in fusion device like ITER. The project aims also to deep insight the physics of plasma turbulence.

Both analytical and numerical methods are used to achieve the objectives. The test particle diffusion in an electromagnetic stochastic field is studied in the framework of the decorrelation trajectory method (DCT). In this kind of stochastic field we must determine the mean square displacements and the radial and poloidal diffusivities using the numerical method and the DCT method. The comparison of the results obtained by these two methods might then allow us to confirm the DCT approach results. These results are important for “Validation of physics-based transport models” and “Plasma edge characterization and modeling”, objectives for ITER.

Some characteristics of the anomalous transport of magnetic field lines and charged particles, features that cannot be described in the context of the standard diffusion paradigm, will be explained using the memory effects. The long memory effects will be studied using fractional models and limited (short) memory effects will be studied using delay systems or hysteresis systems.

The results obtained in this project will be applied to existing large plasma devices but oriented specially to be applied to plasma in ITER device.

For the year 2010 the objectives are:

1. **Simulations of MHD turbulence (TG-T, ULB)**

- 1.1. Study of turbulent zonal flow including test particle and field line transport. Stochastic magnetic field line diffusion and particle diffusion in MHD.

2. **Study of anomalous transport (TG-T, WP10-TRA-05-03, ULB, Association of Hellenic Republic)**

- 2.1. Stochastic modelling with application to the edge turbulent transport. Calculus of the diffusion coefficients for test particles in the edge region of tokamak plasma using the decorrelation trajectory method and numerical simulation.

2.2. Study of the fractional diffusion equation with a coupling between position and momentum space; methods to solve this equation analytically and/or numerically in order to study the radial transport.

2.3. Studies of the sawtooth oscillations based on the relaxation oscillation theory and on mapping models.

- **Specific Objectives**

In this stage of the project, the period January - June 2010, we have attained the following specific objectives from the previous mentioned objectives:

2.1. Stochastic modelling with application to the edge turbulent transport. Calculus of the diffusion coefficients for test particles in the edge region of tokamak plasma using the decorrelation trajectory method and numerical simulation.

2.3. b) Study of the sawtooth oscillations based on mapping models.

- **Resume of the stage**

2.1. Stochastic modelling with application to the edge turbulent transport. Calculus of the diffusion coefficients for test particles in the edge region of tokamak plasma using the decorrelation trajectory method and numerical simulation.

The problem of the diffusion of an ion in a stochastic magnetic field with curvature is treated by starting from Langevin equations of the guiding centre and applying specific approximations. Because the Corrsin approximation ignores the trapping effect which necessarily exists in relatively strongly turbulent plasma, the method of the decorrelation trajectories (DCT) was applied.

2.3.b) Study of the sawtooth oscillations based on mapping models.

Sawtooth oscillations of the plasma parameters (for example a repetitive and rapid crash of the central electron temperature) were explained using the magnetic stochasticity hypothesis: the sawtooth crash is a localized penetration of the hot core plasma into the colder outer region and the penetration region, described as a region of localized magnetic reconnection, is associated with the stochastization of the magnetic field because the increased turbulent transport in the plasma core causes the observed crash of the plasma temperature.

- **Scientific description**

Specific Objective 2.1.

Stochastic modelling with application to the edge turbulent transport. Calculus of the diffusion coefficients for test particles in the edge region of tokamak plasma using the decorrelation trajectory method and numerical simulation.

Coordinators: Lect. Dr. Negrea Marian and Lect. Dr. Iulian Petrisor
WP10-TRA-05-03/MEdC

Milestone 2.1.a: *Test-particle simulations of ion drift in stochastic magnetic fields*

We analyzed the influence of the magnetic Kubo number, the drift Kubo number and the stochastic anisotropy on the diffusion of ions when the stochastic magnetic drifts are taken into account. We have shown that the stochastic drifts provide a decorrelation mechanism of the particles from the magnetic lines. A subdiffusive behaviour of the particle mean square displacement is not possible and the particles diffuse even in the absence of the perpendicular collisional diffusion.

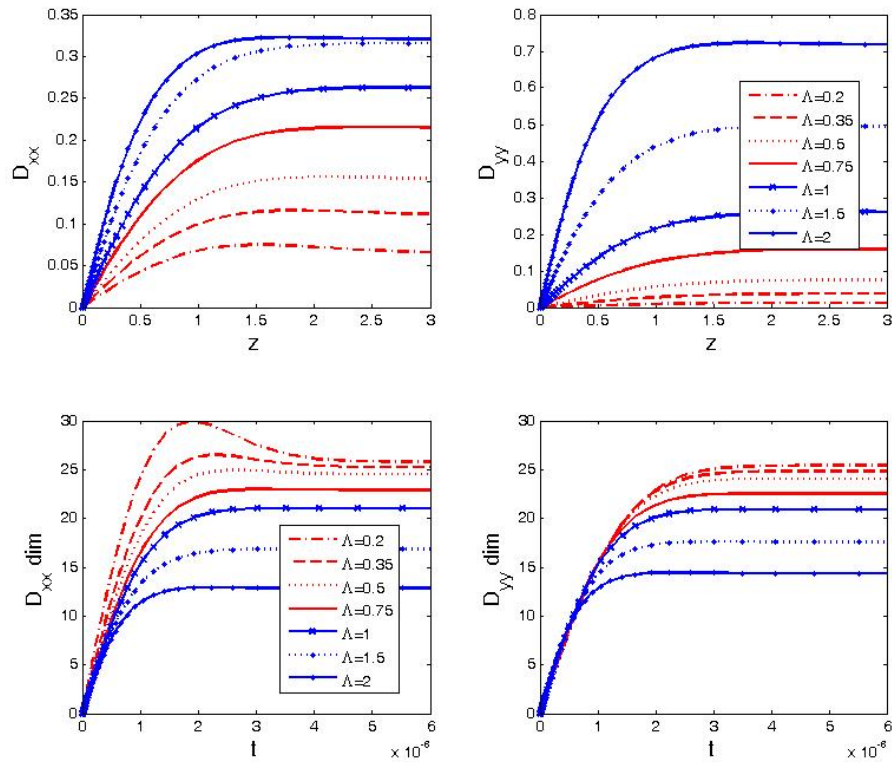


Figure 1. DCT running diffusion coefficients for Be4+ for different values of the anisotropy parameter and for $K_m=0.5$, $K_{dr}=0.2$; the two plots on top represent the dimensionless coefficients and the two plots on bottom the dimensional ones.

We have obtained deterministic decorrelation trajectories for fixed values of the magnetic Kubo number K_m and the drift Kubo number K_{dr} and different values of the anisotropy

parameter Λ in order to see their influence on the shape of the trajectory. An increased value of the anisotropy parameter leads to oscillations around the starting point in a given subensemble. The trapping effect is more pronounced, the larger Λ and K_m are. As an application, we considered impurities in ITER-like conditions, i.e. we assumed an ion temperature $T_i = 8.1$ KeV and a background magnetic field $B_0 = 5.3$ T. The ions we considered are He^{2+} and the impurities Be^{4+} , Ne^{10+} and W^{74+} , as they are relevant for tokamak devices of the ITER type [1, 2].

In parallel to the DCT method, we numerically generated stochastic magnetic field environments and tracked the impurities with test-particle simulations. The resulting diffusion coefficients are presented and compared with those obtained by the DCT method. We intend to analyze in a future paper using toroidal geometry and the Lorentz force, the transport coefficients and to compare them with those from the present study.

Specific objective 2.3.

Studies of sawtooth oscillations based on relaxation oscillation theory and on mapping models

Coordinator: Conf. Dr. Dana Constantinescu

Milestone 2.3.b) Study of the sawtooth oscillations based on mapping models.

The complete or incomplete nature of the magnetic reconnection during the crash stage was studied in [3]. Two magnetic configurations, with monotonous safety factor, respectively with reversed magnetic shear, were studied using the Hamiltonian description of the magnetic field lines and of the mapping technique.

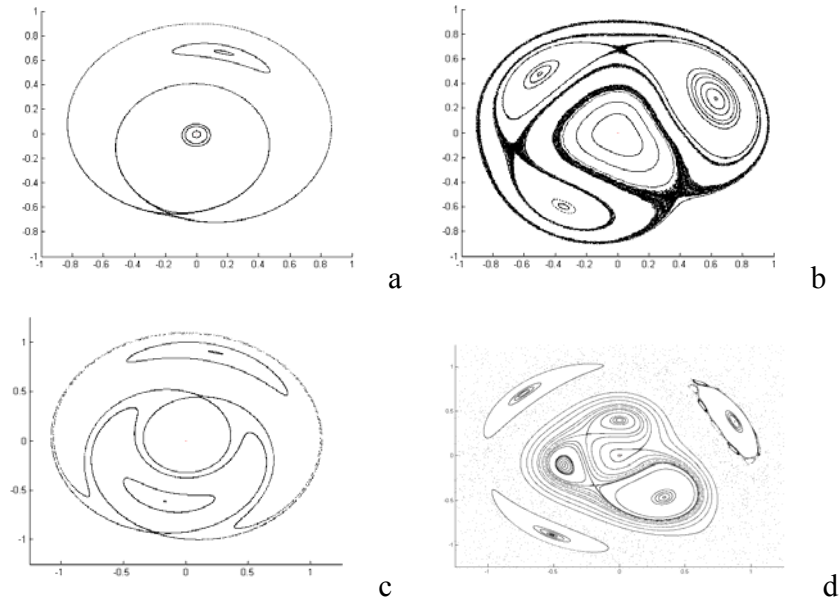


Figure 2 Influence of the higher harmonics. Monotone safety factor: (a) only the (1,1) mode is active, (b) the modes (1,1), (2,2), (3,3) are active. Reversed-shear safety factor: (c) only the (1,1) mode is active, (d) the modes (1,1), (2,2), (3,3) are active.

A perturbation that contains not only the (1, 1) mode, but also higher harmonics –at least (2,2) and (3,3) modes- is considered and the role of these additional perturbations during the sawtooth crash is observed. In our interpretation, the sawtooth oscillations are related to the modification of the minimum value of the safety factor and to the excitation of high modes through two different scenarios:

- for monotonous safety factor q_0 decreases slowly in the rise time, then q_0 rapidly increases in the crash time;
- for reversed shear safety factor q_0 increases slowly in the rise time, then q_0 rapidly decreases in the crash time.

In both cases the modes (2,2), (3,3) are excited just before the crash and are deactivated in the crash time. The stochastization of magnetic field lines appears only for a short time period that is the crash phase itself. The islands are not destroyed and the (1,1) mode remains in the same position after the crash, but all of the temperature is lost in the stochastic phase. The local diffusion coefficients (consequently the electron thermal diffusivity), computed from the mapping models, confirm the stochasticity hypothesis.

The stochastization which is characteristic to sawtooth crash could be interpreted as the collapse of the internal transport barrier associated to the surface $q=1$. In [4] it was shown that the low magnetic shear close to low-order rationals significantly decreases the amplitude threshold of the resonant modes that break the barrier and allow a stochastic transport of the magnetic field.

• Conclusions

2.1. Stochastic modelling with application to the edge turbulent transport. Calculus of the diffusion coefficients for test particles in the edge region of tokamak plasma using the decorrelation trajectory method and numerical simulation.

We considered ion diffusion in a magneto-static, perturbed magnetic field environment, and we find that diffusion is of normal nature. The diffusive process slows down with both, increasing strength of the magnetic perturbation, and increasing mass of the ions considered, respectively. The values of the diffusion coefficients from the test particle simulations are in qualitative agreement with the results yielded by the DCT method.

2.3.b) Study of the sawtooth oscillations based on mapping models.

Our observations show that qualitatively similar results are obtained for any monotonous safety factor. For the reversed shear configuration the stochastization is obtained through the overlapping process of the separatrices of the twin island chains, when they become closer, i.e. q_0 increases.

- **Bibliography**

[1] M. Negrea, I. Petrisor, H. Isliker, A. Vogiannou, L. Vlahos, D. Constantinescu, *On the diffusion of impurities in tokamak plasma*, XV-th Conference On Plasma Physics and Applications, CPPA 2010, July 1-4, 2010, Iasi, Romania

[2] A. Vogiannou, M. Negrea, I. Petrisor, G. Fuhr, B. Weyssow, H. Isliker, L. Vlahos, *Ion transport coefficients in turbulent tokamak plasma*, 9TH SCHOOL OF FUSION PHYSICS & TECHNOLOGY, Volos 19 - 23 April 2010, Greece.

[3] D. Constantinescu, M-C Firpo, M. Negrea, I. Petrisor, *Study of the magnetic reconnection during the sawtooth instability*, XV-th Conference On Plasma Physics and Applications, CPPA 2010, July 1-4, 2010, Iasi, Romania

[4] M. C. Firpo, D. Constantinescu, *Interplay of magnetic shear and resonances in the search for improved confinement in magnetic fusion devices*, submitted for publication to Phys. Rev. Letters.

METODE DE CURGERE OPTICA PENTRU PROCESAREA IMAGINILOR FURNIZATE DE CAMERA VIDEO KL8 DE LA JET

OPTIC FLOW METHODS FOR IMAGE PROCESSING OF THE DATA FROM VIDEO CAMERA KL8 at JET

Etapa 1 - Development of an optic flow method suitable for characterization of plasma boundary phenomena in JET

Teddy CRACIUNESCU, Ion TISEANU, Vasile ZOITA

*EURATOM-MEdC Association, National Institute for Lasers Plasma and Radiation Physics,
Bucharest, Romania*

Introduction

A wide angle view fast visible camera (Photron APX) was recently installed in the Joint European Torus JET [1]. The camera is viewing the full poloidal cross-section of the vacuum vessel and is covering a toroidal extent of $\sim 90^\circ$. The wide angle view is appropriate for the study of pellet ablation, large scale instabilities and plasma wall interactions. Since the high confinement mode of operation (H-mode) is the standard operating regime envisaged for ITER, Edge Localised Mode instabilities (ELM) [2] are of particular importance considering the power loads they can induce on the plasma facing components. Recently it has been proven that the view of the fast visible camera is able to provide useful information about ELMs [3]. Investigations of pellet ELM triggering, as a method to mitigate the ELM-caused heat load on plasma facing components, have been also recently performed on JET by means of the fast visible camera [4]. The fast visible camera observations may support also the validation of existing theories concerning ELM energy transport [5] and the study of filamentary structures observed during the development of the ELM instabilities [6].

Important quantitative information can be obtained by applying image processing techniques to the data provided by the fast visible camera. Specifically, the sequences of ordered images allow the estimation of motion as instantaneous image velocities or discrete image displacements, the so-called *optical flow*. The estimation of motion information from image sequences is a key problem in computer vision. The objective of the analysis consists of finding the vector field, which describes how the image is changing with time (see e.g. Refs. 7-8 for good overviews on this subject). This provides important information about the spatial arrangement of the objects viewed and the rate of change of this arrangement. Discontinuities in the optical flow can help in segmenting images into regions that correspond to different objects. Optical flow can be used also for object detection and tracking, as well as movement detection.

The aim of this paper is to prove that optical flow can be successfully applied to study different fusion plasma relevant issues, including plasma wall interactions, using images from the fast visible camera. It is proved that the optical flow approach is able to offer unique information concerning different plasma physical phenomena.

Methods

The optical flow method attempts to find the vector field which transforms one image into the next image in a sequence of frames. The most widely and accurately used differential methods can be classified into two large categories: i) local methods, such as the Lucas–

Kanade technique [9], which assume a small neighbourhood of constant flow and which are more robust against noise and ii) global methods such as the Horn-Schunck approach [10] which introduce a regularization smoothness term, providing dense flow fields.

The basic assumption of both categories of techniques is that the grey levels of objects in subsequent frames do not change over time, which allows writing:

$$f(x+u, y+v, t+1) - f(x, y, t) = 0 \quad (1)$$

where f is the intensity and the displacement field $(u, v)^T(x, y, t)$ is the optical flow. For small displacements the Taylor expansion can be used in order to obtain the following formulation of the optical flow constraint:

$$f_x u + f_y v + f_t = 0 \quad (2)$$

where subscripts denote partial derivatives.

The problem is prone to instabilities since small perturbations in the signal can create large fluctuations in its derivatives. A typical way to overcome this drawback consists of implementing image smoothing techniques in order to remove noise and to stabilize the differentiation process. The smoothing of the image sequence is performed prior to differentiation by convolving each frame with a Gaussian function:

$$f^{(smooth)}(x, y, t) = (K_\sigma * f)(x, y, t) \quad (3)$$

where σ is the standard deviation of the Gaussian $K_\sigma(x, y)$. The low-pass effect of the Gaussian convolution removes noise and other destabilizing high frequencies. Smoothing can be extended also to the temporal dimension. Of course the smoothing process must be used very carefully: smoothing must suppress noise but not eliminate useful information.

However, from the mathematical point of view, even after proper smoothing is applied, the problem (2) remains ill-posed: a single equation is not sufficient to uniquely compute the two unknowns u and v (the so-called *aperture problem*). In order to cope with the aperture problem, the Lucas-Kanade approach assumes that the unknown optical flow vector is constant within a neighbourhood of size ρ . Therefore u and v can be determined at the location (x, y, t) from a weighted least square fit by minimising the function:

$$E_{LK}(u, v) = K_\rho * \left((f_x u + f_y v + f_t)^2 \right) \quad (4)$$

Using the notation:

$$\begin{aligned}
w &\equiv (u, v, 1)^T \\
|\nabla w|^2 &= |\nabla u|^2 + |\nabla v|^2 \\
\nabla_3 f &= (f_x, f_y, f_t)^T \\
J_\rho(\nabla_3 f) &= K_\sigma * (\nabla_3 f \nabla_3 f^T)
\end{aligned} \tag{5}$$

the quadratic form (4) can be rewritten as follows:

$$E_{LK}(w) = w^T J_\rho(\nabla_3 f) w \tag{6}$$

Minimizing (6) implies to solve the Euler-Lagrange system:

$$\begin{cases} \partial_u E_{LK} = 0 \\ \partial_v E_{LK} = 0 \end{cases} \quad \begin{pmatrix} K_\rho * f_x^2 & K_\rho * f_x f_y \\ K_\rho * f_x f_y & K_\rho * f_y^2 \end{pmatrix} \begin{pmatrix} u \\ v \end{pmatrix} = \begin{pmatrix} -K_\rho * f_x f_t \\ -K_\rho * f_y f_t \end{pmatrix} \tag{7}$$

A sufficiently large value for ρ is very successful in rendering the method robust against noise. The problem remains severe in flat regions of the emission, where the image gradient vanishes and, consequently, the aperture problem persists and the method is unable to produce dense flow fields. This constitutes the major drawback of Lucas-Kanade approach and in general of local gradient methods.

In order to cope with this problem, global methods supplement the optical flow constraint with a regularising smoothness term. The optical flow (u, v) is determined as the minimiser of the global energy functional:

$$E_{HS}(u, v) = \int_{\Omega} \left((f_x u + f_y v + f_t)^2 + \alpha (|\nabla u|^2 + |\nabla v|^2) \right) dx dy \tag{8}$$

where $\alpha > 0$ determines the amount of smoothness and serves as regularisation parameter: larger values for α result in a stronger penalisation of large flow gradients and lead to smoother flow fields. Minimising (8) leads to the Euler-Lagrange equations:

$$\begin{aligned}
0 &= \Delta u - \frac{1}{\alpha} (f_x^2 u + f_x f_y v + f_x f_t) \\
0 &= \Delta v - \frac{1}{\alpha} (f_x f_y v + f_y^2 + f_y f_t)
\end{aligned} \tag{9}$$

At locations with $\alpha|\nabla f| \approx 0$, no reliable local flow estimate is possible, but the regulariser $|\nabla u|^2 + |\nabla v|^2$ fills in information from the neighbourhood (the so-called filling-in effect). Unfortunately global methods have been observed to be more sensitive to noise than local differential methods [11].

Using again the notations (5), relation (8) can be rewritten in the compact form:

$$E_{HS}(w) = \int_{\Omega} \left(w^T J_0(\nabla_3 f) w + \alpha |\nabla w|^2 \right) dx dy \quad (9)$$

Brun et al. [12] noticed the similarity between equation (6) of the Lucas-Kanade method and the first term under the integral in the formulation (9) of the Horn-Schunck method. This suggested a way to extend the Horn-Schunck functional to a combined local-global (CLG) functional, by replacing the matrix $J_0(\nabla_3 f)$ with the structure tensor $J_{\rho}(\nabla_3 f)$ [13] with some integration scale $\sigma > 0$. The price paid for obtaining a combined local-global method is the much more complicated form of the Euler-Lagrange equations:

$$\begin{aligned} 0 &= \Delta u - \frac{1}{\alpha} \left(K_{\rho} * (f_x^2) u + K_{\rho} * (f_x f_y) v + K_{\rho} * (f_x f_t) \right) \\ 0 &= \Delta v - \frac{1}{\alpha} \left(K_{\rho} * (f_x f_y) u + K_{\rho} * (f_y^2) v + K_{\rho} * (f_y f_t) \right) \end{aligned} \quad (10)$$

It can be argued that the smoothness assumption in the quadratic optimization (9) does not respect discontinuities in the flow field. In order to be able to capture also locally non-smooth motion, it is necessary to allow outliers. This can be achieved by replacing $\alpha|\nabla w|^2$ in the second term of (9) with a non-quadratic penalizer: $\alpha\Psi_2(|\nabla w|^2)$. Outliers not only occur in the smoothness term but in the data term as well. It is easy to imagine situations where the optical flow constraint is not fulfilled, e.g. because of occlusion, brightness changes, noise. Consequently the non-quadratic penalizer becomes:

$$E_{CLG}(w) = \int_{\Omega} \left(\Psi_1(w^T J_{\rho}(\nabla_3 f) w) + \alpha\Psi_2(|\nabla w|^2) \right) dx dy \quad (11)$$

The penaliser function Ψ is chosen usually as $\Psi(s^2) = \sqrt{s^2 + \varepsilon^2}$ [14]. The quantity ε is not an additional parameter, but rather ensures the differentiability of Ψ in $s = 0$. It is chosen reasonably small, say $\varepsilon = 0.001$. In general, nonlinear methods give better results at locations with flow discontinuities but require significantly larger computation time (see Refs. 7 and 15).

The sparse linear systems of equations (10) may be solved iteratively, usually by using the successive over-relaxation (SOR) method [16], which ensures a good compromise between

simplicity and efficiency. SOR introduces an additional relaxation parameter $\omega \in (0,2)$; for $\omega = 1$ one obtains the well-known Gauss–Seidel method.

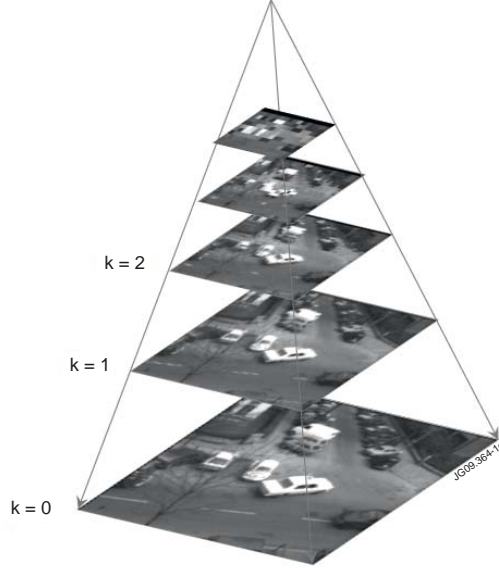


Figure 1 – The pyramid of images in the multi-resolution approach

In the case of displacements that are larger than one pixel per frame, typical of plasma images captured by JET fast visible camera, the cost functional in a variational formulation must be expected to be multi-modal and therefore a minimization algorithm can easily be trapped in a local minimum. In order to find the global minimum we used the multi-resolution coarse-to-fine procedure [17]. A pyramid of images f_k is derived from the original frame f by successive downsampling and Gaussian smoothing steps (Fig. 1). Then the procedure starts at the coarse level, where the displacements (u, v) are small and consequently the linearization of the grey value constancy assumption is a good approximation. This crude estimate is then refined step by step along the pyramidal structure. At resolution k , an increment velocity field (du_k, dv_k) is calculated around the estimate at the previous resolution level $k + 1$, which is obtained by ‘projecting’ (u_{k+1}, v_{k+1}) on the resolution frame k . This means to compensate the second image $f_k(\dots, t + 1)$ for the already computed flow field (the so-called warping step). The warping step is realized by using a backward registration approach that is based on bilinear interpolation. Since the increments (du_k, dv_k) , corresponding to the finer resolution frame, are still small, the brightness constancy assumption is still valid. The final displacement field is obtained by a summation of all motion increments.

The calculated optical flow field may be affected by occlusions. Occlusions appear when two objects that are spatially separated in the 3D space might interfere with each other in the projected 2D image plane. Occlusion modeling is a difficult aspect of the optical flow. In this paper we have used the method suggested by Alvarez et al. [18] that simultaneously compute forward and reverse flow fields, labeling pixels as occluded where the two disagree. A bilateral filter, which incorporates flow from neighboring pixels that are similar in motion

and appearance and that lie outside occluded regions, has also been used in order to improve boundaries [19]:

$$u^{filt}(k) = \frac{\sum_{x_j, y_j} u(x_j, y_j) \cdot w(x, y, x_j, y_j)}{\sum_{x_j, y_j} w(x, y, x_j, y_j)} \quad (12)$$

where:

$$w(x, y, x_j, y_j) = \begin{cases} K\left(\sqrt{(x-x_j)^2 + (y-y_j)^2}; \sigma_x\right) \\ K(I(x, y) - I(x_j, y_j); \sigma_i) \\ K\left(\sqrt{(u-u_j)^2 + (v-v_j)^2}; \sigma_m\right) \\ r(x_j, y_j) \end{cases} \quad (13)$$

An analogous expression can be written for v . The four terms in the filter expression (12) weight the neighbors according to spatial proximity, image similarity, motion similarity and occlusion labeling.

Experiments and Results

The optical flow method has been implemented as described previously. The multi-resolution coarse-to-fine procedure was used in order to deal with large displacements. At each resolution level, the sparse linear systems of equations (10) were solved using the SOR method. After possible detection of occlusions, the velocity field images were filtered using the bilateral filter given by the relations (12÷13). A large number of numerical tests have been performed on data already widely used as benchmarks to test the performance of this kind of image processing (see e.g. Ref. 20). A representative result is presented in Fig. 2 for the famous ‘Yosemite’ sequence with known velocities, available from <http://www.cs.brown.edu/~black/>. The data was originally generated by Lynn Quam at the SRI International Artificial Centre (<http://www.ai.sri.com/>) and used for the first time by Heeger [21] for testing optical flow methods. The sequence was generated by taking an aerial image of Yosemite Valley and texture mapping it onto a depth map of the valley. A synthetic sequence was generated by flying through the valley. There are actually two common sequences: one with clouds and one without. The cloud pattern is fractal and undergoing

Brownian motion. The assumption of brightness constancy does not hold for the clouds. Therefore Brown [22] recommends the use of the version without clouds which contains ground truth optical flow fields.

Fig. 2 reveals that the optical flow algorithm is able to retrieve the vector field with enough accuracy. The correlation coefficient between the image displaying the exact modulus $\sqrt{u^2 + v^2}$ and the calculated one $\sqrt{u_{calc}^2 + v_{calc}^2}$ is ~ 0.83 (this coefficient assumes the value 1 for a perfect matching of the two images).



Figure 2 – Yosemite sequence: image 7 in the sequence (left), modulus of the velocities used to generate the transition from image 6 to image 7 (middle) and modulus of the reconstructed velocity field obtained by applying the optical flow method to the image pair image 6 – image 7 (right).

Numerical tests have been necessary to determine the adjustable parameters of the algorithm: the parameter for Gaussian smoothing σ , the regularization parameter (smoothness term) α , the regularization parameter for SOR algorithm ω , the number of iterations in the SOR implementation, the number of levels of the images pyramid for multi-resolution implementation. The parameters of the algorithm depend on the structure of the image. However, a first approximation can be obtained using synthetic images.

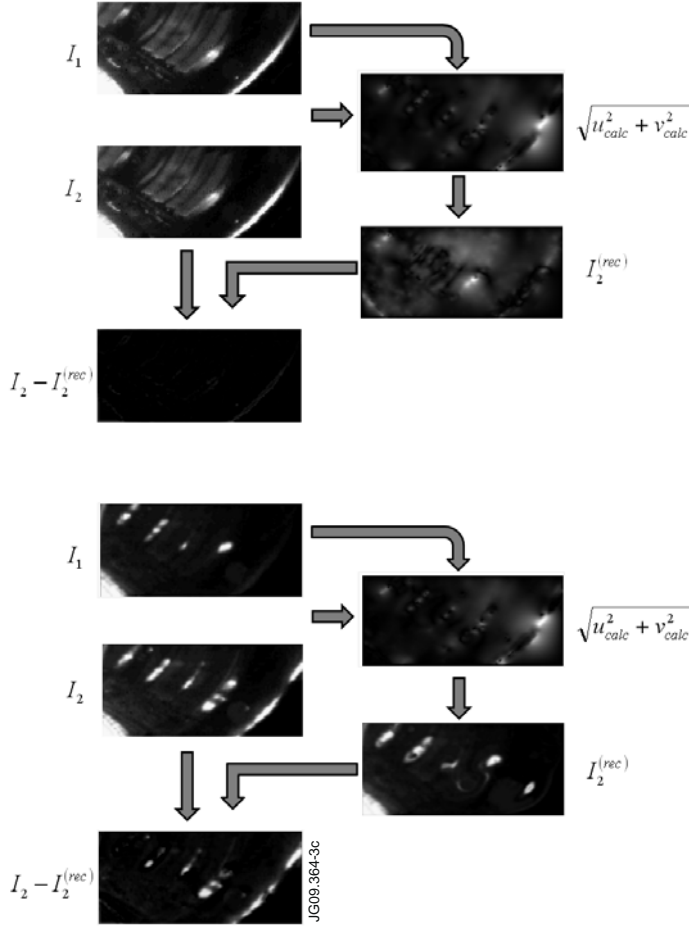


Figure 3 - Illustration of the confidence criterion. The error image can confirm the correct calculation of the optical flow field (top) but also emphasize wrong results, due to new objects appearing in the image sequence (bottom). The error image is represented, as the images in the sequence, on 64 gray-levels.

Real images provided by the JET fast visible camera can be affected by saturation, discontinuous movement, reshaping of image objects, low gray-level in-depth resolution. Therefore, the basic assumptions of the optical flow model may not be verified and the algorithm will calculate an inaccurate vector field. Consequently a criterion to discern between correct and wrong calculated flow fields must be introduced. The optical flow is determined using two images I_1 , I_2 , from a sequence of images. Using the first image and the calculated optical flow, a version $I_2^{(rec)}$ of the second image can be reconstructed. The similarity between I_2 and $I_2^{(rec)}$ can be used in order to assess the accuracy of the optical flow calculations. Therefore the error image $I_2 - I_2^{(rec)}$ has been used as a confidence criterion to determine the validity of the results. An illustrative example is given in Fig. 3, for images taken from a sequence recorded with JET fast visible camera, showing ELM filaments moving up along the poloidal limiters. The confidence criterion is able to detect the failure of the optical flow calculations, determined by strong object reshaping and by the appearance of new objects in the second image.

Conclusion

An algorithm based on the optical flow method, combining the advantages of local methods (robust under noise) and global techniques (which yield dense flow fields), is developed for JET fast visible camera image processing. The method incorporates a multi-resolution coarse-to-fine procedure in order to be able to work with large displacements between consecutive frames. Occlusion detection is also implemented. The method was extensively tested on synthetic images the method and proved to give good results for images with characteristics similar to the images provided by the JET fast-visible camera. It means that images can be affected by saturation, discontinuous movement, reshaping of image objects, low grey-level in-depth resolution. The results were published (see Ref. 23).

The work on this project will continue with the application of the method to the study of various issues relevant to the study of fusion plasmas: pellets, filaments, MARFes. For objects moving close to known structures of the tokamak vacuum vessel, the velocity in the real 3D space has been inferred from the 2D image analysis. The optical flow method is an unique tool able to cope with several different plasma physical phenomena and to provide useful information for modelling.

Acknowledgement

The reported work includes contributions from the following people outside the EUATOM-MEdC Association: Andrea Murari (Consorzio RFX, Associazione ENEA-Euratom per la Fusione, Padova, Italy), Arturo Alonso (Laboratorio Nacional de Fusion, EURATOM-CIEMAT, Madrid, Spain), Peter Lang (Association EURATOM-IPP, Max-Planck-Institut für Plasmaphysik, Garching, Germany) and Gabor Kocsis (RMKI-KFKI EURATOM Association, Budapest, Hungary).

References

- [1] J. A. Alonso, P. Andrew, A. Neto, J. L. de Pablos, E. de la Cal, H. Fernandes, J. Gafert, P. Heesterman, C. Hidalgo, G. Kocsis, A. Manzanares, A. Murari, G. Petravich, L. Rios, C. Silva, P.D. Thomas, Fast visible camera installation and operation in JET, 34th EPS Conference on Plasma Phys. Warsaw, 2 - 6 July 2007 ECA Vol.31F, P-2.124 (2007).
- [2] A. Kirk, H. R. Wilson, G. F. Counsell, R. Akers, E. Arends, S. C. Cowley, J. Dowling, B. Lloyd, M. Price, and M. Walsh, Spatial and Temporal Structure of Edge-Localized Modes, Phys. Rev. Lett. 92(2004)245002.
- [3] J.A. Alonso, P. Andrew, A. Neto, J.L. de Pablos, E. de la Cal, H. Fernandes, W. Fundamenski, C. Hidalgo, G. Kocsis, A. Murari, G. Petravich, R.A. Pitts, L. Rios, C. Silva, Fast visible imaging of ELM-wall interactions on JET, Journal of Nuclear Materials, 390-391(2009)797-800.
- [4] G. Kocsis, J.A. Alonso, B. Alper, G. Arnoux, G. Cseh, J. Figueiredo, D. Frigione, L. Garzotti, J. Hobirk, S. Kalvin, M. Lampert, P.T. Lang, G. Petravich, T. Szepesi, R. Wenninger, Pellet cloud distribution and dynamics for different plasma scenarios in ASDEX Upgrade and JET, 36th EPS Conf. on Plasma Physics, Sofia, Bulgaria 2009, Europhysics Conference Abstracts, Vol. 33E, P-1.151, 2009

- [5] R. Wilson, S. C. Cowley, A. Kirk, P. B. Snyder, Magneto-hydrodynamic stability of the H-mode transport barrier as a model for edge localized modes: an overview, *Phys. Rev. Lett.* 92 (24) (2004) 245002.
- [6] W. Fundamenski, R. A. Pitts, A model of ELM filament energy evolution due to parallel losses, *Plasma Phys. Control. Fusion* 48 (2006) 109–156.
- [7] J. L. Barron, D. J. Fleet and S. S. Beauchemin, Performance of optical flow techniques, *International Journal of Computer Vision*, 12-1(1994)43-47.
- [8] D. J. Fleet and Y. Weiss. Optical flow estimation. In *Mathematical models for Computer Vision: The Handbook*. N. Paragios, Y. Chen, and O. Faugeras (eds.), Springer, 2005.
- [9] B. Lucas, T. Kanade, An iterative image registration technique with an application to stereo vision. In *Proc. Seventh International Joint Conference on Artificial Intelligence*, Vancouver, Canada, 1981, pp. 674–679.
- [10] B. Horn, B. Schunck, Determining optical flow, *Artificial Intelligence*, 17(1981)185–203.
- [11] A. Bruhn, J. Weickert, C. Schnörr, Combining the Advantages of Local and Global Optic Flow Methods, *Proc. of 24th DAGM Symposium Zurich, Switzerland, September 16–18, 2002*, in *Lecture Notes in Computer Science*, 2449(2002)454-462.
- [12] A. Bruhn, J. Weickert, C. Schnörr, Lucas/Kanade meets Horn/Schunck: combining local and global optic flow methods, *Int. J. Comput. Vision*, 61-3(2005)211-231.
- [13] J. Bigün, G.H. Granlund, and J. Wiklund, Multidimensional orientation estimation with applications to texture analysis and optical flow, *IEEE Transactions on Pattern Analysis and Machine Intelligence*, 13(8)(1991)775–790.
- [14] N. Papenberg, A. Bruhn, T. Brox, S. Didas, J. Weickert, Highly Accurate Optic Flow Computation with Theoretically Justified Warping, *International Journal of Computer Vision*, Vol. 67/2, 141-158, 2006.
- [15] I. Cohen, Nonlinear Variational Method for Optical Flow Computation, *Proceedings of the 8th Scandinavian Conference on Image Analysis*, Tromsø, Norway, MAY 25-28, 1993 pp. 523–530..
- [16] D.M. Young, *Iterative Solution of Large Linear Systems*. Academic Press: New York, 1971.
- [17] E. Mémin, P. Pérez, Dense estimation and object-based segmentation of the optical flow with robust techniques. *IEEE Transactions on Image Processing*, 7-5(1998)703–719.
- [18] L. Alvarez, R. Deriche, T. Papadopoulos, J. Sanchez, Symmetrical dense optical flow estimation with occlusion detection, In *ECCV*, pages 721-735, 2002.
- [19] P. Sand, S.J. Teller, Particle Video: Long-Range Motion Estimation Using Point Trajectories. *International Journal of Computer Vision* 80-1(2008)72-91.
- [20] H.H. Nagel – Universität Karlsruhe, Institut für Algorithmen und Kognitive Systeme, Image Sequence Server, http://i21www.ira.uka.de/image_sequences/.
- [21] D. J. Heeger. Model for the extraction of image flow, *J. Opt. Soc. Am. A*, 4(8):1455–1471, 1987.
- [22] M. J. Black, A. Jepson, Estimating optical flow in segmented images using variable-order parametric models with local deformations, *IEEE Transactions on Pattern Analysis and Machine Intelligence*, 18-10(1996)972-986.
- [23] T. Craciunescu, A. Murari, A. Alonso, P.T. Lang, G. Kocsis, I. Tiseanu, V. Zoita, "Application of Optical Flow Method for Imaging Diagnostic in JET", *J. Nucl. Mater.*, 400-3: 205-212, 2010.

**National Institute of Laser,
Plasma and Radiation Physics**

Scientific Report

**To the Contract 1EU-1/11.08.2008
For the year 2010**

Project BS-13 : *Theoretical modeling of the RWM feedback control considering neoclassical toroidal viscosity and error field penetration*

Specific Objective I

The determination of a general RWM dispersion relation for 2-D axisymmetric geometry in the presence of neoclassical viscosity and non-resonant error fields

Coordinator: Dr. I.G. Miron (CS III)
EFDA Task Agreement: WP10-MHD-03-03-xx-01

The aim of the first objective of the present project is to upgrade the previously derived cylindrical mathematical model to an axisymmetric 2-dimensional analytic model capable to illustrate the resistive wall mode (RWM) behavior. The ultimate task is to provide an explicit analytic dispersion relation of the RWM.

A 2-dimensional model provides a more realistic description of the phenomena involved by taking into account realistic plasma shape parameters like the Shafranov shift, toroidicity, ellipticity and triangularity that cannot be considered within a cylindrical model description. Consequently, flux (natural) coordinates will be used into calculus. The calculated metric coefficients will be functions of the above mentioned parameters. The angular dependence of the equilibrium magnetic field together with the irregular plasma shapes are responsible for neoclassical effects that finally give rise to the mechanism of toroidal momentum dissipation and neoclassical toroidal viscosity (NTV) global braking due to the non-resonant error fields destabilizing effect.

The assumption of a thin inhomogeneous resistive wall and an active system consisting of a number of rectangular, radially thin coils and detectors centred at the same local coordinates system is considered, the magnetic flux measured by the detector being amplified and fed back into the coils. Mode coupling effects are also considered.

In order to construct an analytic model, the following approximations are considered:

- *low inverse aspect ratio approximation (the calculus will be performed within the $\mathcal{O}(\epsilon^2)$ approximation, where $\epsilon = a / R_0$ is the inverse aspect ratio);*
- *thin resistive wall approximation*
- *the resistive wall and the active feedback coils and detectors are supposed to lie on magnetic surfaces.*

1) Equilibrium description

Within the low inverse aspect ration approximation, the obtained relations between the cylindrical polar coordinates aligned with the major axis of the plasma, (R, φ, Z) , and the flux (natural) coordinates (r, θ, φ) are:

$$R = R_0 - r \cos \theta - \frac{r^2}{R_0} (1 - \cos \theta) - a\epsilon \left[\Delta + \frac{r\Delta'}{2} (1 - \cos 2\theta) - \frac{E}{4} (3 \cos \theta - \cos 3\theta) - \frac{rE'}{4} (\cos \theta - \cos 3\theta) - \frac{T}{3} (2 \cos 2\theta + \cos 4\theta) - \frac{rT'}{6} (\cos 2\theta - \cos 4\theta) \right] + \vartheta(\epsilon^2) \quad (1)$$

$$Z = r \sin \theta - \frac{r^2}{2R_0} \sin 2\theta - a\epsilon \left[\frac{r\Delta'}{2} \sin 2\theta - \frac{E}{4} (3 \sin \theta - \sin 3\theta) - \frac{rE'}{4} (\sin \theta - \sin 3\theta) - \frac{T}{3} (2 \sin 2\theta + \sin 4\theta) - \frac{rT'}{6} (\sin 2\theta + \sin 4\theta) \right] + \vartheta(\epsilon^2) \quad (2)$$

r is the flux surface label (in $\vartheta(1)$ approximation is the distance from the magnetic axis) and θ is chosen such that the magnetic field lines are straight in (θ, φ) plane to assure the radial dependence only of the magnetic safety factor, $q(r)$. $\Delta(r)$, $E(r)$ and $T(r) \sim \vartheta(1)$ are the Shafranov shift, ellipticity and the triangularity, respectively. ' means the radial derivative. The covariant metric tensors $\{g_{ij}\}_{i,j=1,2,3}$ and the jacobian J are found in [1], whereas $\Delta(r)$, $E(r)$ and $T(r)$ satisfy [2]:

$$r(\Lambda_j') = \left(\frac{r^2}{a^2} - \frac{2rq^2 p'}{\epsilon^2} \right) \delta_{|j|1} + (j^2 - 1) \Lambda_j - 2r(1-s) \Lambda_j' + \vartheta(\epsilon^2) \quad (3)$$

where $s(r) \equiv rq'/q$, $\Lambda_j \equiv \Delta \delta_{|j|1} + E \delta_{|j|2} + T \delta_{|j|3}$ ($j=1,2,3$ and δ Kronecker delta) and $p(r)$ the pressure. Outside the plasma the pressure term disappears. The contravariant components of the equilibrium magnetic field are:

$$B^{r,\theta,\varphi} = \frac{B_0}{R_0} \left[1 + \frac{2r}{R_0} \cos \theta + \vartheta(\epsilon^2) \right] \left(0, \frac{1}{q}, 1 \right) \quad (4)$$

B_0 is the measured, real, toroidal equilibrium magnetic field in the magnetic axis.

2) Linearized perturbed MHD equations

The starting linearized MHD perturbed plasma equations that includes sound wave, flow damping and dissipative effects is [3]:

$$\gamma(\gamma + \nu) \rho \mathbf{v} = -c_s^2 \nabla(\nabla \cdot \mathbf{v}) - \gamma \nabla \Pi + \frac{1}{\mu_0} \{ \nabla \times [\nabla \times (\mathbf{v} \times \mathbf{B})] \} \times \mathbf{B} + \frac{1}{\mu_0} (\nabla \times \mathbf{B}) \times [\nabla \times (\mathbf{v} \times \mathbf{B})] \quad (5)$$

ν is the plasma flow damping due to charge exchange with neutrals, $\rho(r)$ is the mass density, $c_s(r)$ is the plasma sound speed and $\Pi = -3\eta(\mathbf{nn} - \tilde{\mathbf{I}}/3) : \nabla \mathbf{v}(\mathbf{nn} - \tilde{\mathbf{I}}/3)$ is the perturbed stress tensor ($\mathbf{n} = \mathbf{B}/B$). The combined effect of dissipative stabilization and neoclassical viscous torque destabilization is due to the toroidal component of the perturbed stress tensor, $-\mathbf{e}_\varphi \cdot (\nabla \Pi)$, where η is the ion viscosity coefficient. The perturbed magnetic

field is $\gamma \mathbf{b} = \nabla \times (\mathbf{v} \times \mathbf{B})$ and the perturbed plasma velocity is parameterized as $\mathbf{v} = (\gamma/B) \nabla \phi \times \mathbf{B}$, where $-\gamma\phi$ is the perturbed scalar electric potential. From $\exp(\gamma t)$ time dependence of the perturbed quantities, $\gamma = \gamma_0 + i(m\Omega_\theta - n\Omega_\varphi)$, where γ_0 is the pure growth rate of the perturbation and $\Omega_{\theta,\varphi}$ are the poloidal and toroidal angular velocities of the non-ideal MHD layer that develop at the corresponding rational surfaces where the (m,n) perturbation mode appears.

Using the θ and φ covariant components of equation (5) and eliminating $v_{||mn}$ Fourier components of the parallel plasma velocity, after a long and straightforward calculus, we have obtained the following 2-dimensional axisymmetric perturbed plasma system of equations at plasma boundary, within $\vartheta(\varepsilon^2)$ approximation:

$$\sum_{j=0}^4 \gamma_0^j \sum_{l=j}^4 \binom{l}{l-j} \sum_{h=m-3}^{m+3} [i(h\Omega_\theta - k\Omega_\varphi)]^{l-j} \left(P_{h,n,h-m}^l \phi_a^{h,n} + \tilde{P}_{h,n,h-m}^l \phi_a^{h,n'} \right) = 0 \quad (6)$$

$\phi_a^{h,n'} = d\phi_a^{h,n}/dr$ and $P_{h,n,h-m}^l, \tilde{P}_{h,n,h-m}^l$ are explicitly derived coefficients as functions of all the plasma boundary parameters taken into account: $\rho_a, \eta_a, \nu, c_{sa}, q_a, s_a, \Delta_a, \Delta'_a, E_a, E'_a, T_a, T'_a$. Due to the $\vartheta(\varepsilon^2)$ approximation, the mode coupling is limited to six adjacent neighboring poloidal modes of the central harmonic (m,n) (three more negative and three more positive poloidal modes) whereas the equilibrium quantities axisymmetry provides no toroidal mode coupling. However, within a higher approximation, more adjacent poloidal modes can be considered. The system of equations (6) can be viewed as an underdetermined algebraic system of equations with a double number of unknowns $\phi_a^{h,n}, \phi_a^{h,n'}$, $(h, m = m_1, \dots, m_2, n = n_1, \dots, n_2)$ compared to the number of equations. The rest of the equations are provided later by the "feedback part" of the problem.

3) Solving Laplace equation in vacuum

In vacuum the perturbed magnetic field is parameterized as $\mathbf{b} = \nabla \chi$ and satisfy Laplace equation, $\Delta \chi = 0$. To relate the perturbed physical quantities at the levels of plasma, resistive wall, active coils and detectors it is imperative to solve Laplace equation in vacuum.

The obtained form of Laplace equation (after angles integration) in flux coordinates is:

$$D_m^0 \chi^{m,n} + \sum_{\substack{j=-3 \\ j \neq 0}}^3 D_m^j \chi^{m+j,n} + \vartheta(\varepsilon^2) = 0 \quad (7)$$

where $D_m^0 = r^2 \partial^2 / \partial r^2 - r \partial / \partial r - m^2 \sim \vartheta(1)$ and $D_m^j \sim \vartheta(\varepsilon)$ are differential operators. If the solution is searched as $\chi^{m,n} = \chi^{m,n(0)} + \varepsilon \chi^{m,n(1)} + \vartheta(\varepsilon^2)$, where $\chi^{m,n(0)}, \chi^{m,n(1)} \sim \vartheta(1)$, the ε ordering scheme gives:

$$D_m^0 \chi^{m,n(0)} = 0 \quad (8)$$

$$D_m^0 \chi^{m,n(1)} = - \sum_{\substack{j=-3 \\ j \neq 0}}^3 D_m^j \chi^{m,n(0)} \quad (9)$$

Whereas the solution of eq. (8) is obvious, eq. (9) was analytically solved using the variation of parameters method. Finally, in the $r \in [r_1, r_2]$ interval (where $[r_1, r_2]$ can be $[a, r_w]$ or $[r_w, r_f]$, $r_{w,f}$ being the radial flux coordinates at the resistive wall and feedback coils, respectively), the solution in $\vartheta(\varepsilon^2)$ approximation has been obtained:

$$\chi^{m,n}(r) = c_{1r_1r_2}^{m,0}(r)\chi_{r_{1+}}^{m,n} + c_{2r_1r_2}^{m,0}(r)\chi_{r_{2-}}^{m,n} + \sum_{\substack{j=-3 \\ j \neq 0}}^3 [c_{1r_1r_2}^{m,j}(r)\chi_{r_{1+}}^{m+j,n} + c_{2r_1r_2}^{m,j}(r)\chi_{r_{2-}}^{m+j,n}] + \vartheta(\varepsilon^2) \quad (10)$$

where

$$c_{ir_1r_2}^{m,0}(r) \equiv \frac{(r/r_{3-i})^m - (r/r_{3-i})^{-m}}{(r_i/r_{3-i})^m - (r_i/r_{3-i})^{-m}} \sim \vartheta(1), \quad i=1,2 \quad (11)$$

and $\{c_{ir_1r_2}^{m,j}(r)\}_{i=1,2; j=-3,-2,-1,1,2,3} \sim \vartheta(\varepsilon)$ are explicitly analytic obtained coefficients (the $\vartheta(\varepsilon)$ corrections) as functions of $s(r)$ and $\{\Lambda_j\}_{j=1,2,3}$. $\chi_{r_{i\pm}}^{m,n} \equiv \chi^{m,n}(r_{i\pm})$. It has been assumed that the resistive wall and the active feedback coils and detectors lie on magnetic surfaces and $a < r_d < r_w < r_f$ (r_d is the radial flux coordinate of the detector).

In the $[r_f, \infty)$ interval the following solution has been obtained:

$$\chi^{m,n}(r) = c_{f\infty}^{m,0}(r)\chi_{f+}^{m,n} + \sum_{\substack{j=-3 \\ j \neq 0}}^3 c_{f\infty}^{m,j}(r)\chi_{f+}^{m+j,n} + \vartheta(\varepsilon^2) \quad (12)$$

where $c_{f\infty}^{m,0}(r) = (r/r_f)^{-m} \sim \vartheta(1)$ and $\{c_{f\infty}^{m,j}(r)\}_{j=-3,-2,-1,1,2,3} \sim \vartheta(\varepsilon)$ have been derived. From eq. (3), Δ , E and T can be calculated in vacuum:

$$\Delta(r) = (r^2/a^2)[\ln(r/a) + a\Delta'_a - 1/2] + \Delta_a - 1/2(a\Delta'_a - 1/2) \quad (13)$$

$$E(r) = (1/4)[(r^3/a^3)(E_a + aE'_a) + (a/r)(3E_a - aE'_a)] \quad (14)$$

$$T(r) = (1/6)[(r^4/a^4)(2T_a + aT'_a) + (a^2/r^2)(4T_a - aT'_a)] \quad (15)$$

The relations (10) and (12) we have derived are extensively used for the feedback equations derivation.

4) Feedback equations

The calculus is performed for a thin toroidally inhomogeneous resistive wall and an active system consisting of a number of rectangular, radially thin coils and detectors centred at the same local coordinates [4].

The most important relations that involve the feedback system influence on the instabilities are the ones that describe the jump of the scalar potential χ and its radial derivative χ' across the resistive wall and the active coils.

The discontinuity of the tangential perturbed magnetic field across the wall is described by $\chi_{w+} - \chi_{w-} = \mu_0 I_w$, where I_w is the radially integrated perturbed eddy currents induced in the resistive wall. Ampere and Ohm laws lead to $\gamma_0 \mathbf{b}_w = -\nabla \times (\eta_w \mathbf{e}_r \times \nabla I_w)$. \mathbf{b}_w is the perturbed magnetic field inside the wall and \mathbf{e}_r is the radial basis covariant vector. Using the above relations, the continuity of the perturbed normal contravariant magnetic field across the resistive wall is finally described by the following obtained relation:

$$\begin{aligned}
& \gamma_0 \mu_0 \delta_w \sum_n \left\{ \chi_{w+,-}^{m,n} + \sum_{\substack{j=-3 \\ j \neq 0}}^3 (-1)^{\delta_{|j|}} \left[a \varepsilon \Lambda'_j \chi_{w+,-}^{m+j,n} + \frac{m+j}{jr^2} \left(\frac{r^2}{R_0} \delta_{|j|} + a \varepsilon ((j^2-1) \Lambda_j - r(1-s) \Lambda'_j) \right) \chi_{w+,-}^{m+j,n} \right] \right\} \\
&= \sum_n \frac{\tilde{\eta}_{12}}{r^2} \left\{ m^2 (\chi_{w+}^{m,n} - \chi_{w-}^{m,n}) \right. \\
&+ \sum_{\substack{j=-3 \\ j \neq 0}}^3 (m+j) \left[(m+j) \frac{r}{R_0} \delta_{|j|} + \frac{2}{jr} (-1)^{\delta_{|j|}} \left(\frac{3r^2}{R_0} \delta_{|j|} + 2a \varepsilon ((j^2-1) \Lambda_j - r(1-s) \Lambda'_j) \right) \right] (\chi_{w+}^{m+j,n} - \chi_{w-}^{m+j,n}) \left. \right\}
\end{aligned} \tag{16}$$

The particular disposal of the resistive wall (HBT-EP tokamak type) from [4] is used. The plasma column is surrounded by two thin, concentric walls, disposed alternately, at the same radial flux coordinate, r_w . The (aluminium and stainless steel) walls do not overlap (in the angular sense). δ_w is the wall thickness. $\tilde{\eta}_{12}$ describes the toroidal mode coupling phenomenon due to the peculiar disposal of the resistive wall and corresponds to \tilde{T}_{12} from [4], where the aluminium and stainless steel characteristic time constants $\tau_{1,2}$ are replaced by the aluminium and stainless steel resistivities $\eta_{1,2}$. Eq. (16) is valid for both $\chi_{w+}^{m,n}$ and $\chi_{w-}^{m,n}$ (in the left hand) due to thin wall approximation.

To derive the jump relation across the active coils we entirely follow the method presented in [4] but using the flux (natural) coordinates. We have finally obtained:

$$\begin{aligned}
& \chi_{f+}^{m,n} - \chi_{f-}^{m,n} = - \frac{4\mu_0 R_0}{\pi^2 m^2 n R \delta_f \delta \theta_f} s_f^m \sin(m \delta \theta_f / 2) \sin[(n/2)(\Delta \varphi_f + \delta \varphi_f)] \\
& \times \sum_{h,k} \frac{1}{k} \left\{ \gamma_0 r_f \left[\left(c_{1wff}^{h,0} s_f^h S^{h,k,m,n} + \sum_{\substack{j=-3 \\ j \neq 0}}^3 \left(c_{1wff}^{h,0} I_{1f}^j + c_{1wff}^{h-j,j} \right) s_f^{h-j} S^{h-j,k,m,n} \right) \chi_{w+}^{m,n} \right. \right. \\
& + \left. \left(c_{2wff}^{h,0} s_f^h S^{h,k,m,n} + \sum_{\substack{j=-3 \\ j \neq 0}}^3 \left(c_{2wff}^{h,0} I_{1f}^j + h I_{2f}^j + c_{2wff}^{h-j,j} \right) s_f^{h-j} S^{h-j,k,m,n} \right) \chi_{f-}^{m,n} \right] \\
& + (\gamma_0 G_d + G_{pw}) \left[\left(c_{1awd}^{h,0} s_d^h S^{h,k,m,n} + \sum_{\substack{j=-3 \\ j \neq 0}}^3 \left(c_{1awd}^{h,0} I_{1d}^j + h c_{1awd}^{h,0} I_{2d}^j + c_{1awd}^{h-j,j} \right) s_d^{h-j} S^{h-j,k,m,n} \right) \chi_a^{m,n} \right. \\
& + \left. \left(c_{2awd}^{h,0} s_d^h S^{h,k,m,n} + \sum_{\substack{j=-3 \\ j \neq 0}}^3 \left(c_{2awd}^{h,0} I_{1d}^j + h c_{2awd}^{h,0} I_{2d}^j + c_{2awd}^{h-j,j} \right) s_d^{h-j} S^{h-j,k,m,n} \right) \chi_{w-}^{m,n} \right] \left. \right\}
\end{aligned} \tag{17}$$

For an efficient feedback, the coils are centered outside the stainless steel wall segments. R , δ_f , $\delta \theta_f$, $\delta \varphi_f$, $\Delta \theta_f$, $\Delta \varphi_f$ are the coil resistance, thickness, poloidal leg angular extent, toroidal leg angular extent, poloidal angular extent and toroidal angular extent, respectively. $s_i^h \equiv \sin(m \Delta \theta_i / 2) / m$, $r_i = r_d, r_f$. $\{c_{ir_2 r_3}^{h,j}\}_{i=1,2} \equiv \{c_{ir_2}^{h,j}(r_3)\}_{i=1,2}$. G_d is the derivative amplification factor and G_{pw} is the normalized proportional amplification factor. $I_{1,2r_i}^j$ ($r_i = r_d, r_f$) explicitly describe the influence of $\{\Lambda_j\}_{j=1,2,3}$. $S^{h,k,m,n}$ is defined in [4]. Eq. (16) and (17) are extremely

important because they allow to finally gather the influence of the feedback system in terms of $\chi_a^{m,n}$ and $\chi_a^{m,n'}$ and provide the rest of the equations as to complete the system of equations (6). Assuming very small values for $\rho(r)$ and $\eta(r)$ at the edge of the plasma, the continuity of the perturbed magnetic field \mathbf{b} across the plasma boundary is considered. Keeping into account the different parameterizations of \mathbf{b} inside (ϕ) and outside (χ) the plasma, after a long and laborious calculus, we have finally obtained the system of equations:

$$\sum_{j=0}^2 \gamma_0^j \sum_{h,k} \left(F_{m,n}^{j,h,k} \phi_a^{h,k} + \tilde{F}_{m,n}^{j,h,k} \phi_a^{h,k'} \right) = 0 \quad (18)$$

The above system of equations couples an unlimited number of poloidal and toroidal modes. $F_{m,n}^{j,h,k}$ and $\tilde{F}_{m,n}^{j,h,k}$ are explicit analytic derived coefficients as functions of all the feedback parameters taken into account: r_w , r_f , r_d , R , δ_f , $\delta\theta_f$, $\delta\varphi_f$, $\Delta\theta_f$, $\Delta\varphi_f$, G_d , G_p , $\Delta\theta_d$ (detector poloidal angular extent), $\Delta\varphi_d$ (detector toroidal angular extent), δ_{w1} (aluminium wall thickness), δ_{w2} (stainless steel wall thickness), $\Delta\varphi_{w2}$ (stainless steel wall toroidal angular extent), N (the common number of aluminium and stainless steel wall segments), $\{\theta_p\}_{p=1,\dots,M}$ (the randomly disposed poloidal angles where the feedback coils and detectors are centered), Δ_a , Δ'_a , E_a , E'_a , T_a , T'_a (Λ_j and Λ'_j in r_w , r_f and r_d are calculated using eq. (13)-(15)).

5) The general dispersion relation

With the notation:

$$\mathcal{Q}_{m,n}^{j,h,k} = \sum_{l=j}^4 \binom{l}{j} [i(h\Omega_\theta - k\Omega_\varphi)]^{l-j} P_{h,k,h-m}^l \delta_{k,n} \Theta_{h,m} \quad (19)$$

and a similar notation for $\tilde{\mathcal{Q}}_{m,n}^{j,h,k}$, where $\Theta_{h,m}$ is 1 for $h = m-3, \dots, m+3$ and 0 in the rest, the system of equations (6) becomes:

$$\sum_{j=0}^4 \gamma_0^j \sum_{h,k} \left(\mathcal{Q}_{m,n}^{j,h,k} \phi_a^{h,k} + \tilde{\mathcal{Q}}_{m,n}^{j,h,k} \phi_a^{h,k'} \right) = 0 \quad (20)$$

(18) and (20) now form a complete algebraic system with $2L$ equations and $2L$ unknowns $\phi_a^{h,k}, \phi_a^{h,k'}$, where $L = (m_2 - m_1 + 1)(n_2 - n_1 + 1)$. The plasma system of the equations (20) provides a $L \times 2L$ block diagonal matrix within the full matrix of the system. Using the Leibniz expansion [4], the null determinant of the $2L \times 2L$ matrix of the system finally leads to the following compact polynomial form that provides the dispersion relation of the RWM we are interested:

$$\sum_{k=0}^{6L} \gamma_0^k \sum_{\substack{l_1, \dots, l_{2L}=1 \\ \text{distinct}}}^{2L} \text{sgn}(l_1, \dots, l_{2L}) \sum_{\substack{\alpha_1, \dots, \alpha_{2L}=0 \\ \alpha_1 + \dots + \alpha_{2L}=k}}^4 \prod_{s=1}^{2L} \Gamma_{s\alpha_s}^{l_s} = 0 \quad (21)$$

The index ordering transformation is presented in [4]. We have analytically derived $\Gamma_{s\alpha_s}^{l_s}$:

$$\begin{aligned}\Gamma_{s\alpha_s}^{l_s} &= Q_{s\alpha_s}^{l_s} H(L-l_s)H(L-s) + \tilde{Q}_{s\alpha_s}^{l_s} H(l_s-L-1)H(L-s) \\ &+ F_{s\alpha_s}^{l_s} H(L-l_s)H(s-L-1)H(2-\alpha_s) + \tilde{F}_{s\alpha_s}^{l_s} H(l_s-L-1)H(s-L-1)H(2-\alpha_s)\end{aligned}\quad (22)$$

H is the Heaviside unit step function.

Input data: $m_1, m_2, n_1, n_2, \rho_a, \eta_a, v, c_{sa}, q_a, q_0, s_a, \Delta_a, \Delta'_a, E_a, E'_a, T_a, T'_a, r_w, r_f, r_d, R, \delta_f, \delta\theta_f, \delta\phi_f, \Delta\theta_f, \Delta\phi_f, \Delta\theta_d, \Delta\phi_d, G_d, G_p, \delta_{w1}, \delta_{w2}, \eta_{w1}, \eta_{w2}, \Delta\phi_{w2}, N, M, \{\theta_p\}_{p=1,\dots,M}$.

6) Qualitative description of the error field penetration

RWM is not affected by the error fields unless RWM attains its marginal stability ($|\gamma_0| \rightarrow 0$). A static magnetic error field $\mathbf{b}_e = \nabla \chi_e$ in the absence of the plasma is considered ($\Delta\chi_e = 0, \chi_e^{m,n}(0) = \chi_e^{m,n}(\infty) = 0$). For simplicity and relevance reasons, we consider only the jump across the resistive wall for the magnetic error field. Consequently:

$$\chi_e^{m,n} \equiv \begin{cases} \chi_{e+}^{m,n} (r/r_w)^m, & r \leq r_w \\ \chi_{e-}^{m,n} (r/r_w)^{-m}, & r > r_w \end{cases} \quad (23)$$

where $\chi_{e\pm}^{m,n} \equiv \chi_e^{m,n}(r_{w\pm})$. The $\vartheta(\varepsilon)$ term in (23) has been dropped out due to the smallness of $\chi_e^{m,n}$. From the continuity of the normal contravariant magnetic error field across the wall, we have $\chi_{e+}^{m,n} - \chi_{e-}^{m,n} \equiv 2\chi_{e+}^{m,n}$. A straight and simple calculus leads to:

$$\sum_{j=0}^2 \gamma_0^j \sum_{h,k} \left(F_{m,n}^{j,h,k} \phi_a^{h,k} + \tilde{F}_{m,n}^{j,h,k} \phi_a^{h,k} \right) = 2e^{-\gamma_0 t} \sum_{h,k} \beta_{m,n,w-}^{h,k} \chi_{e+}^{h,k} \quad (24)$$

where, $\{\beta_{0w-}^{0,h,k}\}_{h,k}$ are explicitly derived feedback terms. It can be seen that the system of equations (18) becomes (24) in the presence of the error fields.

As long as the RWM is weakly unstable (but not marginally stable) (18) and (20) hold and the determinant of the system is zero:

$$\Delta_{2L \times 2L} \equiv \det \begin{pmatrix} \mathbf{Q} & \tilde{\mathbf{Q}} \\ \mathbf{F} & \tilde{\mathbf{F}} \end{pmatrix} = 0 \quad (25)$$

where the matrices are $\mathbf{Q} \equiv \left(\sum_{j=0}^4 \gamma_0^j Q_{m,n}^{j,h,k} \right)_{\substack{h,m=m_1,\dots,m_2 \\ k,n=n_1,\dots,n_2}}, \quad \tilde{\mathbf{Q}} \equiv \left(\sum_{j=0}^4 \gamma_0^j \tilde{Q}_{m,n}^{j,h,k} \right)_{\substack{h,m=m_1,\dots,m_2 \\ k,n=n_1,\dots,n_2}},$
 $\mathbf{F} \equiv \left(\sum_{j=0}^2 \gamma_0^j F_{m,n}^{j,h,k} \right)_{\substack{h,m=m_1,\dots,m_2 \\ k,n=n_1,\dots,n_2}}, \quad \tilde{\mathbf{F}} \equiv \left(\sum_{j=0}^2 \gamma_0^j \tilde{F}_{m,n}^{j,h,k} \right)_{\substack{h,m=m_1,\dots,m_2 \\ k,n=n_1,\dots,n_2}} \text{ and } \mathbf{B} \equiv \left(2e^{-\gamma_0 t} \beta_{m,n,w-}^{h,k} \chi_{e+}^{h,k} \right)_{\substack{h,m=m_1,\dots,m_2 \\ k,n=n_1,\dots,n_2}}.$

Because it is assumed that the stabilization conditions slightly change from weak instability to marginal stability, intuitively [5], we can assume that, at marginal stability, the influence of the error fields highly destabilizes the RWM:

$$|\phi_a^{h,k}| = \lim_{|\gamma_0| \rightarrow 0} \frac{\det \begin{pmatrix} \mathbf{0} & \tilde{\mathbf{Q}} \\ \mathbf{B} & \tilde{\mathbf{F}} \end{pmatrix}}{\Delta_{2L \times 2L}} \rightarrow \infty, \quad |\phi_a^{h,k'}| = \lim_{|\gamma_0| \rightarrow 0} \frac{\det \begin{pmatrix} \mathbf{Q} & \mathbf{0} \\ \mathbf{F} & \mathbf{B} \end{pmatrix}}{\Delta_{2L \times 2L}} \rightarrow \infty$$

However, this is a pure qualitative description. The valid description of the phenomena will be provided later within the frame of a dynamic model (well-thought $\gamma_0 \rightarrow \partial/\partial t$ substitution) where the NTV destabilizing influence as a result of the non-resonant error field coupling will be presented.

Conclusions

A full axisymmetric 2-dimensional analytic theoretical model for the RWM stabilization has been built within the large aspect ratio approximation, the thin resistive shell condition and the assumption that the resistive shell and the active feedback coils are disposed on magnetic surfaces. A compact dispersion relation of the RWM, (21), has been obtained. No huge numerical codes are needed. A simple Matlab code to solve a polynomial equation is sufficient.

References

- [1] E. Lazzaro and P. Zanca, *Phys. Plasmas* **10** (2003) 2399.
- [2] R. Fitzpatrick, *Phys. Plasmas* **16** (2009) 032502.
- [3] R. Fitzpatrick and J. Bialek, *Phys. Plasmas* **13** (2006) 072512.
- [4] I.G. Miron, *Plasma Phys. Control. Fusion* **50** (2008) 095003.
- [5] R. Fitzpatrick, *Phys. Plasmas* **9** (2002) 3459.

X-RAY MICRO-TOMOGRAPHY STUDIES CFC SAMPLES FOR POROSITY NETWORK CHARACTERIZATION

- WP10-PWI-01-02-01/MEdC (BS_20A) -

EURATOM-MEdC Association, Romania

National Institute for Lasers, Plasma and Radiation Physics, Bucharest, Romania

1. Introduction and objectives

The CFC monoblocks of the ITER divertor vertical target must sustain high heat fluxes of 10 MW/m² during 400 s (normal operation) and up to 20 MW/m² during 10 s (off-normal event). Carbon-carbon fibre composites (CFCs) have a unique combination of high conductivity, low Z and resistance to damage due to high heat loads. Given the demanding environmental requirements in the ITER divertor, specially developed CFCs are required as plasma facing components (PFC) materials.

The problem of fuel retention in carbon material is a major concern because tritium is radioactive, and the amount allowed within the ITER installation is an essential safety issue. From *gas balance analysis*, common features on the retention behaviour have been observed in different machines. It shows an initial high retention rate in a first phase of the discharge, decreasing towards a steady state value in a second phase. So far, most data on retention were obtained in all-carbon machines, so that comparison with carbon free machines (all-W ASDEX Upgrade, future ITER like Wall in JET) needs to be performed for a better prediction for ITER.

Scaling of retention rate as a function of plasma/ machine parameters is only poorly characterized (injection rate, incident flux/fluence, PFC materials, PFC temperature). However, the main retention mechanisms have been identified (co-deposition with C and/or Be, bulk diffusion and trapping in CFC and W) but their relative contributions in ITER conditions are still uncertain, and are a topic of active research, from laboratory experiments, modelling as well as integrated tokamak experiments [1,2].

From earlier investigations the retention in the material bulk was considered to be less critical than the retention in co-deposited layers. Recent gas balance experiments in Tore Supra [3,4] indicated, however, that significant fractions of fuel can be stored in CFC materials via this mechanism. It was attributed to a higher effective diffusion of H in the bulk of CFC due to a relatively high porosity of these materials of $\approx 10\text{-}15\%$.

Hence, the accurate 3D porosity description of the CFC materials would provide an essential input for the quantization of the fuel retention in material bulk. In this project we address the problem of quantitative characterization of the porosity structure of the carbon reinforced fiber (CFC) materials by high resolution X-ray tomography. This topic is included in the EFDA 2010 Work Programme, Task Agreement WP10-PWI-01 "Fuel retention as a function of wall materials foreseen for ITER" organized under the Special Expert Working Group (SEWG) "Gas balance and fuel retention".

Objectives of the task

The aim of this Task Agreement is to improve our knowledge on fuel retention in wall materials foreseen for ITER using particle balance to evaluate “how many” particles are retained in the vessel and post mortem analysis to assess where these particles are retained. It is worth noting that these methods are complementary.

The scientific objectives of the task are to:

- perform an extensive post mortem analysis of PFCs for comparison with integrated particle balance results;
- assess sources of possible uncertainties on both methods (such as disruptions, outgassing, cleaning discharges for particle balance, non toroidal/poloidal uniformity, retention in gaps and hidden areas, bulk diffusion for post mortem analysis);
- establish and perform a complementary analysis programme to progress in identifying the retention mechanisms at stake;
- on a longer term : propose ITER relevant fuel retention diagnostics, from particle balance, in situ and/or post mortem analysis

Within MEdC EURATOM Association we participate at the subtask WP10-PWI-01-02:

Characterization of the retention mechanisms using particle balance and post mortem analysis (AUG, TS, other relevant devices (JET for comparison), analysis in several associations)

The main objectives of this subtask are:

- Perform an extensive post mortem analysis of PFCs for assessing where the fuel retained in the vessel is located: deposited layers, gaps, bulk material, flakes, remote areas, below limiter/divertor in order to improve mitigation measures (in plasma operation as well as for the design of PFCs) and fuel removal techniques
- Comparison with integrated particle balance results.
- Establish and perform complementary analysis program to progress in identifying the retention mechanisms at stake

Our main contribution (WP10-PWI-01-02-02/MEdC/BS/PS) concentrates on the topic: *X-ray micro-tomography studies CFC samples for porosity network characterization* and has following objectives:

- Participation at DITS project - post mortem analysis by providing high resolution tomography measurements on CFC samples
- Qualification of the initial porosity of the new CFC ITER reference material NB41
- Porosity characterization of tungsten coated CFC samples

During the reporting period (January-June 2010) we have carried out the following research activities: i) determination of microtomography scanning parameters for optimum space and density resolution on miniaturized graphite and CFC samples ii) optimized tomography measurement of the 3D model of relevant volumes of CFC materials.

2. Results and discussion

Most experiments were carried out at our newly upgraded X-ray tomography facility NanoCT (Fig.

1). In <http://tomography.inflpr.ro> one gives a more detailed NanoCT system description and its overall parameters. A limited series of experiments were performed on a high end tomography facility which uses an advanced transmission X-ray tube with a high power diamond target and a 16 bits flat

panel detection system.

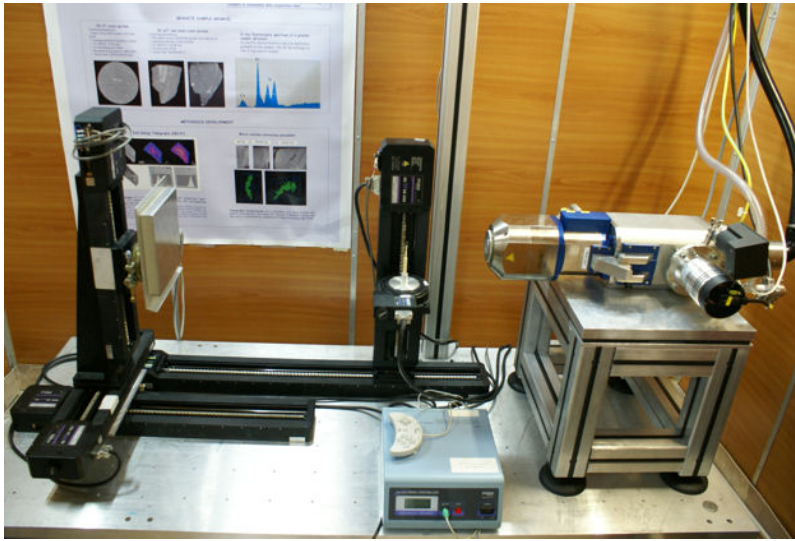


Figure 1 – View of NanoCT facility

Tomography measurements were performed on relatively large volumes of two type of CFC samples (former ITER reference CFC NB31, JET CFC DMS780 and for reference on a porosity free fine-grain graphite EK98).

Moderate resolution measurements of CFC rods of $5 \times 5 \times 5 \text{ mm}^3$ at voxel resolution of approx. $14 \text{ }\mu\text{m}$ with an estimated minimum detectable feature of cca. $15\text{--}20 \text{ }\mu\text{m}$ have been reported in the Annual Report of the previous year (January-December 2009). These measurements were devoted to the optimization of the X-ray source working parameters (high voltage and current) as well as the detection parameters (pitch size and integration time).

Once the optimum parameters have been determined one has preceded to high resolution measurements ($2.5 \text{ }\mu\text{m}/\text{voxel}$) on same CFC samples by the “offset tomography” technique [7].

A set of up to 1440 of radiographies at equidistant angles have been used for high resolution fully 3D tomography. Figure 2 shows representative tomographic images with 14 , 5 and $2.5 \text{ }\mu\text{m}$ per voxel of CFC of type Nb31. The images with $5 \text{ }\mu\text{m}$ and $2.5 \text{ }\mu\text{m}$ were obtained with the newly implemented "offset tomography" scanning method. A set of up to 1440 of radiographies at equidistant angles have been used for high resolution fully 3D tomography. Offset tomography is a powerful technique to almost double the magnification factor (accordingly doubling the space resolution) for a given detector size. Same high resolution ($2.5 \text{ }\mu\text{m}$) tomography cross-sections for the CFC DMS780 sample are also measured and reported elsewhere.

While the maximum resolution of $2.5 \text{ }\mu\text{m}$ per voxel on a relatively large sample is a remarkable performance the images noise might be not sufficient for accurate porosity factor evaluation. In order to reduce the image noise we have carried out following steps: i) reduction of reconstruction artefacts like “ring artefacts” and “beam hardening artefacts” and ii) upgrade the irradiation head of our X-ray tube with a high power diamond target. A 10-fold increase in thermal conductivity has been achieved compared to conventional transmission targets.

Hence high energy electron beams can be kept in focus to maintain small focal spot size for high image resolution. Using a JIMA mask, a test pattern of 2 μm can be clearly resolved even for a target power up to 20 Watts.

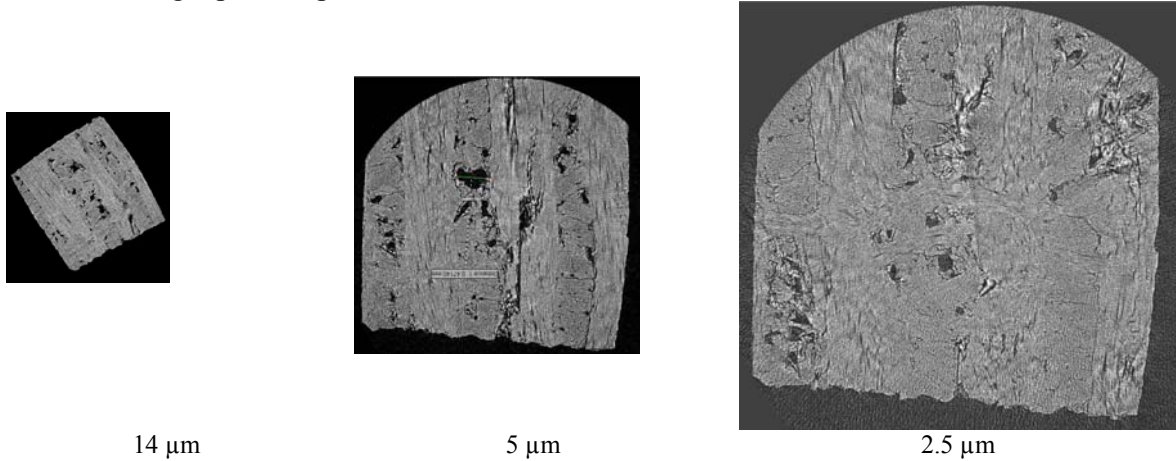


Figure 2 - CFC Nb31 - representative images of tomographic reconstructions with 14, 5 and 2.5 μm per voxel. The images with 5 μm and 2.5 μm were obtained with the newly implemented "offset tomography" scanning method.

Determination of the X-ray focus size by the Micro Resolution Chart for X-ray

In order to optimize the scanning parameters for microCT measurements of the CFC samples we have tested different transmission targets and performed focus spot size measurements using a JIMA mask (see characteristics in the figure below).

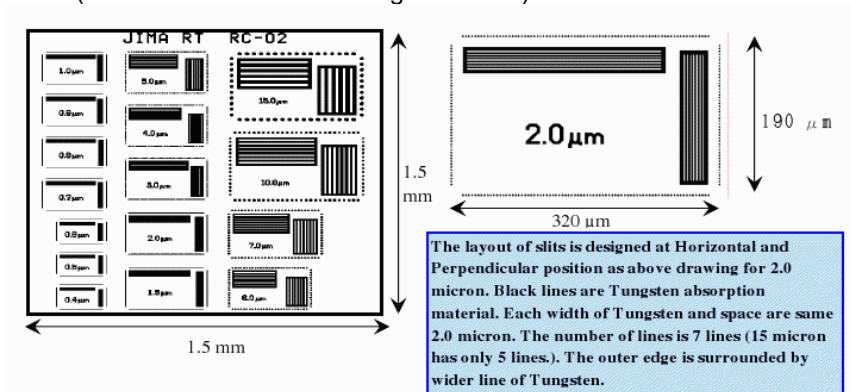


Figure 3 - Micro Resolution Chart for X-ray 0.4-15 μm

Four different types of transmission targets have been tested: the standard W target on aluminum window, thin W target on beryllium window, thin Mo target on beryllium window and W target on diamond window.

Figure 4 shows the resolution obtained with the thin W target on beryllium window. We concluded that a space resolution of 0.8 microns is appropriate for the tomography of the CFC samples.

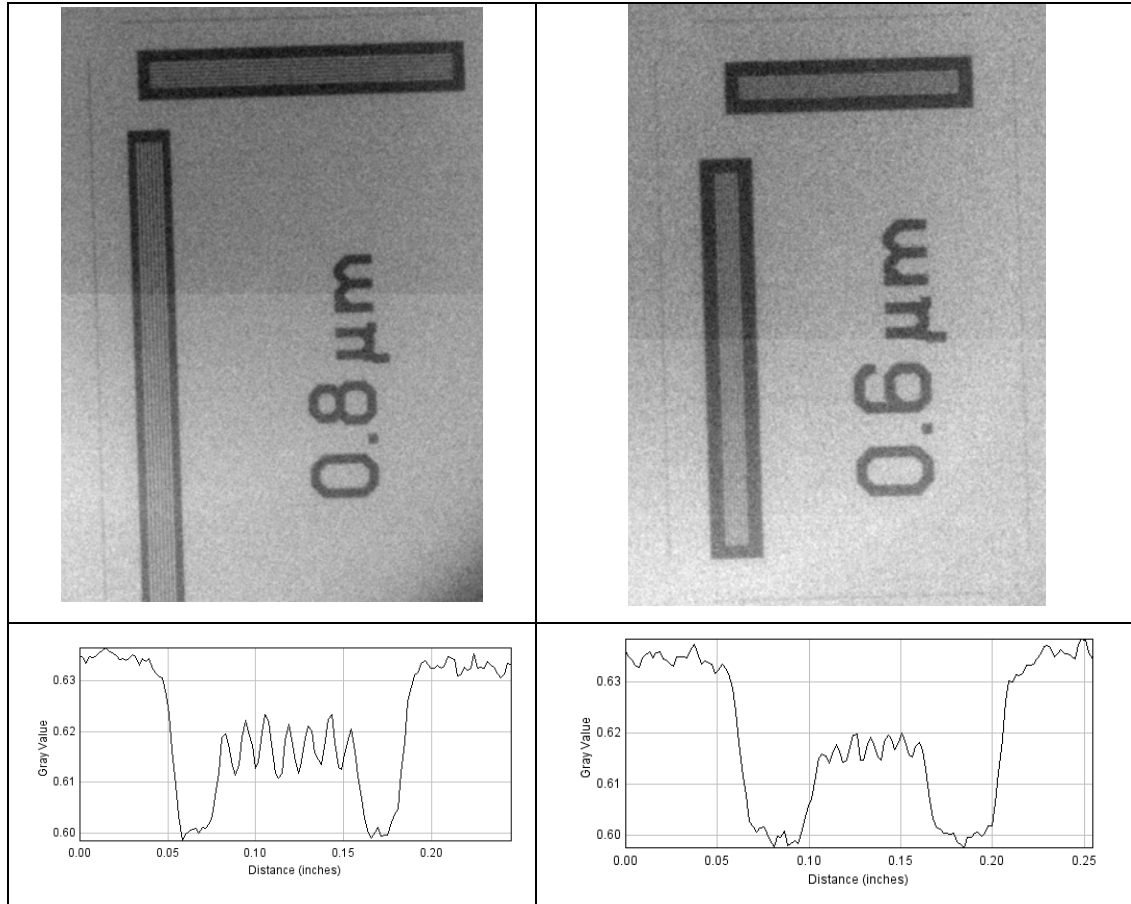
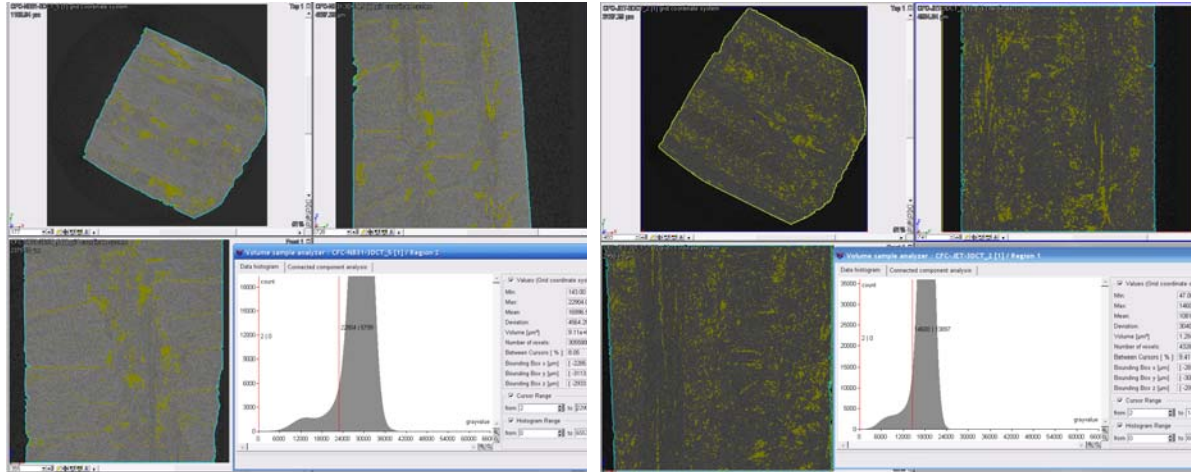


Figure 4 - Micro Resolution Chart images for thin W target on beryllium window

Quantitative evaluation of the sample porosity factor

The 3D reconstructed volumes can be processed in order to determine the main CFC network porosity characteristics. For the quantitative analysis of the porosity structure in terms of total void fraction, network connectivity, wall thicknesses we used a powerful 3-D visualization and measurement software VG Studio MAX of Volume Graphics GmbH, Germany. In Figure 5 we introduce some of the data post-processing steps. The first one is to find an optimal choice for the threshold level, in order to create a correct border between CFC and porous regions. A detailed inspection of this demarcation is performed while navigating through the reconstructed volume along transversal, longitudinal and sagittal cross-sections. After validation, the reconstructed volume is segmented and the porous structure is extracted as an independent object which can be represented also as a 3D structure. With the volume analysis module we determined the absolute value of porosity factor. The defect analysis tool can be used to determine the voids volume/size/projected area distribution.

The porosity factors calculation procedures for the two types of fusion technology relevant CFC samples are illustrated in Figure 5. As input data we used the reconstructed volumes delivered by the high end tomography facility. The porosity factors values are in good agreement with the manufacturer nominal specifications.



CFC NB31: 6 $\mu\text{m}/\text{voxel}$; porosity factor 8.1% CFC DMS780: 6 $\mu\text{m}/\text{voxel}$; porosity factor 9.4%

Figure 5: Post-processing steps of the reconstructed volume data in order to obtain the CFC NB31 and DMS780 porosity factors. The input data were obtained the W target on diamond window.

In Figure 6 one can note that the porosity factor of the NB11 CFC (approx. 12.5%) sample measured in the frame of the DITS post mortem analysis is significantly higher than the new, more advanced NB31 and DMS780 CFC materials.

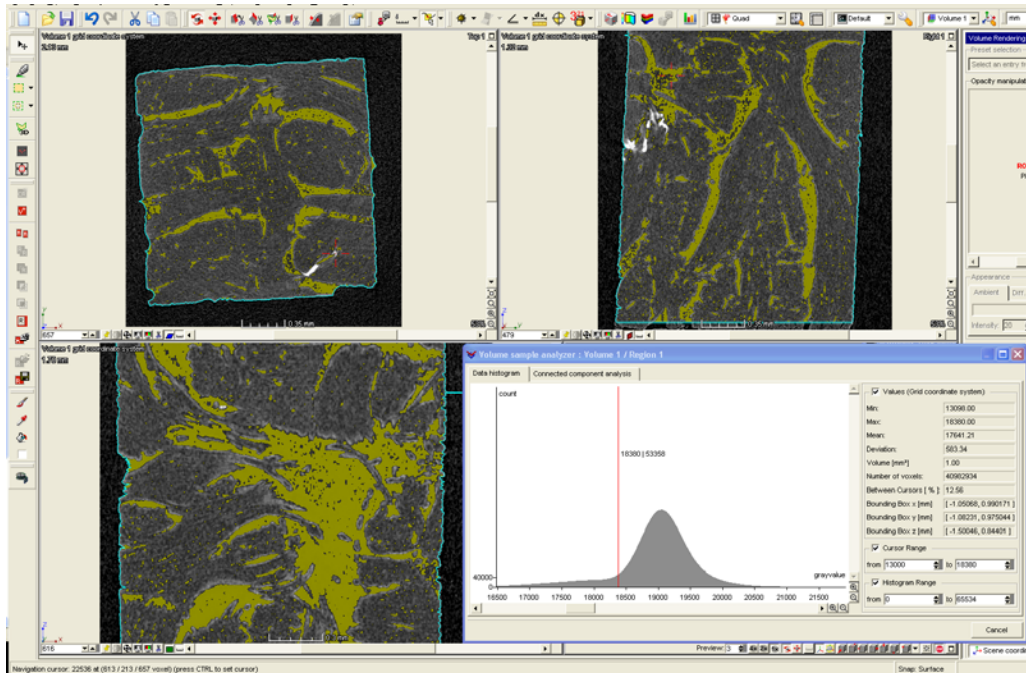


Figure 6: Post-processing steps of the reconstructed volume data in order to obtain the CFC NB11(Tore Supra) porosity factor. The input data were obtained the thin W target on beryllium window.

3. Conclusion and future work

High resolution cone beam tomography has been optimized for CFC samples. One important result was establishing the dependence of the porosity evaluation accuracy on the space resolution and the amount of tomography images noise.

A procedure for the quantitative evaluation of the sample porosity factor has been introduced and tested. For example for CFC NB31 we obtained porosity factors of around 8% and for CFC DMS780 of around 9.4%, in very good agreement with the manufacturer nominal values.

Based on the results obtained during the optimization procedure we began the tomography analysis of the CFC samples received within the Deuterium Inventory in Tore Supra (DITS) post mortem analysis by providing high resolution tomography measurements on CFC samples. Our current 3D micro-tomography reconstructions for relatively large samples of CFC (NB31 and DMS780) could be considered a good basis for the characterization of the initial porosity of the new CFC ITER reference material NB41.

Results on the "X-ray micro-tomography studies on CFC samples for porosity network characterization" will be presented at the Annual meeting of Special Expert Working Groups (SEWG) on «Fuel retention » organized at IPP-Garching 19-21 July 2010. A contribution will be also presented at SOFT 2010, Porto, 27 September - 1st October 2010.

4. Acknowledgement

The research activities to be conducted in this project are relevant for the EFDA 2010 Work Programme, WP10-PWI-01-02-01 "Fuel retention as a function of wall materials foreseen for ITER" organized under the Special Expert Working Group (SEWG) "Gas balance and fuel retention".

References

1. A Kreter et al, Deuterium retention in different carbon materials exposed in TEXTOR, Journal of Physics: Conference Series 100 (2008) 062024
2. A T Peacock, M Merola, M A Pick and R Tivey, Status of CFC development in Europe for ITER, Phys. Scr. T128 (2007) 23–28
3. E. Tsitrone, D. Reiter, T. Loarer, C. Brosset, J. Bucalossi, L. Begrambekov, C. Grisolia, A. Grosman, J. Gunn, J. Hogan, R. Mitteau, B. Pérourié, P. Ghendrih, R. Reichle and P. Roubin, Role of wall implantation of charge exchange neutrals in the deuterium retention for Tore Supra long discharges, J. Nucl. Mater. 337–339 (2005), p. 539.

4. J. Bucalossi, C. Brosset, B. Pégourié, E. Tsitrone, E. Dufour, A. Eckedahl, A. Geraud, M. Goniche, J. Gunn, T. Loarer, P. Monier-Garbet, J.C. Vallet, S. Vartanian, Deuterium in-vessel retention characterisation through the use of particle balance on Tore Supra, J. Nucl. Mater. 363–365 (2007), p. 759.
5. VGStudio MAX, Release 2.0, Volume Graphics, <http://www.volumegraphics.com>
6. I. Tiseanu, T. Craciunescu, C. Dobrea, A. Sima, Advanced X-ray imaging techniques for non-destructive analysis of fusion materials, Romanian Conference on Advanced Materials ROCAM 2009, August 25-28th, 2009, Brasov, Romania

**ANALIZA EROZIUNII STRATURILOR NANOCOMPOZITE PRIN
ABSORTIE/FLUORESCENTA DE RAZE X DE INALTA REZOLUTIE SPATIALA
(X-RAY MICROBEAM ABSORPTION/FLUORESCENCE METHOD AS A NON-INVASIVE
SOLUTION FOR INVESTIGATION OF THE EROSION OF W COATINGS ON
GRAPHITE/CFC)**

WP10-PWI-05-02-01/MEdC/BS/PS (BS-20B)

Ion Tiseanu, Teddy Craciunescu, Cosmin Dobrea, Adrian Sima

EURATOM-MEdC Association, Romania

National Institute for Lasers, Plasma and Radiation Physics, Bucharest, Romania

1. Introduction

Currently, the primary materials choice for ITER (International Thermonuclear Experimental Reactor) is a full beryllium main wall with CFC at the strike points and tungsten at divertor baffles and dome. Since this combination has never been tested in a tokamak, ITER-like Wall project has been launched at JET, consisting of 10 μm W coating of approx. 1,000 CFC tiles.

In connection with this task, the main objectives of our project consist in developing of a non-destructive technique for the evaluation of the W coating uniformity as well as a quantitative mapping of the multilayer compositions and thicknesses.

In 2010 the main objectives of the project are the following:

- Quantitative evaluation of the thickness/uniformity/erosion/deposition of the tungsten coatings on graphite tiles from ASDEX Upgrade and of the tungsten coatings on ITER-like CFC tiles. Marker probes of Al C Ni W will be also measured.
- Comparison with previous quantitative analysis with EPMA, RBS and NRA.
- Elaboration of a technical concept for a compact/low cost instrument based on X-ray micro-fluorescence to be used in high productivity coating analysis. erosion patterns.

During the reporting period a combined X-ray absorption/fluorescence method for erosion analysis was evaluated. Preliminary tests proved that the method is able to provide information about the uniformity of the CFC coating and can be used to determine its thickness. The preliminary experiments proved also that the lateral resolution is $\sim 30 \mu\text{m}$ and the in-depth resolution is $\sim 3\%$ of the layer thickness. The work was continued by establishing a well defined and reliable experimental setup and by validating the technique on real-life samples from ASDEX-Upgrade.

2. Methods and results

The method for erosion analysis was implemented using the Tomo-Analytic system (Figure 1), which we developed especially for fusion materials analysis [1,2]. Tomo-Analytic is a combined X-ray fluorescence (XRF) and cone-beam tomography (3DCT) system for the noninvasive 3-D morphology and composition mapping. With its high space resolution,

delivered by X-ray focalization with a polycapillary lens, the XRF method permits the characterization of complex structures with lateral resolution of around 20 μm . The implementation of a confocal geometry realized with the attachment of a polycapillary conic collimator to the X-ray detector further allows the extension of capabilities of the instrument up to fluorescence tomography (3-D composition mapping). The XRF analysis with Fundamental Parameters (FP) converts elemental peak intensities to elemental concentrations and/or film thicknesses.



Overall performances

Microtomography

Spatial Resolution $\cong 20\mu\text{m}$
 Density Resolution $> 1 \%$
 Sample Dimensions: Diameter $< 40 \text{ mm}$,
 Height $< 200 \text{ mm}$

Reconstruction time $\cong 5 \text{ min}$

Microfluorescence

Spatial Resolution $\cong 30\mu\text{m}$
 Thickness Resolution $\cong 2 \%$ of total layer
 Probe Dimensions: $100 \times 100 \text{ mm}^2$

<http://tomography.inflpr.ro/>

Figure 1 – View of Tomo-Analytic (left) and main technical characteristics (right)

The 3DCT component is configured to take highly resolved (48 μm) radiographic views of the object in order to build a 3-D model of its internal structure. 2-D slices through this volume can be viewed as images, or the 3-D volume may be rendered, sliced, and measured directly. For the NDT inspection of miniaturized samples the microtomography analysis is guaranteed for feature recognition better than 15 μm . 3-D tomographic reconstructions are obtained by a proprietary highly optimized computer code based on a modified Feldkamp algorithm.

The problem of evaluating the thickness uniformity of graphite/CFC with metallic coatings for a large number of samples was addressed also in case of the X-ray fluorescence analysis. In order to reduce the measuring time we replaced the multichannel analyzer (MCA) of the Tomo-Analytic system - Amptek MCA8000A - with a new one FAST MCA-3Series. The new MCA ensures a much faster and more flexible data transfer of spectral data to the PC and allows an improved control of the acquisition process. The MCA-3 Series is a family of PC-based software controlled PCI-bus Multichannel Analyzers. The design is capable to convert incoming signals at up-to 10^6 events/s or collect data at rates of up-to 5 Megaevents/s. The on board ultra fast pulse height analyzing 8k ADC is characterized by a 500 ns conversion time for Pulse-Height Analysis. No dead-time between channels, no end-of-sweep dead-time are also extremely valuable characteristics of the MCA. The dwell time extends from 100 ns to 50s (200ns to 50s using two inputs). The large data memory can be segmented to enable to accumulate successive measurements. Spectra accumulated in sequential PHA mode can be displayed in a two-dimensional array. The operating software allows the integration in the Tomo-Analytic application which was developed on a combined Labview/C++ platform.

2.1 Microbeam fluorescence benchmark

A number of experiments were performed in order to determine the parameters of the system and its usefulness for erosion analysis. The spatial resolution of the micro-beam fluorescence component was determined using a Cu grid (Figure 2.a). The double grid structure (32 μm and 18 μm , respectively) was scanned along a line, using a step of 10 μm and the following X-ray tube parameters: HV = 40 KV, I = 400 mA. At each step the X-ray spectrum was recorded and the evolution of the Cu $K\alpha$ = 8.06 keV peaks areas was recorded along the scanning line. Figure 2.b demonstrates the ability of the system to recognize the thick grid, so a spatial resolution of ~ 30 μm is guaranteed.

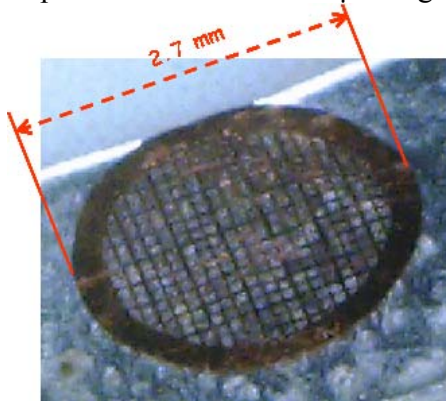


Figure 2.a – Cu grid used for spatial resolution determination. Grid characteristics: border thickness = 260 μm , thick grid = 32 μm , thin grid = 18 μm .

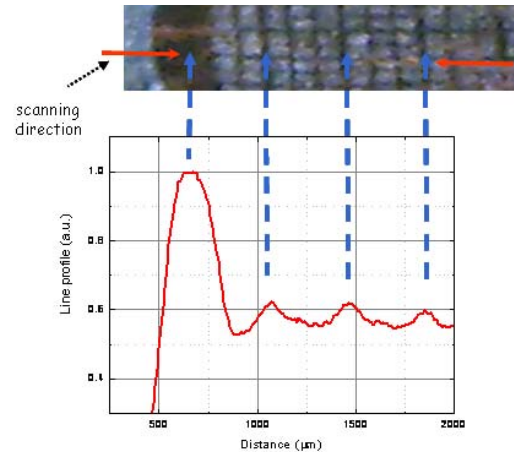


Figure 2.b – and the evolution of the $K\alpha$ = 8.0 keV peaks areas along the scanning line

The possibility to determine the thickness of a coated layer was tested using a test sample with 10 μm Cu on Fe substrate layer (Figure 3). The coating was produced by combined magnetron sputtering and ion implantation technology, developed at INFLPR [4].

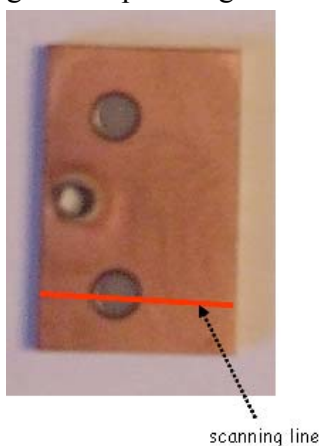


Figure 3 – Test sample for thickness determination: 10 μm Cu on Fe substrate layer.

Erosion circular patterns were produced by a glow discharge optical spectrometry (GDOS) device.

A full width line was scanned using a step of 0.1 mm and the following X-ray tube parameters: HV = 40 KV, I = 400 mA. The stack of spectra is presented in Figure 4. Both 3D and 2D representations demonstrate the ability of the system to map the composition of the sample. It can be observed that Fe peaks are visible even in the regions where Cu coating exists. This is also revealed by the evolution of Cu/Fe peak areas along the scanning line (Figure 4 bottom-left panel)) - the peak areas of Cu ($K\alpha$ = 8.06 keV) and Fe ($K_{\alpha,\beta}$ = 6.4/7.1 keV) were recorded at each scanning step.

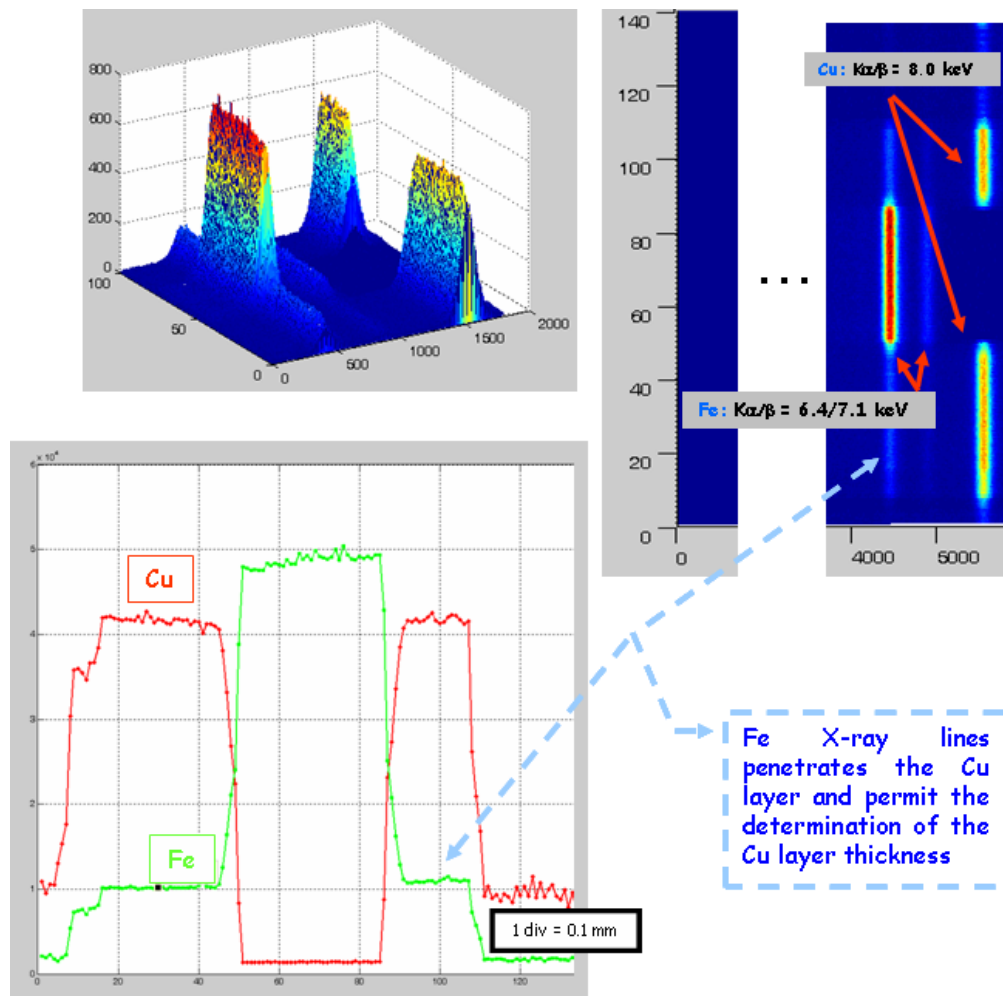


Figure 4 – Results of the fluorescence mapping of a coating layer test sample (10 μm Cu on Fe substrate layer): 3D representation of the stack of fluorescence spectra (top-left), 2D representation of the stack of fluorescence spectra (top-right) and evolution of Cu and Fe $K_{\alpha,\beta}$ peak areas along the scanning line.

As the energy of Fe X-ray fluorescence lines are known, together with the attenuation parameters of the X-ray in Cu, the thickness of the Cu layer can be determined. The accuracy of this determination was $\sim 5\%$.

2.2 Coating thickness of carbon samples

The same method can be also applied for the determination of the coating thickness of CFC samples, but not in a straightforward manner. The micro-beam fluorescence device is not operated in vacuum but in air and the carbon X-ray lines energy is below 1 keV. In consequence the penetration of C X-ray lines through the coating cannot be used for thickness calculation. However, usually, the coating process makes use of an intermediate layer; for example Mo is used as an interface layer between C substrate and the W coating

layer. Therefore the Mo X-ray lines penetrating the W layer can be used to determine its thickness. The maximum thickness of W layer for which this technique remains sensitive enough is limited by the energy of the Mo X-ray lines.

In Figure 5 we present a result of the calibration of the microbeam fluorescence technique for the tungsten thickness measurements.

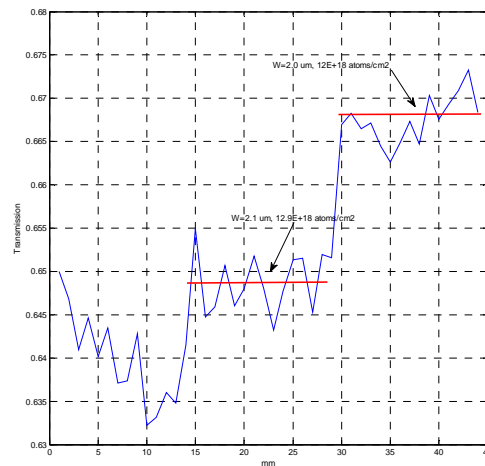


Figure 5 – Calibration of the tungsten thickness measurement by X-ray microbeam fluorescence

For the case of the assessment of the thickness uniformity of graphite/CFC with metallic coatings for a large number of samples, we found that an X-ray transmission technique is a more pragmatic solution in comparison to the X-ray fluorescence analysis. As the Tomo-Analytic system is a configurable and versatile measuring tool, we modified the geometry of the system (Figure 6). The X-ray source has a direction of emission perpendicular to the flat panel detector. The X-rays are detected after passing through the investigated sample where they are attenuated accordingly with the composition and thickness of the materials. The optimal measurement configuration and irradiation parameters were obtained by MCNP-5 Monte Carlo simulations [4].

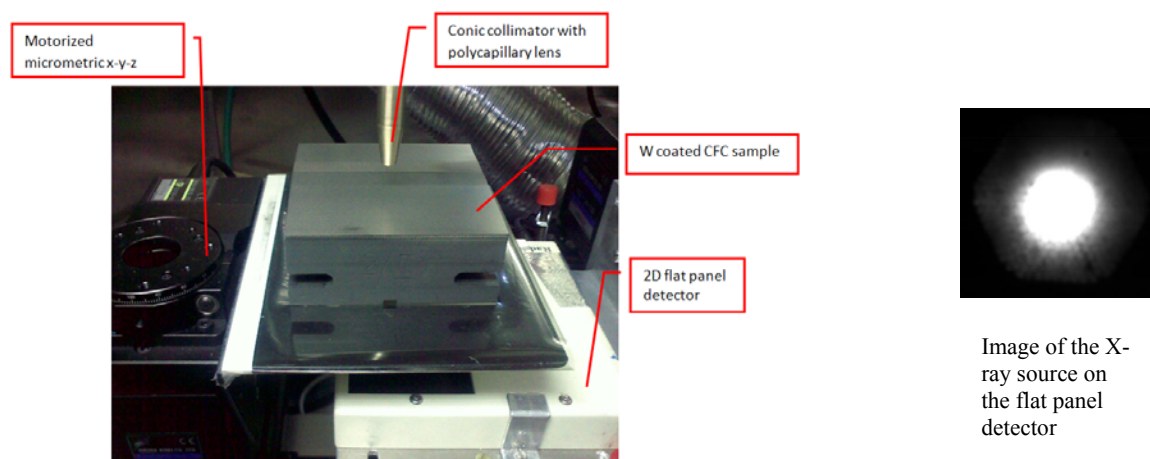


Figure 6 – View of the X-ray transmission geometry

Typical results of the combined X-ray transmission and X-ray fluorescence analysis are presented in Figures 7. a,b.

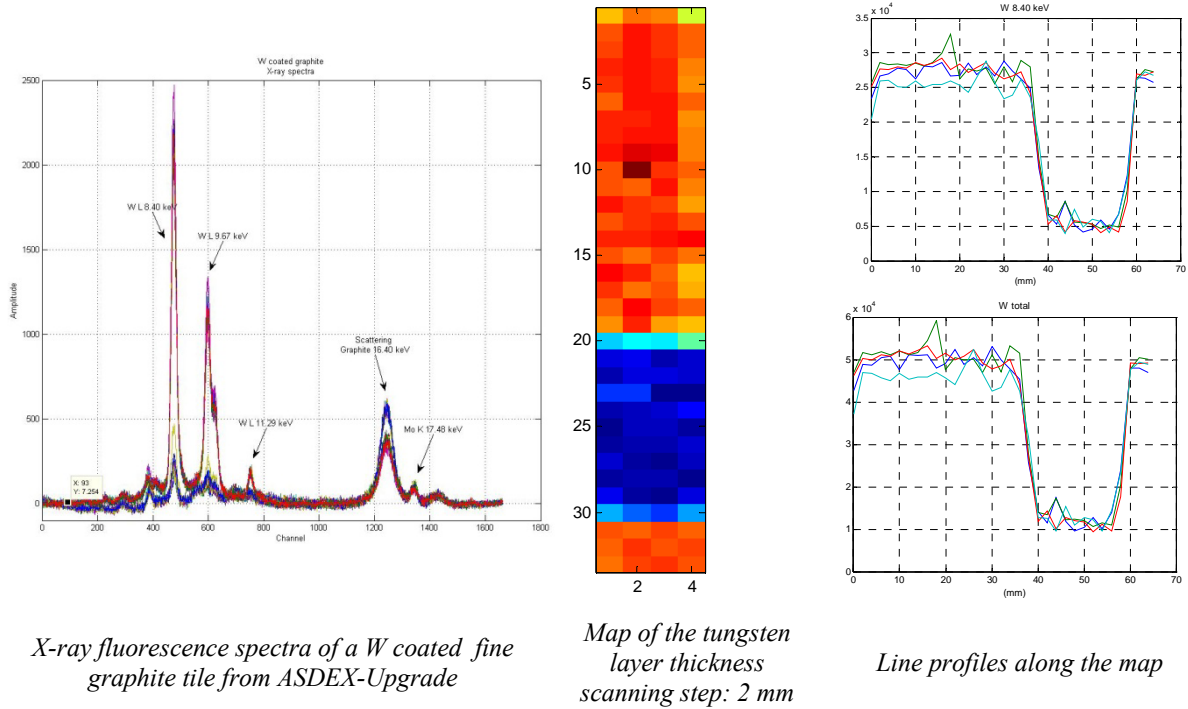
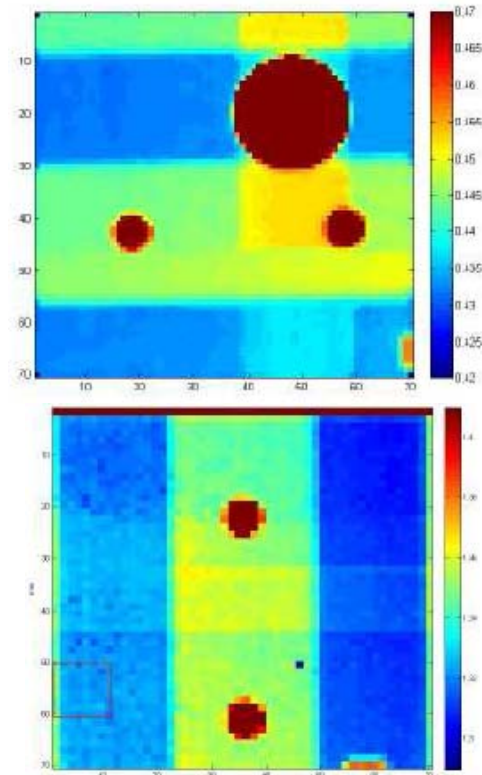


Figure 7.a - Post-mortem analysis of W coated fine graphite tiles from the divertor of ASDEX-Upgrade by X-ray Microbeam fluorescence

The X-ray transmission map can be used for the determination of the absolute value of the thickness of the W coating layer. In order to remove the influence of the fine graphite layer, a calibration sample must be used. The calibration sample is a multi-step one, which has regions with different thickness of fine graphite. As the real tiles contain several cutting up profiles, the CAD model of the tile must be also taken into account. The X-ray transmission ensures fast and high resolution analysis. The images presented in Figure 6.b are obtained for a scanning time of approximately four hours. The 70 x 70 pixels images are obtained for a resolution of 1.0 mm/pixel. The main advantages of the X-ray fluorescence method are: i) it doesn't need a calibration sample for the determination of the thickness of the coating layer and ii) it can detect the composition and thickness of possible deposited layers of intrusions. However the time needed for the inspection of the sample is considerably larger: approximately 60-90 s are needed for the acquisition of a spectrum. Therefore a spatial resolution equal with that one obtained in the case of the X-ray transmission method becomes prohibitive regarding the acquisition time needed. Also, due to the attenuation of the low energy of the emitted X-ray lines, the fluorescence method is limited to thin coating layers (up to $\sim 10 \mu\text{m}$) depending on the coating material. However the combined use of X-ray transmission and X-ray fluorescence methods represent a unique instrument for the post-mortem analysis of the coatings.



Graphite tiles with W coating



X-ray transmission map. The X-ray transmitted intensity was normalized to an average value of the transmission through the graphite. In this way we ignored the very low amount of redeposited W.

Figure 7.b – High resolution post-mortem analysis of W coated fine graphite tiles from the divertor of ASDEX-Upgrade by X-ray Microbeam transmission technique

3. Conclusion

An evaluation of the combined X-ray absorption/fluorescence method for erosion analysis was performed. Individually, each method has its own advantages/disadvantages, but the combined use of X-ray transmission and X-ray fluorescence methods represents a unique instrument for the post-mortem analysis of the coatings. It can provide fast analysis, high spatial resolution and detection of deposited layers and intrusions. The combined method was validated on W coated fine graphite tiles from the divertor of ASDEX-Upgrade.

The work will continue with X-ray fluorescence and tomography coating evaluation for a set of ASDEX-Upgrade tiles and of ITER-like CFC tiles. Marker probes of Al C Ni W will be also measured. A comparison to previous quantitative analysis with EPMA, RBS and NRA techniques will be carried out. Finally, a technical concept for a compact/low cost instrument based on X-ray micro-fluorescence to be used in high productivity coating analysis will be elaborated.

4. Acknowledgement

The research activities to be conducted in this project are relevant for the EFDA Task Agreement TA-4 “Erosion, transport and deposition of wall materials” organized under the Special Expert Working Group (SEWG) “Material Migration”.

References

1. I. Tiseanu, T. Craciunescu, C. Dobrea, A. Sima, Tomo-Analytic - a combined fully 3D X-Ray microtomography and microbeam fluorescence system, PRORA 2009 - Fachtagung Prozessnahe Röntgenanalytik, 26-27 Nov. 2009, Berlin, Germany.
2. I. Tiseanu , T. Craciunescu, C. Dobrea, A. Sima, Advanced X-ray imaging techniques for non-destructive analysis of fusion materials, Romanian Conference on Advanced Materials ROCAM 2009, August 25-28th, 2009, Brasov, Romania
3. C. Ruset et. al, W coatings deposited on CFC tiles by Combined Magnetron Sputtering and Ion Implantation technique, Physica Scripta, Vol. T128, pg 171-174 (2007)
4. MCNP-5 - Los Alamos National Laboratory, 2005. MCNP – A General Monte Carlo N-Particle Transport Code, Version 5, vols. I–II, LA-UR-03-1987 and LA-CP-03-0245

SCIENTIFIC REPORT

Task title: Removal of codeposited materials from gaps with a plasma torch / Indepartarea materialelor codepuse de pe suprafete plane si castelate cu torta de plasma

Code: WP10-PWI-02-04-01/MEdC/BS

Outline

1. General objectives of the project
2. The objectives of the activities in the Sem I 2010
3. Summary of obtained results
4. Description of the work. Results and conclusions
5. Future work

1. General objectives of the project

The long term material codeposition on walls of Tokamaks is associated with tritium retention issues, which become prominent in PFCs with gap structures. Removal of codeposited layers by the plasma torch at atmospheric pressure is based on scanning of the surface with a small size plasma source, and this technique is promising in respect with “in situ” cleaning of walls. ***The purpose of this project is to investigate the possibility to operate the plasma torch with reactive gases, aiming to remove more efficient the carbon and, in addition, mixed codeposited layers from flat and castellated surfaces.***

2. The objectives of the activities in the present stage of the project

In the frame of the project the Romanian team will have the following activities:

The removal efficiency should be improved for carbon and the cleaning of mixed carbon/metal layers must be approached in relationship with the plans of using metals (tungsten, beryllium) for next JET experiments and ITER. The solving of these requirements asks for use of reactive gases. The project proposes:

- ***Manufacturing of new constructive elements of the plasma torch, suitable to work in reactive gases;***
- ***Studies of stability of source operation in air and other reactive gases.***

- Experiments of inside gap cleaning of carbon and mixed layers with nitrogen/argon/reactive gases plasma torch;
 - Assessment of cleaning on the bottom of narrow gaps;
 - Examination of aspects regarding source integration with a robotic arm.
- At the present stage of the project there were fulfilled the first two objectives;
The following activities were performed:
- Study of the influence of reactive gases (nitrogen, air, others) on the lifetime and stability of torch operation.
 - Manufacturing of new constructive elements of the plasma torch, suitable to work in reactive gases; improvement of flexibility

3. Summary of the obtained results / Rezumatul rezultatelor obtinute

The removal of co-deposited carbon layers by a plasma torch operating with reactive gases at atmospheric pressure was approached in the context of EFDA Plasma Wall Interaction activities. In previous experiments plasma torch operation in argon and nitrogen and its use for cleaning were studied. The cleaning experiments were successful on flat surfaces and also inside gaps (of 0.5-1.5 mm wide). The present contribution focuses on the investigation of torch operation with reactive gases and gas mixtures (using oxygen, air, argon/ammonia, argon/hydrogen and argon/oxygen). In order to limit the torch damage by the enhanced plasma reactivity, changes were made over the plasma torch components (on the RF electrode materials and on its cooling). The new designed plasma source is more robust, compact and easier to be integrated on a robotic arm, being compatible with cleaning of the codeposited layers. The operation domains (RF power, gas flow rates, and ratio of gases in the mixtures) were studied, resulting in establishing the optimum working parameters of the plasma torch with reactive gases. These parameters were selected considering the following criteria: expansion of plasma jet outside the interelectrode space; stable operation without spots and arcing, and no excessive heating of the electrodes. The cleaning experiments performed with plasmas generated in reactive gases, realized on flat surfaces, showed that oxygen and oxygen containing mixtures have the highest effectiveness for laboratory made co-deposited layers removal.

4. Description of the work. Results and conclusions

Work performed

In the first part of the project the removal of a-C:H layers from the inside of gaps with width of 0.5-1.5 mm was demonstrated. It was observed then that the cleaning rates are higher for narrow gaps and that they are higher at the top part (entrance) of the gaps.

For improving the cleaning operations, the work with reactive gases was foreseen. It was thought that possible higher removal rates could be obtained by using reactive gases like oxygen, air, ammonia, hydrogen or their mixtures. But working with reactive gases could have also led to shortage of the device lifetime and limited

domains of operation. For testing and researching the operation domains of the plasma torch, several aspects were taken into consideration, like the electrodes oxidation, wider range of plasma impedance with various gases, and the instability of operation. Thus, part of the research and upgrade of the plasma source had to include new materials resistant to oxidation, cooling of the electrodes, research on matching, firmer connections, high quality cables, research on operation domains, and discharge stability in various gases.

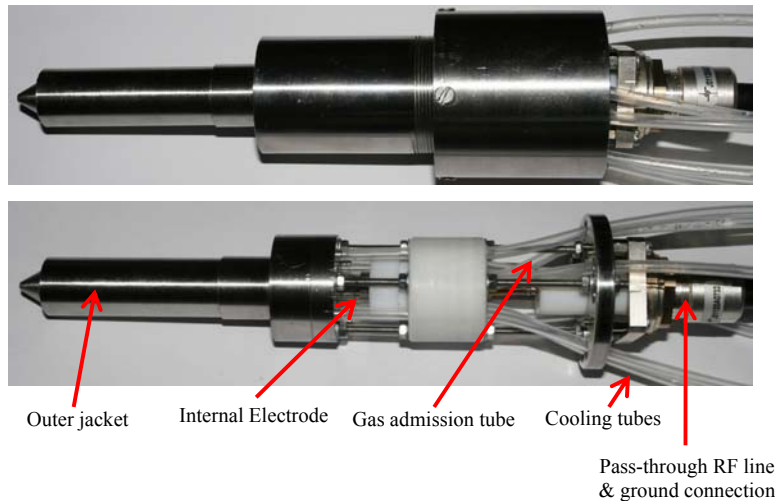


Figure 1: Image of the plasma torch with the outer jacket mounted (upper case) and without the outer jacket mounted to show the internal components (lower case)

The work performed had included changes of the RF electrode materials and manufacturing. The brass was replaced thoroughly with stainless steel material for RF electrode. The diameter of the active RF electrode was increased from 8 mm to 10 mm. The gas admission was changed from an internal one through the RF electrode, to an outer one. The direct connection of the RF cable was also modified, avoiding the use of the RF- 7/16 connector. Also, changes were performed to the internal electrode cooling system. The Polyethylene Terephthalate (PET) tubes were replaced with Fluorinated Ethylene Propylene (FEP) tubes (resistant to temperature, shriveling and plying). The water volume in RF electrode was increased from 2.3 cm³ to 3.4 cm³, while the water inlet and outlet's inner diameter were also increased from 1 mm to 1.8 mm. By performing such modifications the water flow rate increased from 0.6 to 1.5 liter/ min, thus enabling a much faster cooling and a longer lifetime of operations. Figure 1 below shows the final assembly of the plasma torch, with and without the outer jacket mounted.

The final result made the torch much more robust, more compact and flexible and easier to be integrated on a robotic arm. Also the changes of the materials made it more resistant on corrosion.

Results and discussions

For the torch's operation in reactive gases, most of the work involved the establishment of the possible values for the power (P), gas flow rate values (F), and gas flow rate ratios for stable and reliable operation.

The criteria used in the determination of the operation domains included the plasma jet visibility (the expansion had to be visible outside the interelectrode space), the stability of operation (without spots and arcing), and no excessive heating had to exist

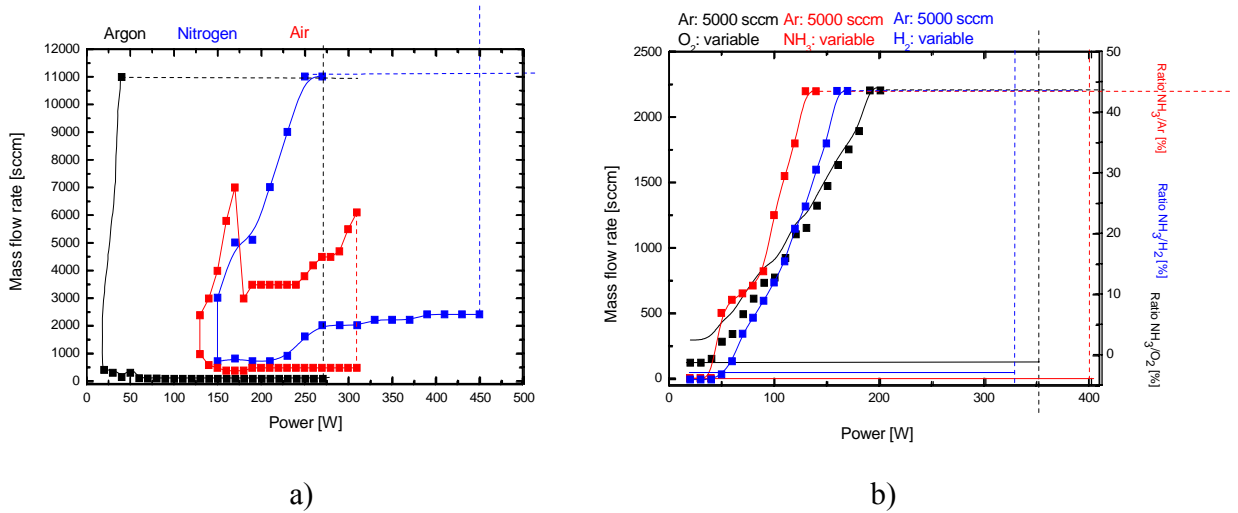


Figure 2: Operation domains
a) in pure gases, b) in gas mixtures

(the returning cooling water should be still cold, with no visible reddish of the nozzle). The criteria were accomplished by using power and flow rate measurements, the jet appearance was studied by imaging techniques, and the cleaning ability was demonstrated through a cleaning example.

The operation domains in pure gases were established (Figure 2a). From the graph it

was concluded that the operation in nitrogen and air require more power and that

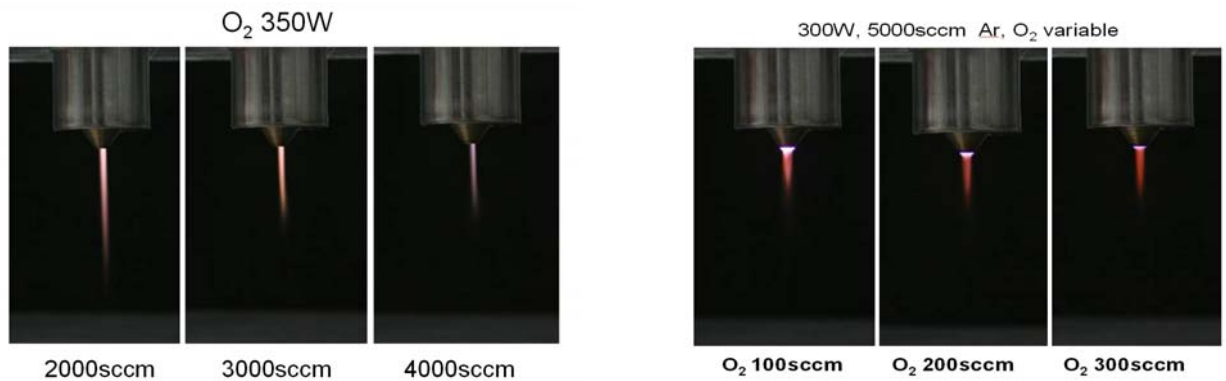


Figure 3 Images of the plasma jet in oxygen (left) and in argon-oxygen mixture (right)

the domain in air is restricted to a smaller area. For the optimum operation of the plasma source in nitrogen, air and argon, the central regions of the domains should be used. For the operation domains in gas mixtures it was observed that the operation in Ar/O₂ requires more power, while the operation in ammonia is the easiest.

For the establishing of the operation domains the research was done also by imaging techniques that showed different aspects of the plasma jet outside the torch. Two such sets of images done in oxygen or oxygen containing mixture (in this case argon with oxygen) are presented in Figure 3.

Of the encountered problems its worth mentioned that in pure O₂ or large O₂ content (over 10%) and air the long time operation was not proved. The nozzle does not resist for long periods of time in oxygen and perhaps it should be changed in Mo or W material. Also the insulator (quartz) is eroded fast and other materials should be used or a change in design could be approached.

5. Conclusions

As it has been proved, the torch operates optimally in Ar, N₂, Ar/NH₃, Ar/H₂ gases, although some problems of the discharge with oxygen containing gases still remain. The best cleaning results are in oxygen, Ar/O₂, air, nitrogen.

The plasma device is a versatile and feasible device for cleaning applications of the tiles inside the Tokamak reactor.

Future work

The following activities are in view:

- Experiments of cleaning with plasma torch working in nitrogen/argon/reactive gases;
- Cleaning of carbon layers from laboratory coated flat and castellated surfaces;
- Cleaning of mixed layers from laboratory or Tokamak exposed surfaces.

Publications

1. G. Dinescu et al. *Removal of codeposited materials from gaps with a plasma torch*, presentation at Joint Meeting of EFDA Taskforce Walls Interactions SEWGs and Emerging Technology System Integration (ETS) 8-11 June 2010, Garching, Germany

SCIENTIFIC REPORT

Task title: LABORATORY MODELS FOR CODEPOSITED LAYERS /
MODELE DE LABORATOR PENTRU STRATURI CODEPUSE

Code: WP10-PWI-02-04-02/MEdC/BS

Outline

1. General objectives of the project
2. The objectives of the activities in the Sem I 2010
3. Summary of obtained results
4. Description of the work. Results and conclusions
5. Future work

1. General objectives of the project

Laboratory made co-deposited layers are of high importance for the validation of fuel removal techniques (by laser, discharge, etc) and of monitoring techniques. Various groups have applied lasers, oxidation, and discharges in order to remove codeposited layers, but the results are difficult to compare, because each group has utilized its own synthesized material. ***The purpose of the project is to realize and characterize a family of materials, similar to the codeposited layers, in order to be used as laboratory models for the fuel removal or monitoring experiments.*** The problem is complex, because two or three materials are to be incorporated in the same layer, and these materials must be relevant for the fusion technology. As example of possible models one may mention amorphous hydrogenated layers, diamond like layers, carbon layers admixed with metals.

2. The objectives of the activities in the present stage of the project

The deposition of mixed carbon/metal layers/hydrogen must be approached in connection with the plans of using metals (tungsten, beryllium) for next JET experiments and ITER. The project main objectives are:

- ***Realization and characterization of model co-deposited layers for their use in conjunction with fuel removal techniques***
- Studies of the deposition and chemical transformation of Al/C + hydrogen layers, or (if possible to work with) Be/C + hydrogen layers, or similar layers

At the current stage of the project there was in view the first objective; for its accomplishment there were pursued the following activities:

- Deposition of layers containing carbon/metals
- Characterization of the deposited layers as concerning the structure, morphology, composition

3. Summary of the obtained results

Composite a-C:H/W (matrix of hydrogenate amorphous carbon with incorporated tungsten particles) layers, as laboratory models for the co-deposited layers, were synthesised using a sequential deposition method: the substrate (graphite, W, silicon) is alternatively exposed to two plasma sources mounted on the same deposition chamber: a magnetron (for metal incorporation) and a Plasma Enhanced Chemical Vapour Deposition (PECVD) source, using acetylene as precursor, for hydrogenated amorphous carbon deposition. The two mentioned plasma deposition processes are independent and sequential (every plasma source is ignited only when the substrate is in front of it, while during the substrate moving between the plasma sources there are created specific conditions to each deposition process: pressure, gas composition, RF power, etc.). The material morphology, structure and composition were investigated using specific techniques: atomic force microscopy (AFM), scanning electron microscopy (SEM), energy dispersion X-ray spectroscopy (EDX), ellipsometry and X ray diffraction (XRD). The deposited material has a typical composite structure (tungsten nanocrystals with the size in 1-2nm range embedded in an hydrogenated amorphous carbon a-C:H matrix). The material composition, can be tuned by proper setting the magnetron applied power or the exposure time of the substrate to each of the plasma sources.

4. Description of the work. Results and conclusions

4.1 Experimental setup

The sequential deposition [1] process takes place by alternatively exposing the substrate to two plasma sources mounted on the same deposition chamber: a magnetron (for metal incorporation) and a Plasma Enhanced Chemical Vapour Deposition source (with acetylene precursor) for hydrogenated amorphous carbon deposition. The two mentioned plasma deposition processes are independent and sequential (every plasma source is ignited only when the substrate is in front of it, while during the substrate moving between the plasma sources there are created specific conditions to each deposition process: pressure, gas composition, RF power, etc.).

The time sequence of one deposition cycles is presented in fig.1:

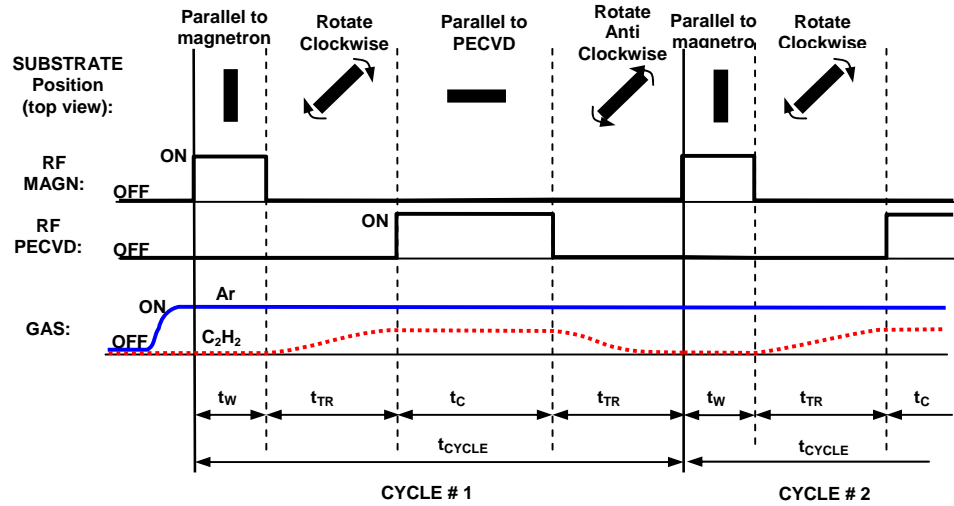


Fig. 1: Temporal diagram of one cycle in the sequential deposition process.

The sequential deposition process parameters can be classified in two categories:

- **plasma parameters:** PECVD and magnetron RF applied powers P_C and P_W , and working gases mass flow rates
- **temporal parameters:**
 - t_W and t_C - exposure time to magnetron and respectively to PECVD plasma;
 - t_{TR} - transport time between plasma sources,
 - N_{CYC} - the number of cycles.

Some of the enumerated parameters must to be fixed for avoiding unwanted effects during the sequential deposition process. In particular, the PECVD processes lead to dust formation in situation when the deposition parameters do not have optimum values. Previous studies [2] of a-C:H deposition imposed fixing the PECVD process parameters to the following values: RF applied power $P_C=80W$ and process gas mass flow rates of **70sccm for Ar and 5sccm for C₂H₂**; increase of the applied RF power to over 100W and of the C₂H₂

over 8sccm lead inevitable to carbon dust formation during the sequential deposition process and not to deposition rate increase as is expected. Also, fixing the transport time to the value $t_{TR} = 5s$ assure total evacuation of C_2H_2 from the reactor prior the magnetron deposition (avoiding in this way the magnetron target poisoning) and a stationary value of C_2H_2 during the PECVD process (see Fig.1).

The remaining process parameters for tuning the composition and structure of the deposited composite layers are: magnetron RF power and plasma exposure times t_W and t_C .

4.2. Composite a-C:H/W sample preparation and characterization.

For characterization of the deposited layers and correlations of these properties with the sequential process parameters there were deposited a number of sample layers for which deposition parameters were systematic varied as follows:

-Sample set I: The influence of cycle deposition times t_W and t_C over the structural and compositional properties of the W/a:CH deposited layer was studied by systematic varying these parameters (like is presented in Table 1) such as the plasma exposure time per cycle $t_W+t_C=13s$. The total number of cycles was $N_{CYC}=80$.

Table1: The samples deposited for studying the dependence of their properties (structure, morphology and composition) over the temporal parameters of the sequential deposition method. Samples codification consist in pairs of the (t_W , t_C) times, in seconds.

Short description of probes	Probe code (t_W , t_C)	Material	t_W [s]	t_C [s]	N_{CYC} /Total deposition time [h:m:s]	Total thickness [nm]	RMS [nm]
Probes with variable t_W and t_C such as $t_W+t_C=13s$, $N_{CYC}=80$	(2,11)	a-C:H/W	2	11	80 /30m40s	335	3.4
	(4,9)	a-C:H/W	4	9	80 /30m40s	360	3.1
	(6,7)	a-C:H/W	6	7	80 /30m40s	427	2.3
	(8,5)	a-C:H/W	8	5	80 /30m40s	403	-
	(10,3)	a-C:H/W	10	3	80 /30m40s	423	2.7
Reference (unicomponent) probes	a-C:H _{REF} (6,7)	a-C:H	6	7	80 /30m40s	139	1.4
	W _{REF} (6,7)	W	6	7	80 /30m40s	192	4.3

Two reference layers (a:CH_{REF}(6,7), containing only a:CH and W_{REF}(6,7), containing only W, were deposited by sequentially deposition, in conditions similar to W/a:CH(6,7) for comparing the process of sequential process deposition of mono-component layers with the composite sequential process deposition. During the reference probes sequential deposition

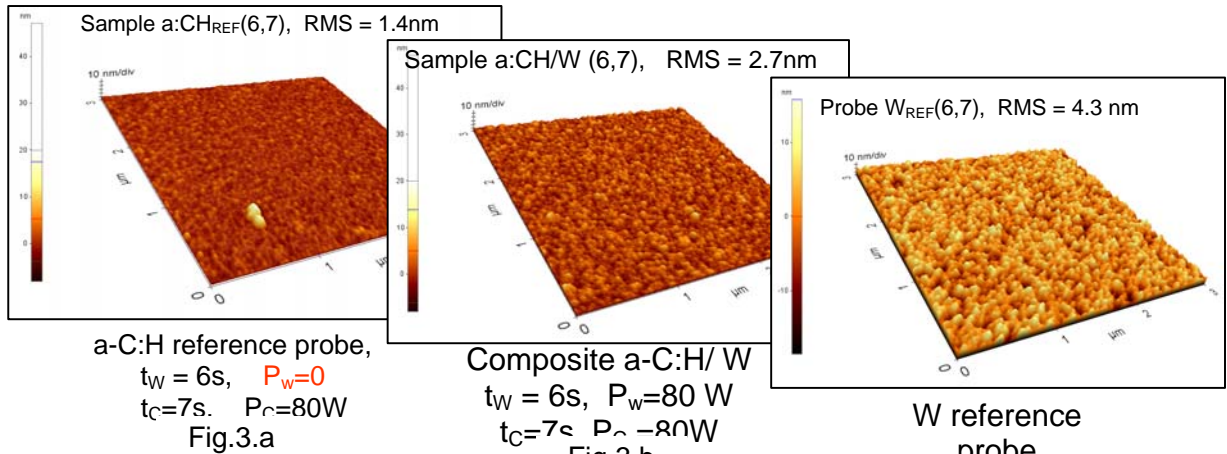
only the corresponding plasma source was sequentially ignited (PECVD plasma source for probe a:CH_{REF}(6,7) and magnetron for W_{REF}(6,7)).

- **Sample set II:** the magnetron RF power P_W was varied (100W, 80W, 60W, 45W and 30W) while the plasma exposure times were fixed to $t_W=6s$ and $t_C=7s$

The surface topography and thickness of the deposited films were investigated using a Park Systems XE-100 atomic force microscope. The film thickness was measured on a step margin obtained during layer deposition by masking. The SEM measurements were performed using a FEI model Inspect S scanning electron microscope while EDX measurements were performed using an EDAX Inc. model with a SiLi detector. The structure of a-C:H/W layers was investigated by X-ray diffraction using a Panalytical X'Pert PRO system in a Bragg-Brentano geometry. The tungsten concentration of a-C:H/W composite layers was determined by means of ellipsometry for sample set II.

4.3 Results and discussions.

The results of AFM measurements (layers **thickness and roughness - RMS**) are presented in Table1. The thickness of the deposited a:CH layers increase slightly while the roughness of the deposited W/a:CH layers is slightly decreasing while t_W is increasing (from 3.4nm for $t_W=2s$ to 2.7nm for $t_W=10s$). In contrast, there is a clear difference between the roughness of the reference probes compared with that of W/a:CH(6,7) like is shown in Fig.3 a, b, c.



In Fig.4 is presented the **surface morphology** of the composite a-C:H/W sample (6,7) (see Table1); the SEM image was recorded with 20000x magnification. The surface presents a granular aspect, with grain size of about 14nm.

Composite layer structure: The XRD diffractograms of the a-C:H/W composite probes (2,11), (6,7), (10,3) and tungsten reference probe W_{REF}(6,7) were obtained in 2 theta configuration and are presented in fig.5. The diffraction peaks corresponding to film components and substrate (C and W(110) and Si(002)) are observed. The diffraction peak corresponding to W(110) is very pronounced and narrow for the tungsten reference sample, while for the composite samples it decreases and is enlarged. By comparing the diffractogram of composite samples (10,3), (6,7) and (2,11), one can observe that the height of the peaks is

lower for the samples with lower tungsten content whilst the carbon peaks behave oppositely. From the profile of the tungsten peaks the size of the particulates in the film can be estimated by Debye-Scherrer formula. It results that the a-C:H/W layers contains tungsten nanocrystals with sizes in the range 1-2nm. Their dimension is higher for the samples deposited at higher t_W values.

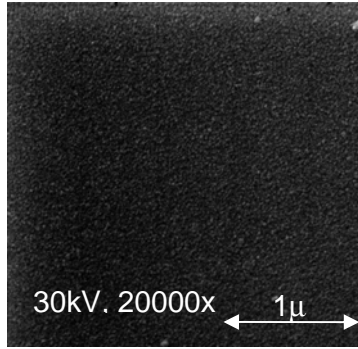


Fig.4: SEM image of a the (6,7) a-C:H/W probe performed on a $2\mu\text{m} \times 2\mu\text{m}$ area.

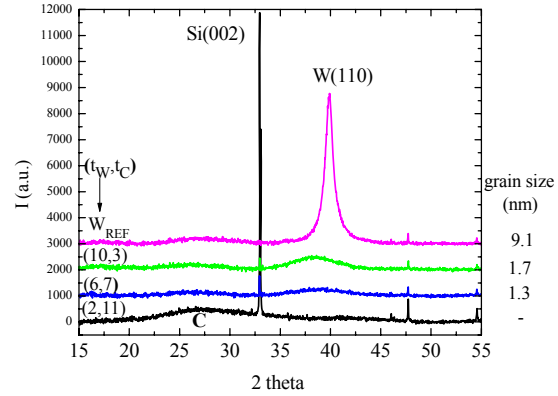


Fig.5: The XRD diffractograms of the a-C:H/W composite probes (2,1), (6,7) (10,3) and on the tungsten reference probe.

Film composition: The results of EDX measurements performed on the a-C:H/W composite layers (2,1), (6,7) and (10,3) from sample set I are presented in fig. 6.a. Beside the strong carbon C K and tungsten W M lines, the presence of oxygen OK line is observed; it originate probably from contamination during the deposition or post-processing contamination from the ambient atmosphere. The concentration of the films metallic and carbonic components increase (respectively decrease) while the exposure time to the

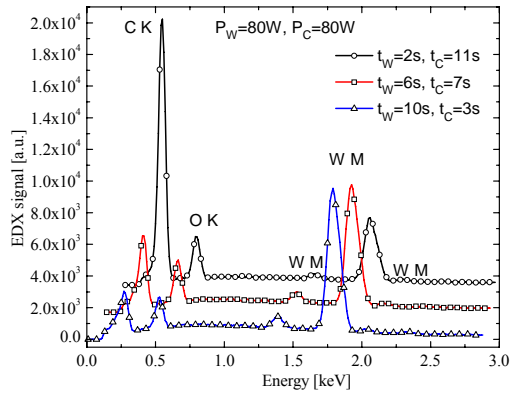


Fig.6a: EDX signal for the a-C:H/W samples (2,1), (6,7), and (10,3).

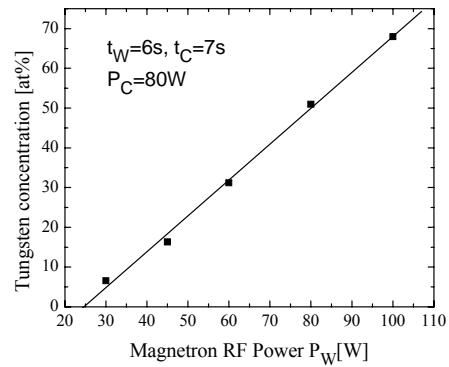


Fig.6b: Dependence of the W atomic elemental concentration on magnetron power

magnetron t_W is increased.

The graph in fig.6b present the dependence of tungsten atomic concentration on applied RF magnetron power for a-C:H/W composite layers from sample set II.

It is obvious that both increase of plasma exposure time t_W and RF magnetron power lead to increase of metallic component concentration in the deposited layer. However, due to possibility of target poisoning, especially at low RF magnetron powers, it is preferable to

control the metallic component concentration by adjusting the plasma exposure times (t_w, t_c) while the plasma parameters (including magnetron power P_w) are kept constant.

4.5. Conclusions

Laboratory models for tokamak reactors co-deposited layers were synthesised as composite a-C:H/W (matrix of hydrogenated amorphous carbon with incorporated tungsten particles) layers by means of a sequential deposition method. It consist in alternatively exposing the substrate (graphite, W, silicon) to two plasma sources mounted on the same deposition chamber: a magnetron (for metal incorporation) and a Plasma Enhanced Chemical Vapour Deposition (PECVD) source, using acetylene as precursor, for hydrogenated amorphous carbon deposition. The two mentioned plasma deposition processes are independent and sequential (every plasma source is ignited only when the substrate is in front of it, while during the substrate moving between the plasma sources there are created specific conditions to each deposition process: pressure, gas composition, RF power, etc.). The sequential process parameters are classified in plasma parameters and temporal parameters; for performing a study regarding the properties of deposited layers, these parameters were systematic varied. The material morphology, structure and composition were investigated using specific techniques: atomic force microscopy (AFM), scanning electron microscopy (SEM), energy dispersion X-ray spectroscopy (EDX), ellipsometry and X ray diffraction (XRD). The deposited material has a typical composite structure (tungsten nanocrystals with the size in 1-2nm range embedded in an hydrogenated amorphous carbon a-C:H matrix). The material composition can be tuned by proper setting the magnetron applied power or the exposure time of the substrate to each of the plasma sources; the second method is preferred due to possibility of avoiding target poisoning.

4.6. Future work

The following activities are in view:

- **Improvement of the sequential deposition method:**
 - setting up a process monitoring system (more probably OES);
 - improvement of the deposition rates;
- Deposition and study of a-C:H/Me layers with other metallic components relevant for fusion technology (Mg, Al)
- Studies regarding the changing of composite layers in contact with different gases.

4.7. References.

1. T. Acsente, E. R. Ionita, C. Stancu, C. Luculescu, G. Dinescu, *Properties of composite a-C:H/metal layers deposited by combined RF PECVD/Magnetron sputtering techniques*, Presented at E-MRS 2010 SPRING MEETING; submitted to Thin Solid Films as a E-MRS 2010 Symposium L article
2. J Winter , J Berndt , S-H Hong , E Kovačević , I Stefanović and O Stepanović , *Dust formation in Ar/CH₄ and Ar/C₂H₂ plasmas* , Plasma Sources Sci. Technol. 18, 034010, (2009)

SCIENTIFIC REPORT

Task title: PRODUCTION OF CONTROLLED LABORATORY CO-DEPOSITED LAYERS FOR FUEL REMOVAL STUDIES / PRODUCEREA DE STRATURI SUBTIRI PENTRU STUDII DE CURATARE CU PLASMA

Code: WP10-PWI-02-04-03/MEdC/BS

Outline

1. General objectives of the project
2. The objectives of the activities in the Sem I 2010
3. Summary of obtained results
4. Description of the work. Results and conclusions
5. Future work

1. General objectives of the project

Removal of the material codeposited on Tokamaks walls and PFC is very important for safe working of plasma fusion machines. In this context, there were performed fuel removal experiments using different approaches (atmospheric pressure plasma jets, laser ablation, discharges). *The purpose of this project is realization of stable composite layers of hydrogenated carbon with metal inclusions, with well predefined composition, to be used for fuel removal experiments using different approaches.* Also the project points on investigation of the time stability of the composite layers in presence of ambient open atmosphere.

2. The objectives of the activities in the present stage of the project

The deposition of mixed carbon/metal layers with pre-defined composition is necessary linked to the plans of using metals (tungsten, beryllium) for next JET experiments and ITER. The project objectives are:

- *Definition of parameters for which layers with pre-defined carbon/metal content are obtained; composition characterization.*
- *Submission of composite layers for validation of fuel removal procedures*
- Identification of the agents of the fast chemical change in metal (aluminum)/carbon + hydrogen layers at contact with the ambient

At the current stage of the project there were in view the first two objectives and for that accomplishment was pursued the following activities:

- Identification of parameter ranges for which layers with pre-defined carbon/metal content are obtained;
- Deposition of samples in well established conditions and their submission for validation of fuel removal techniques (with atmospheric pressure plasma torch and other available techniques at partners).

3. Summary of the obtained results / Rezumatul rezultatelor obtinute

Summary of the obtained results

Laboratory models for the fusion reactors co-deposited layers, consisting in composite a-C:H/W (matrix of hydrogenated amorphous carbon with incorporated tungsten particles) layers having predefined composition, were synthesised using a sequential deposition method: the substrate (graphite, W, silicon) is alternatively exposed to two plasma sources mounted on the same deposition chamber: a magnetron (for metal incorporation) and a Plasma Enhanced Chemical Vapour Deposition (PECVD) source, using acetylene as precursor, for hydrogenated amorphous carbon deposition. The two mentioned plasma deposition processes are independent and sequential (every plasma source is ignited only when the substrate is in front of it, while during the substrate moving between the plasma sources there are created specific conditions to each deposition process: pressure, gas composition, RF power, etc.). Using EDX analysis there were identified the sequential process parameters leading to predefined layer composition by adjusting the substrates exposure times to the plasma sources (t_W for magnetron and t_C for PECVD deposition processes) [1]. Using this method there were deposited thick (in range 1-4 μ m) carbon, metal and composite samples which were submitted for plasma cleaning experiments.

4. Description of the work. Results and conclusions

4.1 Experimental details

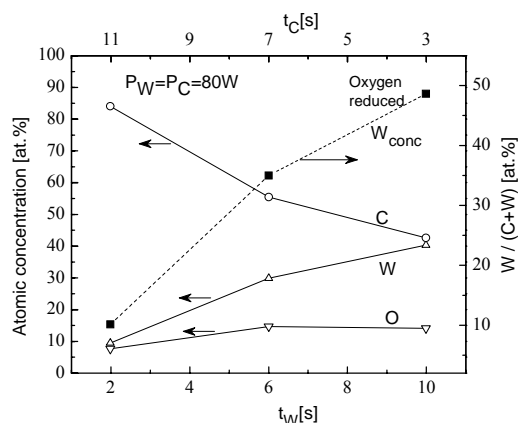


Fig.1: The dependence of the elemental atomic concentration obtained from the EDX investigations, upon the exposure times t_W and t_C .

The sequential deposition process takes place by alternatively exposing the substrate to two plasma sources mounted on the same deposition chamber: a magnetron (for metal incorporation) and a Plasma Enhanced Chemical Vapour Deposition source (with acetylene precursor) for hydrogenated amorphous carbon deposition. The sequential deposition process was described largely in [1] where was proved the ability of this method in producing a-C:H/W composite layers with predefined elemental concentration only by adjusting the substrate exposure times to plasma sources (t_W to magnetron and t_C to PECVD plasma source); the dependence of composite

layers components concentration open these two parameters is presented in fig.1. The remaining deposition parameters was fixed as follows: PECVD R.F. applied power $P_C=80\text{W}$, process gas mass flow rates of 70sccm for Ar and 5sccm for C_2H_2 , transport time of the substrate between plasma sources $t_{\text{TR}} = 5\text{s}$. Adjustment of the layer thickness was performed by the value of the repeated deposition cycle number N_{CYC} .

The sequential deposition setup can also be used for deposition of pure metallic (tungsten) or hydrogenated carbon layers by fixing the substrate in a position parallel to the corresponding plasma source.

4.2. Results

Using the presented deposition parameters there were deposited samples with predefined W/C concentration ratio as requested for cleaning experiments:

- Samples of composite a-C:H/W having $4\mu\text{m}$ thickness, containing 40 at% tungsten, (deposited for $t_w=4\text{s}$, $t_c=9\text{s}$); samples were deposited on tungsten and optically polished graphite substrates for $N_{\text{CYC}}=830$ Cycles, total deposition time $5\text{h } 18' 10''$;
- Samples of pure tungsten (thickness in range $1\text{-}4\mu\text{m}$) deposited on tungsten substrate
- Samples of pure hydrogenated a-C:H (thickness in range $1\text{-}4\mu\text{m}$) deposited on graphite substrate

The prepared samples were submitted to the following Euratom partners:

- For the plasma-torch cleaning experiments (MEdC, G. Dinescu)
- For CIEMAT Spain (F. Tabares)
- For CNRS Toulouse (L. Pitchford)
- CEA – Saclay (Alexandre Semerok – May 2010).

4.3. Conclusions

- Composite a-C:H/W layers with elemental predefined concentrations were deposited as laboratory models for the fusion reactors co-deposited layers. The deposition was performed by means of a sequential deposition method. Using EDX analysis there were identified the sequential process parameters leading to predefined layer composition by adjusting the substrates exposure times to the plasma sources (t_w for magnetron and t_c for PECVD deposition processes) [1].
- Using this method there were deposited thick (in range $1\text{-}4\mu\text{m}$) composite samples and mono-component layers (pure tungsten and pure hydrogenated carbon) on tungsten and graphite substrates. These samples were submitted for plasma cleaning experiments.

4.4.Future work

- deposition of more composite samples and submission for cleaning experiments, as it will be required;
- Characterization of the changes produced by the contact of metal/carbon layers with the ambient air

4.5. References.

- 1. T. Acsente**, E. R. Ionita, C. Stancu, C. Luculescu, G. Dinescu, *Properties of composite a-C:H/metal layers deposited by combined RF PECVD/Magnetron sputtering techniques*, Presented at E-MRS 2010 SPRING MEETING; Submitted to Thin Solid Films as a E-MRS 2010 Symposium L article

BS18 A

RST in extenso

Titlul complet al Proiectului BS 18A:

Studiul influenței tratamentului termic în formarea de compusi stabili Be-C, Be-W și C-W. Influența iradierii cu fascicule de electroni produse de tunul TVA.

(Study of the thermal treatment influence in formation of the stable Be-C, Be-W and C-W alloys . TVA gun electron beam irradiation influence. (BS-PS))

Etapă I

Activitatea I

50-200 nm Be/C, Be/W and C/W coatings on graphite and silicon.

Task: TA PWI 2010, Chapter 6: Determination of expected alloys and compounds in ITER relevant conditions and their influence on PWI processes and fuel retention

Sub-task: TA WP10-PWI-06-01-02/MEdC/PS: TVA gun electron beam irradiation influence on mixed films prepared using TVA method

Title of the report: 50-200 nm Be/C, Be/W and C/W coatings on graphite and silicon.

Task Force on Plasma Wall Interaction

Area: SEWG ITER Material Mix

Principal investigator: Cristian P. LUNGU,

Research team: A. Anghel, C. Porosnicu, I. Jepu, A.M.Lungu, P. Chiru, C. Ticos, C. Luculescu

National Institute for Laser, Plasma and Radiation Physics, Association
EURATOM MEdC

CONTENTS

Abstract.....	4
1. Introduction.....	5
2. Sample preparation.....	6
3. SEM cross-section and AFM morphology analyses.....	7
4. Thermal treatment.....	9
5. XPS analyses.....	11
6. Influence of the substrate nature on deuterium retention and release studies for beryllium films deposited on carbon and tungsten.....	14
7. CONCLUSIONS.....	15

Abstract

The present project is performed under Task Agreement PWI 2010, Chapter 6: Determination of expected alloys and compounds in ITER relevant conditions and their influence on PWI processes and fuel retention

The aim of this project is to improve our knowledge on material mixing in ITER relevant environment, in particular: (i) formation and properties of mixed materials; (ii) fuel retention in mixed materials; (iii) Study of reaction kinetics for Be-W and Be-C (for instance Be / W inter-diffusion, Be sublimation from Be / W alloys)

150-200 nm as well as 5nm - 20 nm Be/C, Be/W and C/W multilayer coatings on graphite, silicon and tungsten were prepared using thermionic vacuum arc (TVA) method. The morphology and the film composition on the surface and the depth were determined by Scanning Electron Microscopy (SEM), Energy Dispersive Spectrometry (EDS), Atomic force Microscopy (AFM), X-ray Photoelectron Spectroscopy (XPS) and Rutherford Backscattering Spectroscopy (RBS). The deuterium implantation and release were studied using Nuclear Reaction Analysis (NRA) and Thermal Desorption Spectrometry (TDS) with the support of IPP Garching.

1. Introduction

The current design of ITER involves the use of beryllium (Be), carbon fiber composite (CFC) and tungsten (W) as plasma facing materials. It is expected that Be eroded from the first wall and ionized in the *scrape-off-layer* (SOL) plasma will be mainly re-deposited at divertor surfaces leading to the formation of mixed materials films and corresponding changes of the original material properties of W and C. The in-vessel fuel retention inventory is one of the key issues affected by the mixed material systems. Its and the development of control strategies require a detailed knowledge of both retention and release behavior of such mixed systems.

Both Be-W alloy formation and Be-C (carbide) formation of Be, W and C compounds have been investigated in well controlled laboratory experiments and principal mechanisms are understood. However more knowledge is needed on the dynamics of these processes under high impinging flux conditions and transient surface temperature changes. In addition, studies of ternary systems including Be, W and C and/or oxygen, have just started and need more dedicated experiments.

Association Euratom-MEdC has substantial expertise in the preparation of pure and compact layers using the original method of thermionic vacuum arc (TVA). There is a major collaboration with IPP Garching, FZJ Juelich, Germany, TEKES, Finland which have experimental facilities, thermal testing and film property characterization equipment.

150-200 nm Be/C, Be/W and C/W multilayers coatings on graphite and silicon were prepared using thermionic vacuum arc (TVA) method. The morphology and the film composition on the surface and the depth were determined by Scanning Electron Microscopy (SEM), Energy Dispersive Spectrometry (EDS), Atomic force Microscopy (AFM), X-ray Photoelectron Spectroscopy (XPS) and Rutherford Backscattering Spectroscopy (RBS). The deuterium implantation and release were studied using Nuclear Reaction Analysis (NRA) with the support of IPP Garching during a research stage of one of the members of the Romanian research team.

2. Sample preparation

In order to study the influence thermal treatment on the film and interlayer film formation, thin multilayer films containing beryllium and a cap layer of tungsten or carbon films were deposited on graphite, silicon and tungsten substrates kept at room temperature during coatings, using thermionic vacuum arc method (TVA).

The parameters used for Be deposition e.g. chamber pressure, filament current, discharge potential, discharge current, deposition rate, substrate temperature and film thickness are shown in Table 1.

The schematic and a detail of the anode-cathode assembly for W depositions are shown in Figs. 1 and 2, respectively. Such an arrangement has been used for the deposition of high melting temperature materials as Re, Nb and C.

The anode, a W or graphite rod of 8-10 mm in diameter and 30-80 mm in length (instead of W rod we used 20-30 tungsten wires of 1 mm diameter put together) was sustained by a Mo holder and a water cooled electrical feedthrough.

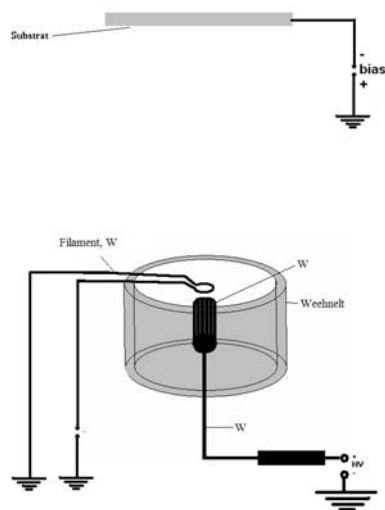


Fig.1 Sketch of the TVA system for W deposition



Fig.2 Photograph of the multi-wire W anode and the circular cathode.

During the deposition of the films, the thickness was monitored using a quartz balance QMB-7. To gain trustful information the quartz balance was previously calibrated for beryllium, tungsten or carbon measurements taking into account that the thickness of the film has a dependence of sample's position related to the source.

The parameters used for multilayer film depositions are listed in Table 1.

Table 1 Parameters used for Be, W and C multilayer film depositions

Parameter	Be deposition	W deposition	C deposition
Deposition chamber pressure	8.5×10^{-6} torr	2×10^{-5} - 7.6×10^{-6} torr	1×10^{-5} - 6×10^{-6} torr
I_{filament}	49.8 A	60 A	59 A
$U_{\text{discharge}}$	1300V	2500V	1500V
$I_{\text{discharge}}$	1000 mA	1.5 – 1.6 A	1 A
Deposition rate	0.9 nm/s	0.1 nm/s	0.2 nm/s
Film thickness	200 nm	50 nm	50 nm

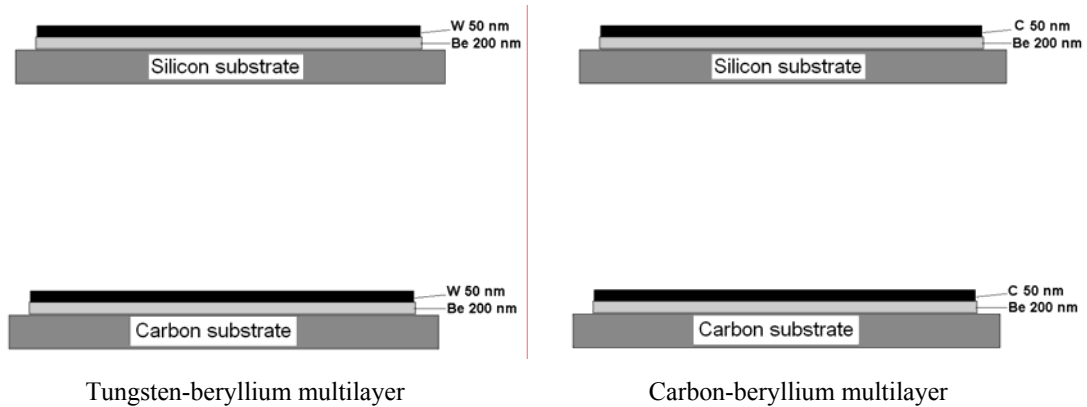
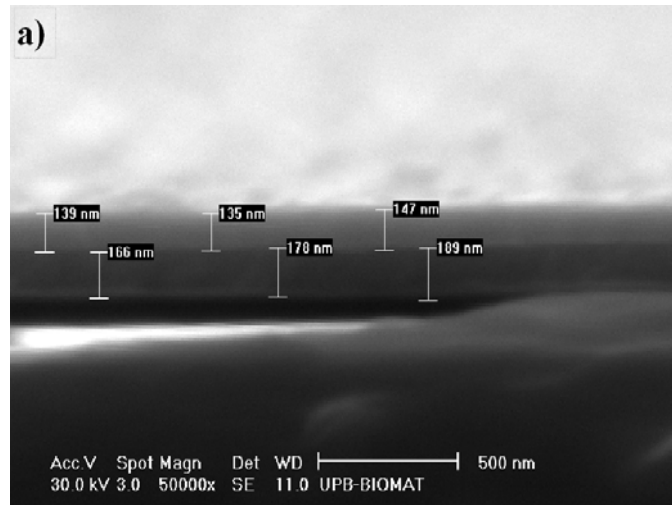


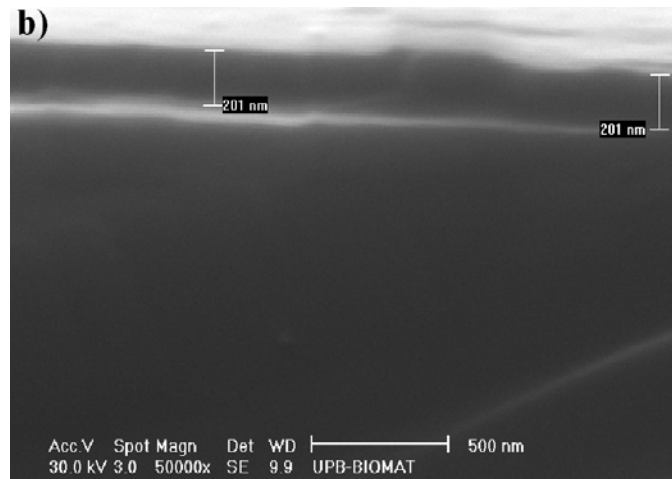
Fig. 3 Types of multilayer films used in the study

3. SEM cross-section and AFM morphology analyses

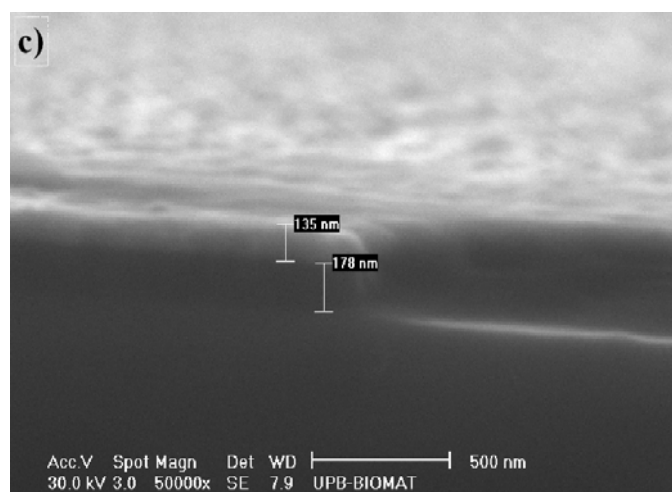
Cross-sectional scanning electron microscopy (SEM) analyses of the prepared samples were performed using a Philips ESEM XL 30 TMP apparatus. The SEM images of the multilayer W-Be films deposited on silicon substrates are shown in Fig. 4. The substrate temperatures were kept constant during depositions at RT, 200 and 300°C, respectively. The measured layer thickness using the SEM facility was in good agreement with the “*in-situ*” quartz balance monitor measurements: W layer: 119-147 nm, Be layer: 166-201 nm



a) deposited at room temperature



b) deposited at 100°C



c) deposited at 300°C

Fig. 4 Cross section SEM image of the multilayer Be-W film on silicon

The morphology of the prepared films was characterized using a Nanotec Scanning Probe Microscope in dynamic mode (non-contact). The RMS roughness values were found in the range of 3-5 nm. Typical AFM images are shown in Fig.5.

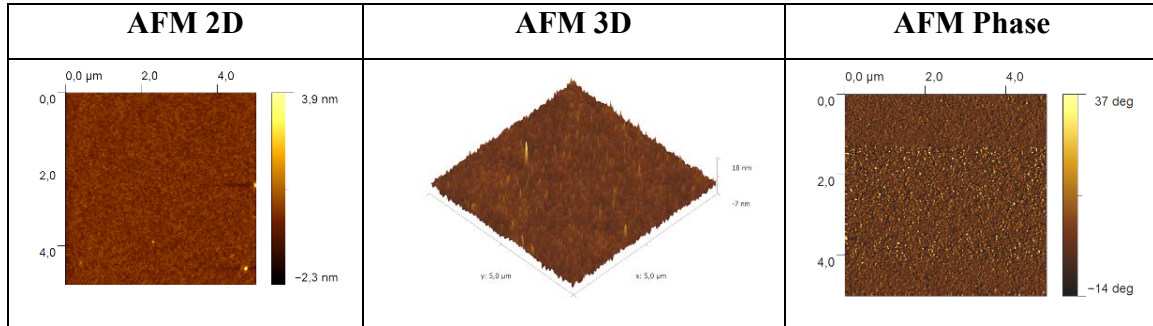


Figure 5 AFM images of the multilayer Be-W film on silicon

4. Thermal treatment

A new facility was developed in order to perform thermal treatment at a maximum temperature of 1200°C of the samples in high vacuum. The set of samples used for the thermal treatment was deposited at room temperature, containing 20nm beryllium film, covered by 5 nm tungsten or carbon.

The high vacuum pump system maintains 10^{-8} torr inside a quartz tube where the samples to be analyzed are loaded. One by one, these samples are directed towards the edge of the tube that was introduced inside a cylindrical heater. This way, all the samples can be treated one by one, with a high control of the sample temperature. For sample temperature control, a thermocouple monitors continuously the oven temperature. Using a calibration between the sample and the oven temperature the input power of the oven was controlled so that a certain temperature ramp was used, as well as a steady temperature during the treatment.

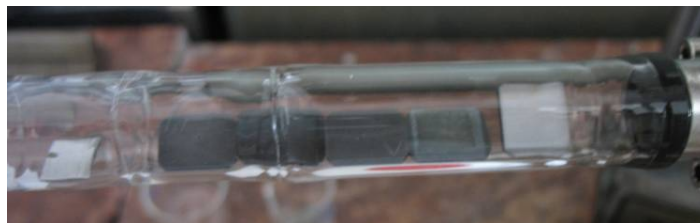


Fig. 6 Picture showing the quartz tube and 4 samples to be thermally treated.

The temperatures chosen for the thermal treatment were 350, 750 and 1000°C for 30 minutes. These temperatures were used considering the previously results on the alloy formation at these temperatures.

The temperature and pressure were constantly monitored and presented in Fig. 7 for the beryllium- tungsten multilayer films. For the beryllium-carbon films, no significant differences were observed.

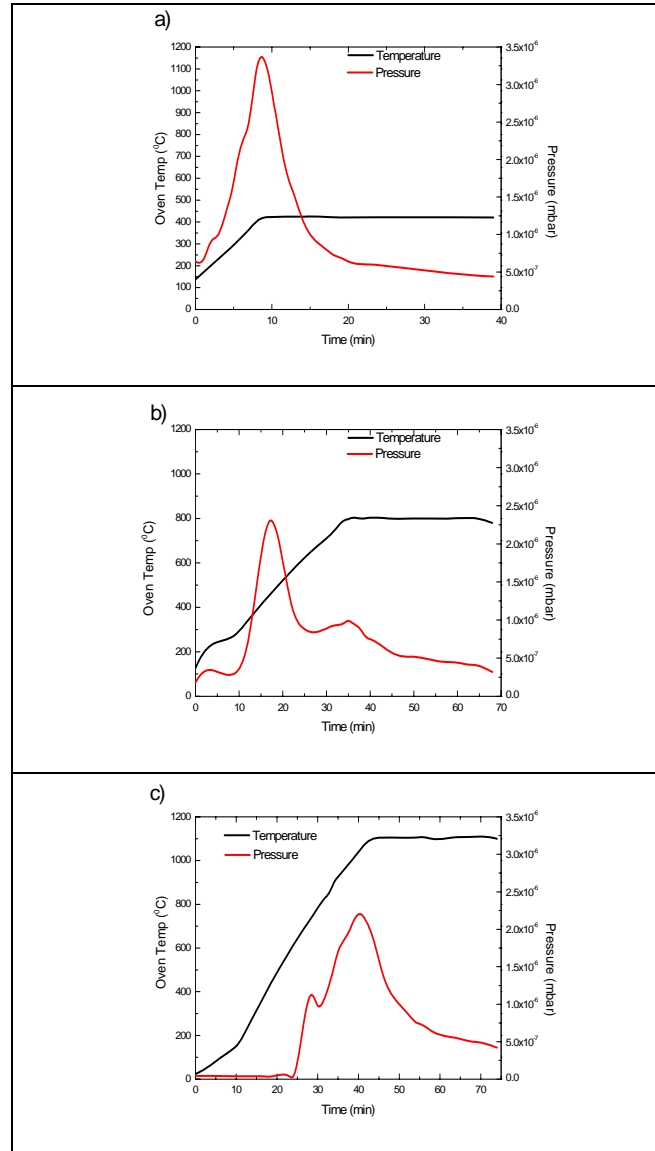


Fig. 7 Temperature and pressure versus time during thermal treatment: a) 300°C; b) 750°C; c) 1000°C.

5. XPS analyses

Using an X-ray Photoelectron Spectrometer from SPECS, Germany, the prepared samples were analyzed in order to infer the formation of chemical bonding and reaction kinetics for Be-W and Be-C

The multilayer sample C(5nm)/Be(20nm)/graphite was analyzed before and after thermal treatment. The result of measurements being presented in Figs. 8 -12. Comparing the peaks evolutions before and after the thermal treatments we can observe that almost all the beryllium reacted. The shift of the C1s peak towards the bonding energy of the carbide compounds corroborated with the Be1s shift suggests the formation of the Be_2C inside the film.

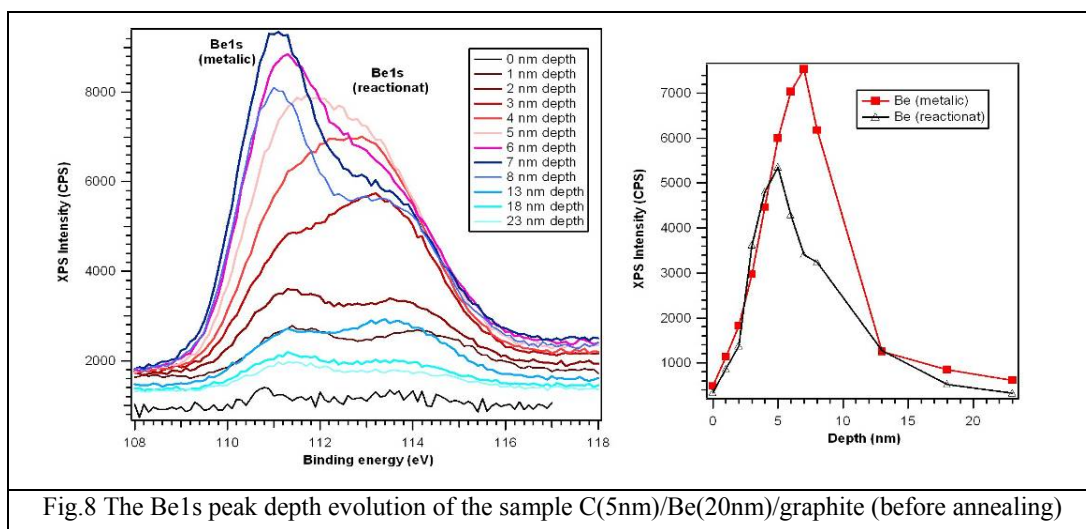


Fig.8 The Be1s peak depth evolution of the sample C(5nm)/Be(20nm)/graphite (before annealing)

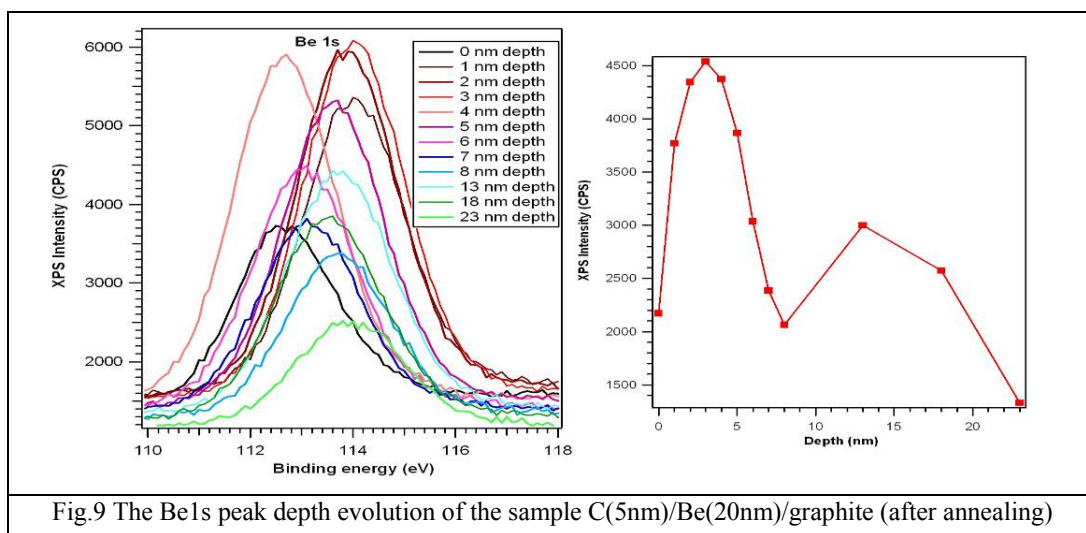


Fig.9 The Be1s peak depth evolution of the sample C(5nm)/Be(20nm)/graphite (after annealing)

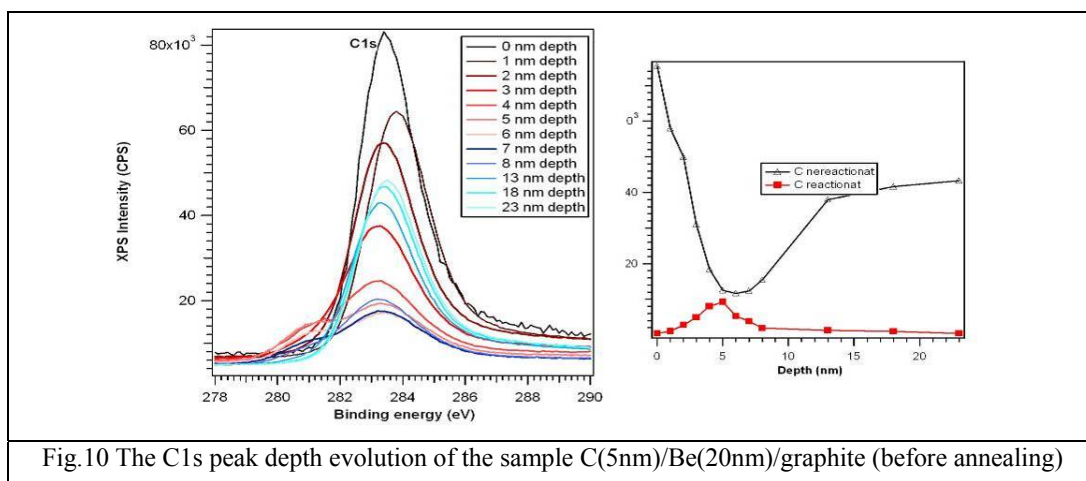


Fig.10 The C1s peak depth evolution of the sample C(5nm)/Be(20nm)/graphite (before annealing)

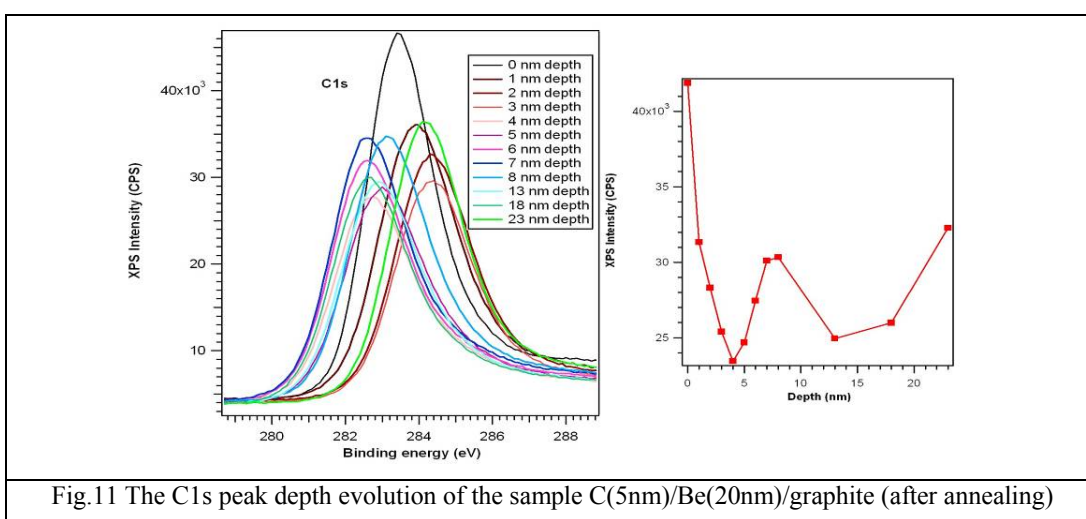
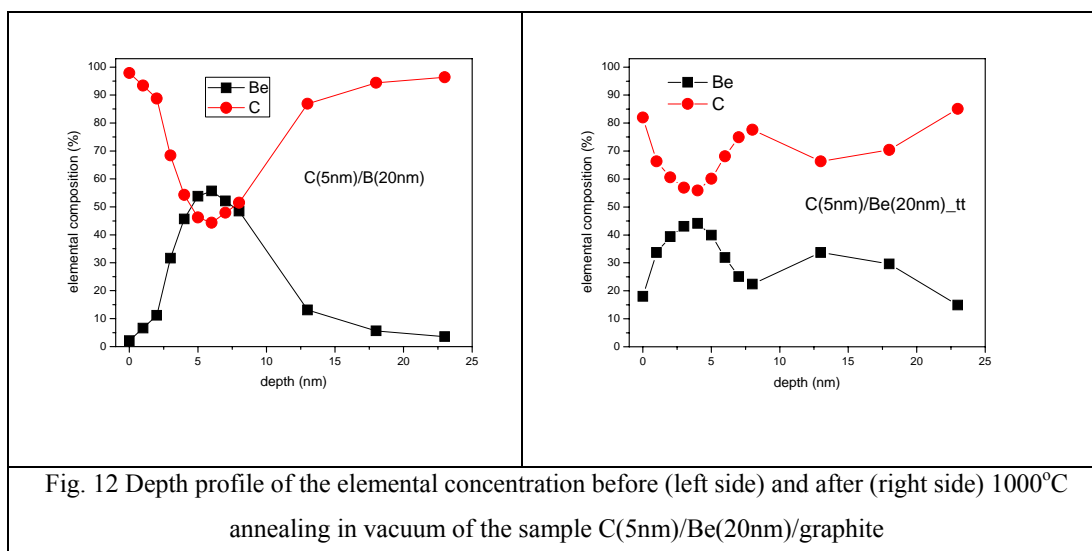


Fig.11 The C1s peak depth evolution of the sample C(5nm)/Be(20nm)/graphite (after annealing)



As shown in Fig 12, analyzing the sample C(5nm)/Be(20nm)/graphite we observe the decrease of the C concentration until 5 nm followed by an intermixing with Be, until 8 nm depth. At further depth inside the multilayer film, the concentration of Be element decreases presumed due to the strong diffusion of the C element from the graphite substrate. Accordingly, the Be layer has a thickness of maximum 10 nm, appearing strong mixed with C atoms. After the annealing at 1000°C, we observed a homogenization of the whole film presenting a significant C-Be mixture formation, centered on a 30at% concentration of Be and 70at% C, sustaining the statement of the small thickness of Be layer and the strong diffusion of the C element from substrate.

In the XPS analysis of the multilayer sample W(5nm)/Be(20nm)/graphite before and after thermal treatment we have to take in account the depth profile behavior of the C1s peak , due to the graphite substrate influence (Figs. 12-16).

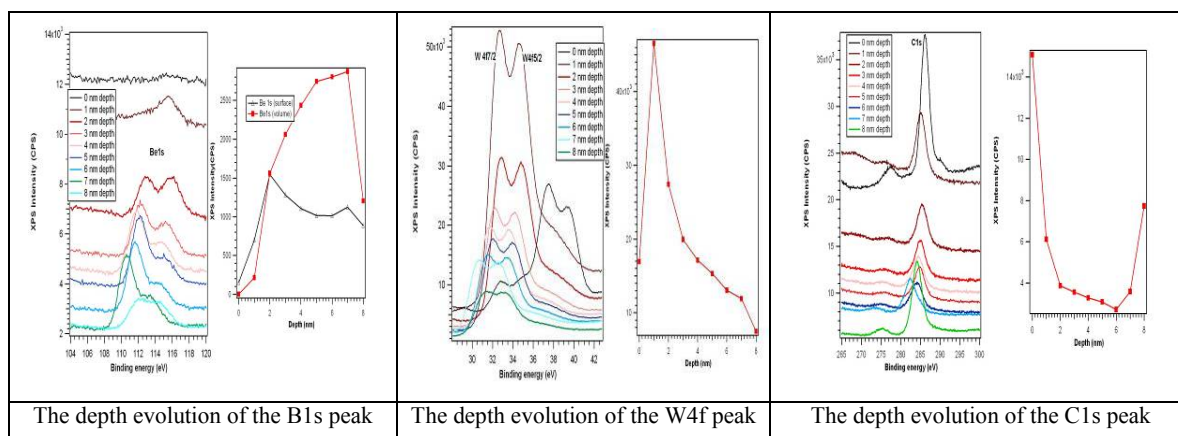


Fig.13 The Be1s, W4f and C1s peaks depth evolution of the sample W(5nm)/Be(20nm)/graphite (before annealing)

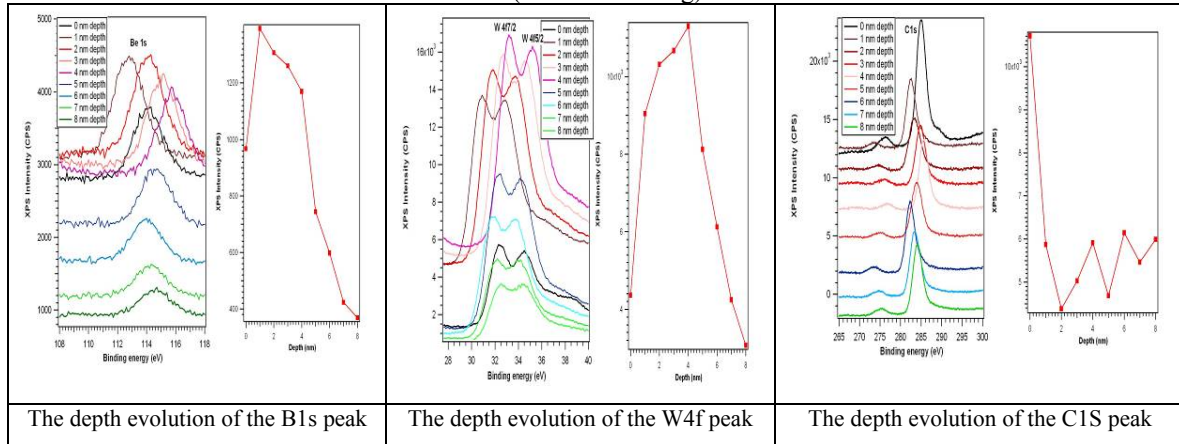


Fig.14 The Be1s, W4f and C1s peaks depth evolution of the sample W(5nm)/Be(20nm)/graphite (after annealing at 1000°C)

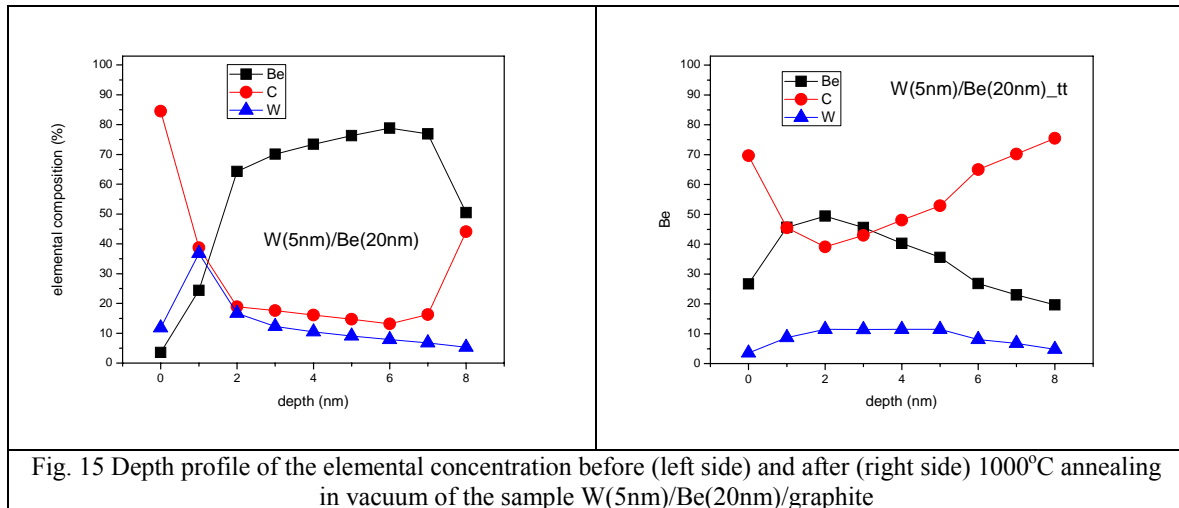


Fig.15 shows the strong diffusion of the C element inside the W layer, close to the film surface (excepting the first point of the measurement where the higher concentration of the C element is determined by the usual contamination with carbon from the atmosphere after deposition). We can observe further the weakness of the W layer (significant concentration only on 2-3 nm) and the strong migration of the C element from the graphite substrate thru the Be layer since 8 nm depth (as previous observation we expected that the be layer to be thinner than 10 nm). After the annealing at 1000°C the multilayer structure become homogenous at relative concentrations of 6at%W, 40at%Be and 54% C. We can conclude that the W top layer measured 2 nm in thickness and the Be layer was of 10 nm. A

strong migration of the C element was detected from the graphite substrate inside the only 12 nm multilayer structure.

The samples will be subject to deuterium retention and desorption studies to be performed at IPP Garching.

6. Influence of the substrate nature on deuterium retention and release studies for beryllium films deposited on carbon and tungsten

Pure beryllium films were prepared for this study using 12mm X 14mm X 1-3mm carbon and tungsten substrates

Deuterium implantation was performed at IPP Garching in the High Current Ion Source. The energy of D ion beam was 600 eV D_3^+ (meaning 200 eV/D) at an incident direction normal to the target surface at room temperature. The fluence was 5×10^{22} D/m² for each sample. After the implantation, the amount of D retained in the films was determined by Nuclear Reaction Analysis (NRA) using ^3He ion beam, having energy of 690eV.

Fig. 16 shows deuterium distribution inside the deposited Be films both on C and W substrates. A clear difference of the retained deuterium depth profiles depending on the type of the substrate. A possible explanation of the distinct behavior concerning deuterium retention can be the substrate structure influence on the deposited film compactness. In the Be films deposited on C substrate it can be observed that deuterium was implanted to higher depths than in the films deposited under same conditions but on W substrate. This distinct behavior of the deposited films under the same conditions can be due to the fact that the film structure has the mark of the surface structure of the used substrate.

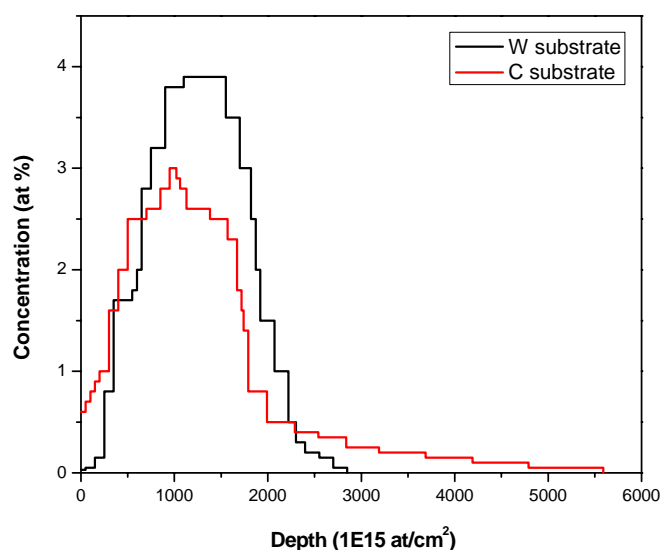


Fig. 16. NRA depth profile of the retained deuterium inside the film

After deuterium implantation and NRA analysis for deuterium distribution inside the studied films, there have been performed analysis measurements Thermal Desorption Spectroscopy (TDS), using TESS facility available at IPP-Garching. In order to perform the measurements, the samples were introduced inside a quartz tube connected to a high vacuum system, degassed by heating at around 1050 K for 12 hours. The samples were heated in an oven, connected and controlled by a dedicated computer system. The temperature for heating the samples was around 1050 K on a 0.25 Ks^{-1} ramp scale, optimized for linearity. A quadrupole spectrometer was used in order to analyze the desorbed particles. For the mass spectrometer calibration D_2 and H_2 were used after each measurement. Figures 17 and 18 present D_2 and HD molecules evolution with time and temperature.

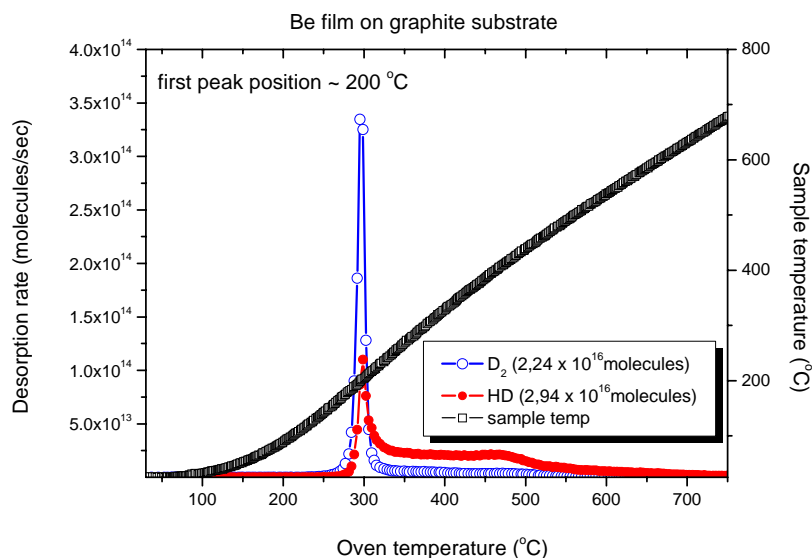


Figure 17. TDS spectra of the D_2 and HD molecules obtained for the beryllium films deposited on graphite substrates.

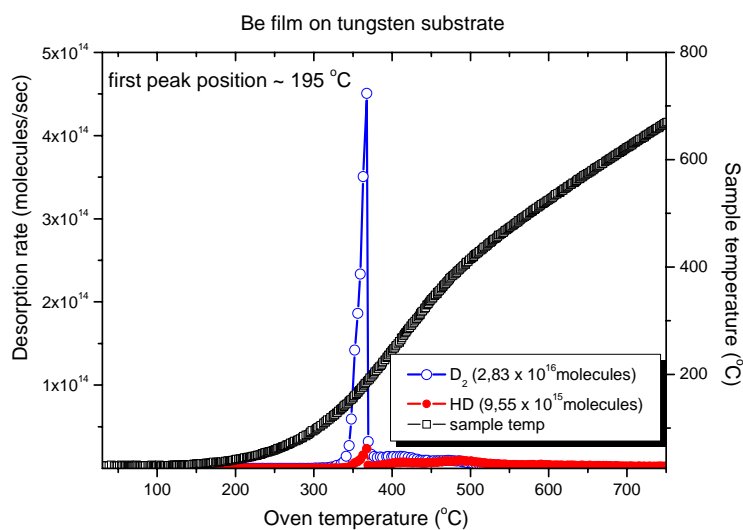


Figure 18. TDS spectra of the D_2 and HD molecules obtained for the beryllium films deposited on tungsten substrates.

As it is shown in the figures above, from TDS spectra analysis, most deuterium retained inside the films was released (89%), as molecular deuterium (D_2). The remaining deuterium was released as HD and D_2O . Desorption of the molecular deuterium peak ($\sim 200^\circ\text{C}$) is in good agreement with the results obtained on pure crystalline bulk beryllium. This

desorption peak is specific to crystalline beryllium and it is caused by low energy defects presence. The lack of higher temperature peaks (higher trapping energy) proves that the film's structure was not modified during the deuterium ion implantation. NRA analysis using a beam of ^3He and having the energy of 800 keV confirmed that all the deuterium was released during the TDS experiment.

7. CONCLUSIONS

Thin multilayer films containing beryllium (20 - 200 nm) and a cap layer of tungsten (5 -150 nm) or carbon (5-50 nm) were deposited on graphite, silicon and tungsten substrates kept at room temperature during coatings, using thermionic vacuum arc method (TVA).

The substrate temperatures were kept constant during depositions at RT, 200 and 300°C, respectively. Some films were annealed in high vacuum condition at 350, 750 and 1000°C for 30 minutes.

AFM measurements on the prepared films roughness show smooth film with RMS roughness values in the range of 3-15 nm

XPS analysis of C(5nm)/Be(20nm)/graphite multilayer non-thermally treated infer the decrease of the C concentration until 5 nm followed by an intermixing with Be, until 8 nm depth. At further depth inside the multilayer film, the concentration of Be element decreases due to the strong diffusion of the C element from the graphite substrate. After the annealing at 1000°C, a homogenization of the whole film was produced presenting a significant C-W mixture formation, centered on a 30at% concentration of Be and 70at% C. After the annealing at 1000°C, the W(5nm)/Be(20nm)/graphite multilayer structure become homogenous at relative concentrations of 6at%W, 40at%Be and 54% C. A strong migration of the C element was detected from the graphite substrate inside the 12 nm film.

After deuterium implantation (energy of D ion beam of 600 eV D_3^+), performed at IPP Garching on the Be layers deposited on graphite and tungsten substrates, the amount of D retained in the films was determined by Nuclear Reaction Analysis (NRA) using 690eV ^3He ion beam. A clear difference of the retained deuterium depth profiles depending on the type of the substrate was observed, due to the substrate (W or graphite) structure influence on the deposited film compactness.

Thermal Desorption Analysis (TDS) performed heating the samples until a maximum temperature of 700°C reveal that the most deuterium retained inside the films was released (89%) as molecular deuterium (D₂). The remaining deuterium was released as HD and D₂O. NRA analysis using a beam of 800 keV ³He confirmed that all the deuterium was released during the TDS experiment.

Comunicari la Conferinta internationale

1. A. Anghel, C. Porosnicu, C. P. Lungu, K. Krieger, K. Sugiyama, J. Roth, 19th International Conference on Plasma Surface Interactions, PSI 2010, May 24-28, 2010, San Diego, USA
2. A. Anghel, C. Porosnicu, C. P. Lungu, K. Sugiyama, C. Krieger and J. Roth, Thermal Treatment Influence on Be/C Mixed Material Formation and Fuel Retention E-MRS 2010, Spring Meeting, Strasbourg, France, June 7-11 2010
3. Cristian P. Lungu, Characterization of Beryllium Containing Compounds Prepared Using TVA Method, Report on task agreements: WP10-PWI-06-01-02/MEdC/PS, WP10-PWI-06-02-02/MEdC/PS, Joint SEWG Meetings, Material Migration and Material Mixing, FZJ Juelich, Germany, 30.06.-02.07.2010.

BS18 B

RST in extenso

Titlul complet al Proiectului BS 18B:

Study of the thermal treatment influence in formation of the stable Be-C, Be-W and C-W alloys . TVA gun electron beam irradiation influence. (BS-PS) (Studiul influenței tratamentului termic în formarea de compusi stabili Be-C, Be-W și C-W. Influența iradierii cu fascicule de electroni produse de tunul TVA)

Etapa I

Activitatea I

Production of Be-C-W mixed layers with different relative concentrations

Task title: TA PWI 2010, Chapter 6: Determination of expected alloys and compounds in ITER relevant conditions and their influence on PWI processes and fuel retention

Sub-task: **Sub-task:** TA WP10-PWI-06-02-02/MEdC/PS: D-retention in mixed materials containing H, D and He

Title of the report: Production of Be-C-W mixed layers with different relative concentrations

Task Force on Plasma Wall Interaction

Area: SEWG ITER Material Mix

Principal investigator: Cristian P. LUNGU,

Research team: C. Porosnicu, A. Anghel, I. Jepu, A.M.Lungu, P. Chiru, C. Ticos, C. Luculescu

National Institute for Laser, Plasma and Radiation Physics, Association
EURATOM MEdC

CONTENTS

Abstract.....	4
1. Introduction.....	5
2. Preparation of the samples	6
2.1 Preparation of mixed Be-C-W layers.....	6
2.2 Preparation of co-deposited Be-D layers.....	8
3. Morphological and compositional characterization of the prepared samples.....	10
3.1 SEM and EDS measurements.....	10
3.2 XPS analysis.....	10
3.3 RBS analysis.....	17
4. CONCLUSIONS.....	20

Abstract

The present project is performed under Task Agreement PWI 2010, Chapter 6: Determination of expected alloys and compounds in ITER relevant conditions and their influence on PWI processes and fuel retention

The aim of this project is to improve our knowledge on material mixing in ITER relevant environment, in particular: (i) formation and properties of mixed materials; (ii) fuel retention in mixed materials

In this purpose there were deposited 50-200 nm in thickness Be-C-W ternary system films with different relative concentrations of the three elements (Be, C and W) on graphite and silicon substrates using the thermionic vacuum arc method developed at NILPRP. Some samples were prepared in the presence of the residual oxygen and additional D gas.

The samples were analyzed in Romania by SEM (Scanning Electron Microscopy), EDS (Electron Dispersion Spectroscopy), AMS (Accelerator Mass Spectrometry) and XPS (X-ray Photoelectron Spectroscopy).

During research stages at IPP Garching Germany the prepared samples were analyzed using RBS technique.

1. Introduction

The current design of ITER involves the use of beryllium (Be), carbon fiber composite (CFC) and tungsten (W) as plasma facing materials. It is expected that Be eroded from the first wall and ionized in the *scrape-off-layer* (SOL) plasma will be mainly re-deposited at divertor surfaces leading to the formation of mixed materials films and corresponding changes of the original material properties of W and C. The in-vessel fuel retention inventory is one of the key issues affected by the mixed material systems. Its and the development of control strategies require a detailed knowledge of both retention and release behavior of such mixed systems.

D retention in mixed layers deposited on surfaces of the three ITER PFMs has been investigated for all relevant binary material combinations. However, only few data exist on the influence of layer structure and layer thickness for D-retention in both the layers and the deep bulk regions below. More experiments of this kind are required.

Association Euratom-MEdC has substantial expertise in the preparation of mixed materials using the original method of thermionic vacuum arc (TVA). There is a major collaboration with IPP Garching, FZJ Juelich, Germany, TEKES, Finland which have experimental facilities, thermal testing and film property characterization equipment.

Be-C-W mixed layers with different relative concentrations were prepared using simultaneously thermionic vacuum arc discharges. The morphology and the film composition on the surface and the depth were determined by Scanning Electron Microscopy (SEM), Energy Dispersive Spectrometry (EDS), Accelerator mass Spectrometry (AMS), X-ray Photoelectron Spectroscopy (XPS) and Rutherford Backscattering Spectroscopy (RBS).

2. Preparation of the samples

2.1 Preparation of mixed Be-C-W layers

In order to obtain a variable Be-C-W ratio, a setup presented in Fig. 1 was developed. The distance between the anodes was 20 cm and the sample holder-anodes distances were around 25 cm, as the particle flux depends on the distance and the incident angle. The two

anodes and the substrates were positioned so that a different particle flux was present for each sample in a deposition batch.

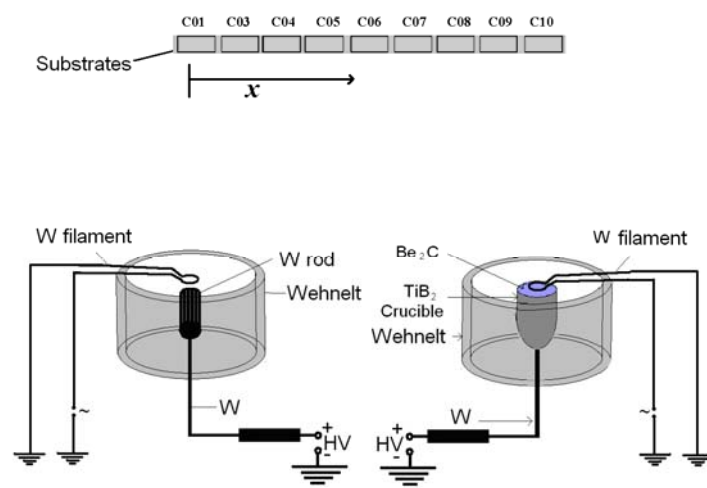


Figure 1. Schematic representation of the Be-C-W thermionic vacuum arc deposition system.

The high temperature resistant TiB_2 crucible was filled with beryllium and carbon powder and previously heated at more than 1500°C , knowing that beryllium carbide is obtained by heating the elements beryllium and carbon at elevated temperatures (above 900°C). It also may be prepared by reduction of beryllium oxide with carbon at a temperature above $1,500^\circ\text{C}$:



As a result, after heating the crucible at 1500°C for 30 minutes, the resulting powder changed color into yellow, indicating the formation of the compound. The powder was sent to the XRD analysis in order to infer the Be_2C formation.

The relative concentration control between all of the three components of the thin film were made by choosing the proper electric parameters for discharges and by proper positioning of the substrates in respect with the two plasma sources. Due to the different distances of the substrates to the two anodes the concentration of the W element in the Be-C-W ternary system will decrease or increase constantly with “x” position. Several samples were placed at different distances to the two evaporation sources (as shown in Fig.1), being possible to obtain almost continuum concentration variation.

The electron beams evaporate both the beryllium carbide powder and the tungsten rod used as anodes, by applying high voltages (1-5kV) between cathodes and respectively

anodes. Bright plasmas in pure tungsten and beryllium carbide were ignited simultaneously. The plasmas were independently controlled by the electron beams (thermo-electrons) emitted by the heated cathodes and the applied voltage on the anodes, in order to obtain the desired concentration.

For each batch, carbon and silicon substrates were used. The carbon substrates were mirror polished fine grain graphite. The substrates were 12 mm by 14 mm rectangular shape. An oven was used to heat the samples at 100°C. This way, the atoms and the ions from the plasma, reach the substrate without causing thermal shocks and the lack of thermal shocks decreases the possibility of getting defects caused by mechanical stress.

The substrates were placed on a holder that was mounted inside the deposition chamber, and put in thermal contact with the oven. The measured deposition parameters were:

- ✓ Substrate temperature
- ✓ I_{fW} - The heating current of the filament for tungsten
- ✓ I_{acr} - The arc current for W during the deposition
- ✓ U_{aCr} - The arc voltage for W during the deposition
- ✓ I_{fBe} - The heating current of the filament for beryllium carbide
- ✓ I_{aBe} - The arc current for Be₂C during the deposition
- ✓ U_{aBe} - The arc voltage for Be₂C during the deposition

These parameters are presented in the table below:

Table 1. The parameters for the depositions performed

Run No	I_{fW} (A)	I_{aW} (mA)	U_{aW} (V)	I_{fBe_2C} (A)	I_{aBe_2C} (mA)	U_{aBe_2C} (V)
1	52	800	2000	36.8	1000	850
2	62	1200	1500	40	700	1000

2.2 Preparation of co-deposited Be-D layers

Using a typical thermionic vacuum arc system, were performed preliminary Be-D co-depositions. The process parameters are listed below:

Set 1:

D gas introduced laterally into the reaction chamber: (i) Base pressure (initial pressure) : $P_i = 6 \cdot 10^{-6}$ torr; (ii) Deposition chamber pressure (with D flow): $P_D = 3.4 \cdot 10^{-5}$ torr
 Parameters during Be-D co-deposition: Ifilament=56A; Udischarge=630V;
 Idischarge=0.87A; Be deposition rate=1.6nm/s; Ubias=-700V
 Substrates (12mm X 14mm): Be – 2 off; Si – 2 off; Graphite – 4 off
 Final thickness (measured using in-situ quartz balance FTM7): 400nm
 Sample name sent to AMS analysis: Be400nm+D3/C1

Set 2:

D gas introduced laterally into the reaction chamber: (i) Base pressure (initial pressure) : $P_i = 7 \cdot 10^{-7}$ torr; (ii) Deposition chamber pressure (with D flow): $P_D = 4.4 \cdot 10^{-5}$ torr.
 Parameters during Be-D co-deposition: Ifilament=52.2A; Udischarge=950V;
 Idischarge=1.3A; Be deposition rate=2nm/s; Ubias= ground
 Substrates (12mm X 14mm): Si – 4 off; Graphite – 3 off ; Be 2 off (10 mm X 30mm + 20mm X 400 mm)
 Depunere 26.01.2010 – restul spectrelor

Set 3:

D gas introduced in front of the substrates: (i) Base pressure (initial pressure) : $P_i = 6 \cdot 10^{-7}$ torr; (ii) Deposition chamber pressure (with D flow): $P_D = 4.2 \cdot 10^{-5}$ torr
 Parameters during Be-D co-deposition: Ifilament=48.2A; Udischarge=1200V;
 Idischarge=1.4A; Be deposition rate=2nm/s; Ubias= ground
 Substrates (12mm X 14mm): Si – 4 off; Graphite – 4 off ;

The D amount co-deposited into the prepared was measured using an Accelerator Mass Spectrometer (AMS) of the NIPNE-HH National Institute, Magurele-Bucharest (Fig. 2). The AMS facility uses the 8 MW-FN 15, HVEC Tandem Accelerator. The ion injector deck of the AMS facility in Bucharest comprises: Injector deck polarized - 60 kV; second platform, polarized -30 kV with respect to the injector deck; the 40 NC-SNICS; the analyzing magnet; slits and retractable Faraday Cup; pre-acceleration NEC tubes. The detection systems for AMS at NIPNE contains: 1) Array of Si(Au) pin detectors, for light particle detection; 2) Bragg-gas filled detector, for medium mass nuclei; 3) E-DE gas filled detector with TOF discrimination, for heavy nuclei

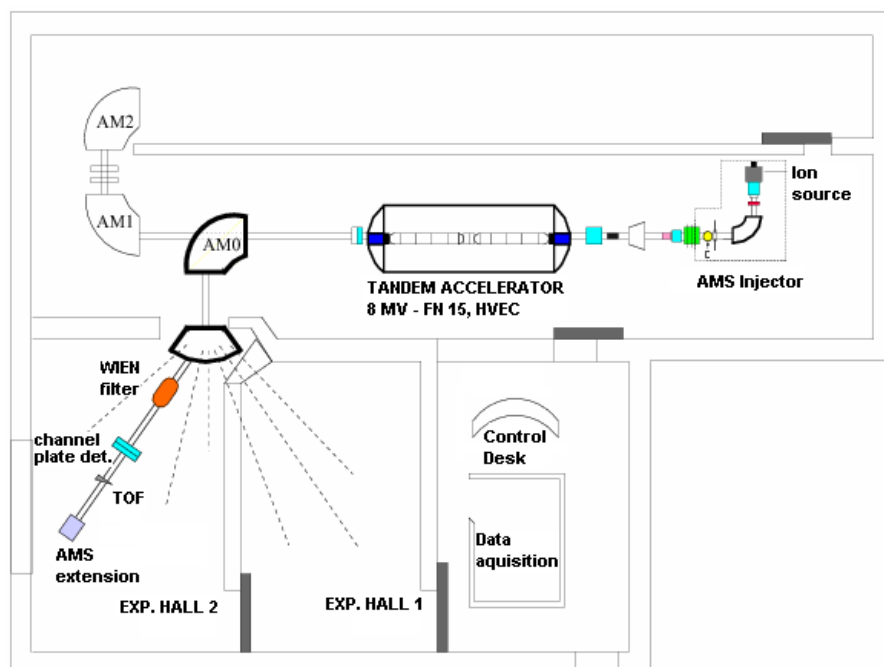


Fig.2 A schematic drawing of the AMS facility at NIPNE – Magurele-Bucharest

A typical AMS spectrum presented in Fig.3 shows the high sensitivity in detecting a very low numbers of D atoms ($6 \cdot 10^{18}/\text{cm}^2$) co-deposited with Be film.

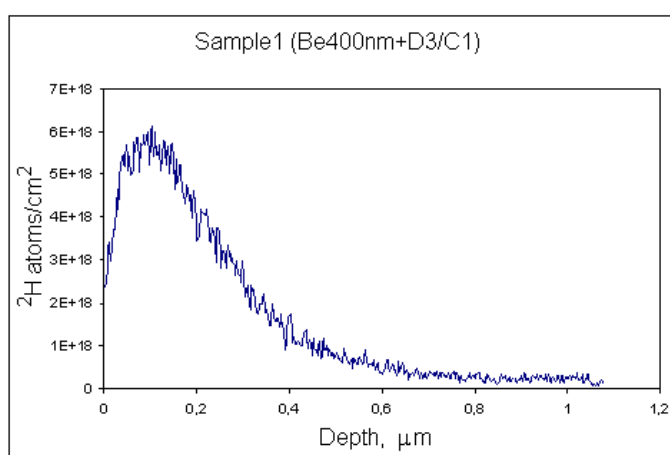


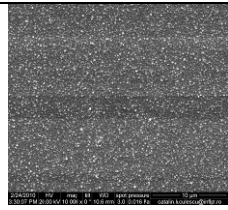
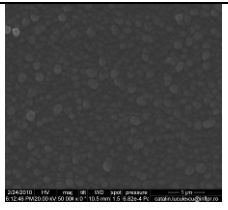
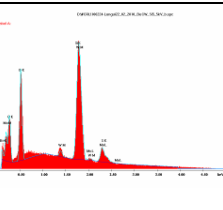
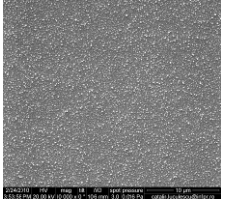
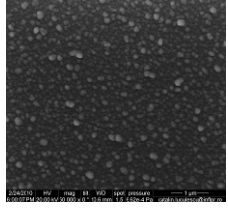
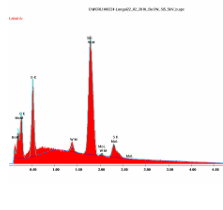
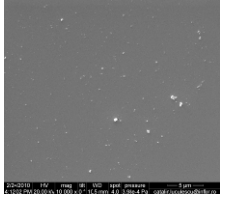
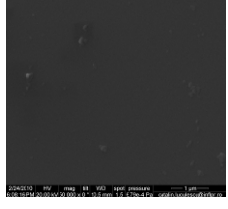
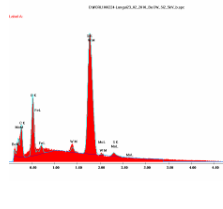
Fig.3 AMS spectrum of the Be-D co-deposited sample

3. Morphological and compositional characterization of the prepared samples

3.1 SEM and EDS measurements

SEM, EDS measurements were performed in order to observe the surface morphology and the relative atomic concentration distribution of the three elements inside the film. Although EDS does not give information about the depth profile because it integrates the signal of the distorted electrons, it can give accurate information about the composition.

Table 2. SEM and EDS analyses

Sample Code	SEM 10.000 X	SEM 50.000 X	EDS	Concentration (at%)
22.02.2010 Be+C+W on Si 2 (Run1)				Be - 25.34at% C – 27.21at% W – 23.31at% O – 23.64 at%
22.02.2010 Be+C+W on Si 5 (Run1)				Be - 22.00 at% C – 30.44 at% W – 25.27 at% O – 22.29 at%
23.02.2010 Be+C+W on Si 2 (Run 2)				Be – 19.70 at% C – 29.20 at% W – 27.65 at% O – 23.42 at%

The relative concentrations of the three elements measured using EDS analysis were in the range of 19-25 at% Be, 25-31at% C and 23-28% W in both runs; an increased concentration of W into the prepared films was determined, as expected, due to the chosen deposition parameters. The oxygen concentration into the prepared films was in the range of 23-26%. More accurate information about depth profile was required.

3.2 XPS analysis

Using a modern X-ray Photoelectron Spectrometer from SPECS, Germany, the prepared samples were analyzed in order to infer the formation of chemical bonding during

simultaneous depositions. For a better systematization of the results, a code was given to each sample, considering the date of the deposition and the position on the holder.

Run 1, position 03; Be-C+W/graphite: Code: 22c03

Run 1, position 06; Be-C+W/graphite: Code: 22c06

Run 2, position 01; Be-C+W/graphite: Code: 23c01

Run 2, position 04; Be-C+W/graphite: Code: 23c04

The following 4 Be-C-W thin films have been measured using XPS analysis (5 depth points, as follows: 0 nm, 3 nm, 6 nm, 9 nm and 12 nm): 22C03, 22C06, 23C01 and 23C04. The samples with 23 prefix have been obtained using a W deposition rate higher of that of the samples with 22 prefix. For numbers increasing “x” index, the graphite substrates positioning was closer to the W anode (evaporator). It can be concluded that from the deposition point of view, there are expected higher W concentration on 22C06 sample than on 22C03 sample and higher W concentration on 23C04 sample than on the 23C01 sample respectively. Globally, the two samples belonging to the 23 series (Run 2) shall present W concentrations higher than the ones belonging to the 22 series (Run 1).

The XPS method is a very effective surface analysis technique which can offer qualitative and quantitative information on species at the material surface, on chemical bonds in which these are mixed up, etc (it is also known as electron spectroscopy for chemical bond – ESCA). The method is based on electron photoemission from the depth layers of different elements, under the incidence of a monochromatic X radiation. The energy of the expelled electrons can be expressed using the relation $E_c = h\nu - BE - \Phi$, where BE is the bond energy of the extracted electron and Φ is the work of extraction specific to the material (it is a constant measure for a given material and it is much lower than the bond energy; it characterizes only the solid state). The experiment consists in sending a monochromatic X radiation beam (typical energies over 1500eV) on the sample and using an electron analyzer, to register the electrons which come out of the material with different kinetic energies. On the basis of the relation established above, it can be estimated the bond energy adequate to each kinetic energy, in such a way that from the spectral point of view, to be possible to represent the number of electrons corresponding to different bond energies. It is obviously that around the resonance conditions occurs an increase of the events number, obtaining this way resonance peaks corresponding to different bond energies. Each element is characterized using a set of

spectral lines. The lines position within the spectrum are very sensitive to the chemical bonds in which the valence electrons are involved and thus allow to specify the phase type or the compounds in which different electrons are involved. In our case, there have been directly selected the energy domains corresponding to Be, W and C it was accentuated the evolution of these lines intensities especially. The photoelectron spectroscopy studies (associated with depth profile) have been performed using a dedicated photoemission chamber (SPECS GmbH). The X rays source consists in a Mg cathode providing energy radiation of 1253.6 eV. The resulted photoelectrons are analyzed using a *Phoibos 150 mm* analyzer, operating with an energetic window of 50 eV and a spectral resolution of 0.2 eV.

In order to offset the load effects on the surface, it was used a flood gun operating at an acceleration energy of 1 eV and an electron current of 0.1 mA. The depth profile was performed using a high intensity Ar⁺ ion gun (IQE 12/38). The current established on the sample was of 10 mA at an ion acceleration voltage of 5kV. The sample investigated depth was estimated from the elementary crystallographic point of view, taking into account the type of the crystalline structure specific to the material and assuming that each Ar⁺ ion incident on the sample discharges one of its atoms. The spectral regions associated to Be and W for 22C03 and 22C06 samples are presented in Figs. 4-8.

Related to Be, it is observed that on the surface it appears especially as an oxidized form. Once with getting into depth, this form diminishes its weight, on the basis of metallic Be ratio increase. The two ratios saturates, reaching a relative ratio of 50%-50% from the depth of 6 nm. Anyway, it must be mentioned the presence of oxidized Be even in the most deep layer of the film

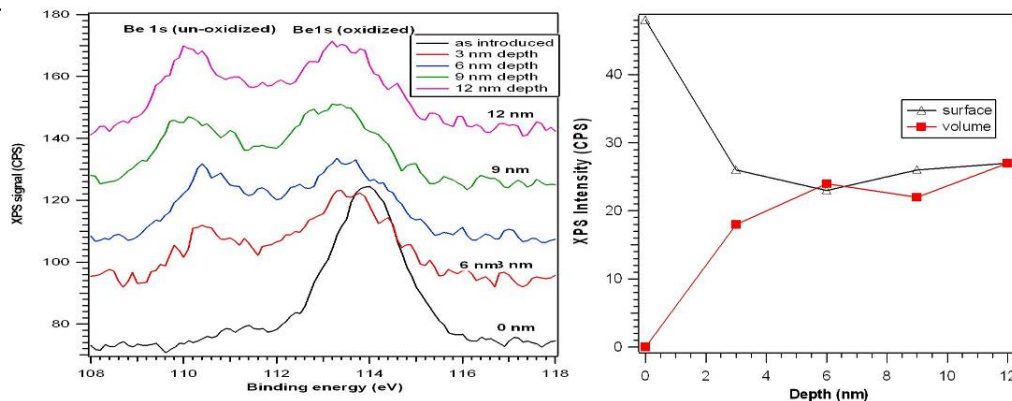


Fig. 4. Spectral region associated to Be for 22C03 sample (on the left). On the right, the evolution of the spectral lines intensities for the two species in the spectrum. (oxidized Be – black line and metallic Be - red line)

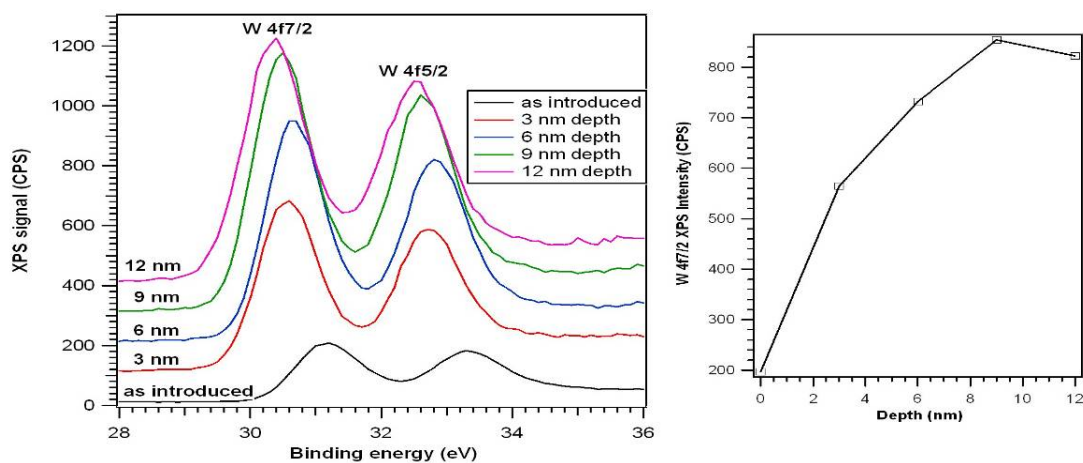


Fig. 5. Spectral region associated to W for 22C03 sample (on the left). On the right, the evolution of line $4f_{7/2}$ intensity (considered as a reference line for metallic W analysis)

Related to tungsten, two aspects must be mentioned. On the surface, the intensity of the 2 specific peaks is much weaker than in volume and the lines are displaced in the spectrum to higher energies, suggesting a higher electro negativity (the origin – a possible oxidation?). Volume W is closer to metallic W, but the small moves of the depth lines can suggest the possible different surroundings of this. W ratio clearly increases in depth which, under the conditions in which C and Be appear to reach a saturation value, suggest the film composition change, in depth inclusively (the W maximum relative ratio is reached at around 9 nm).

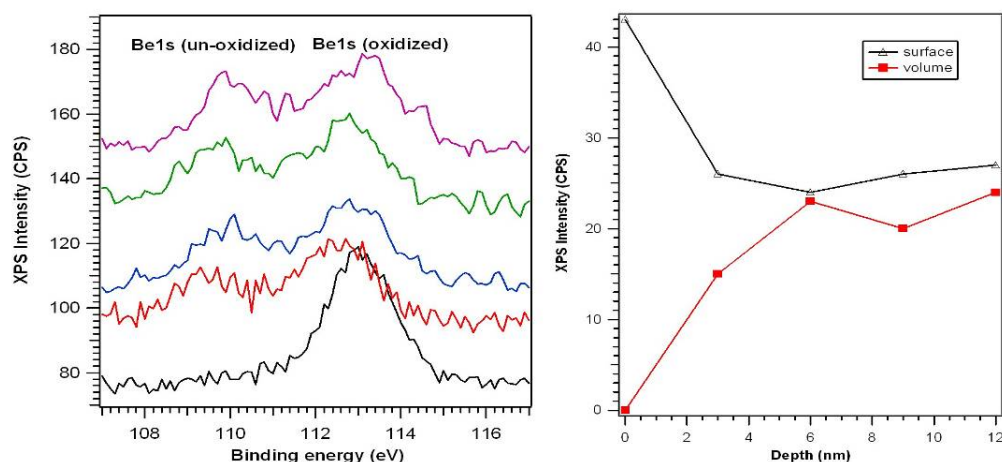


Fig. 6. Spectral region associated to Be for 22C06 sample (on the left). On the right, the evolution of the spectral lines intensities of the 2 species highlighted in the spectrum (oxidized Be – black line and metallic Be – red line)

The same information is presented for 22C06 sample (Figs. 5-6). A very similar behavior with the above mentioned sample is observed, the only difference being the

increased intensity of the W line (in absolute values 1050 cps against 850 cps in the previous sample). Anyway, this observation appears to be in agreement with a higher concentration of W, due to the substrate position on the deposition holder. As a percentage, this might indicate an increase of the W relative content with about 25% (if the W content of the first sample will be of 10% according to RBS measurement, the content of the second sample will be of 12.5%; we mention that we work to determine the elemental percentage from XPS). This is in good agreement with the RBS measurements shown in Figs. 12-17.

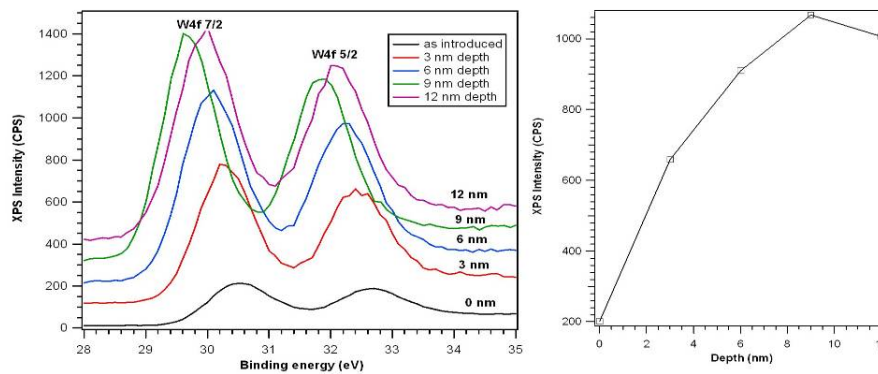


Fig. 7. Spectral region associated to 22C06 sample (on the left). On the right, the evolution of line $4f_{7/2}$ intensity (considered as a reference line for metallic W analysis)

The same types of results are presented in Figs 6-9 for 23C01 and 23C04 samples. It is obvious that the samples with 23 marks have a different behavior from the ones with 22.

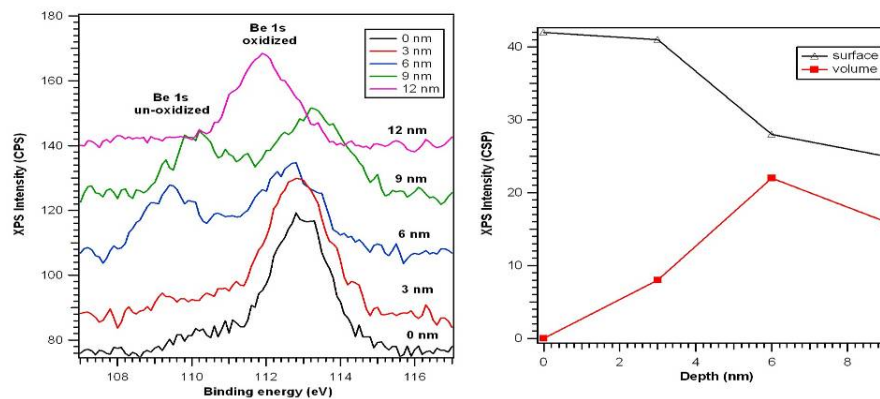


Fig. 8. Spectral region associated to Be for 23C01 sample (on the left). On the right, the evolution of the spectral lines intensities of the 2 species highlighted in the spectrum (oxidized Be – black line, and metallic Be – red line)

Related to the sample 23C01, highlights oxidized Be, even at a depth of 3 nm. At 6 nm depth, the percentage of oxidized Be is getting closer to the one of the metallic Be. At 9 nm

depth, the move to the right of both peaks suggests an additional oxidation and formation of a different chemical bond at 12 nm depth. (To be observed the different peaks position in Fig. 6). Related to W (Fig.7), the same sample could indicate the additional oxidation tendency in the first 3 nm, and only after this depth to be obtained W closer to the metallic one. Plus, unlike the first set containing 2 samples, this time was obtained a maximum concentration at about 6 nm, the W concentration decreasing at higher depths.

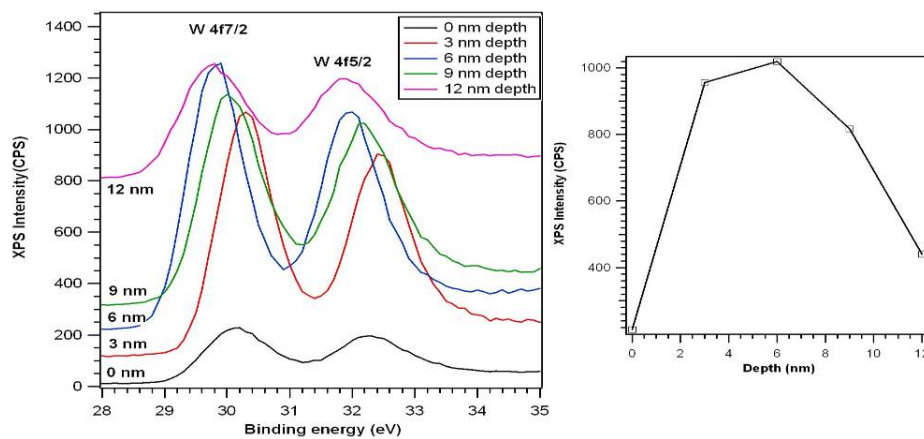


Fig. 9. Spectral region associated to W for 23C01 sample (on the left). On the right, the evolution of line $4f_{7/2}$ intensity (considered as a reference line for metallic W analysis)

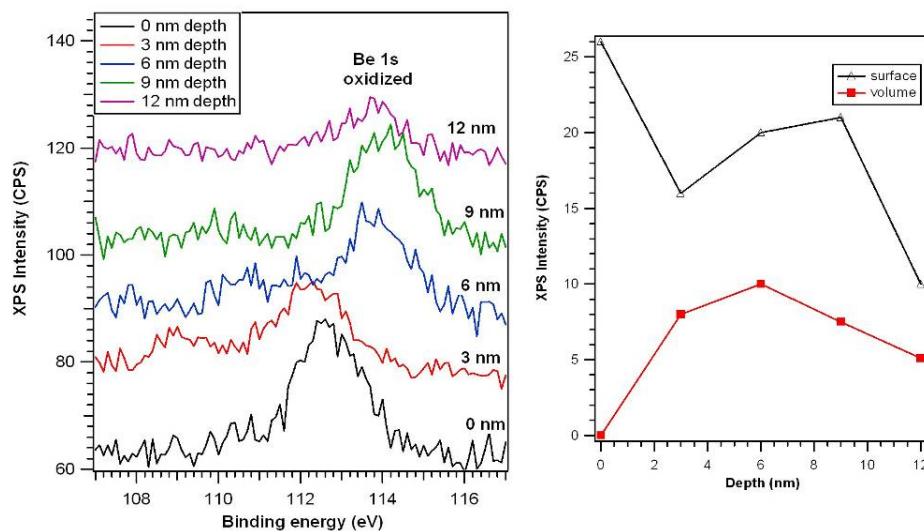


Fig. 10. Spectral region associated to Be for 23C04 sample (on the left). On the right, the evolution of the spectral lines intensities of the 2 species highlighted in the spectrum (oxidized Be – black line and metallic Be – red line)

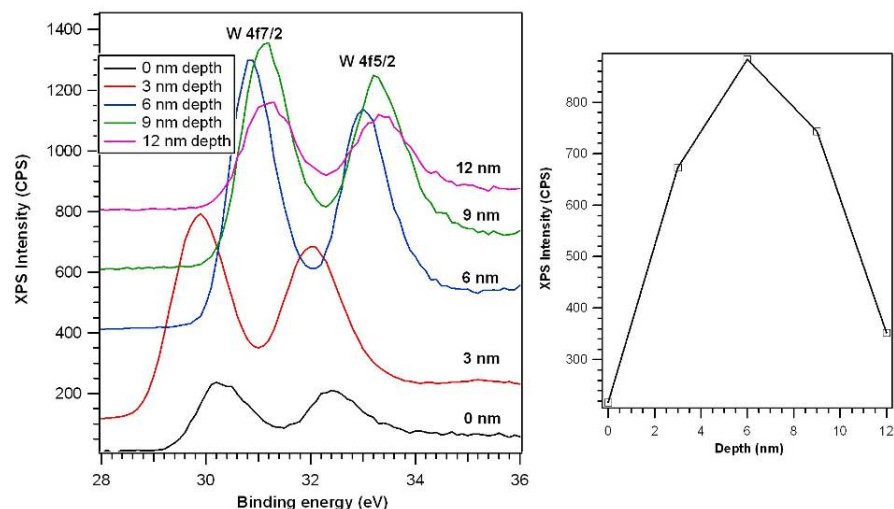


Fig. 11. Spectral region associated to W for 23C04 sample (on the left). On the right, the evolution of line $4f_{7/2}$ intensity (considered as a reference line for metallic W analysis)

Finally, for 23C04 sample it is observed a very pronounced oxidation of Be (almost impossible for metallic Be to be formed), and the peak of the oxidized one is additionally moving to higher energies (showing an electro negativity even more higher than the one of the surface) (Fig.8). Related to W, oxidization becomes more active at higher depths, the closest lines to the metallic W correspond to some 3nm depths. The same variation of W concentration with the depth is observed, as shown in Fig. 9, similar to 23C01 sample. The shifts in the peaks bonding energy allow us to assume the formation of Be_xC_y , Be_sW_t and C_mW_n compounds.

XPS elemental depth profiles presented in Figs. 12 and 13 show the relative elemental concentration for the two runs.

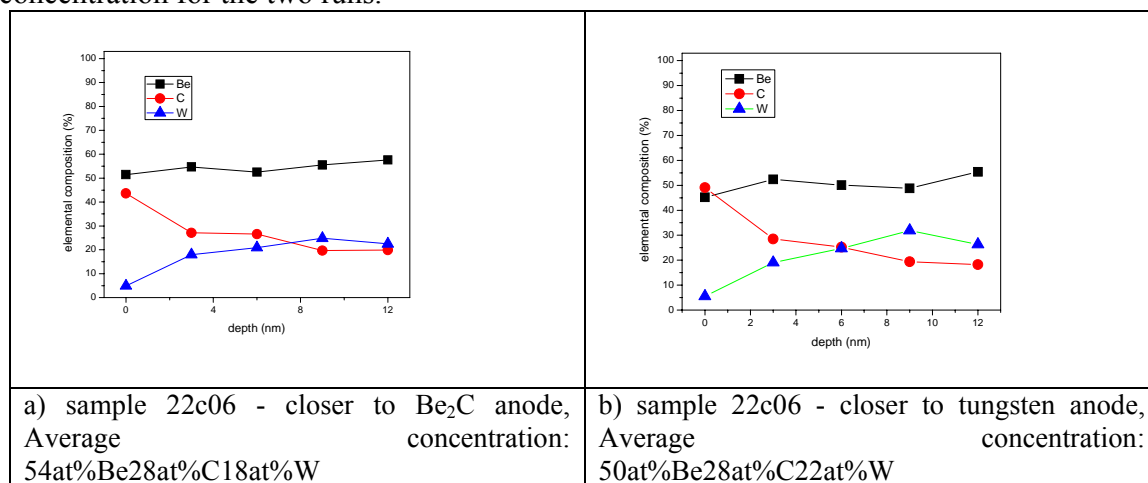


Fig. 12 Elemental depth profile for the samples prepared in the first run

It can be observed the increase of the average concentration of W, (*sample closer to the Be₂C anode: 54at%Be28at%C18at%W, sample closer to the tungsten anode: 50at%Be28at%C22at%W*) according to the positioning towards the tungsten anode the relative flat concentration of C element between the samples and W concentration increase with the film depth on the basis of the decrease of the C concentration.

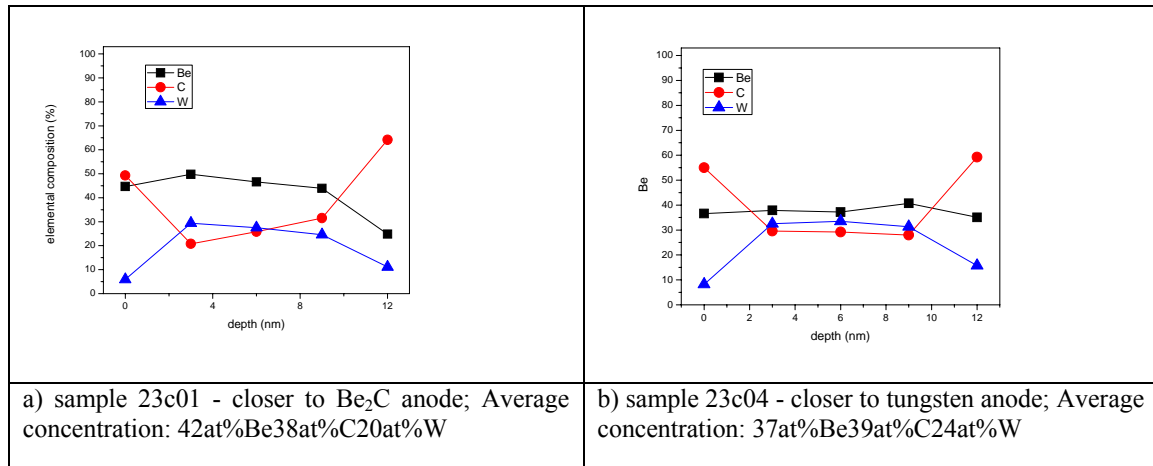


Fig. 13 Elemental depth profile concentration for samples deposited in the second run

For the second run we observed the increase of the average W concentration (*sample closer to the Be₂C anode: 42at%Be38at%C20at%W, sample closer to the tungsten anode: 37at%Be39at%C24at%W*) in accord with the substrate position relative to the evaporators and W increased deposition rate, as well as the constant concentration of the C element and the parabolic evolution of the concentration of W and C on compensational base.

3.3 RBS analysis

RBS measurements were performed to investigate the depth profile of the films compositions, including information about the oxygen. In this respect had been used a ⁴He energy beam of 2.6 MeV. The beams energy value was chosen taking into account the interaction cross section of ⁴He and Be to avoid the non-Rutherford interaction that may cause errors in the data interpretation. The fitting of the experimental data was done using SIMNRA code, developed at IPP Garching

Six samples were analyzed (three from each run, depending on the samples positions).

The depth profiles resulting from the simulation of the experimental spectra are presented in Figs. 14-19:

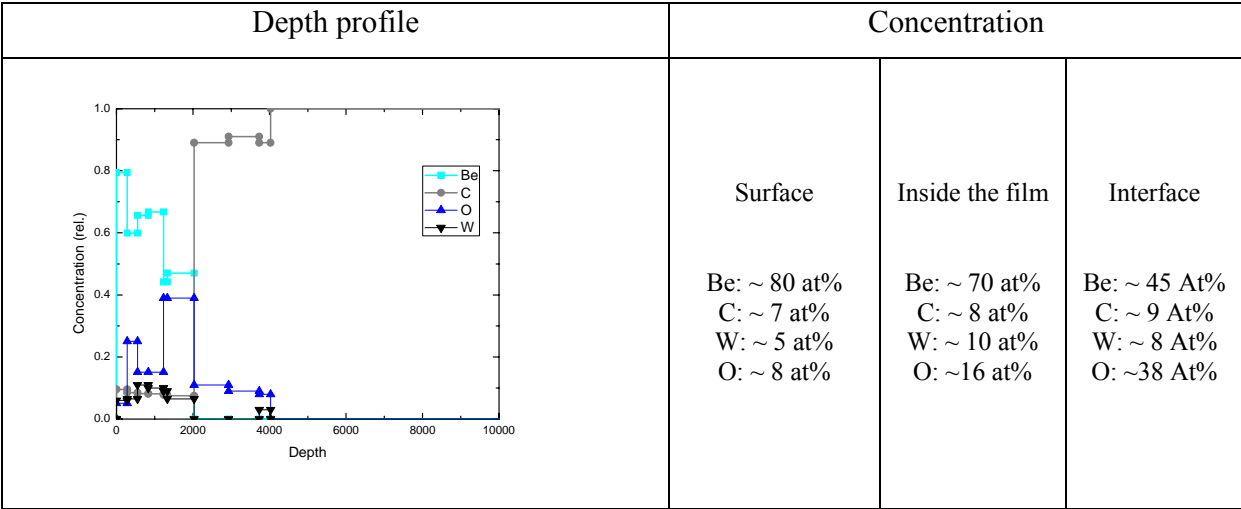


Fig. 14 RBS dept profile of the sample (Run 1) settled above the Be₂C evaporator

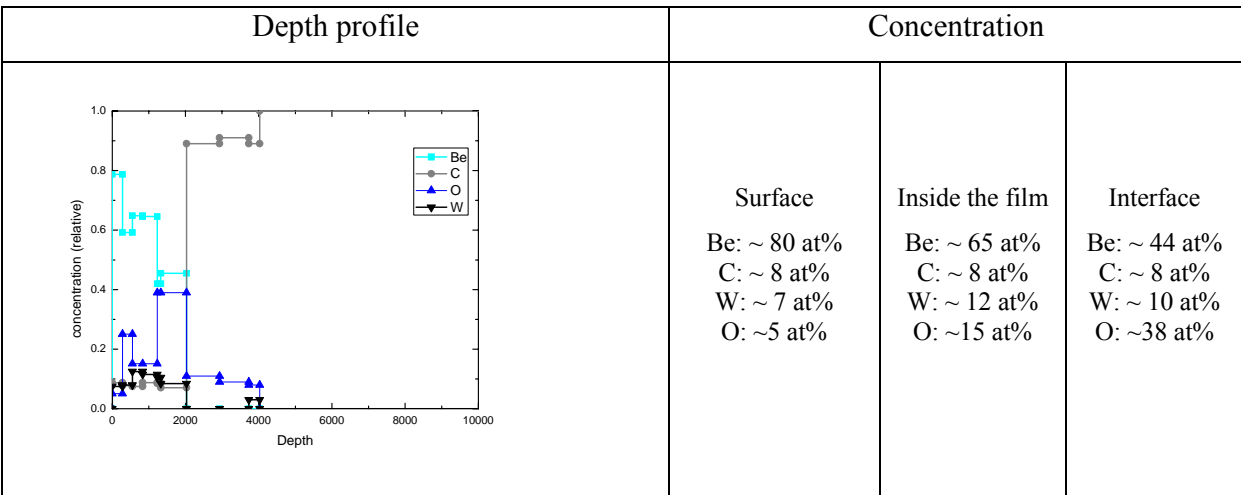


Fig. 15 RBS dept profile of the sample (Run 1) situated at the same distance from the two evaporators

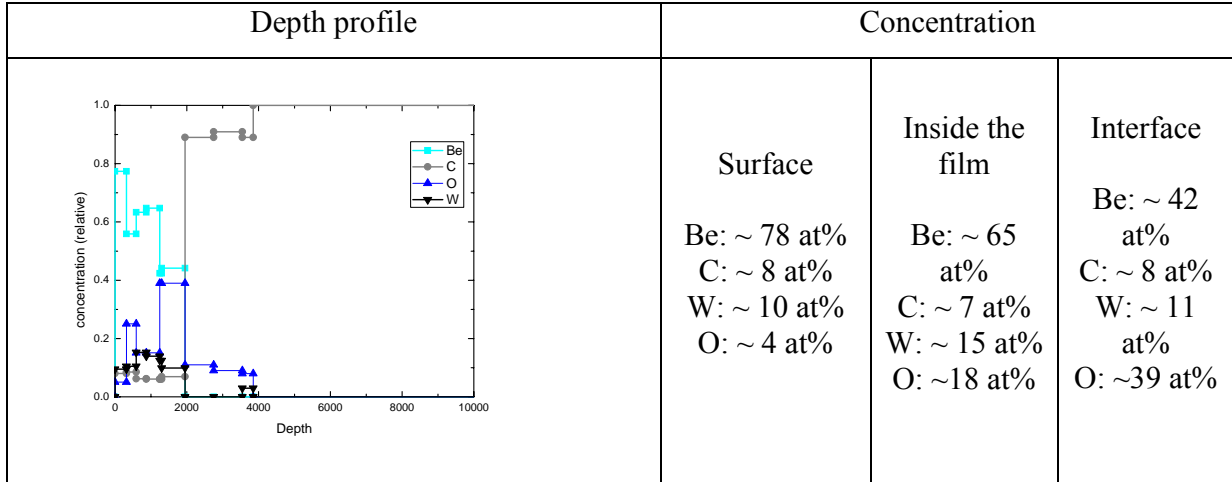


Fig. 16 RBS dept profile of the sample (Run 1) situated above the tungsten anode

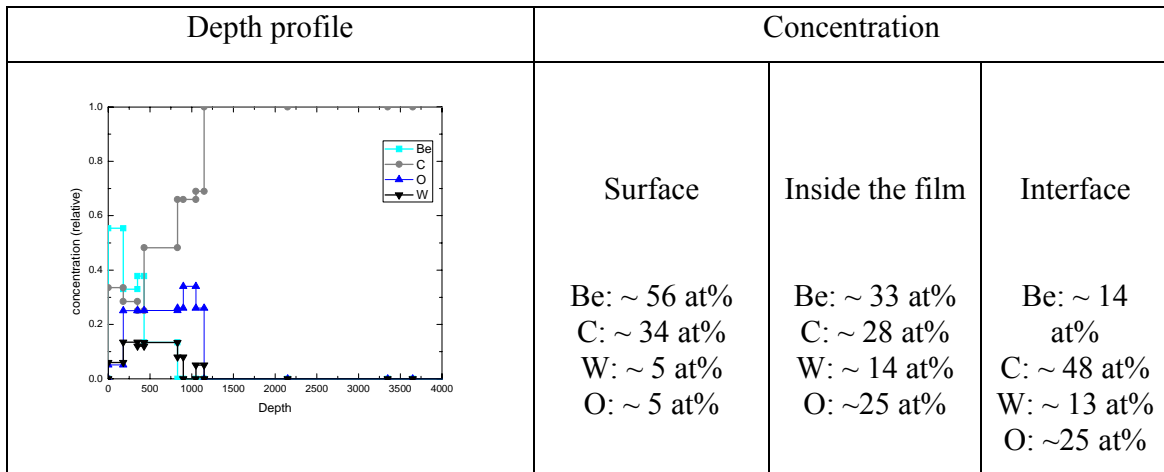


Fig. 17 RBS dept profile of the sample (Run 2) situated above the Be₂C anode

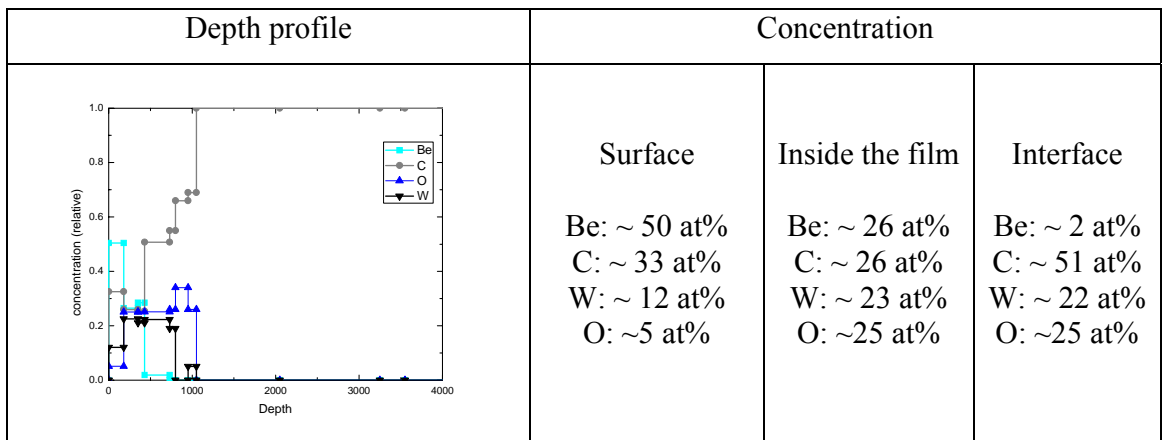


Fig. 18 RBS dept profile of the sample (Run 2) situated at the same distance from the two anodes

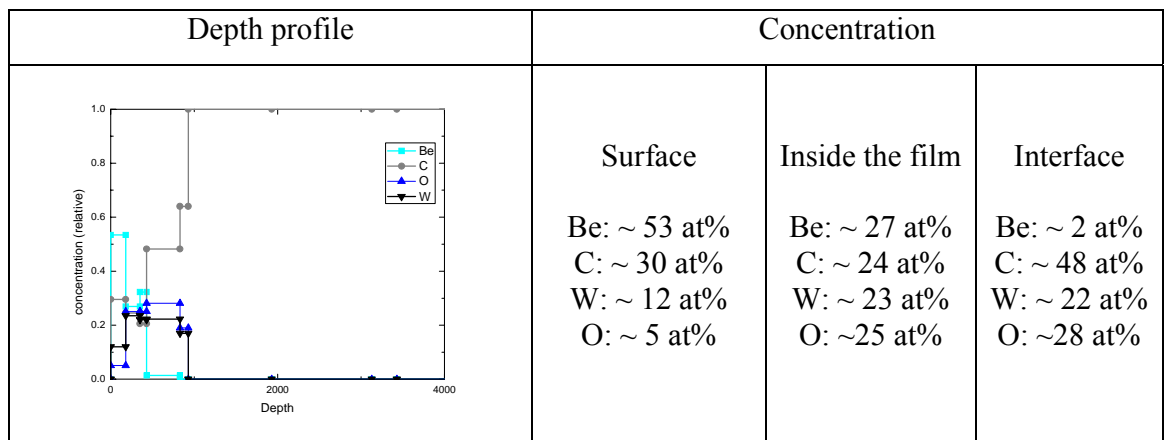


Fig. 19 RBS dept profile of the sample (Run 2) situated above the tungsten anode

It is shown that inside the film the formation of three component mixture occurred (Be, W and C). Also, the interface is diffuse due to the porosity of the graphite substrate, the presence of high Oxygen level being explained by the trapping of it inside the substrate before the deposition started.

The samples prepared during Run 1 and 2 contain Be-C-W mixed elements. They were deposited using an anode crucible containing Be and C and a distinct W anode. As result of RBS measurements, the variation of the atomic concentrations inside the prepared films was found in the range of 65-70 at% Be, 7-8 at% C, 10 – 23 at% W; and 15-18 at% O for Run 1 and of 26-33 at% Be, 24-28 at% C, 14-23 at% W; and 25 at% O for Run 2 proving the full capability of TVA method to produce mixed layers in order to simulate the mixed material composition after a fusion device campaign.

4.CONCLUSIONS

Be-C-W mixed layers with different relative concentrations were prepared using simultaneously thermionic vacuum arc discharges. A crucible filled with Be and C powders was previously heated and used as first evaporator, while the second evaporator consisted in a tungsten rod inserted in a TVA system.

SEM analyses of the prepared samples revealed smooth morphological surfaces, while the EDS analyses show the elemental concentrations of the mixed materials in the range of 19-25 at% Be, 25-31at% C, 23-28% W with oxygen inclusions of about 23-26%.

The concentration of D into the co-deposited Be-D layers were found in the range of $1-8 \cdot 10^{18}$ atoms/cm², analysis performed using an Accelerator Mass Spectrometry (AMS) method.

Systematically studies on the depth profile relative concentrations performed using a modern X-ray Photoelectron Spectrometer from SPECS, Germany infer the formation of mixed Be-C-W layers with possible formation of Be_xC_y, Be_sW_t and C_mW_n compounds. Typical average concentrations of the prepared layers were of *54at%Be28at%C18at%W, 50at%Be28at%C- 22at%W, 42at%Be38at%C20at%W and 37at%Be39at%C24at%W*

Using the facilities of the IPP Garching, RBS analyses on the prepared films show layers having relative elemental concentrations in the range of of 26-33 at% Be, 24-28 at% C, 14-23 at% W; and 25 at% O in good agreement with the others analysis methods.

The prepared films will be used for D implantation and fuel retention studies.

Comunicari la Conferinte internationale

1. C. Porosnicu, A. Anghel, K. Sugyama, K. Krieger, J. Roth, C.P.Lungu, Influence of beryllium carbide formation on deuterium retention and release, 19th International Conference on Plasma Surface Interactions, PSI 2010, May 24-28, 2010, San Diego, USA
2. C. Porosnicu, A. Anghel, C.P.Lungu, K. Sugyama, K. Krieger, J. Roth, E-MRS 2010, Beryllium Concentration Influence on Deuterium Retention and Release in Be/C Composite Films, Spring Meeting, Strasbourg, France, June 7-11 2010
3. Cristian P. Lungu, Characterization of Beryllium Containing Compounds Prepared Using TVA Method, Report on task agreements: WP10-PWI-06-01-02/MEdC/PS, WP10-PWI-06-02-02/MEdC/PS, Joint SEWG Meetings, Material Migration and Material Mixing, FZJ Juelich, Germany, 30.06.-02.07.2010.

RST in extenso

**PRODUCEREA ACOPERIRILOR DE BERILIU PENTRU PLACILE DE INCONEL
PENTRU PROIECTUL „PERETE DE TIP ITER”**
(PRODUCTION OF BERYLLIUM COATINGS FOR INCONEL CLADDING TILES FOR
THE ITER-LIKE WALL PROJECT)

Activitatea 1:

Be coatings on IWGL, IWC and DPC inconel tiles

Activitatea 2:

Be coatings on test coupons.

Activitatea 3:

Thickness characterization

Abstract

The project's aim is the coating of about 1000 inconel tiles to be used on the first wall of the JET fusion device in Culham, UK. During the 2010 were planned coating activities of 8 μm beryllium thick films on inconel tiles, beryllium coatings on test samples and film thickness characterization. Starting with January 2010, UKAEA sent to the Nuclear Fuel Plant (NFP) – Pitesti the Inconel tiles in few lots. Because during the 2009 were not performed beryllium coatings due to the postponed schedule was necessary, at the beginning of 2010, the re-testing of the deposition systems. New beryllium coatings were performed on test samples, repeating the The next step consisted in deposition on real Inconel dump-plates in the presence of specialists from JET (Les Pedrick) and EFDA (Zoita Vasile)

The third step consisted in 8 μm thickness beryllium film deposition using thermal evaporation method on IWGL Clading, IWC and Dump Plates Inconel tiles. Were performed thickness tests, adherence tests as well smear tests on the plastic bags used for the coated tiles packing.

The coated tiles were collected by a transport company under the CCFE-Culham management.

Be coating on Inconel tiles

Starting with January 2010, CCFE sent to the Nuclear Fuel Plant (NFP) – Pitesti the Inconel tiles in few lots:

Be Coating Schedule

Tile System	Latest Arrival Date
IWGL Cladding	8-Feb-2010
IWC	31-Mar-2010
Dump Plates	30-Apr-2010

Due to the fact that in 2009 were not performed beryllium coatings due to the postponed schedule was necessary, at the beginning of 2010, the re-testing of the deposition systems. New beryllium coatings were performed on test samples, repeating the procedures carried out during the qualification of the evaporation method.

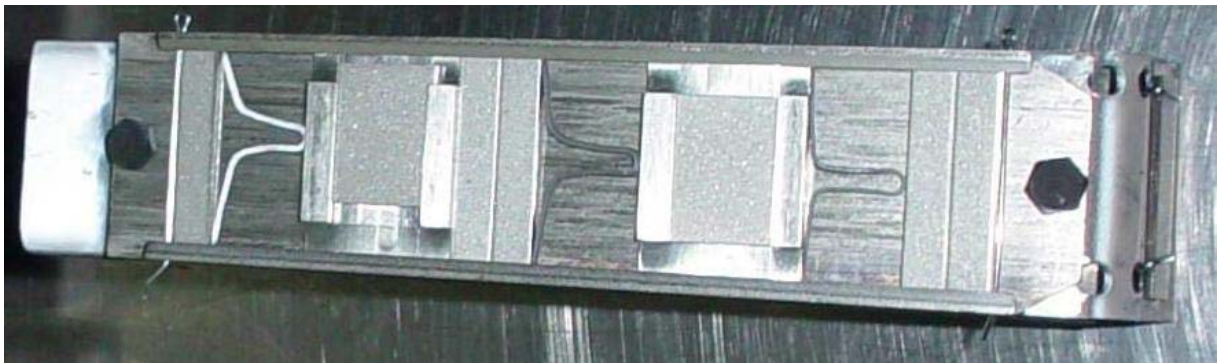


Fig.1 Photograph of the witness samples

First, were used as substrates, Inconel plates of 5 mm x 10 mm and 15 mm x 20 mm sizes. Thickness was found in the range of 7.09 – 7.97 μm and adherence tests were satisfactory, as shown in Fig.2. (The documents accompanying the witness samples and the pre-production lot are presented in Annex 1 and 2)

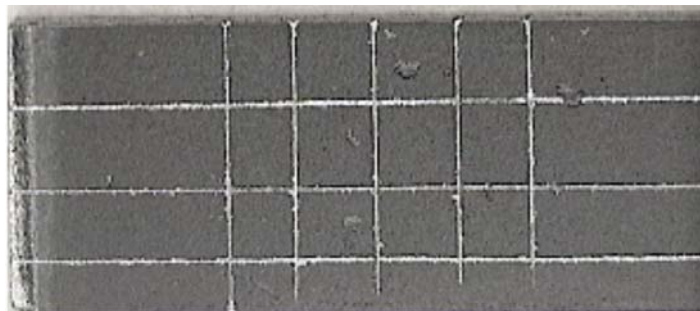


Fig.2 The adherence test performed on the witness samples.

The next step consisted in deposition on real Inconel dump-plates in the presence of specialists from JET (Les Pedrick) and EFDA (Zoita Vasile)

The third step consisted in 8 μm thickness beryllium film deposition using thermal evaporation method on IWGL Cladding, IWC and Dump Plates Inconel tiles.



Fig. 3. Adjusting IWGL tiles on the jigging device



Fig. 4 IWGL tiles after coatings

Were performed thickness tests (Fig 5), adherence tests (Fig.2) as well smear tests on the plastic bags used for the coated tiles packing. Every pre-production and production lot was accompanied by a document as those shown in Fig.6.

The coated tiles were collected by a transport company under the CCFE-Culham management.

F.C.N.

BULETIN CONTROL
DEPUNERE BERILIU

Nr. 2461

Produs:

☐ DPC
☐ IWC
☐ IWGL

Cod depunere: 10. Be YET 6

DATA: 12.02.2010

METODA DE MASURARE: MMC 401

CAL 1

MM 7 - Be/2y

MM 8 - Be/Ino

☐ Calificare
☒ Pre-productie

☐ Productie

Executat:

Nume Agapi V

Semnatura

Data 22.02.2010

Verificat:

Nume

Semnatura

Data

Resultatul verificarii

Admis

Respins

Agapi V

22.02.2010

Caracteristici verificate

1. Grosime strat Beriliu: $\bar{x} = 2,55 \mu m$

supr. plana

☐ 8+10 μm

☒ 5+10 μm

SUS

MILLOC

JOS

☐ Be/2y

☒ Be/Ino

7,87 μm

7,64 μm

7,93 μm

2. Test aderența strat Be

☒ Admis

☐ Respins

Agapi V

22.02.2010

3. Control vizual piese și probe

☒ Admis

☐ Respins

Agapi V

22.02.2010

Observatii

4,52 μm pe zona curbată

Formular 4J01

FISE INSOTITOARE SUBLOT

TEST PRE-PRODUCTIE

FCN

PITESTI

nr. transp. 060543

data lansare 17.02.10

COD DEPUNERE

10. Be YET 6

COD PASTILA Be

09 Be Be 3 01

COD PIESE

6Z10L

6Z13R

6Z8R

(770100201)

(770100204)

(770100213)

6Z15L

6Z16R

6Z9R

(770100201)

(770100201)

(770100214)

6Z16L

6Z8L

6Z9L

(770100201)

(770100213)

(770100214)

Nr. crt.

OPERATII

OPERATOR

1

Depunere Be

g 6,80

DATA 19.02.2010

MARCA 387

SEM. NAT. Agapi V

2

Evaluare grosime

A/R

DATA 22.02.2010

MARCA 313

SEM. NAT. Agapi V

3

Aderența

A/R

DATA 22.02.2010

MARCA 313

SEM. NAT. Agapi V

4

SRP xx / yy

A/R

5

Depunere completare

g

6

Evaluare grosime

A/R

7

Aderența

A/R

8

Ambalare

A/R

DATA 22.02.2010

MARCA 313

SEM. NAT. Agapi V

SEF SCHIMB

NOTA:

A = Admis

R = Respins

XXXX = cod piese

XX/YY = tip SRP

g = grame

Fig.5 Typical document certifying thickness measurement

Fig.6 Typical document accompanying any pre-production and production lot.

110

RST in extenso

TT19 5.1b

PROJECT : (PRODUCEREA ACOPERIRILOR DE BERILIU PENTRU PLACILE
MARKER PENTRU PROIECTUL „PERETE DE TIP ITER”)

Faza: iunie 2010

Activitate I

Ni and Be coatings on marker tiles provided by JET

CONTENT

Abstract.....	3
1. Deposition of Ni and Be layers on the beryllium marker blocks.....	4
2. Evaporation process.....	5
3. Production run.....	6
4. Conclusions.....	10

Abstract

The aim of the project represents the coating with 2 μm Ni films followed by coatings of 8 μm Be films on marker tiles made of full beryllium blocks, using the thermionic vacuum arc method (TVA). The marker tiles will be installed on the first wall of the JET device in Culham, UK in order to determine the erosion grade of the wall after the experimental fusion campaigns.

At the beginning of the year 2010 were received a lot of 23 marker tiles in order to be coated. At NILPRP, Elementary Processes in Plasma and Applications group was organized the production flux in order to perform the coatings in the best conditions. The form and the dimensions of the marker tiles were analyzed carefully in order to design and manufacture the jigging devices to ensure a uniform coating. The Ni and Be coatings were realized during 6 production runs, fulfilling the quality and production documentation. Were performed thickness and adherence measurements on the witness samples deposited in the same deposition runs as the marker tiles. Were carried out the documentations concerning the transfer of beryllium marker tiles and was obtained the needed authorization delivered by the Romanian Authority which control the activities in connection with the use of nuclear materials. During May 2010 the lot of 23 marker tiles was delivered to the JET, Culham and we received the confirmation that the tiles arrived in good conditions.

1. Deposition of Ni and Be layers on the beryllium marker blocks.

In order to obtain Ni and Be layers in the same deposition run, a setup presented in Fig. 1 was developed. The distance between the anodes was 20 cm and the sample holder-anodes distances were around 25 cm, as the particle flux depends on the distance and the incident angle. The two anodes and the substrates were positioned so that a similar particle flux was present for each sample in a deposition batch.

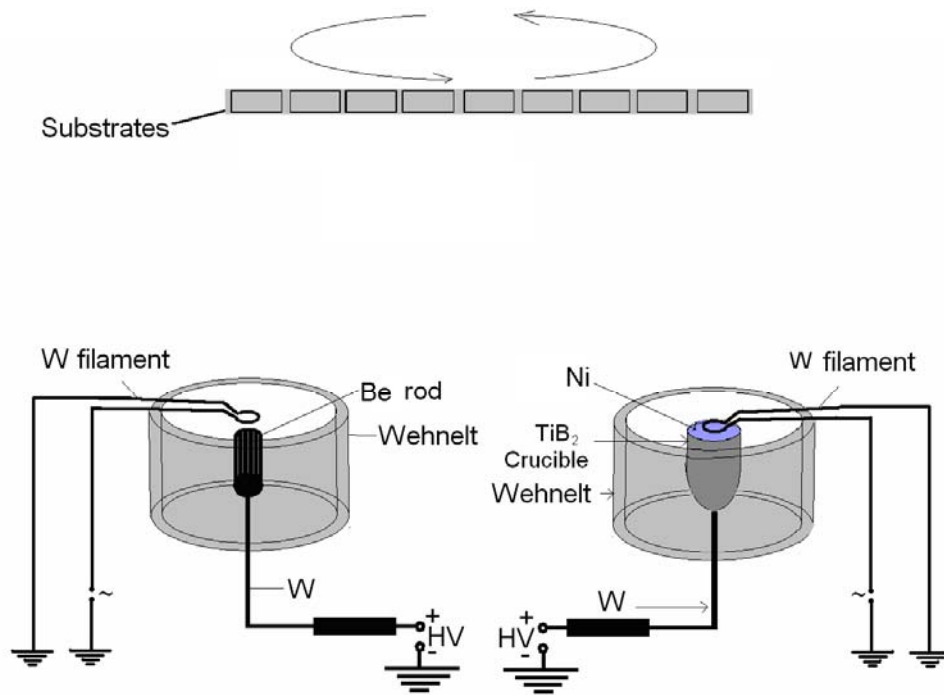


Figure 1. Schematic representation of the Ni-Be thermionic vacuum arc deposition system.

The high temperature resistant TiB₂ crucible was filled with a Ni cylinder. Beryllium rod was evaporated in a separate TVA system, water cooled in the lower part. Only the upper part of the Be rod was melted by the electron beam and the TVA discharge was ignited in pure Be vapors. The electron beams evaporate both the Ni material contained in the TiB₂ crucible and after Ni deposition the accelerating electron beam voltage was connected to the TVA system used for Be evaporation. The plasmas were independently controlled by the electron beams (thermo-electrons) emitted by the heated cathodes and the applied voltage on the anodes, in order to obtain the desired thickness.

The marker tiles and the witness samples were placed on a holder that was mounted inside the deposition chamber, and put in thermal contact with the oven. The measured deposition parameters were:

- ✓ Substrate temperature
- ✓ I_{fW} - The heating current of the filament for Ni evaporator
- ✓ I_{acr} - The arc current for Ni during the deposition
- ✓ U_{aCr} - The arc voltage for Ni during the deposition
- ✓ I_{fBe} - The heating current of the filament for beryllium evaporator
- ✓ I_{aBe} - The arc current for Be during the deposition
- ✓ U_{aBe} - The arc voltage for Be during the deposition

These parameters are presented in the table below:

Table 1. Example of the set of deposition parameters for Ni and Be depositions

Run No	I_{fNi} (A)	I_{aNi} (A)	U_{aNi} (V)	I_{fBe} (A)	I_{aBe} (A)	U_{aBe} (V)
4	42	1.5	1300	48	1	1900

2. Evaporation process

The process consisted in five steps:

- I. First step was of obtaining a low pressure inside the discharge chamber, about $4-6 \cdot 10^{-6}$ torr. Inside the vacuum chamber there was an oven that could be controlled to obtain a specific temperature. One of the oven purposes is to obtain a good value of the vacuum. The other purpose is to increase the tiles temperature up till 250^0-300^0C . This first process lasted between 3 and 4 hours, depending on the size of the tiles that were being coated. The tiles with a higher volume needed an extended period of time to reach the desired temperature.
- II. The second step consists in an argon gas glow discharge that was made to ensure a proper cleaning of the tiles. The pressure of argon gas inside the vacuum chamber was set to $2-3 \cdot 10^{-2}$ torr. By applying a negative bias voltage on the tiles, a glow discharge localized on the area of the tiles appeared. This process took 15 - 20 minutes, depending on the values of the voltage and the current. The bias voltage applied on the tiles was -850

V, with an electrical current of 60 mA. After the end of this step, a period of time of about 10-15 min was necessary to obtain a pressure lower than 10^{-6} torr inside the deposition chamber.

- III. Step no.3 consisted in Ni coating of the beryllium tiles. The filament heating current was of 40-50A, depending on the distance between the cathode and the anode. This distance vary in time because of the Ni evaporation, so that it is needed a constant increase of the input power. On the anode a high voltage potential had been applied, of about 1.5kV. The electrons from the cathode were accelerated by this high voltage potential. Firstly, nickel started to melt locally up till the point of plasma ignition. The plasma was created in pure nickel vapors. The thickness of the film was of 2-3 μm . After obtaining the desired thickness, the process of nickel coating stopped, the whole coating experiment going forward with step IV.
- IV. Fourth step was beryllium coating of the tiles. The beryllium cylinder for evaporation was placed in a cooled stainless steel anode, so that the melting occurred only at the surface. A filament heating current of 45A-55A was used. The electrons from the heated filament have been accelerated by an voltage at the anode of 1.7-1.9kV. Beryllium first melted at the surface, and by increasing the input power the ignition of the pure vapors occurred. The thickness of the beryllium film was of 7-9 μm .
- V. Final step consisted in the cooling down of the installation. The coated tiles have been taken out when its temperature was under 50°C .

In all period of the coating, a negative bias voltage was applied on the tiles, with a value of -750V and a bias current of 5-15 mA, which insured a better coating by rejecting the electrons, and accelerating the positive ions of beryllium

3. Production run

Technological record, an official document, accompanied every deposition run. The parameters used for deposition of Ni+Be on the Be tiles is presented in the document shown below as an example. We can see the maximum number of tiles deposited in the same deposition run (8 tiles). The tiles used for coating were: **P F70201024/293, P F70201024/290, P F70201025/485, P F70201026/082, P F70201026/153, P 70201025/463, P F70201026/335, P**

F70201026/103 and also the **WP-1**, was deposited as a witness probe. The positioning of the tiles inside the vacuum chambers is presented in the following document:

TECHNOLOGICAL RECORD

for Ni and Be coatings of Be Marker tiles by Thermionic Vacuum Arc (TVA) method
PRODUCTION-Run No.....4..... Date 12th May. 2010

1. RUN IDENTIFICATION

1.1. Customer: Culham Science Center – JET

1.2. Contract No: Task Agreement **JW6-TA-EP2-ILB-01**

1.3. No. and date of the document accompanying the tiles; total number of tiles: 23, Arrival date in NILPRP April 2010..

1.4. Load content (tile identification numbers): **P F70201024/293, P F70201024/290, P F70201025/485, P F70201026/082, P F70201026/153, P 70201025/463, P F70201026/335, P F70201026/103, W P-1**

Name of the person who filled in the identification data:

Ionut Jepu

Signature.....

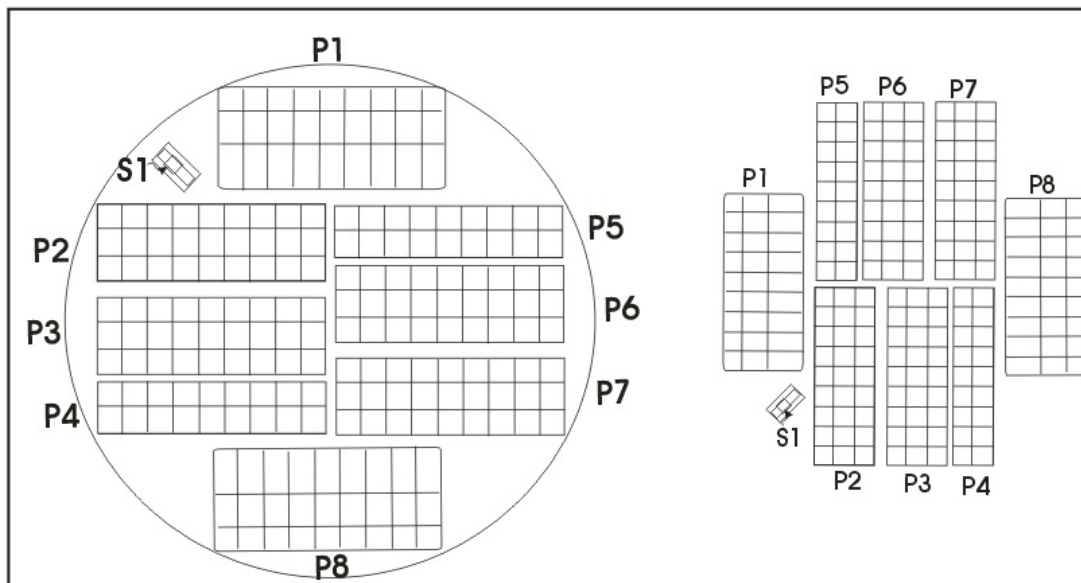
2. JIGGING DEVICES

Drawings identification numbers:

Name of the person who approved the jiggging devices: **Cristian Lungu**

Signature

3. TECHNOLOGY USED: Thermionic Vacuum Arc (TVA) technology, Code: INFLPR-L26-PEPA-TS-01
 version:.....



4. TECHNOLOGICAL PARAMETERS

Record			
Loading of the Be tiles			
Tile reference number~	P F70201024/293	P F70201026/103	P F70201026/335
Tile Position reference~	P1	P2	P3
Tile reference number~	P F70201025/463	P F70201025/458	P F70201026/082

Tile Position reference~	P4	P5	P6
Tile reference number~	P F70201026/293	P F70201024/290	
Tile Position reference~	P7	P8	
Witness sample reference numbers	W P-1		
Sample Position reference	S1		
Loaded holder, Photograph~	Jpeg No. 4140/4170		

Outgassing

Oven temperature set to 450deg C

Target chamber pressure less than 5×10^{-5} torr

Time (mins)	Oven temperature deg C	Tile temperature		Pressure (x 10^{-6} torr)
		reading	deg C	
0	20		20	7
46	447		130	9
85	450		147	7.3
120	448		170	4.2
180	447		225	2.1

Glow Discharge Cleaning

DC Supply ~ Vdc=-850V, Idc=60 mA

Time (mins)	Oven temperature deg C	Tile temperature		Pressure (x 10^{-2} torr)
		reading	deg C	
5	360		209	1.8
10	311		190	2
15	291		180	2

Substrate heating turned off.

6	Nickel Coating
	Cathode filament heating. Vac <u>42</u> A
6(a)	Oven pressure (target $< 5 \times 10^{-5}$) ~ start 8×10^{-6} Torr, end 4.6×10^{-6} Torr
6(b)	Tile surface temperature ~ start 300 deg C, end 415 deg C
6(c)	DC discharge Supply ~ Vdc= 1300 V , Idc= 1.5A
6(d)	DC bias Supply ~ Vdc= -750V , Idc= 5mA
6(e)	Length of time for Ni Coating~ (Target 120mins) 84 mins
6(f)	Thickness reading on QMB (Target 2000=2 μ) ~ 1.720~2 μm
7	Beryllium Coating
	Cathode filament heating. _____ Vac 48 A
7(a)	Oven pressure (target $< 5 \times 10^{-5}$) ~ start 2.2×10^{-6} Torr, end 8.8×10^{-7} Torr
7(b)	Tile surface temperature ~ start 370 deg C, end 385 deg C
7(c)	DC discharge Supply ~ Vdc= 1900 V , Idc= 1.A
7(d)	DC bias Supply ~ Vdc= -750 V , Idc= 5 mA
7(e)	Length of time for Be Coating~ 43 mins
7(f)	Thickness reading on QMB (Target 7000=7 μ) ~ 6.110~7.5 μm

8	Stopping the deposition process	
8(a)	Tile temperature when exposed to air Target 50 deg C) 47 deg C	
9.	Packing the marker tiles	Operator
9(a)	Use gloves	
9(b)	Seal each Be in a separate Polythene bag clearly marked with its JET reference number and the coating date	A.Lungu
9(c)	Seal each witness sample in a separate Polythene bag clearly marked with its reference number and the coating date.	C.Lungu

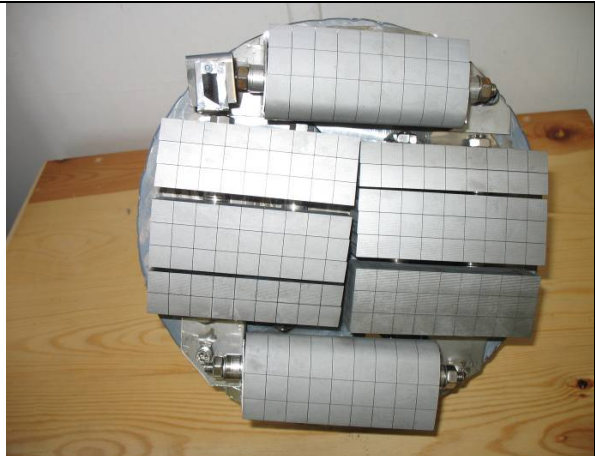
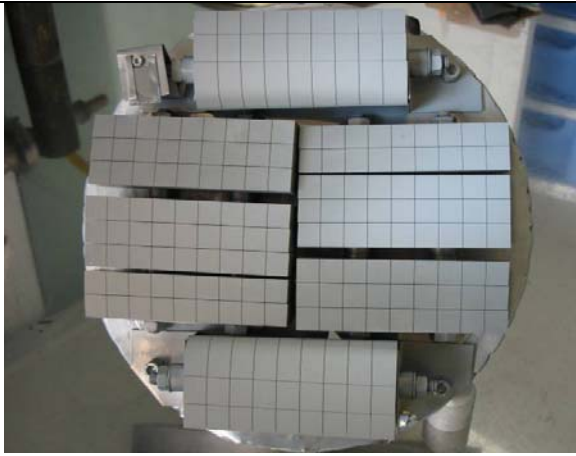
Name of the person who recorded the set of technological parameters:

Ionut Jepu

Signature.....

10	Quality control	Thickness: 7-11µm Adherence: very good		
----	-----------------	---	--	--

Dr. Cristian P. Lungu, Contract Liaison Officer

	
PRODUCTION-Run 4/12.05.2010 IMG_4140 (Before Ni+Be deposition)	PRODUCTION-Run 4/12.05.2010 IMG_4170 (After Ni+Be deposition)

The lot of 23 beryllium tiles were coated with 2-3 µm Ni and 7-9 µm Be. After coatings, the tiles were double heat sealed, packed in carton crates and put together in a wooden box. The plastic bag surfaces, carton crates and wooden box were smeared and the smear products (25 mm paper filters) were sent to NFC-Pitesti in order to analyze the Be contamination. The results of the measurements show Be content under the detection limit (< 0.1 µg/filter).

4. Conclusions

Coatings of 2-3 μm Ni and 7-9 μm Be for coating on a number of 23 marker tiles, were produced using thermionic vacuum arc (TVA) method. The tiles will be installed at JET fusion device in Culham, UK as part of the ITER-like wall experiment. TVA method uses coatings from two different sources, on one hand the Nickel and on the other hand Beryllium, without opening the vacuum chamber between these two depositions. Having inside both systems for producing plasma in pure vapors of Nickel and Beryllium contributed to the compactness, adherence and purity of the films. The purity of the thin films was also able to be obtained because of the absence of a buffer gas inside the vacuum chamber. The control of the ion energy and of the electron flux by handling the exterior plasma parameters is another advantage of using the thermionic vacuum arc method. By controlling the exterior plasma parameters like the heating current filament, the discharge voltage, the distance between electrodes, the deposition rate was also controlled. Because the films thickness on the tiles was very important, the control of the deposition rate made possible the process stopping to a desired thickness.

Scientific Report

To the Contract 1EU-2/11.08.2008
For January - June 2010

Project BS-3A: *Anomalous Transport in Plasma: Role of collisions, turbulence and wave-plasma interaction in transport. Application to ITER.*

Plasma Theory Group: N. Pometescu, Gy. Steinbrecher

- **General Objectives**

The aim of this project is to make progress in understanding the transport in fusion plasma from devices like ITER. The role of collisions, turbulence and wave-plasma interactions and also the correlation between them for driving transport of particles and energy will be analysed. Complex features like long-range correlations, intermittency in plasma edge turbulence, edge transport barriers, core impurity transport with different dominant core turbulence and different radio-frequency heating scheme will be analysed. For that are used both analytical and numerical methods. Previously developed stochastic models will be adapted to study long-range correlations, self-similarity and intermittency. Gyrokinetic semi-Lagrangian codes with collision term will be adapted to the study of the particle transport in tokamak.

The results obtained in this project will be applied to existing large plasma devices but are oriented specially to be applied to plasma in ITER device.

For the year 2010 the objectives are:

1. Impact of central electron heating on both electron and ion temperatures, and on particle and impurity densities.
2. Numerical experiments with low dimensional kinetic models of the impurity transport.
3. Study of the turbulent structures and intermittency by stochastic differential equations.
4. Characterization of long-range correlations and multi-scale physics in L-mode plasmas and during edge improved confinement regimes.

- **Specific Objectives**

In this stage of the project, January-June 2010 we have attained the following specific objectives from the previous mentioned objectives:

1. Impact of central electron heating on both electron and ion temperatures, and on particle and impurity densities.
2. Numerical experiments with low dimensional kinetic models of the impurity transport.
3. Study of the turbulent structures and intermittency by stochastic differential equations.
- 4a. Long-range correlations influence on the impurity transport.

- **Resume of the stage**

1. *Impact of central electron heating on both electron and ion temperatures, and on particle and impurity densities.*

Milestone 1a: *Diffusion coefficient of electrons at random transition between two temperature profiles in magnetized plasma due to electron heating.*

In pellet fuelling of Ohmic and Lower Hybrid - driven discharges in Tore Supra [1], the experimental results show for electrons in the central region, a temporal evolution of the central electron temperature oscillating between Ohmic discharge temperature and the discharge with Lower Hybrid power induced temperature. Using Langevin equations on describe the transport of the guiding centers of charged particles. The radial variation of the running diffusion coefficients is analyzed for transition between the two temperature profiles observed in experiments [2].

Milestone 1b: *Study of the dispersion equation for multi-species plasma with ITG turbulence in the presence of the radio-frequency heating*

The influence of the radio-frequency heating on the impurities transport was studied through comparative analysis of two discharges in JET: the reference discharge #69808 without RF power and discharge #68383 with the maximum ICRF power of 8.3 MW is applied to electrons in Hydrogen Minority Heating scheme.

3. *Study of the turbulent structures and intermittency by stochastic differential equations*

The problem studied was the stability under parametric random perturbations of the drift waves. The main goal is to extend the results from Refs. [5-9], to the equations of the drift wave turbulence. In this stage we studied the possibility of stochastic extension of the simplest model. In the Hasegawa-Mima model of the density gradient drift waves, a random term was added to the constant driving density gradient. The results are the following:

There exists a threshold, depending on the wave vector, for the random density fluctuation intensity, such that the modes with non-zero wave vector remains stable below this threshold. This threshold decreases with $|\mathbf{k}|$.

The mode with $\mathbf{k}=0$ is always destabilized. Exact algebraic method was elaborated for the study of the destabilization. This stability pattern is a candidate for the explanation of the long-range spatial correlations of the electric field.

4a. *Long-range correlations influence on the impurity transport.*

The possibility to study of the L-H transitions is related to the new category of bifurcations triggered by the increase of the noise intensity or its correlation time. This class of transitions, related to the decrease of the heavy tail exponent due to the increase of the noise intensity was studied in the works [9, 10]. The decrease of the heavy tail exponent is related to the increase of the intermittency.

In the previous reduced models of the noise driven intermittency, the random linear system was modified, by a singular Bernoulli transformation of the variable. The new stochastic differential equation is identical to the Landau mean field model of the instability growth and of the noise driven intermittency from [11]. The output of this model was coupled with the Rutherford equation for the magnetic island width from [12-13]. The resulting system of non-linear stochastic differential equation was solved in the limit of driving stochastic noise modeled by a Wiener process. It was found that there is a *counter intuitive transition* from the regime of low noise intensity, with a single maximum, to the regime with two separated maxima for higher noise intensity. This behavior will be used in the study of the hysteresis effects.

• Scientific description

Specific Objective I

1. *Impact of central electron heating on both electron and ion temperatures, and on particle and impurity densities.*

Coordinator: Lect. Dr. Nicolae Pometescu.

Co-operations: TG-T WP10-TRA-03-03, Université Libre de Bruxelles and Chalmers University, Sweden

Milestone 1a: *Diffusion coefficient of electrons at random transition between two temperature profiles in magnetized plasma due to electron heating.*

In pellet fuelling of Ohmic and Lower Hybrid - driven discharges in Tore Supra [1], the experimental results show for electrons in the central region, a temporal evolution of the central electron temperature oscillating between Ohmic discharge temperature and the discharge with Lower Hybrid power induced temperature. Using Langevin equations for the guiding center motion of the charge particles on analyze the transport along and perpendicular to the main magnetic field. The model includes collisions and therefore a

thermal velocity which we relate to the plasma temperature evolution through a stochastic process and a magnetic field represented as another stochastic process which is independent of the thermal velocity [2]. The combined effect of collisions and magnetic fluctuation in the zeros order guiding center approximation leads to particle sub-diffusion in the perpendicular direction. We look for effects given by transition between the two temperature states and the radial variation of the running diffusion coefficients is analyzed for transition between the two temperature profiles – see figure 1.

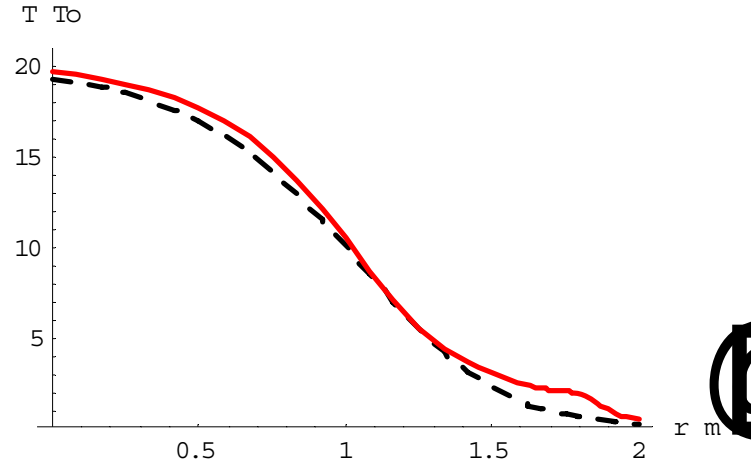


Figure 1: The two profiles of electron temperature: the dashed line correspond to electron temperature without heating and the solid (red) line correspond to electron temperature with LH heating

The difference between the two temperatures, according to experiment, is about 1 keV , see figure 2:

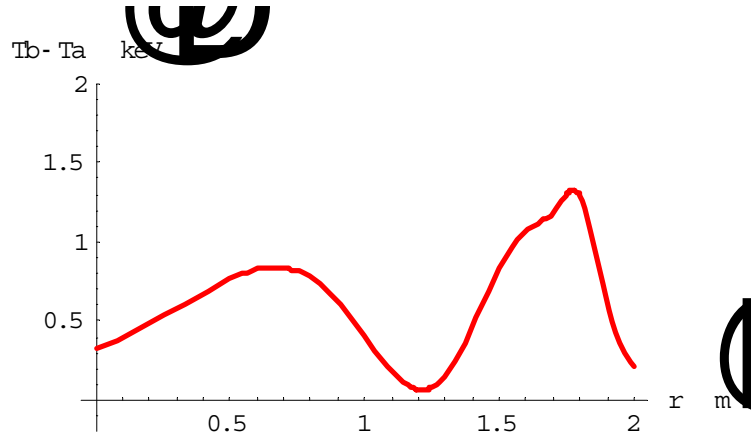


Figure 2: The difference between the two electron temperatures

For the running diffusion coefficient we obtain a variation given in figure 3. From figures 2 and 3 we note that the running diffusion coefficient has one maximum value for about $r \approx 0.9a$ and the difference between the temperatures has two maximum values, for $r \approx 0.3a$ and for

$r \approx 0.85a$. From here we conclude that the running diffusion coefficient is less sensible to the difference between the two temperatures in the central region than the difference between temperatures in the plasma edge region.

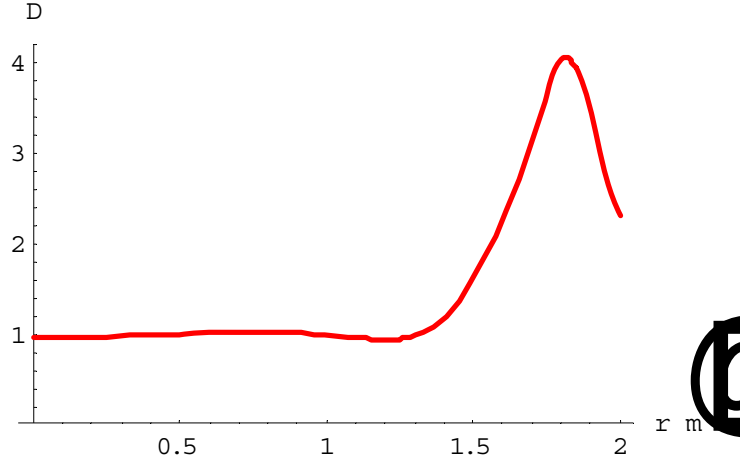


Figure 3: The dimensionless running diffusion coefficient D for the case of strong collisionality

This agrees with experimental observation that diffusion coefficient is greater in edge plasma region.

Milestone 1b: Study of the dispersion equation for multi-species plasma with ITG turbulence in the presence of the radio-frequency heating

The influence of the radio-frequency heating on the impurities transport was studied through comparative analysis of two discharges in JET: the reference discharge #69808 without RF power and discharge #68383 with the maximum ICRF power of 8.3 MW is applied to electrons in Hydrogen Minority Heating scheme. With this goal we use equation for the impurity density perturbation due to ITG/TE modes in plasmas with radio-frequency heating, obtained in [3] by using multi-fluid Weiland model with trace impurity approximation. The influence of the heating on the density perturbation profile is taken into account by the specific profiles of electron/impurity density and temperature profile for the two shots.

In order to represent the radial variation of the impurity density perturbation for the two shots we need to find the eigen-frequency modes for ITG instability. The frequency modes are determined resolving the dispersion equation resulting from the following particular condition imposed on the density perturbation due to the ITG mode: the relative impurity density perturbation is equal with 0.01 from the relative free electron density perturbation. Motivation for this condition is the concentration of Ni impurity in plasma is 1% and the free electrons (supposed with adiabatic behavior) participate to equilibrate the charge perturbation due to ITG mode. This condition simplifies considerably the complexity of the dispersion equation [4].

Specific Objective II

3. *Study of the turbulent structures and intermittency by stochastic differential equations.*

Coordinator: Prof. Dr. György Steinbrecher

Co-operations: TG-T WP10-TRA-05-01, C.E.A. Cadarache, France

Milestone: *Turbulent structures and intermittency.*

In the previous works from Refs. [5, 6, 7] a new methodology for the study of the noise – driven intermittency was elaborated. In [5], for the study of the intermittent events in the plasma boundary, by using the mathematical results from [8], the class of the reduced models studied in [9] were generalized adapted. The intermittency in this class of models is related to the probability large excursions related to the heavy tail.

The mathematical aspects are related to the problem of stochastic linear approximation in the study of the stability problem of the non linear partial differential equations was studied. Explicit results were obtained in the study of the dispersive wave destabilization in [5].

The problem studied in this work is the stochastic counterpart of the study of large time behavior of the linear deterministic differential equations with time dependent coefficients, or in other term: parametric excitation. In this category of deterministic linear system the typical interesting phenomena are: parametric resonance, parametric stabilization of the inverted pendulum. The analogue of these effects is studied in the framework of the drift waves driven by stochastic density gradient

The methods from [5-9] used for the study of the stability under parametric stochastic perturbations of the physical systems and described by non linear differential equations, was used here in the study of the equations of the density gradient drift waves.

The problem studied was the stability under parametric random perturbations of the drift waves. The main goal is to extend the study from [5, 6] to the equations of the drift wave turbulence. In this stage we studied the possibility of stochastic extension of the simplest model. In the Hasegawa-Mima model of the density gradient drift waves, a random term was added to the constant driving density gradient. The random density gradient term was modeled by a spatial and temporal white noise. The physical origin of this stochastic fluctuation of the density gradient is related to the turbulence that originates from the plasma core.

The methodology used was the Galerkin discretization of the linearized Hasegawa-Mima equation that contains a random background term. As a result, a system of classical stochastic differential equation of the Ito type was obtained. By the methods from [5-7] from these stochastic evolution equations a set of deterministic linear differential equations were obtained for fixed time spatial correlation function of the electrostatic potential. These

equations were solved by discrete Fourier transform and the evolution of the second order moments of the random electric field was obtained. The results are the following:

In analogy to the stochastic Klein-Gordon equation, also in the framework of stochastic Hasegawa-Mima equation there exists a threshold, depending on the wave vector, for the random density fluctuation intensity, such that the modes with non zero wave vector remains stable below this threshold. This threshold decreases with $|\mathbf{k}|$.

The mode with $\mathbf{k}=0$ is always destabilized. Exact algebraic method was elaborated for the study of the destabilization. This stability pattern is a candidate for the explanation of the long-range spatial correlations of the electric field.

Specific Objective III

4a. *Long-range correlations influence on the impurity transport.*

Coordinator: Prof. Dr. György Steinbrecher

Co-operations: EFDA WP – III.2.1, C.E.A. Cadarache, CNRS Marseille, France

Milestone: *Comparative study of different plasma regimes and description of the transition in term of global parameters.*

The possibility to study the L-H transitions is related to the new category of bifurcations triggered by the increase of the noise intensity or its correlation time. This class of transitions, related to the decrease of the heavy tail exponent due to the increase of the noise intensity was studied in [9, 10]. The decrease of the heavy tail exponent is related to the increase of the intermittency.

In the reduced model elaborated, the noise driven random linear system was modified by a singular Bernoulli transformation of the variable. The new stochastic differential equation is identical to the Landau mean field model of the instability growth and saturation, with the specification that it also contains a random driving term. This model is a generalization and a mathematically rigorous version of the noise driven intermittency models from [11]. The control parameter that determines the intensity of the output noise is related to the fuelling rate of the tokamak. The output of the random dynamical system that models the on-off intermittency was coupled with the Rutherford equation for the magnetic island width from [12-13]. In this stage the new results are the following:

The resulting system of non-linear stochastic differential equation was solved in the limit of driving stochastic noise modeled by a Wiener process. In this case an analytic form for the probability distribution function was found. The change of the qualitative aspects of the probability density function was studied. It was found that there is a *counter intuitive transition* from the regime of low noise intensity, with a single maximum, to the regime with two separated maxima for higher noise intensity. In the latter case there is a regime where by the increase of the noise intensity the probability of transition forms the higher maxima to the

lower decrease. This apparently paradoxical behavior will be used in the study of the hysteresis effects.

- **Conclusions**

1. *Impact of central electron heating on both electron and ion temperatures, and on particle and impurity densities.*

1a: In pellet fuelling of Ohmic and Lower Hybrid - driven discharges in Tore Supra [1], the experimental results show for electrons in the central region, a temporal evolution of the central electron temperature oscillating between Ohmic discharge temperature and the discharge with Lower Hybrid power induced temperature. From the study we conclude that the running diffusion coefficient is less sensible to the difference between the two temperatures in the central region than the difference between temperatures in the plasma edge region.

1b: The influence of the radio-frequency heating on the impurities transport was studied through comparative analysis of two discharges in JET: the reference discharge #69808 without RF power and discharge #68383 with the maximum ICRF power of 8.3 MW is applied to electrons in Hydrogen Minority Heating scheme. In order to represent the radial variation of the impurity density perturbation for the two shots we find the eigen-frequency modes for ITG instability solving the dispersion equation resulting from a particular condition imposed on the density perturbation due to the ITG mode.

3. *Study of the turbulent structures and intermittency by stochastic differential equations.*

By the methods from [1-3] from these stochastic evolution equations a set of deterministic linear differential equations were obtained for fixed time spatial correlation function of the electrostatic potential. These equations were solved by discrete Fourier transform and the evolution of the second order moments of the random electric field was obtained.

4a. *Long-range correlations influence on the impurity transport.*

The intermittency in the edge plasma turbulence was studied by generalization of the low dimensional heavy tail models to high dimensions, in order to include a stochastic version of the Hasegawa-Mima equation. It was proved that under the perturbation generated by the turbulence in the plasma core, the long wave modes are destabilized first and has intermittent behavior. The short waves are more robust under small amplitude parametric noise. A noise driven intermittency model, was adapted to the elaboration of reduce stochastic models of the hysteresis effects. The study of the statistical properties of the intermittent events in the edge plasma turbulence is essential in the evaluation of the intermittent heat loads on the plasma facing components of large tokamaks.

• References

- [1] A Geraud, J Bucalossi et al. *Pellet fuelling in Tore Supra long discharges*, Journal of Nuclear Materials 337-339, (2005) 485-489
- [2] N. Pometescu, B. Weyssow, *Random transition between two temperature profiles in magnetized plasma*, “4th International Workshop & Summer School on Plasma Physics”, July 5-10, 2010, Kiten, Bulgaria
- [3] H Nordman, R Singh, T Fülöp, L-G Eriksson and all, „*Influence of radio frequency ponderomotive force on anomalous impurity transport in tokamaks*”, Phys. Plasmas **15**, 042316 (2008)
- [4] G Steinbrecher, N Pometescu, *Long Range correlations and influence of the RF-heating on particle transport in fusion plasma*, Association Day, Iasi, July 2, 2010
- [5] G. Steinbrecher, X. Garbet, “*Stochastic Linear Instability Analysis*”, International Workshop on “Hamiltonian Approaches to ITER Physics”, CIRM, Marseille, 2-6 November 2009.
http://www.cirm.univmrs.fr/web.ang/liste_rencontre/programmes/AbstractsProgRenc395.pdf
- [6] V. N. Kuzovkov, W. von Niessen, “*Random walk approach to the analytic solution of random systems with multiplicative noise-The Anderson localization problem*”, Physica A **369** (2006), 251-265.
- [7]. X. Garbet, G. Steinbrecher, “*On-off intermittency. Exact results*”. Presented at the “Solvay Workshop <A Tribute to Radu Balescu>”, Brussels, 6-8 March 2008.
- [8] Steinbrecher, W. T. Shaw. “*Quantile Mechanics*”, European Journal of Applied Mathematics, **19**, 87, (2008).
- [9] Steinbrecher G., Weyssow B., “*Generalized Randomly Amplified Linear System Driven by Gaussian Noise. Extreme Heavy Tail and Algebraic Correlation Decay in Plasma Turbulence*”, Physical Review Letters **92**, 125003 (2004).
- [10] G. Steinbrecher, X. Garbet, B. Weyssow, “*Stochastic version of the linear instability analysis*”. Annals of Univ. Craiova, Physics AUC, vol. 19, 107-123.
http://cis01.central.ucv.ro/pauc/vol/2009_19/9_pauc2009.pdf
- [11] S. Aumaître, F. Pétrélis, K. Mallick, “*Low frequency noise control on-off intermittency in bifurcation systems*”, Phys. Rev. Lett. **95**, 064101, (2005).
- [12] D. A Gates et al, “*Neoclassical islands in COMPASS-D*”, Nucl. Fusion **37**, (1997), 1593-1606.
- [13] R. J. Buttery et al, “*Onset of the neoclassical tearing modes on JET*”. Nucl. Fusion **43**, (2003) 69-83.

EURATOM – MEdC ASSOCIATION
National Institute for Laser, Plasma and Radiation Physics

Title of the project:
“Material deposition and composition of walls”
EFDA Task Agreement Code: WP08 – TGS – 01 – 04
CfP WP08 09 – PC Topical Groups 13 June 2008

Interim Report for the period 01.01.2010 – 30.06.2010
(only MEdC tasks)

Authors: C.Ruset

Head of the EURATOM-MEdC Research Unit,
Dr. Florin Spineanu

Project officer,
Dr. C. Ruset

Bucharest 2010

CONTENT

1. General objective of the project	3
2. Specific objectives for the period January – March 2010	3
3. Results and discussion	3
4. Conclusions	5
Annex 1	6

1. General objective of the project

In the framework of this task a Laser Induced Breakdown System (LIBS) is proposed to be manufactured for in situ investigation of the wall composition, including material deposition, without breaking the vacuum. The system has to be calibrated with the specific materials which are supposed to be on the tokamak wall, that is W, Mo, C.

The role of the MEdC Association is to provide coated samples with various compositions of these materials using the Combined Magnetron Sputtering and Ion Implantation (CMSII) deposition technique.

The depth profiles of the concentrations for the coating constituents will be measured by Glow Discharge Optical Spectrometry (GDOS) technique, which is currently used for quality control of the W layers deposited by CMSII technology.

2. Specific objectives for the period January – March 2010

Specific objective for MEdC for the period January – March 2010 was to provide hydrogen containing W-C coatings. All these associations have LIBS equipments and they need calibrated samples in order to calibrate the laser system.

3. Results and discussion

Hydrogen containing coatings

An important target for LIBS measurements is determination of the tritium contamination of the wall in a nuclear fusion reactor. This means measurement of the tritium concentration at the wall without breaking the vacuum into the reactor chamber. Before reaching this level, preliminary experiments should be carried out with hydrogen. This is why MEdC Association was asked to produce, if possible, hydrogen containing coatings. Such type of coatings was not included in the Task Agreement.

The coating experiments were carried out with the CMSII-Experimental Unit. Two types of coating were deposited on steel and Ti substrates. The first type (Coating A) was titanium deposited on carbon steel substrate because it is recognized that Ti is a very good absorber for hydrogen. The second type (Coating B) was C-W coating deposited in a hydrogen reach atmosphere. Some details about the coating conditions are given below.

Coating A.

The discharge was initiated in Ar at 8.0 sccm and then gradually the Ar flow rate was decreased up to 2.0 sccm and hydrogen was introduced into atmosphere. The hydrogen flow rate was adjusted until the discharge was stable. The deposition duration was 2h and 20 min. Under these conditions the deposition rate was 1.7 $\mu\text{m/h}$. This means about 3 times smaller than in pure Ar.

Coating B.

The deposition atmosphere was adjusted in the same manner like for coating A. Although the deposition duration was 3h, the coating thickness was only 0.5 μm . The W concentration into the coating is about 31 at.%.

The explanation for this very low coating rate is the drastic drop of the sputtering rate when about 80% of Ar was replaced with hydrogen. Distribution of the samples to the Associations is shown in Table 1.

The Glow Discharge Optical Spectrometry (GDOS) depth profiles (Figs.1 and 2) show the thickness of the layers and the concentrations of constituents. Hydrogen channel is not calibrated. There is a factory calibration which can not be correct because the lens was cleaned twice and after each cleaning the methods should be re-calibrated with standard

reference samples. At the moment no hydrogen reference samples are available in MEDC Association.

Table 1 Characteristics of the samples (Lot 3) to be used for LIBS experiments

No.	Association	Number of samples	Identification of samples	GDOS profiles	Coating					
					Thick-ness (μm)	Composition (at.%)				
						C	W	Ti	O	H
1	CEA France	2	EU-571	EU-571-2	3.8	~ 5	-	89	~5	~ 1
		2	EU-572	EU-572-1	0.5	~ 45	~ 31	-	~23	~0.5
2	ENEA Italy	1	EU-571	EU-571-2	3.8	~ 5	-	89	~5	~ 1
		1	EU-572	EU-572-1	0.5	~ 45	~ 31	-	~23	~0.5
3	TARTU Estonia	1	EU-571	EU-571-2	3.8	~ 5	-	89	~5	~ 1
		1	EU-572	EU-572-1	0.5	~ 45	~ 31	-	~23	~0.5
4	IPPLM Poland	1	EU-571	EU-571-2	3.8	~ 5	-	89	~5	~ 1
		1	EU-572	EU-572-1	0.5	~ 45	~ 31	-	~23	~0.5

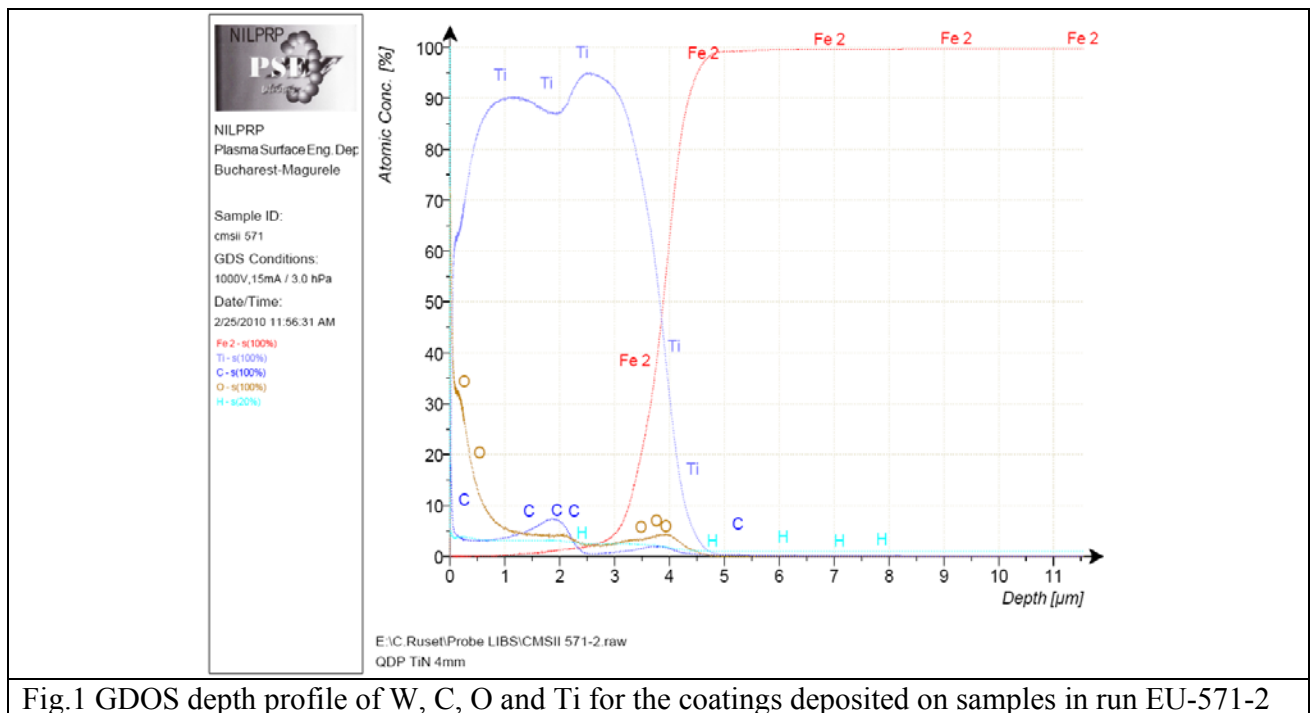


Fig.1 GDOS depth profile of W, C, O and Ti for the coatings deposited on samples in run EU-571-2

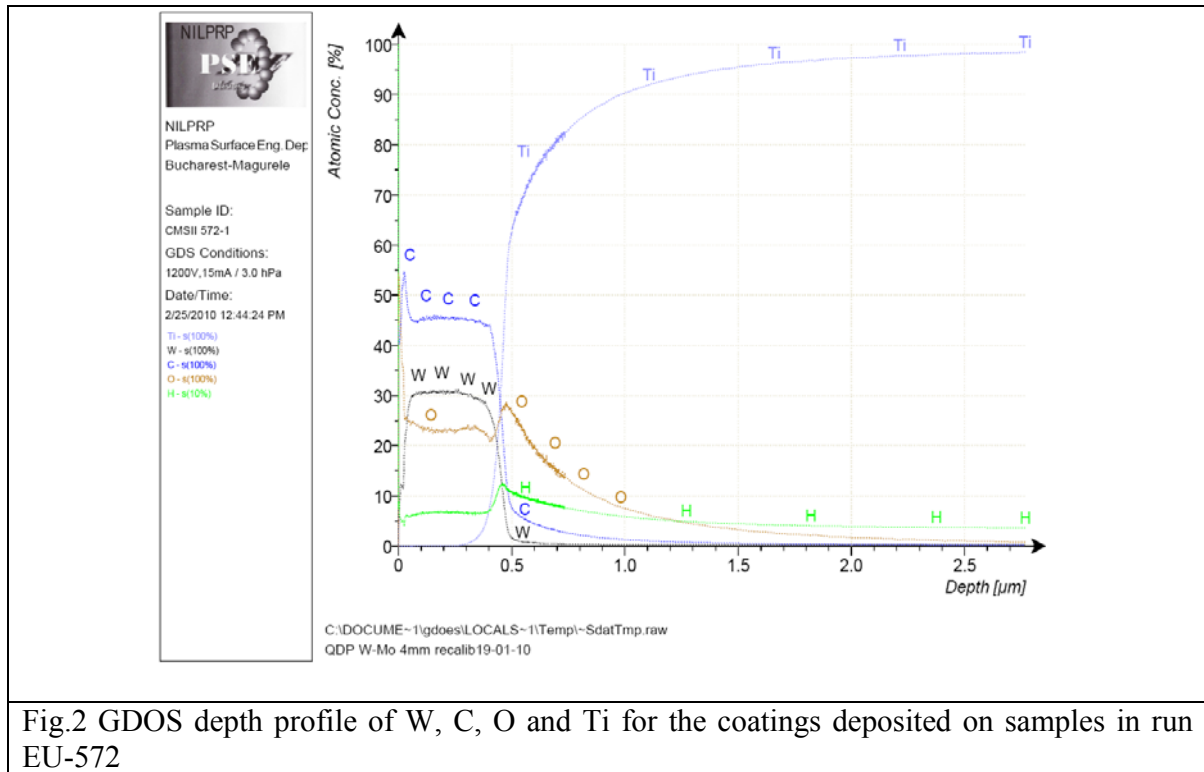


Fig.2 GDOS depth profile of W, C, O and Ti for the coatings deposited on samples in run EU-572

Both coating thicknesses (3.8 μm and 0.5 μm) measured by GDOS were confirmed by optical microscopy observations.

4. Conclusions

- The project is finished. It was demonstrated the possibility to use LIBS technique for the measurement of the wall composition including the depth profiles of the surface constituents.
- The MEdC tasks in the framework of the project were accomplished. The following types of samples were produced and delivered to the EURATOM Associations involved in the project:
 - W coatings of 12-15 μm , with Mo interlayer deposited on Ti substrates
 - C-W coatings with 15 at.% and 27 at.% W with thicknesses of 8.5 μm and 12 μm respectively
 - Ti and C-W hydrogen containing coatings.
- It was pointed out that LIBS technique would be adequate for measurement of tritium contamination for the tokamak wall. This subject could be investigated in the framework of other project.

EURATOM – MEdC ASSOCIATION
National Institute for Laser, Plasma and Radiation Physics

Title of the project:
“Plasma Wall Interaction –
Providing W coated CFC samples for fuel retention
measurements”
EFDA Task Agreement Code: WP10-PWI-01-01-01/MEdC/BS

Interim Report for the period 01.01.2010 – 30.06.2010
(only MEdC tasks)

Authors: C.Ruset, E.Grigore, I.Munteanu, N.Budica

Head of the EURATOM-MEdC Research Unit,
Dr. Florin Spineanu

Project officer,
Dr. C. Ruset

Bucharest 2010

CONTENT

1. General objective of the project	3
2. Specific objectives for the period January – June 2010	3
3. Results and discussion	3
4. Conclusions	4
Annex 1	5

1. General objective of the project

In the framework of the ITER-like Wall project approx. 2,000 CFC tiles from the new JET wall are coated with W layers of 10-15 μm and 20-25 μm using Combined Magnetron Sputtering and Ion Implantation (CMSII) technology. The change from carbon to metallic wall is expected to result into a significant decrease of the fuel retention. The W coatings deposited by CMSII technique are very dense, pore-free and have a nano-crystalline structure. The fuel retention was never measured on this type of coatings. Since a significant proportion of the ITER-like wall consists of W coatings it was defined as objective for the present project determination of the fuel retention for this type of coatings.

2. Specific objectives for the period January – March 2010

Specific objective for MEDC in the period January – June 2010 was to provide W coated CFC samples for fuel retention measurements. The samples are to be exposed in TEXTOR tokamak at FZ Jülich and then analyzed in comparison with non-coated samples exposed under the same conditions.

3. Results and discussion

A number of 16 samples with approx. dimensions 59 x 10 x 5 mm and a special geometry have been manufactured from CFC material. Twelve samples have been W coated with 10-15 μm and 20-25 μm both parallel and perpendicular to the fiber planes. The lot of 6 samples coated with 20-25 μm is shown in Fig.1. The coating thickness was measured by Glow Discharge Optical Spectrometry on witness samples coated in the same run with CFC samples. Four samples cut parallel and perpendicular to fibers remained un-coated as reference. All samples have been sent to FZJ and installed on the roof-like test limiter in TEXTOR to be exposed to plasma. Their arrangement is shown in Fig.2. The main characteristics of the W coated samples are shown in Table 1.



Fig.1 Lot of 6 samples coated with 20-25 μm W

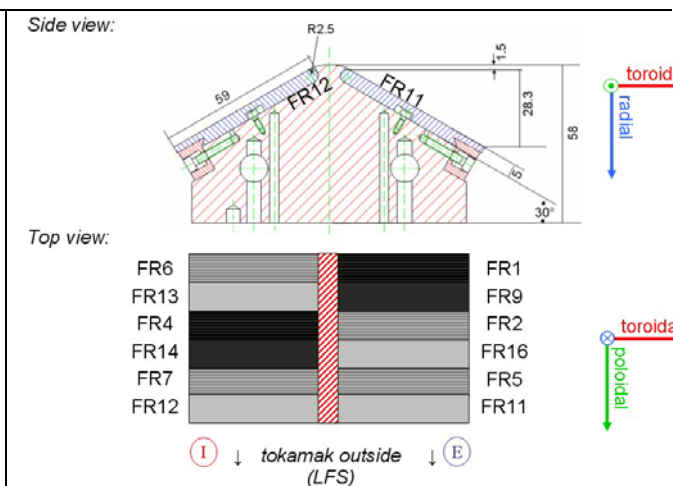


Fig.2 Arrangement of the samples on the „roof” limiter

The fuel retention will be investigated for W coatings of 10-15 μm and 20-25 μm applied both parallel and perpendicular to the fiber planes. A comparison with un-coated CFC will be made.

Table 1 Specification on the W coated CFC samples for fuel retention measurements

No.	Sample identification	Coating		Limiter side
		with respect to fiber orientation	thickness	
1	FR 4	perpendicular	not coated	I
2	FR 14	parallel	not coated	I
3	FR 6	perpendicular	10-15 μm	I
4	FR 13	parallel	10-15 μm	I
5	FR 7	perpendicular	20-25 μm	I
6	FR 12	parallel	20-25 μm	I
7	FR 1	perpendicular	not coated	E
8	FR 9	parallel	not coated	E
9	FR 5	perpendicular	10-15 μm	E
10	FR 11	parallel	10-15 μm	E
11	FR 2	perpendicular	20-25 μm	E
12	FR 16	parallel	20-25 μm	E
13	FR 3	perpendicular	10-15 μm	Reserve
14	FR 15	parallel	10-15 μm	Reserve
15	FR 8	perpendicular	20-25 μm	Reserve
16	FR 10	parallel	20-25 μm	Reserve

4. Conclusion

- The CFC samples for fuel retention measurements have been manufactured, coated and sent to FZJ for deuterium loading and analyses.
- This milestone of MEdC Association was accomplished.

EURATOM – MEdC ASSOCIATION
National Institute for Laser, Plasma and Radiation Physics

Title of the project:
**“Manufacturing and testing of W-coated CFC tiles for
installation in JET for the ITER-like Wall project**

EFDA Task Agreement Code: JW6-TA-EP2-ILC-06

**Interim Report for the period 01.01.2010 – 30.06.2010
(only MEdC tasks)**

Authors: C.Ruset, E.Grigore, I.Munteanu, N.Budica, D.Nendrean

Head of the EURATOM-MEdC Research Unit,
Dr. Florin Spineanu

Project officer,
Dr. C. Ruset

Bucharest 2010

CONTENT

1. General objective of the project	3
2. Specific objectives for the period January – June 2010	3
3. Results and discussion	3
4. Dissemination of results	4
5. Conclusions	4
Annex 1	5

1. General objective of the project

As it was stated in the previous reports, the main objective of the project is W coating of particular tiles for the main chamber and divertor tiles for the new JET wall. In total there are approx. 1,800 tiles which have to be coated with layers of 10-15 μm and 20-25 μm .

2. Specific objectives for the period January – June 2010

The W coating activity in the first semester of 2010 was focused on the Main Chamber tiles. At the same time, at the technical meeting which occurred at JET on 25.03.2010 it was decided that a new lot of 62 divertor tiles has to be coated as spares. A priority list containing 288 remaining tiles to be W coated with 10-15 μm and 20-25 μm at that moment was issued. Priorities were organized on 6 levels. The final date for the Task Agreement was delayed from September to November 2010.

3. Results and discussion

The priority list induced some difficulties in the W coating production because the jiggging devices have to be changed frequently and this reduces the productivity. During the reporting period a number of 561 tiles of which 512 for the main chamber and 49 for divertor have been coated and delivered to JET in 4 consignments. A particular attention was paid to IWGL (Be) tiles which have been coated and sent in USA to be assembled together with the Be tiles. A batch of IWGL (Be) and Shinethrough protection tiles is shown in Fig.1a. The two axes rotation device was used in order to achieve a good uniformity of the coating on two or three sides of the tiles. For the big tiles like G1 and G8 the central rotation jiggging device was used (Fig.1b).



(a)



(b)

Fig.1 W coated IWGL (Be) and Shinethrough protection tiles (a) and G1, G8 divertor tiles (b)

Approximately 10% of the coated tiles were sent to IPP Garching for high heat flux tests in GLADIS. The tests revealed the good quality of the coatings with “zero” defects.

In addition to the tiles mentioned above, a number of 75 divertor LBSRP tiles were coated with 20-25 μm .

A synthesis of the coated tiles and delivered to JET is shown below.

- Divertor tiles: 743 (93%)

- Main chamber tiles: 918 (91%)

4. Dissemination of results

An interview concerning the W coating of CFC tiles for the ITER like Wall project at JET was given by Cristian Ruset for JET insight bulletin. It is published in the June 2010 issue.

5. Conclusions

1) „ITER like Wall” project is very important for both ITER and JET. It will provide information about the plasma-wall interaction under these particular conditions, about the transport of the wall particules through the plasma and about the capacity of these materials to sustain the real thermal loads they are subjected at.

2) EURATOM MEaC Association brings a significant contribution to the project by coating with W all the tiles which have to be coated. This means about 1,800 tiles of different shapes and dimensions. More than 90% of these tiles are coated.

REPORT on PROGRESS

**Stage of research performed in the frame of the
contract nr. 1EU-8 / 01.03.2010**

entitled

**MICRO AND NANO-STRUCTURAL ANALYSIS BY T.E.M., X-EDS,
E.E.L.S., XRD AND MOESSBAUER SPECTROSCOPY OF THE
PROCESSED MATERIALS IN VARIOUS TECHNOLOGICAL STAGES
OF O.D.S. FERRITIC STEELS (O.D.S.F.S.) AND O.D.S. W-ALLOYS
ELABORATION**

**concerning the following activities mentioned in the
EFDA WP10-MAT-ODSFS task agreement**

WP10-MAT-ODSFS-01-01/MEdC/BS

WP10-MAT-WWALLOY-01-01/MEdC/BS

**P.I. Dr. Corneliu Sarbu
project responsible**

**Natl. Inst. for Mater. Physics
Magurele-Bucharest, Romania**

June 2010

CONTENT

General and partial objectives	pag-4
Abstract	pag-5
Results of the research performed until June 30th	
The materials. The instruments	pag-6
The XRD results	pag-7
The X-EDS microanalysis results obtained by TEM and SEM	pag-9
The experimental X-EDS data acquired from the two MA fabricated powder alloys	pag-12
The Moessbauer spectroscopy results	pag-20
The classical TEM results	pag-22
The HRTEM results	pag-23
About the applicability of EELS method	pag-24
Conclusions	pag-26
Bibliography	pag-27
Annex 1-RST	pag-28

GENERAL OBJECTIVES

The reported research aims at matching the two following general objectives:

(i) Developing the present generation of nano-structured ODSFS by optimising the chemical composition and determining a set of parameters for the Mechanical Alloying (MA) process and the subsequent Thermal-Mechanical Treatments (TMT), aimed at reproducing the main microstructure features identified as responsible for the high strength and the limited loss of fracture toughness after irradiation. The optimisation will concentrate on chemical composition of the 14Cr-Y-W-Ti (14YWT) type.

(iii) Developing an optimised generation of nano-structured & nano-grained ODSFS. The ODS ferritic steel is a driving system and the aim is the fabrication of ODS ferritic steels with improved plasticity. The nano-grain sized 14YTW alloys will be produced on the laboratory scale using (i) High Energy Ball Milling (HEBM), (ii) consolidation, i. e. extrusion and/or spark plasma sintering, and (iii) thermo-mechanical treatment (TMT). The effect of hot extrusion parameters on microstructure and mechanical behaviour will be characterised to select the best fabrication route for an optimised strength-ductility relation. The microstructure is expected to be characterized using transmission electron microscopy (TEM), atom probe tomography (APT), and related methods.

PRESENT STAGE OBJECTIVES HAVING JUNE 30 AS DEADLINE

According to the contract, the partial objectives assumed for the first round of analysis (deadline June 30, 2010) are:

- a) analysis of a powder of mechanically alloyed alpha-Fe with Y₂O₃
- b) analysis of a powder of mechanically alloyed alpha-Fe with Ti and Y₂O₃
- c) analysis of consolidated samples (if supplied in due time by the foreign partner) obtained from these powders;
- d) analysis of final ODSFS samples (if supplied in due time by the partner), obtained by extrusion from the consolidated materials;

We have to pointed out that, according to the contract, our work of analysis is highly dependent on the supply of samples by our foreign partner.

Not all the above mentioned *objectives proposed for the 1-st round of research (deadline June 30)* were accomplished till end of June 2010, because of the delay in the supply of samples from our partner. Therefore, until June 30-th only the *partial objectives labelled above as (a) and (b) are accomplished*.

The contract stipulation (see Section B-4) referring to this foreseen situation is mentioning that: “if necessary, the analysis of samples supplied with delay by our Portuguese partner will be extended beyond June 30, 2010”.

ABSTRACT

A couple of powders fabricated by the Mechanical Alloying (MA) procedure was studied. These powders are intended to be used as starting materials in subsequent procedures leading to an ODS steels (ODSFS).

The informations we will supply to the powders producer are important for the setting of MA process parameters, which has a technological importance.

We drew the general conclusion that there is a clear inhomogeneity of the elemental composition of the powders, which means that the MA parameters should be modified.

RESULTS OF THE RESEARCH PERFORMED UNTIL JUNE 30th

The materials. The instruments

We have investigated 2 samples of mechanically alloyed (M.A.) powders, intended to have the following elemental composition:

Fe-Cr-Y-Ti (labelled as sample-1)

Fe-Cr-Y (labelled as sample-2)

which were kindly supplied by Dr. Jose Brito-Correia from the Association IST, i.e. Instituto Superior Tecnico (Universidade Tecnico de Lisboa), Lisbon, Portugal.

The samples were prepared by mechanical alloying (MA) starting with pure elements, according to the already reported recipe: Fe (99%, 44 μm), Cr (99.95%, particle size < 25 μm), Y (99.9%, median particle size 500 μm) and Ti (99.9%, particle size < 105 μm). The milling was done in stainless milling media, at 400 rpm for 18 hours, in a planetary mill model Retsch PM100MA. One of the batch milling charge was constituted of 17.16 g Fe, 2.82 g Cr and 0.02 g Y. The other batch milling charge was: 17.05 g Fe, 2.82 g Cr, 0.06 g Y and 0.07 g Ti.

The target composition in view to result for MA of powders was:

85.2wt%Fe-14.1wt%Cr-0.3wt%Y-(0.3wt%Ti)

The dissolution of Y₂O₃ in the Fe-Cr solid solution during MA was previously communicated [1] in the litterature.

The instruments used for micro and nano-characterization are:

(1) X-ray diffractometer Bruker D8 Advance, in Bragg-Brentano configuration, working with filtered Cu-K α radiation. The powder diffractograms were acquired by setting high quality parameters: angular steps of 0.02deg and dwell times of 8s/step and 9s/step.

(2) analytical TEM electron microscope model JEM-200CX-TEMSCAN, generating an electron beam of maximum 200kV. It is equipped with an attachment allowing the work in SEM mode besides TEM mode. It is equipped also with an X-EDS spectrometer model EDS2004 made by IXRF Systems Inc., 15715 Brookford Drive, Houston, Texas. It operates with a detector mounted in high position, i.e. working at a takeoff angle of 72deg., which is favourable because the sample has not to be tilted away from horizontal in order to acquire a good quality spectrum. In the TEM mode of operation (at 40, 80, 120, 160 and 200 kV) the electron beam cannot be focussed as microbeam, which means that the focussed beam can analyse only particles as a whole which frequently includes also some of its surroundings. In the SEM mode of operation the achievable focussing is that of micrometers diameter.

The main advantage offered by this instrument is that it can work in SEM mode at much higher accelerating voltages than in dedicated SEM microscopes. These highly

focussed energetic beams can penetrate and generate X-rays from very deep levels inside the material.

(3) dedicated SEM microscope model Zeiss EVO, with a maximum acceleration voltage of 30kV. It is equipped with a Bruker made X-EDS spectrometer.

(4) analytical (HR)TEM electron microscope made by FEI, model Tecnai™ G-2 F-30 S-TWIN, operated at 300kV. This instrument is able to generate very finely focussed electron beams (up to nanometer size diameters). It is equipped with an X-EDS spectrometer made by EDAX, the detector being positioned at low level (detector angle 14.6deg), which means that it can work when shifted very close to the sample (at 11.8mm). This is allowing a very good collection of the X radiation.

The XRD results

The high quality X-ray diffractograms generated by the 2 samples and acquired in angular steps of 0.02° and with a dwell time per step of 9s are looking very similar, as shown in Fig-1.

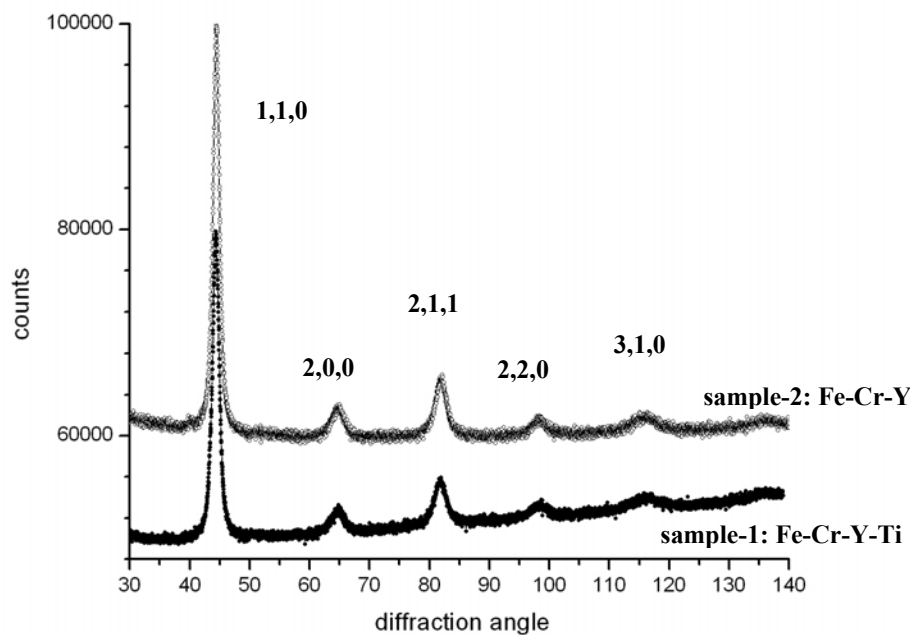
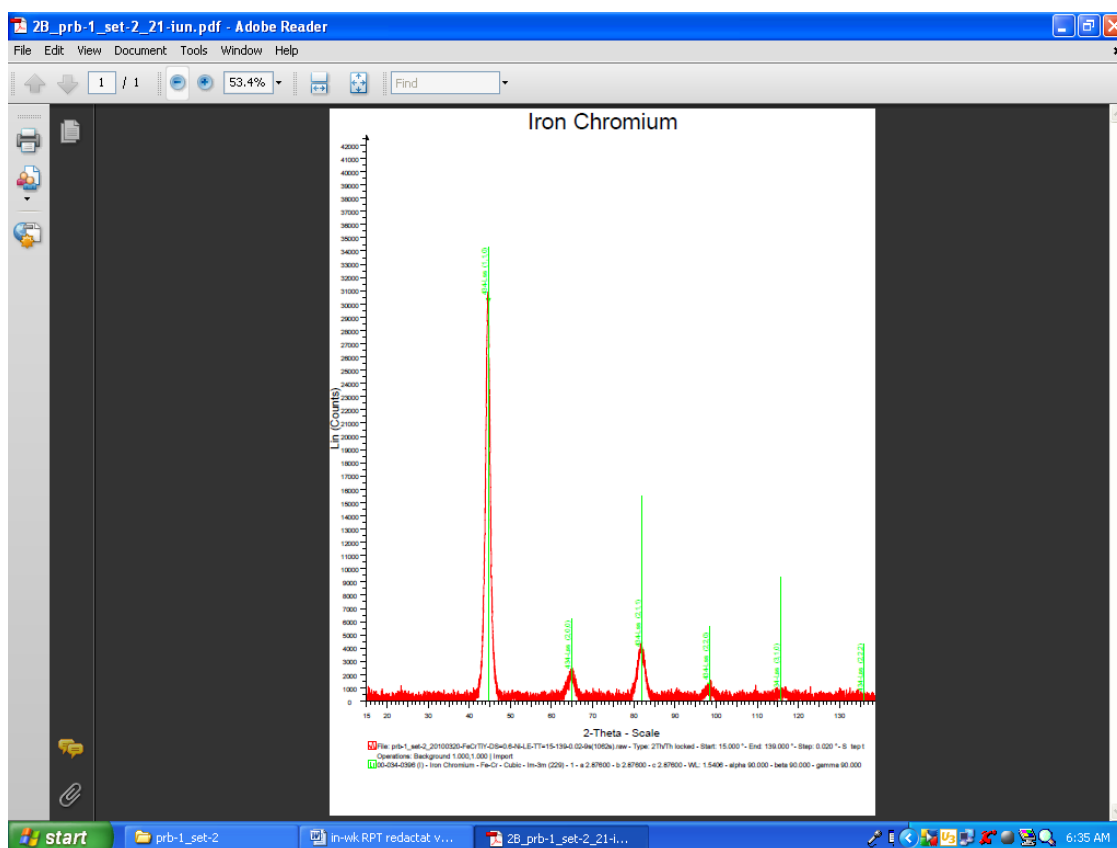


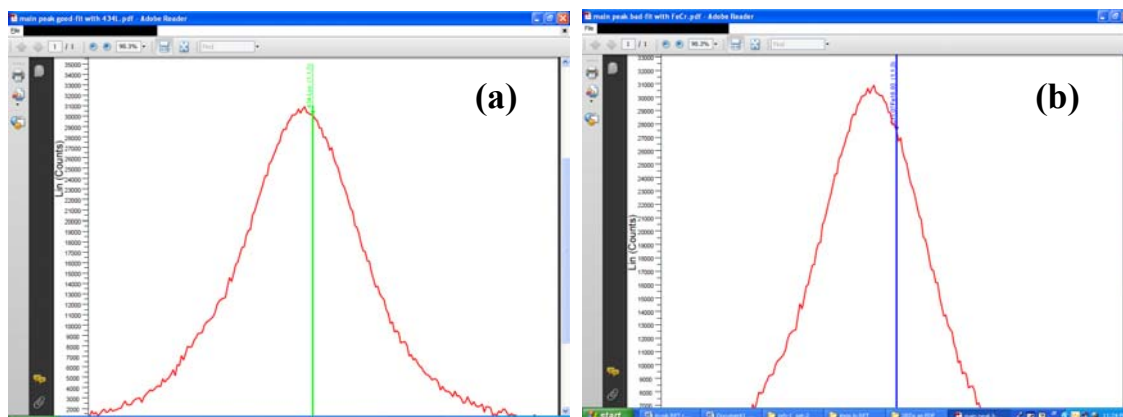
FIG-1

The peaks pattern of the 2 samples corresponds very well to the cubic b.c.c. crystallographic structure (Im-3m, SG 229) and can be indexed as shown. It is to be noticed that the diffraction lines are largely broadened, the FWHM of peaks being almost the same in both diffractograms.

The Powder Diffraction Files (PDF) database used for matching the 2 diffractograms has shown best fit for both with the PDF-file nr. 00-034-0396. This is the reference for the matrix (solid solution of Fe and Cr) of the 434L ferritic stainless steel. This very good fit is demonstrated in FIG-2.



A worse fit occurs with the PDF-file nr. 03-065-7775 which is the reference of another b.c.c. structure of a Cr-Fe solid solution labelled as Cr1.07Cr18.93. A comparison of the different quality of the two fits can be best revealed by looking at the strongest reflexion (1,1,0), as shown in FIG-3 (a) and (b). FIG-3(a) proves that the fit with the b.c.c. structure (Im-3m, SG 229, matrix of 434L steel, lattice constant 0.2876nm) is better than the fit (see FIG-3(b)) with the similar structure of Cr1.07Fe18.93 (having a lattice constant of 0.2869nm). The same fitting quality is valid for all the peaks of the experimental diffractograms.



The application of Scherrer formula to the strongest (1,1,0) reflection peak, after manually measuring the FWHM, leads to the value of less than 10nm (about 8 nm) of the average dimension of the crystallites present in both samples. We have no reason to consider any strong influence of mechanical stress on the crystallites, as long as the sample is a powder and therefore this average value is taken as being due only to particles dimensions statistic distribution. The experimentally determined average value of about 8nm is confirmed also by the inspection of the TEM images. A Rietveld fit of the same two experimental diffractograms led to a value, averaged over the whole diffractogram, very close to 8nm.

The data provided by TEM and SAED (i.e. selected area electron diffraction) led us to the conclusion that there is no observable *amorphous component* in the two materials.

CONCLUSION. The XRD study of the two powders fabricated by MA by starting with pure powders of Fe, Cr, Yttria and Ti shows (a) that a solid solution is formed, with a crystalline structure very close to that of the ferritic matrix of the 434L steel, and (b) that the alloys powders are of nanometric size, with an average size value of about 8nm. No amorphous component is to be supposed as present in the two materials.

The X-EDS microanalysis results by TEM and SEM

The X-EDS test analysis of a pure Yttria sample

It is well known that stray X radiation is always present when X-EDS analysis is performed in the TEM mode. That is due to the X-ray fluorescence induced in the materials surrounding the sample. In order to identify the stray X radiation specific to the JEM-200-CX microscope, the most intensively used for performing the X-EDS analysis of our samples, a standard sample was prepared from powder of pure Yttria (Y₂O₃) on substrate of carbon thin film.

The X-EDS spectra acquired in SEM mode from the standard Yttria sample are shown in FIG-4 for the analysis performed at 200kV and in FIG-5 for that performed at 40kV. The choice of the two values of accelerating voltages (40kV and 200kV) was driven by the fact that all the subsequent analysis of particles in the 2 samples of interest was done with electron beams with energy of either 200keV or 40keV. A rich counting statistics of 100K counts was acquired for both accelerating voltages. It is to be pointed out that in SEM mode the electron beams have the finest diameter of focussing and the lowest rate of stray radiation generation. It was selected a platelike particle of the pure Yttria particle, semi-transparent to the 200kV beam, but too thick for being transparent for the 40kV beam.

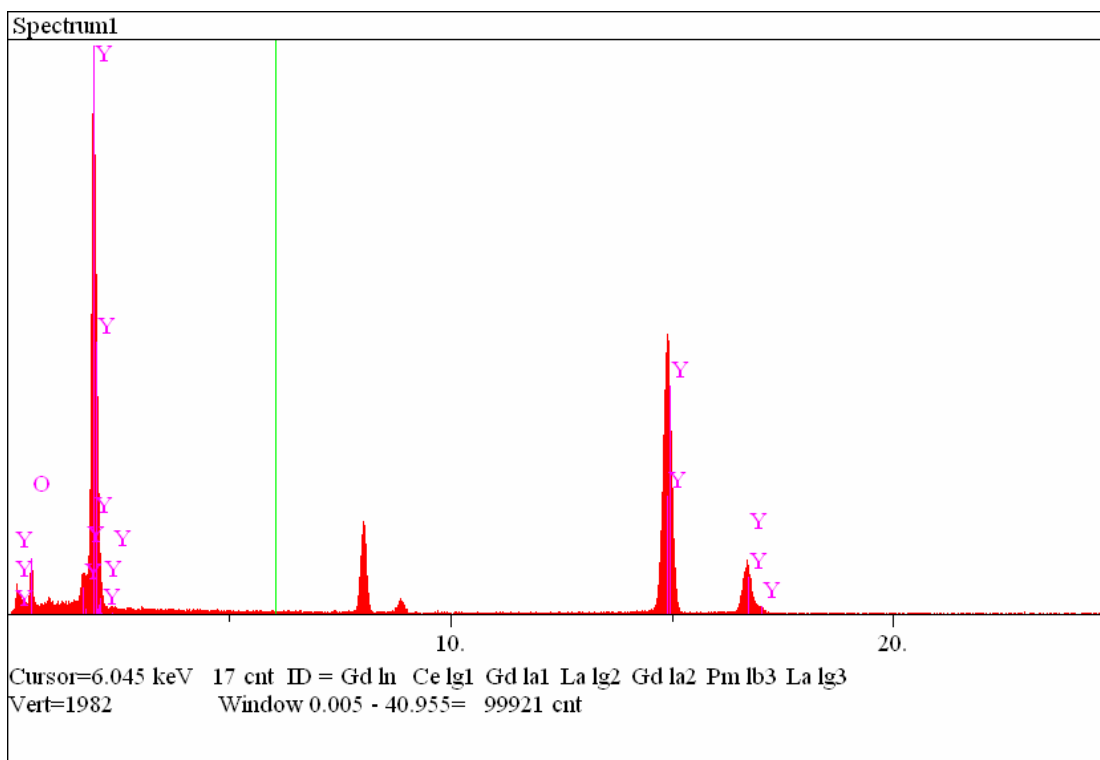


FIG-4(A). X-EDS entire spectrum of 100K counts, acquired from a platelike particle of pure Y₂O₃.

In FIG-5(B) is shown that the only stray radiation present in the spectrum is that generated by Cu, which is a familiar and permanent presence in any X-EDS spectrum acquired in a transmission electron microscope. In FIG-5(C) is shown the spectrum shape in the energy range from 0 to the energy specific to the main Cu peak. The spectrum shape in this range is showing only the presence of a pure background counting. This one should be the shape to be observed when no impurity or elements in minor quantity are present in the analysed particle. It can be considered as a reference shape.

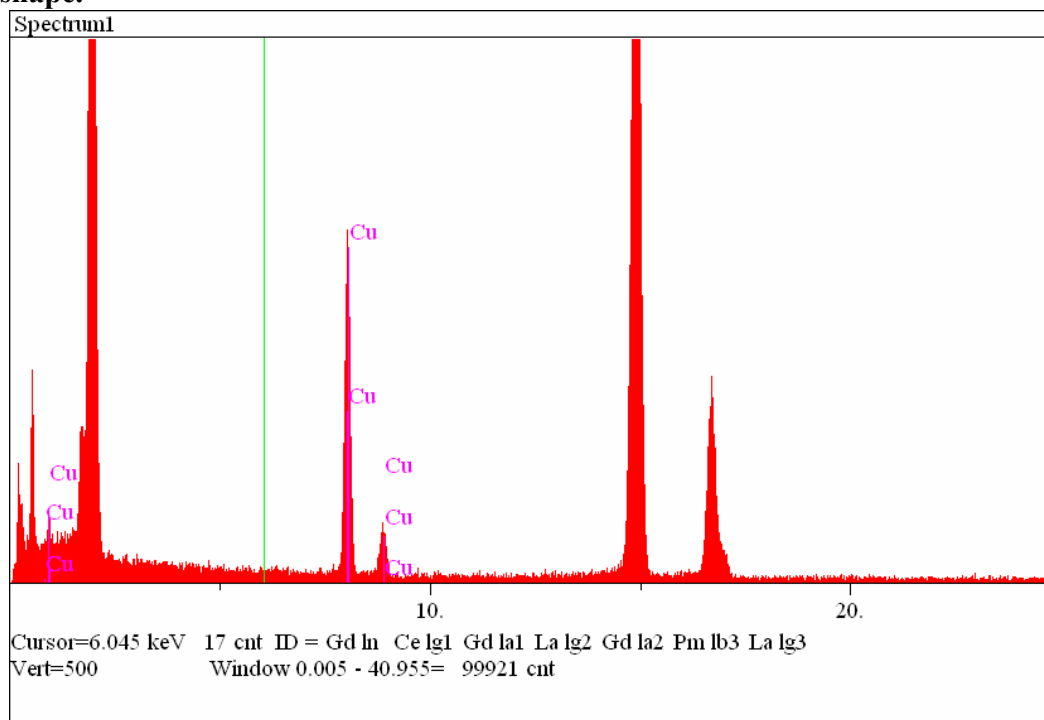


FIG-4(B) shows that in our reference X-EDS spectrum the only stray radiation is that normal for an acquisition in TEM, generated by Cu

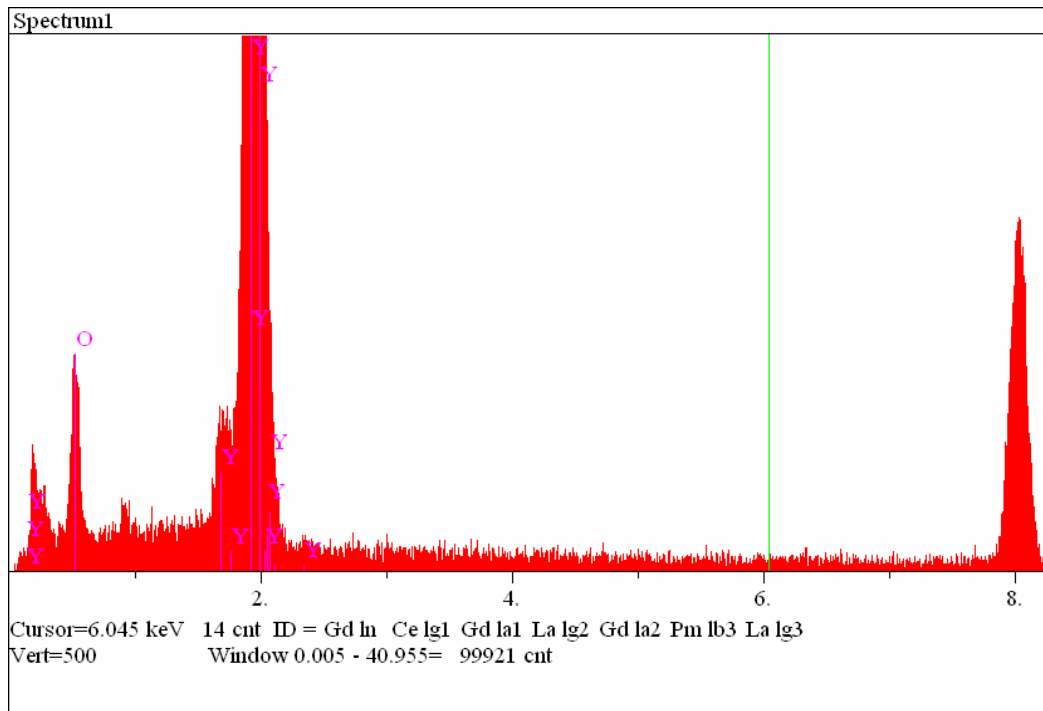


FIG-4(C) shows the normal shape of background in the energy range from 0 to 8keV

CONCLUSION. Except for Cu, no other stray radiation should be detected in the X-EDS spectra as generated by the structural materials of the TEM we used.

The experimental X-EDS data acquired from the two powder alloys fabricated by MA

Careful X-EDS analysis of a total of 26 particles in the two samples was performed in the following two manners:

(a) in TEM by focussing the beam and statically directing it either to illuminate an entire single particle (including a small area of its surroundings) or only a small fraction of an entire particle area (including a small area of its surroundings). The accelerating voltage was always of 200kV when performing analysis in this mode.

(b) in TEM, but putting the electron beam under the control of the SEM device, which means that it is strongly focussed to a diameter of micrometers, i.e. by using a much finer beam than in TEM mode. The accelerating voltage was either of 40kV, or of 200kV and the beam was either statically focussed on a point of the particle, or scanned over a very small area of the particle.

The results are collected in Table-1 for sample-1 and in Table-2 for sample-2. In these tables are mentioned also some features which are important for understanding the particular mode in which a particle was analysed, as are:

(a) whether the analysis was done on a single point (on-point) or by scanning a selected area;

(b) how many counts were accumulated in the spectrum and how long lasted the analysis;

- (c) whether the particle is thick or semi-transparent or transparent to the electron beam;
- (d) which kind of correction was used for the quantitation;
- (e) comments about the quantification accuracy;
- (f) comments about the visibility of the Yttrium-L peaks in the spectrum;

TABLE-1 (concerning Ti-containing sample-1, besides Y)

Particle label	SEM or TEM kV e-beam	Total counts (livetime)	Composition wt%	Observations
p-1 very thick particle	TEM 200kV whole particle illuminated	~356K 500s	Ti 8.010 \pm 2.037 Cr 6.770 \pm 1.544 Fe 15.342 \pm 2.082 Y 69.878 \pm 17.519	consistent O peak detected; Si, S peaks visible; Y peak not clearly visible; moderate error of the Y quantification
p-2 thin layer of dispersed material	"	~27K 300s	Ti 1.501 \pm 0.621 Cr 8.653 \pm 1.154 Fe 65.567 \pm 3.631 Y 24.280 \pm 13.858	consistent O peak detected; Y peak not clearly visible high error of the Y quantification
p-3	"	100K 500s	Ti 1.822 \pm 0.180 Cr 8.190 \pm 0.298 Fe 84.159 \pm 1.280 Y 5.830 \pm 2.383	consistent O peak detected; Si peak clearly visible; Y peak hardly visible; high error of the Y quantification
p-4	"	41.2K 500s	Ti 1.458 \pm 0.202 Cr 8.514 \pm 0.380 Fe 84.053 \pm 1.606 Y 5.975 \pm 3.028	Mn, Zn low peaks present; Y peak not visible; Si very low amount, peak visible; Ti peak not visible; high error of the Y quantification
p-5 very thin platelike particle	"	41.7K 500s	thin film correction Ti 5.510 \pm 2.321 Cr 2.320 \pm 0.988 Fe 62.482 \pm 25.637 Y 29.688 \pm 23.013	huge O peak; no other elements detected; Y peak hardly visible high error of the Y quantification
p-6			-	The X-EDS spectrum was strongly distorted because of the much too high rate of radiation to be processed by the detector
p-7	"	25.6K 500s	Ti 7.461 \pm 4.409 Cr 6.047 \pm 3.242 Fe 8.289 \pm 3.321 Y 78.204 \pm 37.470	huge Si peak; O peak very high; Y peak hardly visible; high error of the Y quantification
p-8 thin large transparen	TEM 200kV two separate	on area-1 147K	on area-1, applying the thin-film correction Ti 14.472 \pm 5.994	obvious composition inhomogeneity of the single crystalline parts

t platelike particle complex of several single crystals, as shown in the SAED	areas were analysed	on area-2 290K	Cr 15.850 ±6.258 Fe 47.231 ±10.994 Y 22.448 ±11.575 on area-2, applying thin film correction Ti 11.083 ±3.177 Cr 7.979 ±2.301 Fe 15.247 ±2.871 Y 65.691 ±23.326	moderate and high error in the Y quantification
p-9 thick particle, first in a group of 3	SEM 40kV micro-beam focussed on-point	500s about 25K	Ti 1.832 ±0.279 Cr 9.145 ±0.490 Fe 81.349 ±1.915 Y 7.675 ±4.086	very high error of the Y quantification
p-10 thick particle, second in idem	"	500s ~90K	Ti 1.715 ±not-registered Cr 9.055 ±idem Fe 85.566 ±ibidem Y 3.664 ±ibid	An error occurred in the registration of the quantification error value for Y
p-11 thick particle, 3rd in ibidem	"	500s ~90K	Ti 1.553 ±not-registered Cr 9.227 ±idem Fe 85.292 ±ibidem Y 3.928 ±ibid	idem
group-of-particles-p-12	SEM 40kV micro-beam scanning on selected area	500s ~40K	Ti 1.574 ±0.191 Cr 9.016 ±0.360 Fe 87.106 ±1.570 Y 2.304 ±1.809	high error of the Y quantification
group-of-particles-p-13	"	500s ~30K	Ti 1.711 ±0.247 Cr 8.892 ±0.442 Fe 86.126 ±1.890 Y 3.618 ±2.747	high error of the Y quantification
group-of-particles-p-14	"	500s ~50K	Ti 1.505 ±0.161 Cr 10.060 ±0.401 Fe 87.740 ±1.571 Y 0.695 ±0.286	
p-26 thick particle	SEM 200kV micro-beam scanning a selected area	900K 963s	Ti 1.697 ±0.038 Cr 8.499 ±0.066 Fe 85.870 ±0.287 Y 3.934 ±0.437	a very small Y-peak is clearly visible Fe, Cr, Ti but also visible Si, S, Zn, Ca very low error of Y quantification
p-26 same particle explored on-point	SEM 40kV on-point	500K 1585s	Ti 2.016 ±0.080 Cr 9.120 ±0.135 Fe 83.360 ±0.547 Y 5.504 ±0.985	idem

TABLE-2 (concerning sample-2,that should not contain Ti)

Particle	SEM or	Total counts	Composition	Observations
----------	--------	--------------	-------------	--------------

label	TEM kV e-beam	(livetime)	wt%	
p-15	TEM 200kV smallest beam focussed on particle	500K 3387s	Ti 1.372 ±0.045 Cr 8.656 ±0.084 Fe 88.407 ±0.394 Y 2.159 ±0.442	in X-EDS spectrum Y-peak is visible highest precision of Y quantitation
same p-15 particle analysed with a different beam intensity & up to 700K counts in spectrum	"	700K 3145s	Ti 1.388 ±0.042 Cr 7.974 ±0.078 Fe 88.984 ±0.372 Y 1.654 ±0.364	Y-peak is hardly visible high precision of Y quantitation
p-16 this is an Yttria particle	"	350K 2321s	ZAF correction O 0.000 ±0.000 Y 100.000 ±0.925 Thin film corr. O 10.684 ±0.303 Y 89.316 ±0.826	oxide quantification cannot be done correctly
p-17 it is a transparent agglomerat of nano- crystals as seen in its bright field t.e.m. image	"	500K 1699s	Thin film correct. Ti 1.625 ±0.079 Cr 14.172 ±0.233 Fe 83.982 ±0.576 Y 0.221 ±0.045	Ti-peak is high & visible Si, Mo & Ca peaks are present high precision of Y quantitation
p-18	"	500K 1718s	Thin film corr. should be the best Ti 1.515 ±0.050 Cr 14.399 ±0.155 Fe 83.807 ±0.380 Y 0.278 ±0.033	huge amount of Si detected much less amounts of Mo, Ca, Al detected high precision of Y quantitation
p-19 thick particle	"	500K 891s & 900K 1415s	For 500K counts ZAF corr. only Ti 1.351 ±0.043 Cr 8.376 ±0.083 Fe 87.847 ±0.380 Y 2.426 ±0.451 For 900K counts ZAF corr. only Ti 1.353 ±0.032 Cr 8.194 ±0.061 Fe 88.652 ±0.286 Y 1.801 ±0.291	Y peak clearly visible Very low amount of Si and Ca Ti-peak high high precision of Y quantitation
p-20	"	50K		A lot of Mo & Zn presence

this is not an alloy particle		time not recorded		detected no Fe, Cr, Ti, Si visible a bit of Ca
p-21 semi-transparent to electron beam	"	75K 1517s	Thin-film corr. Ti 2.265 \pm 0.538 Cr 14.481 \pm 1.357 Fe 79.859 \pm 3.242 Y 3.395 \pm 1.021	Fe, Cr, Si high Ti not visible low precision of Y quantitation
p-22 very thick particle	"	100K ?s counter error & 280K 2470s	For 100K Ti 1.526 \pm 0.128 Cr 8.043 \pm 0.228 Fe 86.953 \pm 1.037 Y 3.478 \pm 1.484 & For 280K Ti 1.391 \pm 0.143 Cr 8.933 \pm 0.281 Fe 72.265 \pm 0.965 Y 17.410 \pm 3.118	Fe, Cr, Ti high Y hardly visible Low and medium precision of Y quantitation
p-23 very thick	"	500K 1607s	ZAF correction Ti 1.392 \pm 0.052 Cr 8.186 \pm 0.099 Fe 86.867 \pm 0.445 Y 3.555 \pm 0.644	Ti peak high low peaks of Si & Ca Y presence visible only in the background subtracted spectrum
p-24 thin transparent particle which seems to be Yttrium oxide	"	100K 878s	Quantification considering only Y & O O 0.000 \pm 0.000 Y 100.000 \pm 1.996 excluding O Ti 0.209 \pm 0.043 Cr 0.078 \pm 0.020 Fe 0.076 \pm 0.016 Y 99.636 \pm 1.989	
p-25 semi-transparent	"	200K 2671s	Thin film corr. Ti 1.734 \pm 0.129 Cr 13.336 \pm 0.357 Fe 84.48 \pm 0.916 Y 0.441 \pm 0.101 & ZAF correction Ti 1.709 \pm 0.127 Cr 7.935 \pm 0.213 Fe 81.424 \pm 0.882 Y 8.932 \pm 2.046	High amount of Si Low amount of Ti Y peak not visible good precision of Y quantitation

DISCUSSION of X-EDS results

In spite of the frequent mention in Table-1 and Table-2 that the Y peak is not visible in the experimentally acquired spectra, there are reasons to accept the existence of Y in the samples.

(a) the Y series-L of peaks are energetically very close to the Si-K peak and Si is frequently detected as clearly present in the sample. The Si peak origin is not clear, but it cannot result as an artefact due to the microscope, as proven by the pure Yttria spectrum shown above, where no Si peak is visible. The Y series of L-peaks could be in most cases obstructed by the neighbouring Si-K peak. That could be an explanation for the quantification results supplied by the spectrum processing software in spite of the lack of clear visibility of the Y peak and for the very high error in the Y quantification. The quantitative data supplied by the software in spite of the lack of clear visibility of Y peak shows that the assesment of Y presence in the corresponding particles is doubtful but not excluded de plano.

For an example of the frequently observed shape of X-EDS spectra in the energy range where Si-K and Y series-L peaks are not clearly visible see FIG-5(A). The quantitative data supplied by the quantification software are based in most cases on the kind of spectra shown in FIGS-5(A)&(B).

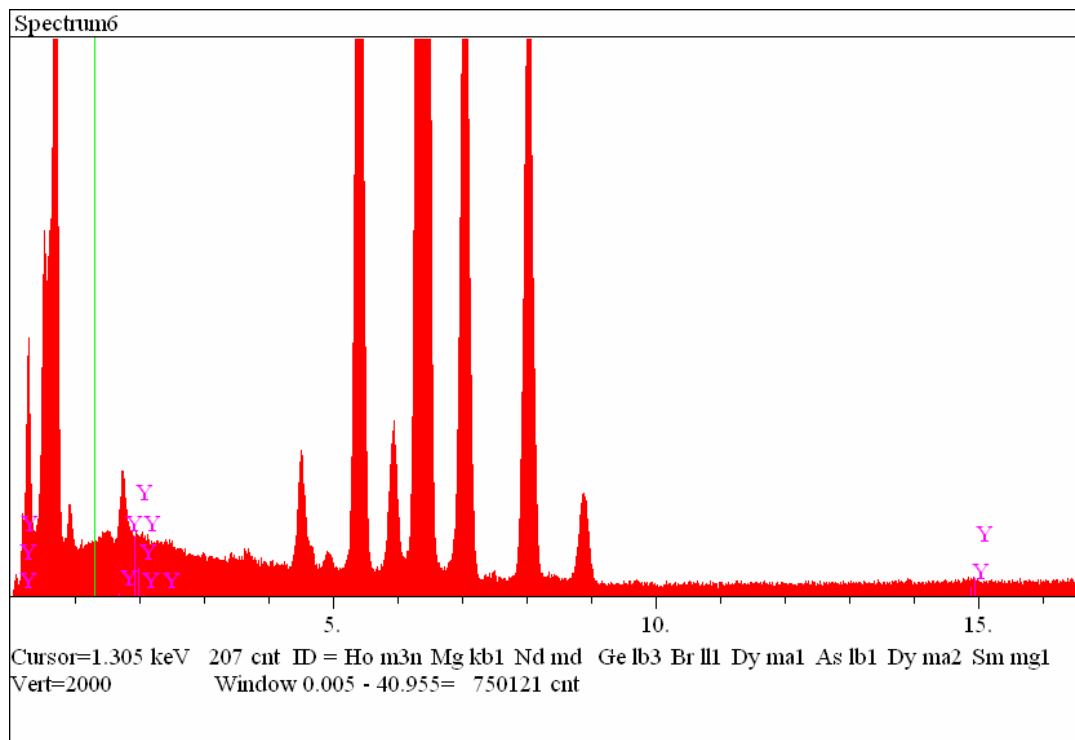


Fig-5(A) Spectrum contains an accumulation of 750K counts

After background subtraction, the quantification software generates a shape model of the peaks to be quantified, as shown in FIG-5(B), finally assesing on this ground a wt% to the required elements. The resulting quantification error for Y is high in these circumstances.

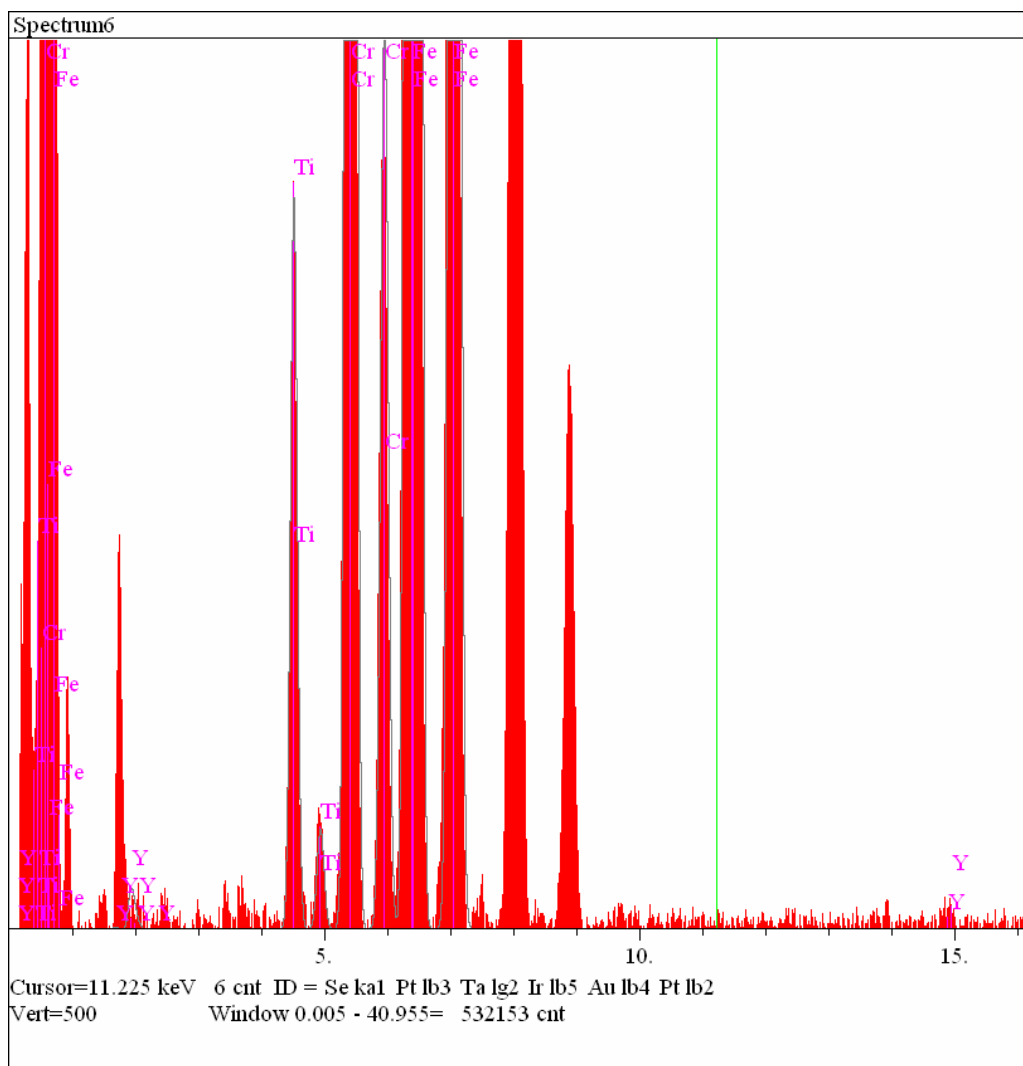


Fig-5(B) The software modelling of the quantified elements peaks. Here the presence of Y is undoubted due to the visibility of its peaks around the 15keV energy value and in spite of the low visibility of its peaks in the energy range around 2keV

(b) in few cases the Y peak presence in the spectrum is clearly visible, in spite of the presence of Si-K peak next to and preceding it and of a S-K peak following it, as shown in FIG-6(A). In these circumstances the quantification error for Y is much lower. It is based on background subtracted spectra and modelled peaks as shown in FIG-6(B), which are looking similar to those already shown in FIG-5(B).

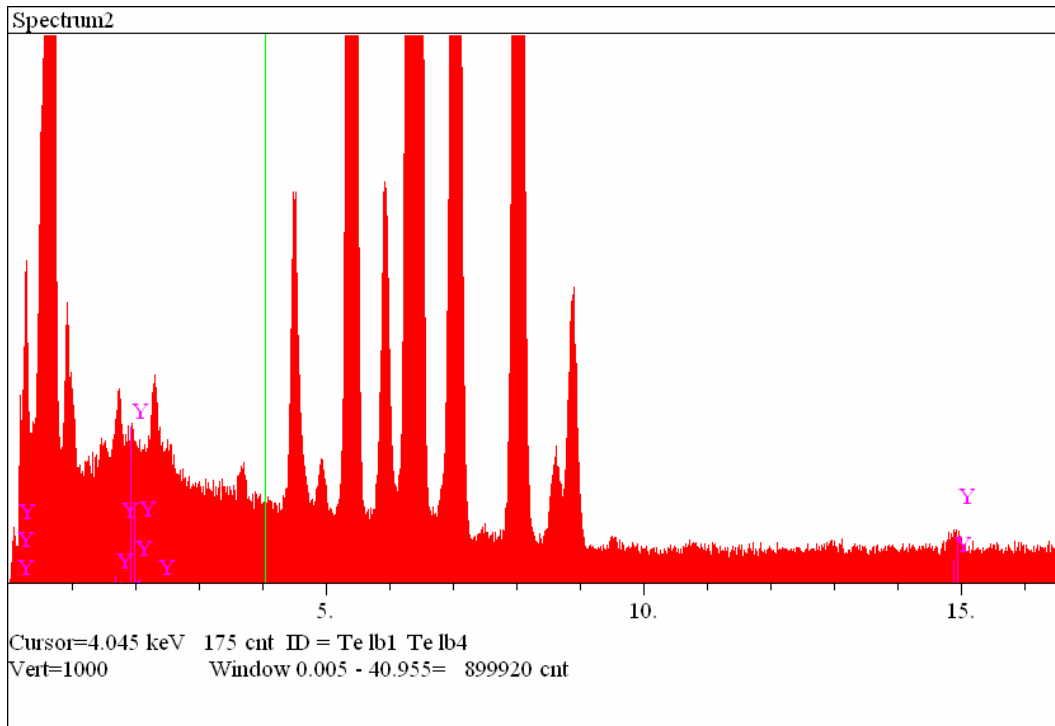


Fig-6(A). Spectrum contains 900K counts

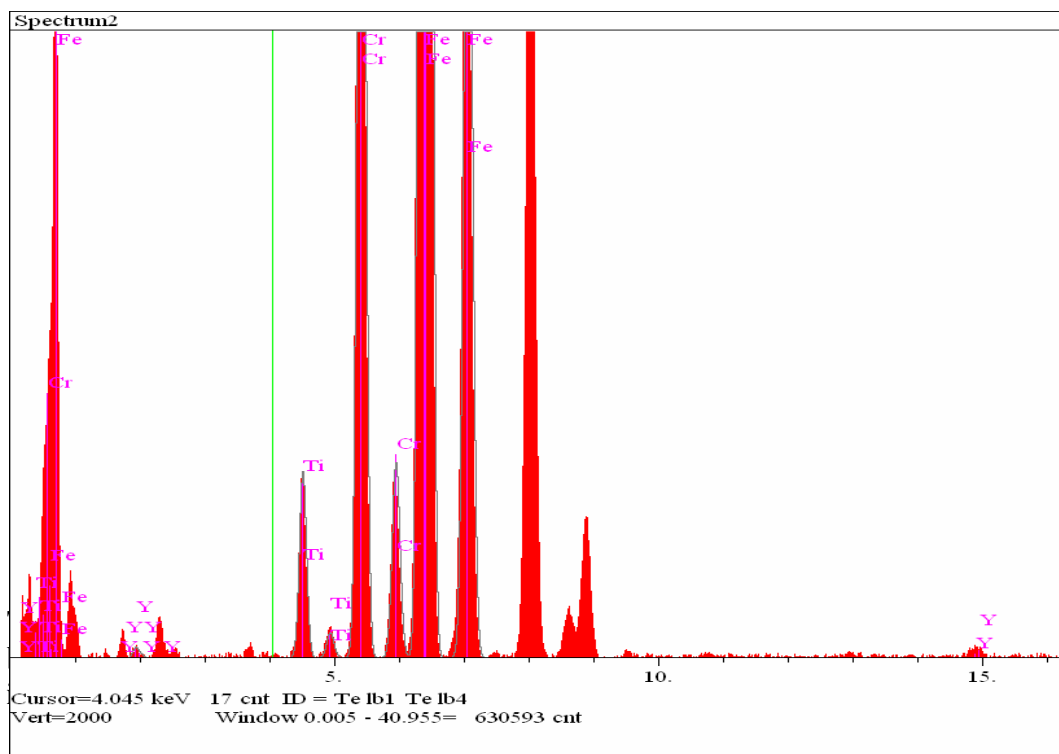


Fig-6(B)

Final conclusions concerning the X-EDS results

(a) The Y content is not uniformly distributed in the alloy particles. This is supported also by the observation that there are Ytria particles not dissolved into the Fe-Cr matrix.

(b) Ti is present almost overall, even in sample-2 which is supposed not to contain this element.

(c) a few particles were detected which contain impurities. The presence of Si is observed in most cases.

The Moessbauer spectroscopy results

The Moessbauer spectra obtained from the two alloy samples are shown in next FIG-7 and FIG-8. The comparison of each of these two spectra with the spectrum of pure alpha-Fe shown in FIG-9 is evidencing a clear distortion of the alpha-Fe crystal lattice. This is mainly due to the formation of Fe-Cr solid solution during the MA process and on a much more reduced scale to the penetration in the Fe-Cr solid solution crystal b.c.c. type lattice of other foreign atoms.

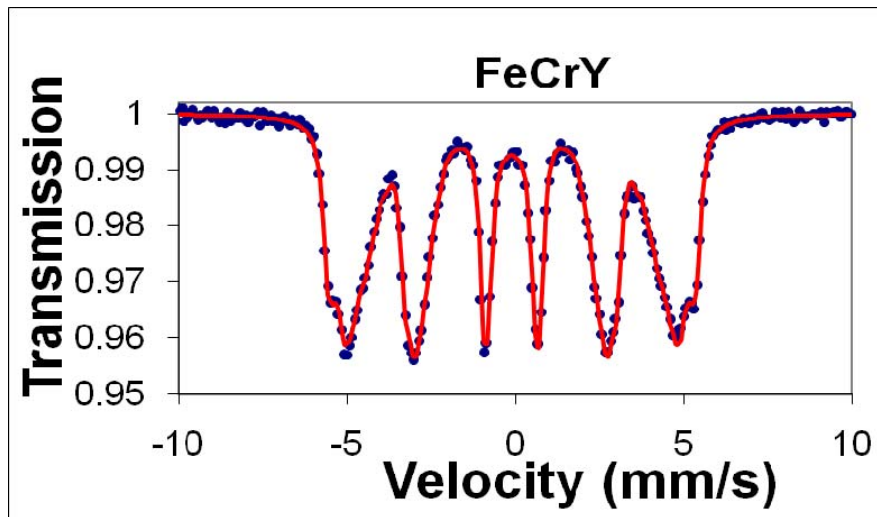


FIG-7

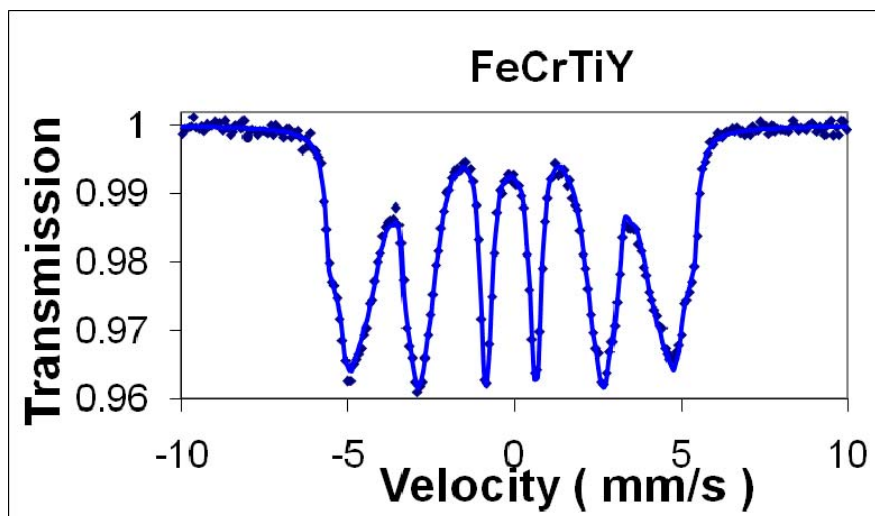


FIG-8

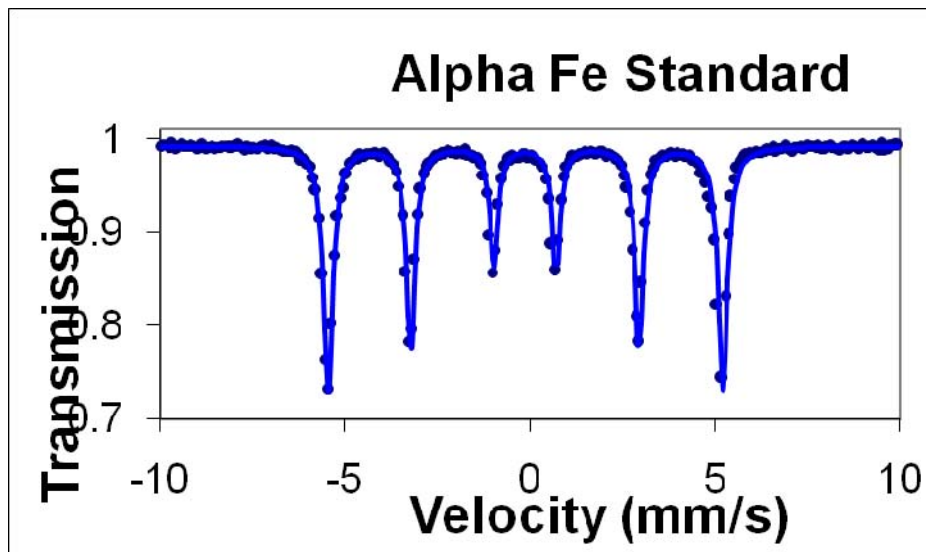


FIG-9

It is to be noticed the high similarity of the two Moessbauer spectra shown in Fig-7 and Fig-8. This is an evidence for that the crystall lattice formed by MA alloying in the two samples are perfectly similar.

The Moessbauer spectroscopy cannot detect which are the foreign atoms, others than Cr that did penetrate the crystal lattice. It can only estimate that on average, the amount of Cr in the b.c.c. solid solution Fe-Cr is about 15%

The classical TEM results

The classical TEM was used for getting images of the crystallites which are responsible for the distortion of XRD peaks discussed above. By means of dark-field imaging it was assessed that the powder particles are agglomerations of both very small crystals and much bigger ones. To illustrate this aspect we show in FIG-10 an image revealing the very small crystallites and in FIG-11 an image revealing an agglomeration made up from much larger crystallites. These images are typical for both analysed powder alloys. Images from FIG-11 are self-explanatory.

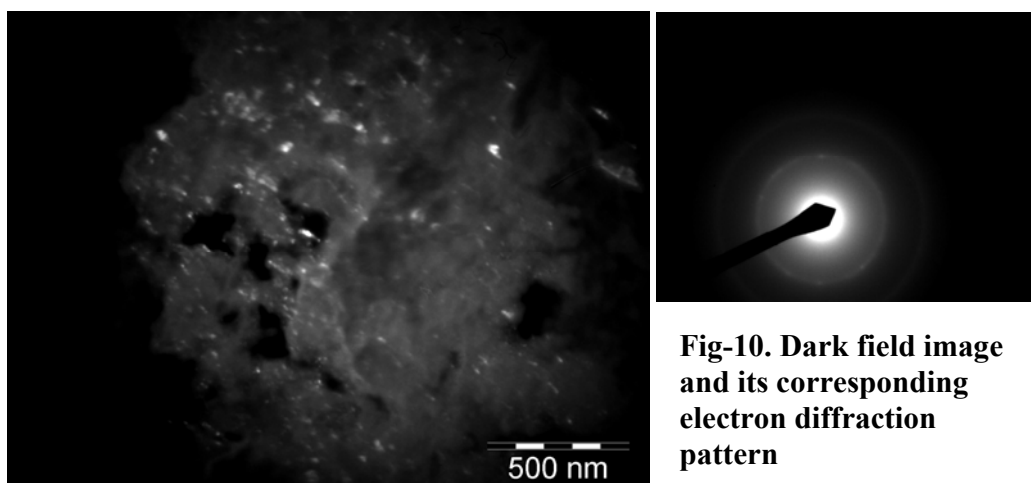


Fig-10. Dark field image and its corresponding electron diffraction pattern

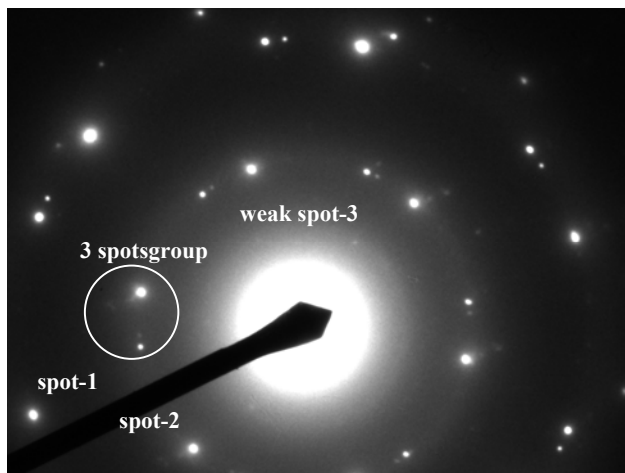


Fig-11(A)

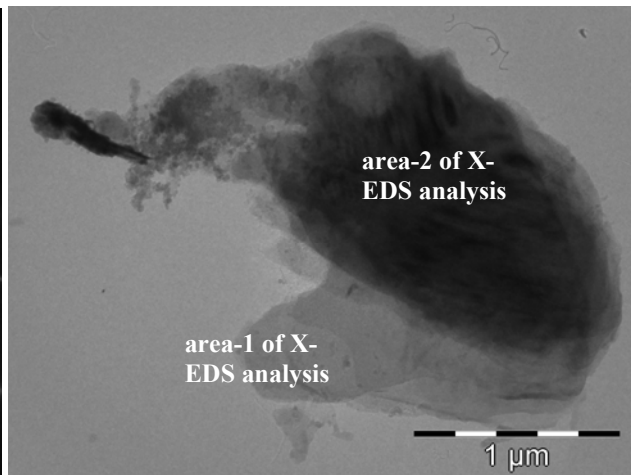


Fig-11(B)

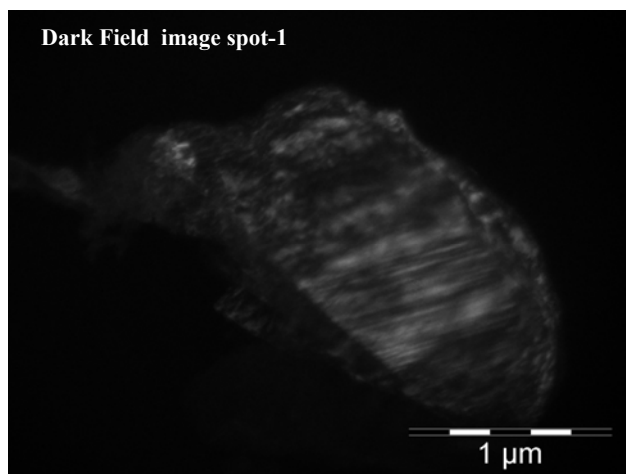


Fig-11(C)

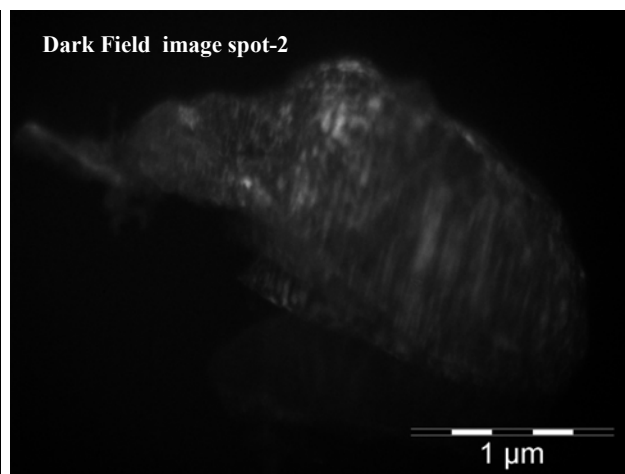


Fig-11(D)

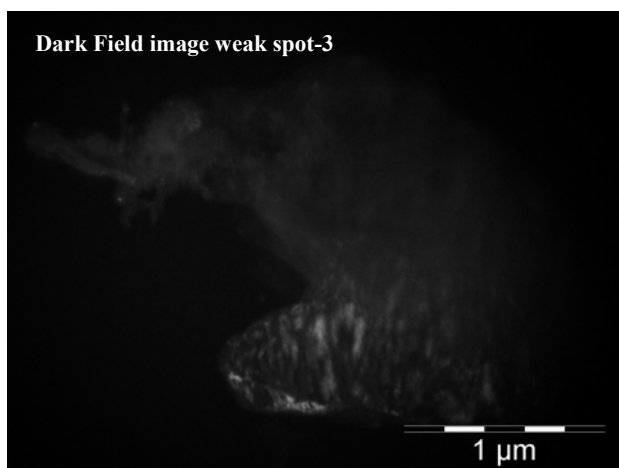


Fig-11(E)

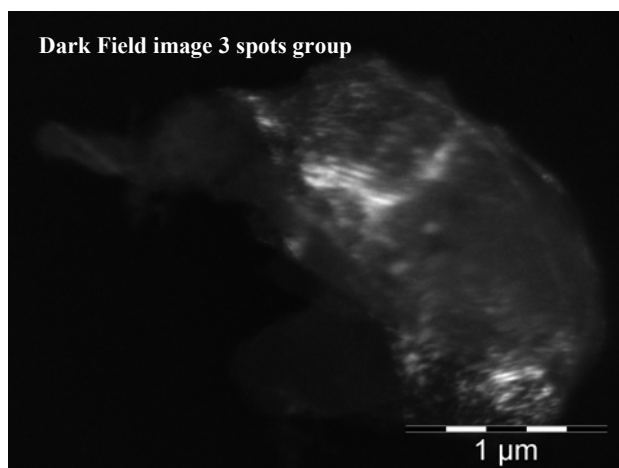


Fig-11(F)

The HRTEM results

The HRTEM technique confirms the results already obtained by means of other methods. In FIG-12 is shown a HR bright field image on which it can be measured the dimensions of the smallest particles in the powders.

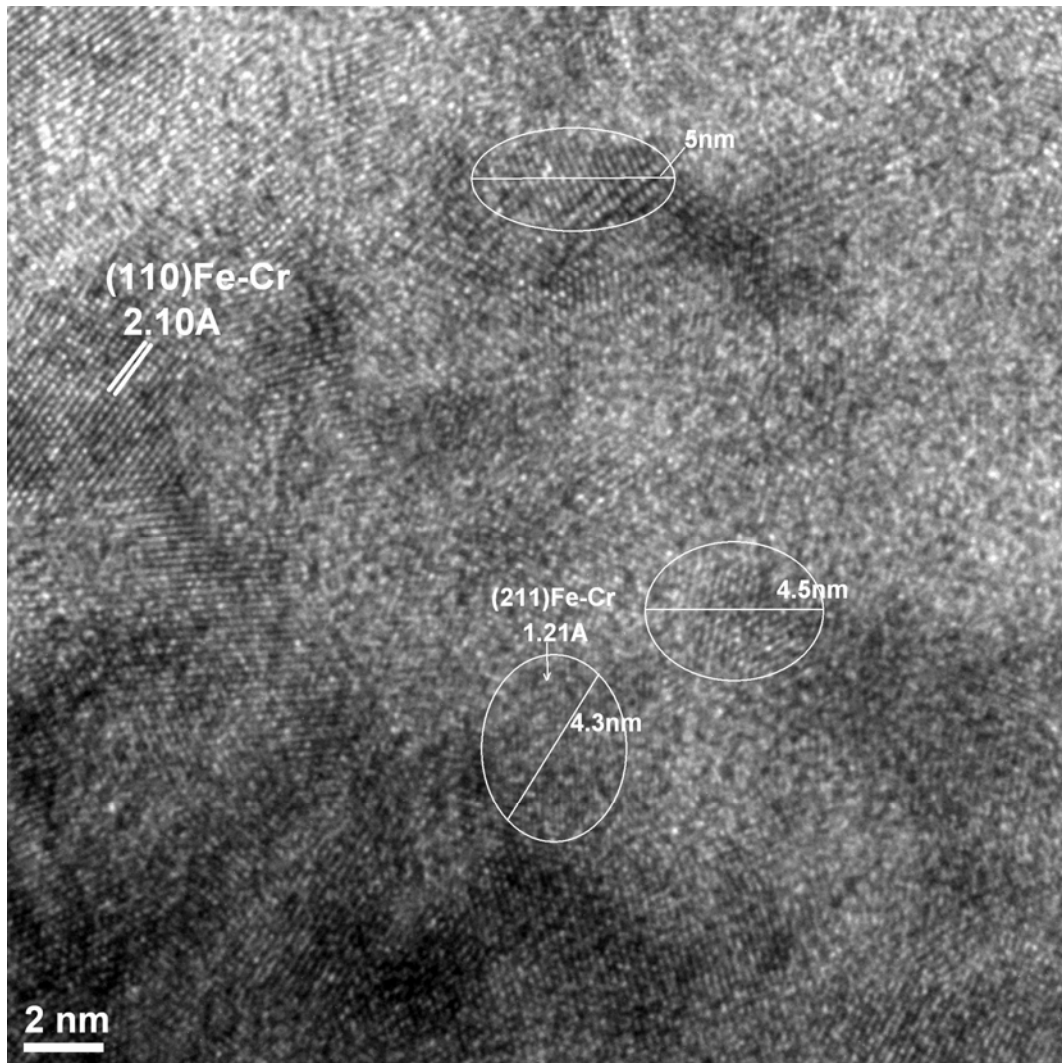


Fig-12 HRTEM image of smallest particles observed in sample-1

About the applicability of EELS method

It was made an attempt to get EELS spectra from the particles of the two samples. Because of the thickness of supporting carbon film, the spectra were of a low quality and did not allow any valuable observations. In these circumstances, it is hopeless to get energy filtered images, for which the thickness demands are even more strict than for getting EELS spectra.

We hope to be able in the future to find a method of samples preparation allowing to get EELS spectra and energy filtered images.

CONCLUSIONS

The main conclusion of our research is that there is a clear inhomogeneity of the elemental composition of the MA prepared powders aiming at a content of Fe-Cr-Y and Fe-Cr-Y-Ti.

There are impurities all over the two samples, which could affect the final material to be produced by consolidation and hot extrusion.

The crystallites composing the two samples are of a nanosize distribution, a fact that was aimed by the powders producer.

The penetration of Y in the Fe-Cr b.c.c. nano and micro-crystals is not yet uniform, which rises the problem for the powders manufacturer of modifying the parameters of MA process.

The methods we used for characterization of the two powder samples can give satisfactory results.

BIBLIOGRAPHY

- [1] M.J.Alinger et al., *J.Nucl.Mater.*, 323-333 (2004) 382-386.

Progress Report
On
Atomic Data Calculation in support of AMNS activity

EFDA Task Agreement TFL

Code:
WP10-ITM-AMNS-ACT2

WP10-ITM-AMNS-ACT3
Atomic, Molecular, Nuclear and Surface Data in ITM

1. Introduction

The aim of the project is to contribute to **atomic data calculation in support of AMNS activity and to further development and maintenance of a module for implementing AMNS data to ITM-TF codes (WP10-ITM-AMNS-ACT2, WP10-ITM-AMNS-ACT2)**.

The ITM has identified a broad need for data relating to atomic, molecular, nuclear and surface physics data (AMNS). The AMNS group has been implemented as a Task under the TF leadership to identify and report, in collaboration with the relevant ITM projects (ISIP), on the detailed ITM needs for AMNS data, to propose a strategy (software) for implementing AMNS data to ITM-TF codes.

AMNS data are needed in several of the ITM modelling projects, but especially in IMP#3 and IMP#5. A consistent approach, taking into account the specific requirements of the ITM while maintaining the work aligned with other European efforts in this area, is therefore required.

The present work refers to the calculation of atomic data for plasma spectroscopy (for ADAS). These data have to be implemented in a given standardized data format into the ITM data base. All codes in the ITM, which require atomic data, will draw it from ADAS via common mechanism. In the case of Atomic data, the ADAS database can provide virtually all the data needed by the ITM-TF.

The project aims to obtain accurate atomic data for C atoms and for Co IV ion, using the R-matrix theory and codes. These data necessary for spectral identification will be stored in a databases in order to be incorporated in the ITM –TF codes. In the first stage we studied effect of resonance phenomena on collision strengths and cross sections for electron impact excitation with C atoms and Co IV ion. respect to these objectives, our work is focused on the following main activities:

- i)* Atomic data calculation for C atoms and Co IV ions.
- ii)* To aid to data delivery, a common software interface for the ITM codes will be suggested. This proposal makes use of the existing: ITM Gateway facilities for data storage, Relational databases, MDSplus, HDF5, ADAS, and ITM UAL.

2. Summary of Results

One objective has been envisaged for the period January-June 2010: To investigate the effect of two-particle one hole resonances on cross sections and collision strength for specific target ions.

1. Single and two-particle-one-hole resonance structure in the low energy inelastic scattering of electrons by atomic systems

Two independent calculations have been carried out for **C atoms**:

- a) In the first calculation, 28 target states have been included in the R-matrix extension. These are all 22 states with configurations $1s^22s^22p^2$, $1s^22s^22p3l$ ($l=0,1,2$), $1s^22s^22p4s$ and $1s^22s2p^3$ that lie below the first ionization threshold, together with the further three $1s^22s2p^3$ states that lie just above this threshold and the doubly excited $1s^22p^4$ states that lie at still higher energies.
- b) In the second calculation, an additional 20 states with configurations $1s^22s^22p4l$ ($l=1,2,3$) and $1s^22s^22p5s$ will be included in the R-matrix expansion. Hence, in the first 28-state calculation all states with $n \leq 3$ will be included in the expansion while in the second 48-state calculation all states with $n \leq 4$ will be included. The energy levels of the states lying below the ionization threshold and included in the two calculations are provided.

The aim of the calculation is to provide cross sections and collision strengths over a wide temperature range : more accurate target states will be used to obtain accurate results close to threshold. Some evidence of resonance structures at low energies have been observed.

A total of 14 different target symmetries are taken into account. Wave functions for the target states have been constructed using configuration interaction expansion involving all possible coupling for the 7 configurations listed above. The electronic orbitals are written as linear combinations of Slater orbitals whose parameters will be optimised using the atomic structure code CIV3.

In the external region FARM uses a combination of propagation techniques to propagate the R-matrix from the boundary of internal region of the R-matrix box, to a radius where a Gailitis expansion of the asymptotic wave function can be applied. An estimate can also be made of the contribution to the cross section from higher partial waves omitted from the

calculation. Finally, the cross sectiona for the $1s^2 2s^2 2p^2 \rightarrow 1s^2 2s^2 2p\ 3l$ transitions will also be shown as a series of figures.

The largest differences in cross section results have been studied for the dominant transitions of form $1s^2 2s^2 2p^2 - 1s^2 2s 2p^3$ in case of carbon.

Results of a series of calculations intended specifically to explore the role of single-particle and two-particle-one-hole (2p-1h) resonances in scattering process in the vicinity of selected thresholds of **atomic carbon** and **Co IV ion** are also. The R-matrix method is used to calculate collision strengths for low energy inelastic scattering of electrons by these atomic systems. Since the collision models applied are very closed, the differences in the resulting cross sections and collision strengths reflect the differences in the target description. Of particular interest here is the formation of 2p-1h intermediate resonant states in which the dominant configuration has two electrons in ‘excited’ orbitals leaving one electron ‘missing’ from the initial-state orbitals. The role of configuration interactions allowing for distortion of the initial- state and excited-state orbitals due to electron correlation effects is explored.

3. Scientific progress report

The new topics addressed here are to support the multidisciplinary of the proposed project through the following research areas: atomic and ionic spectroscopy of divertor and edge plasmas, study of microscopic phenomena yielding models for opacity and study of macroscopic processes yielding relevant quantities for spectroscopy. The present proposal is devoted to resonance phenomena in collisions of light atoms and ions with electrons and photons.

The difficulties in theoretical calculations of these processes come from the interference effects between the direct and the indirect processes. One approximation widely used to treat these phenomena is distorted wave approximation (DWA) (Griffin et al. 1987, Chen et al.1990). Following this approximation the intermediate resonance state is independent of its decay. A second approximation (Burke et al 1983) uses the R-matrix method to evaluate excitation cross section to the autoionizing states. In this case the interference effects with the direct process are neglected. The R-matrix method with one suitably chosen pseudo-state to

represent continuum electrons (Berrington et al 1997, Bartschat et al 1996) accurately includes both direct and indirect processes as well as the interference effects between them.

In the present project the atomic excitation lying in the continuum part of atomic spectra is theoretically studied. Particularly, the main issue addressed here is the situation when the single-particle states are strongly coupled to more complicated configurations mainly two-particle-one-hole states giving rise to the spreading width of the resonances. These processes are difficult to study, both experimentally and theoretically, because their formation and decay are time dependent processes (Stancalie V., *Laser and Particle Beams* 2009, 27, pp 345-354, Stancalie V, *Nuclear Instruments and Methods B: Beam Interactions with Materials and Atoms* 2009, 267, pp 305-309).

The present work aims to develop two approaches that offer a partial solution to these problems. The first of these is the single-photon reaction approach. The high-lying single-particle states, in one-photon transfer reaction, manifest themselves as broad ‘resonance’-like structures superimposed on a large continuum. It has been very successful in describing atomic structure properties as well as photo-ionization and electron-impact excitation processes, especially in the near-threshold resonance regime (Stancalie V., *Physics of Plasmas* 12, 043301(2005), *Physics of Plasmas* 12, 100705(2005)). The second is the R-matrix approach for electron-scattering process. The method has been previously used to calculate atomic data and generalized oscillator strength for Li-like Al ions (Stancalie V, Burke V.M., Sureau A., *Phys. Scr* 1999, Stancalie V. *Phys. Scr* 2000, Stancalie V. et. al *Laser and Particle beams* 2006, 2007). The basic idea in the present proposal is to extend the calculation including the scattering states in the R-matrix representation which may cause that the corresponding radius becomes too large. A series of target model calculation has been initiated in order to explore the role of single- and two-particle-one-hole resonances in electron-atom collisions. Since the collision models applied are very close, the differences in the resulting cross sections or collision strengths reflect the differences in the target description. Of particular interest here is the formation of two-particle-one-hole intermediate resonant states (M.P. Scott, Burke P.G., Burke V. M. , Hibbert A., Noble C. J., Stancalie V., *ICAMDATA* 2007) in which dominant configuration has two electrons in the ‘excited’ orbitals leaving one electron ‘missing’ from the initial-state orbitals. The role of configuration interactions allowing for distortion of the initial state and excited-state orbitals due to electron correlation effects is explored. Application refers to light element atom carbon and Co IV ions in tokamak plasmas.

3.1. Collision calculation for Carbon atoms

Extensive calculations of carbon cross sections were carried out by Dunseath et al. [*J. Phys. B: At. Mol. Opt. Phys.* 1997] and Zatsarinny et al. [*Phys. Rev. A* 2005]. The first work reported results from two independent R-matrix calculations including 28 and 48 target states respectively, in the close-coupling expansion. The reported results have shown some discrepancies between theoretical and experimental excitation energies. However, the authors detected some resonance structures at lower energies. The work by Zatsarinny et al. was based on the *B*-spline R-matrix code placing more attention on the accuracy of the target wavefunctions. The differences between predicted excitation energies and cross sections reach up to a factor of 2 when comparing with the work by Dunseath et al..

In the present work we initiate an independent calculation which is of particular importance in demonstrating the presence of real two-particle-one-hole intermediate resonance in electron collision with carbon atom. In this calculation we include both single and double excitations in both the target and scattering wave functions. The process under consideration is:

$$e^- + C (1s^2 2s^2 2p^2) \rightarrow C^* (1s^2 2s^2 2p^3, 1s^2 2s 2p^4) \rightarrow C (1s^2 2s^2 2p^2, 1s^2 2s 2p^3 \text{ or } 1s^2 2p^4) + e^- \quad (1)$$

Three separate calculation have been performed: calculation (A) where the intermediate states in the equation (1) are not included; calculation (B) where intermediate states are introduced by including, explicitly, in the (N+1)-electron collision wavefunction configurations $2s^2 2p^3$ and $2s 2p^4$; and calculation (C) which extend the calculation B with additional twelve states of C derived from the configurations $1s^2 2s 2p^3$ and $1s^2 2p^4$. Finally, theoretical excitation energies and linestrengths will be provided for atomic carbon.

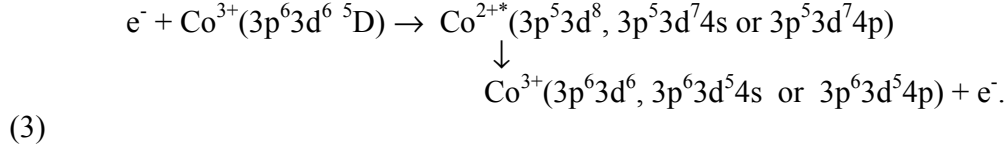
The above first two calculations for carbon atom, which do not include the $2s 2p^3$ and $2p^4$ configuration, explore the importance of including configuration interaction wavefunctions in the target-state expansion and in the (N+1)-electron quadratically integrable function expansion. In the first calculation, we represent the target states by the single $1s^2 2s^2 2p^2$ configuration and thus include only the (N+1)-electron quadratically integrable function expansion (1). In the second calculation we also include the $2s 2p^3$ and $2p^4$ configurations in the target state representation and the intermediate states in (N+1)-electron configurations in expansion (1), for completeness. The third and larger calculation will show the effect on the

collision strengths of including the 12 additional terms with the configuration $1s^2 2s 2p^3$ and $1s^2 2p^4$. To perform electron collision calculation we use the RMTXII code for the internal region and FARM for the external region. The excitation cross sections and collision strengths are provided for low electron collision energy in order to illustrate the presence of real two-particle one-hole resonance states.

3.2. Collision calculation for Co IV

The Co IV ion is isoelectronic with Fe III ion discussed by McLaughlin *et al.* (2007). Due to higher nuclear charge number the low energy spectrum is simpler. In particular, for Co IV ion, $1s^2 2s^2 2p^6 3s^2 3p^6 3d^6$ 5D ground configuration, the energies of the $3d^5 4p$ terms are lying between $3d^6$ and $3d^5 4s$ states but overlapping both. We therefore decided to carry out a first calculation (Calculation A) in which 136 LS terms of just the three configurations $3d^6$, $3d^5 4s$ and $3d^5 4p$ were included in the *R*-matrix expansion.

In order to account for the virtually excited states resulting when the colliding electron penetrates the charge distribution of the target, we have considered the following excitation ways:



The second calculation, Calculation B, retains also 136 LS terms arising from the three configurations above (Calculation A) augmented with $3p^4 3d^8$, $3p^4 3d^7 4s$ and $3p^4 3d^7 4p$ in the target state expansion and the configurations $3p^5 3d^8$, $3p^4 3d^9$, $3p^5 3d^8$, $3p^4 3d^9$, $3p^4 3d^8 4s$ and $3p^6 3d^5 4s^2$ in the $(N+1)$ -electron quadratically integrable function expansion. In order to have a consistent set of wave functions for the N and $(N+1)$ –electron wave functions, the $(N+1)$ electron configuration data have been obtaining by adding one electron to the N electron configurations in all possible ways. Hence, we can include these $(N+1)$ -electron configurations in the collision wave function by including the CI wave functions with configuration $3p^5 3d^7$ in the basis set used in the CI expansion of the N -electron target states.

These first two calculations explored the importance of including configuration interaction wave functions in the target-state expansion and in the $(N+1)$ -electron quadratically integrable function expansion (1). In figures 1 and 2 we show a plot of collision strengths against incident electron energy as obtained from the Calculation A and the Calculation B,

respectively, for the transition from the ground state $3d^6 (^5D^e)$ to the first excited state $3d^6(^3P^e)$, for the $^4F^e$ symmetry. This symmetry has been selected as it provides the largest contribution to the total collision strength for this transition. The Rydberg series of resonances converging to thresholds below approximately 3 Ryd are not strongly affected by the inclusion of the additional configurations. From parity consideration, the enhancement of the Rydberg resonance structure in the region of 3 Ryd – 4 Ryd is due to the inclusion of the $3p^53d^74p$ configuration in the expansion of the $(N+1)$ -electron collision wavefunction.

At higher energies, very distinctive resonances appear in the second calculation between 4.3 and 4.8 Ryd which are absent from the first calculation. Our analysis shows that these are real two particle-one hole physical resonances arising from the intermediate $(N+1)$ -electron states. We have separately investigated the position of $3d^54d$ and $3d^54s^2$ terms carrying out three 4-state LS-coupled R -matrix calculation by including the above three-state calculation (Calculation A) extended with the $3d^44s4p$, $3d^44s^2$, or $3d^54d$ configuration in the target state expansion and the configurations $3d^54s^2$, $3d^54p^2$, $3d^54d^2$, $3d^54s4p$, $3d^54p4d$ in the $(N+1)$ -electron quadratically integrable function expansion. It was found that the $4d$ terms are lying between $4p$ and $4s^2$ states but overlapping both.

The third and largest calculation, Calculation C, shows the effect on the collision strengths of including additional 48 levels with electronic configuration $3p^53d^7$. In this calculation the target states were represented by nine configurations $3d^6$, $3d^54s$, $3d^54p$, $3p^43d^8$, $3p^43d^74s$ and $3p^43d^74p$, $3p^53d^7$, $3d^44s^2$ and $3d^44s4p$, and correspondingly the $(N+1)$ -electron configurations $3p^63d^7$, $3p^63d^64s$, $3p^63d^64p$, $3p^63d^64s^2$, $3p^63d^54s4p$, $3p^63d^54p^2$, $3p^53d^8$, $3p^43d^9$, $3p^43d^84p$, $3p^43d^74s4p$, $3p^53d^74p$, $3p^43d^74p^2$, $3p^53d^64s^2$, $3p^53d^64s4p$ and $3p^53d^64p^2$. Configurations included in target representation corresponding to 9- state LS coupled R -matrix calculation are shown in Table 4.

Thus comparison of Calculation B with Calculation A will show the presence of any resonance structure due to intermediate Co III resonance states in equation (3), while further comparison with calculation C will illustrate the effect on such features of the inclusion of the specific target states with which these resonances are associated. In figure 3 we present graph of the collision strengths against incident electron energy for the third calculation and the same transition plotted in figures 1 and 2. This figure shows new Rydberg series of resonances associated with $3p^53d^7$ states. It is found that the inclusion of additional the 48 states associated with $3p^53d^7$ state yields to additional resonance structures while the resonance structure observed in figure 2 is moved down in energy, very slightly.

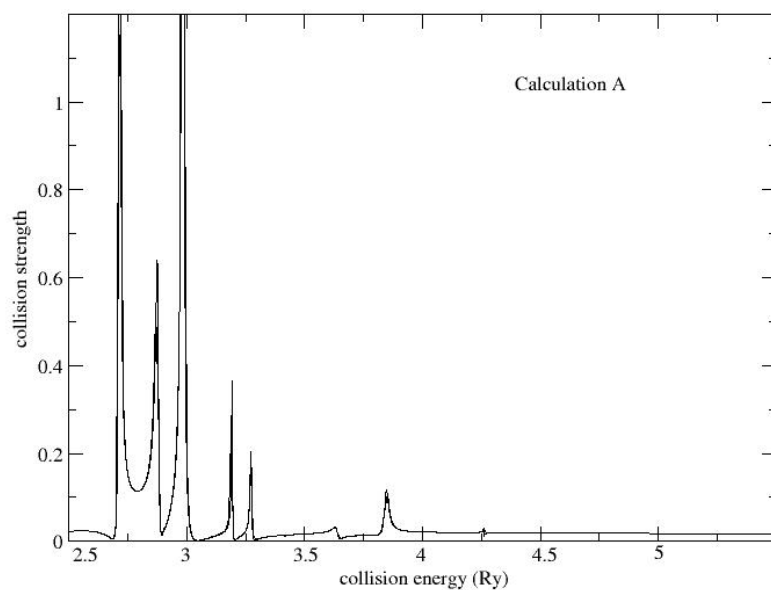


Fig. 1. Collision strength for the $^5D^e - ^3P^e$ transition of Co^{3+} . The curve corresponds to the first calculation: Calculation A. In this first calculation the only $3d^6$, $3d^54s$ and $3d^54p$ target states are included into the R -matrix expansion

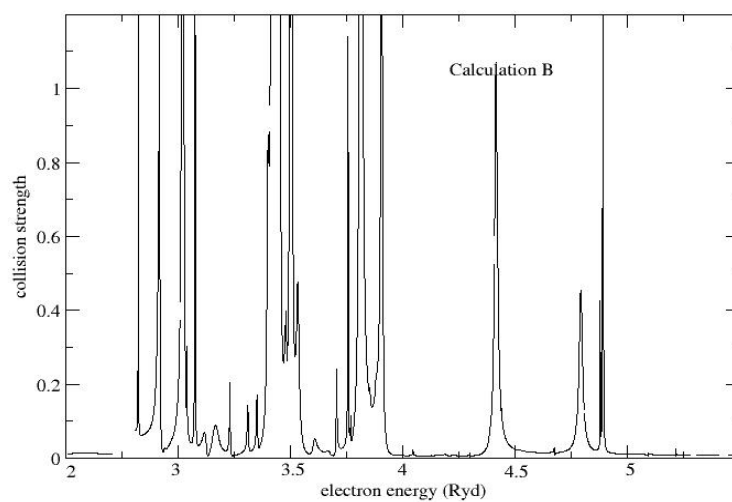


Fig. 2. Collision strength for the $^5D^e - ^3P^e$ transition of Co^{3+} . The curve corresponds to the second calculation: Calculation B. In this calculation six target state configurations $3d^6$, $3d^54s$, $3d^54p$, $3p^43d^8$, $3p^43d^74s$ and $3p^43d^74p$ are included into the R -matrix expansion.

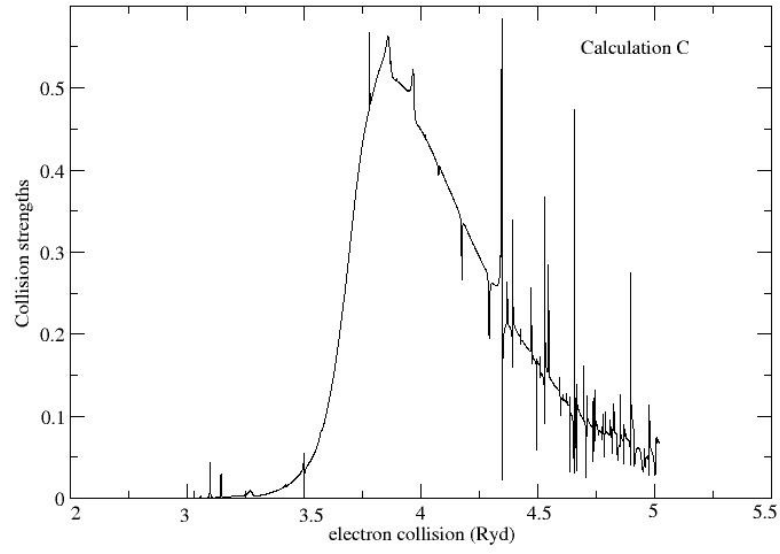


Fig. 3. Collision strength for the $5D^e - 3P^e$ transition of Co^{3+} . The curve corresponds to the third calculation: Calculation C. In this calculation nine target state configurations $3d^6$, $3d^54s$, $3d^54p$, $3p^43d^8$, $3p^43d^74s$, $3p^43d^74p$, $3p^53d^7$, $3d^44s^2$ and $3d^44s4p$ are included into the R -matrix expansion.

4. Conclusions

1. We have carried out the first detailed calculations of electron-impact excitation of forbidden transitions amongst states with $3d^6$, $3d^54s$ and $3d^54p$ configurations in Co^{3+} . We have initiated the LS-coupling calculation where the only 136 states arising from these three configurations are retained. In summary, we have performed three target model calculations: a) 3 LS-coupled R -matrix calculation including $3d^6$, $3d^54s$ and $3d^54p$ states in the N -electron wave function expansion; b) we included in the R -matrix expansion all 136 LS coupled states which arise from six target configuration $3d^6$, $3d^54s$, $3d^54p$, $3p^43d^8$, $3p^43d^74s$ and $3p^43d^74p$ looking at the effect of configuration interaction. c) 9-state LS –coupled R -matrix calculation. Starting with the 136-level model, we included in the R -matrix expansion all 184 LS coupled states which arise from nine target configuration $3d^6$, $3d^54s$, $3d^54p$, $3p^43d^8$, $3p^43d^74s$, $3p^43d^74p$, $3p^53d^7$, $3p^53d^64s$ and $3p^53d^64p$. We explored the effect of including configuration interaction wave functions both in the target states expansion and in the $(N + 1)$ -electron quadratically integrable functions expansion. The target states have been represented by elaborate configuration interactions in an attempt to account for electron correlation effects where it is essential to include the $3p^2 \rightarrow 3d^2$ core excitation in both the target and scattering wave functions. We found that this give rise to very distinctive two-particle one hole resonances at higher energies.

Finally, we mention that preliminary calculation including 272 states with a maximum 841 channels which includes the $3p^63d^54d$ configuration has been started. This large calculation requires more timing consuming with serial version of the R -matrix package program. In a future study we plan also include the states arising from the $3p^63d^54d$ configurations and to calculate collision strengths and effective collision strengths between all the states.

2. We have implemented three target model calculation intended specifically to study the effect of two particle one hole resonances on collision strengths and cross sections for electron impact excitation in carbon atoms. The high-lying single-particle states, in one-photon transfer reaction, manifest themselves as broad ‘resonance’-like structures superimposed on a large continuum. Of particular interest here is the formation of 2p-1h intermediate resonant states in which the dominant configuration has two electrons in ‘excited’ orbitals leaving one electron ‘missing’ from the initial-state orbitals. The role of configuration interactions allowing for distortion of the initial- state and excited-state orbitals due to electron correlation effects is explored.

Progress Report
On

**Prepararea standaradelor si a probelor din scuturile de carbon
ale instalatiei de fuziune JET**

Stan Sion

CONTENT

1.	Project Objectives	181
2.	Objectives of Step 1	181
3.	Summary of the performed work in Step 1	181
4.	Scientific description	182
4.1.	General description of the AMS depth profiling method at NIPNE Bucharest	Error! Bookmark not defined.
4.2.	Preparation of standard samples	Error! Bookmark not defined.
4.3.	Preparation technique	Error! Bookmark not defined.
4.4.	Experimental tests	Error! Bookmark not defined.
4.5.	Experiments for testing and calibration of the new experimental set up for depth profiling of tritium concentrations in carbon samples	Error! Bookmark not defined.
4.5.1.	Optimization experiments and results	Error! Bookmark not defined.
4.5.2.	Data evaluation method	Error! Bookmark not defined.
	CONCLUSIONS	184

1. Project Objectives

The aim of this project is to study the behaviour of materials with relevance for the construction of fusion reactors (Tokamaks). Tritium and deuterium retention and release (detritiation) will be investigated with emphases on the potential safety and environmental benefits of fusion power production. The experimental method to be used in this material research project is the most sensitive analyzing method known today, called Accelerator Mass Spectrometry (AMS). Its sensitivity is 10^{-15} for the isotope/element ratio and measures, one by one, every atom produced from the material to be analyzed. With its level of high analysing sensitivity AMS is the only experimental method capable to determine with very good efficiency the Tritium concentration.

Conventional ion beam techniques such as Rutherford backscattering (RBS), Nuclear reaction Analyses (NRA) and elastic recoil detection analyze (ERDA) can hardly measure Tritium.

AMS, due its functioning way, is able to scan the concentration of the isotope (T, D, etc) in the depth of the investigated material and deliver the depth profile of the concentration. By this measurement, of the depth profile of the implanted Tritium and Deuterium into the bulk of materials, AMS determines also the energy of the incident particles (incident energy- penetration depth relation). Therefore it can be applied as an efficient diagnose tool for the fusion experiments in Tokamaks. Diagnose and analyse are produced off-line, at the end of discharging campaigns in the Tokamak. Small cuts (10 x 10 x 4 mm) from the plasma facing components (PFC) are enough for an AMS analyse. It was proven that AMS suitable addresses material research topics declared as crucial issues by the European Development Agreement (EFDA) like: "Analyzes of selected plasma components (PFC) , material samples to support transport studies and in situ detritiation activities" and " Development of in-situ diagnostic for the characterisation of deposited layers and/or coatings.

These kind of experimental material research are today of an imperative need since the construction of the first test fusion reactor ITER was started 2009 at Cadarache in the south of France. The reactor is expected to start operating in 2018 and many issues of research are still open in material behavior at high plasma temperatures and exposed to intense fluxes of ionized particles.

The general project objectives are as follows:

- Selection and preparation of samples from the divertor tiles of JET.
- Preparation of standards (adequate for the samples from JET).
- AMS analyzing experiments to determine the Tritium concentration Depth Profiling in divertor tiles from JET
- Complete distribution of Tritium retention in the divertor tiles from JET
- Data interpretation and conclusions.

2. Objectives of Step 1

The objectives of actual stage are:

- Selection and preparation of samples from the divertor tiles of JET.
- Preparation of standards (adequate for the samples from JET).

3. Summary of the performed work in Step 1

AMS sample were cutted from the divertor tiles from. Samples from capganes from 1998 to 2007 were prepared for measurement by AMS. AMS will perform in the present research a depth profiling (DP) of the Tritium concentration of in carbon samples from JET divertor. The depth scanning is done by sputtering with accelerated ^{133}Cs ions on the sample surface at its location in the ion source. Measuring continuously the produced rare ions of Tritium one will register in the detector different beam currents according to the concentration at the depth of scattering.

Following samples were prepared for the AMS analyses:

3 samples **2IW G1 A** from the 2004 -2007 discharges champagne: no.2, 5, 10

1 sample **2IW G3 A** from the 2004 -2007 discharges champagne: no.8

2 samples **2BN G6 D** from the 1998-2007 discharges champagne: no.1, 4

3 samples **2ON G7 A** from the 2004 -2007 discharges champagne: no.1, 5, 8

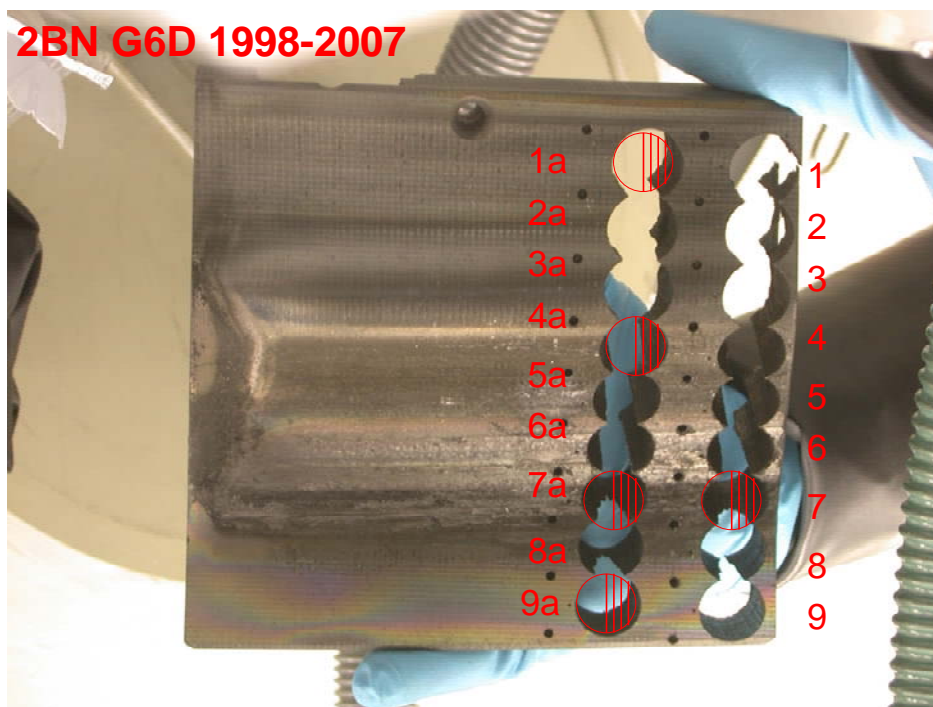
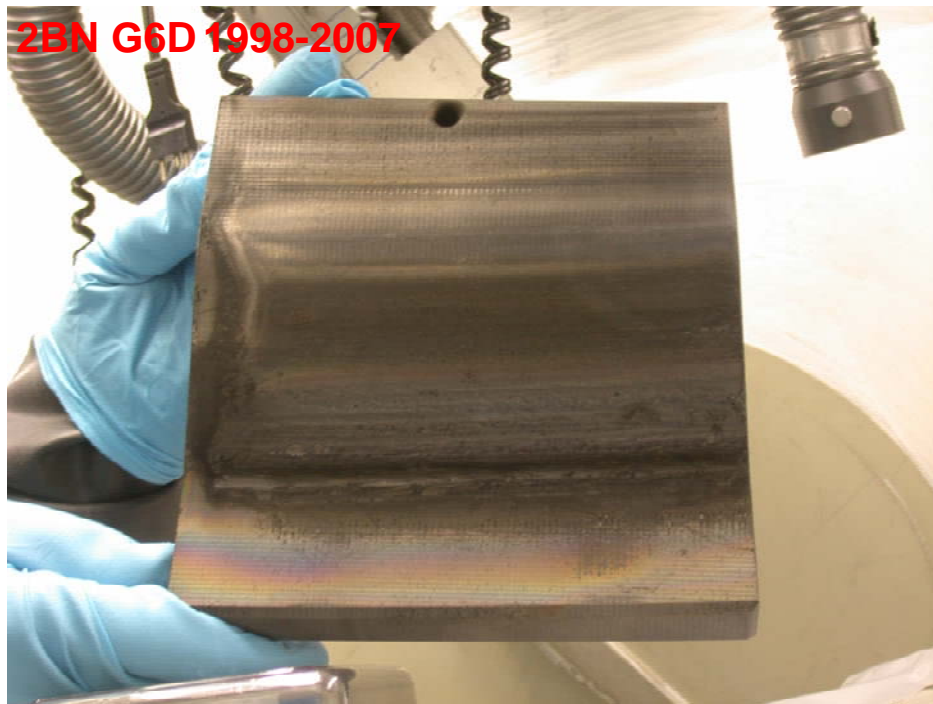
4 samples **2ON G8 A** from the 1998-2007 discharges champagne: no.2, 6,8,11

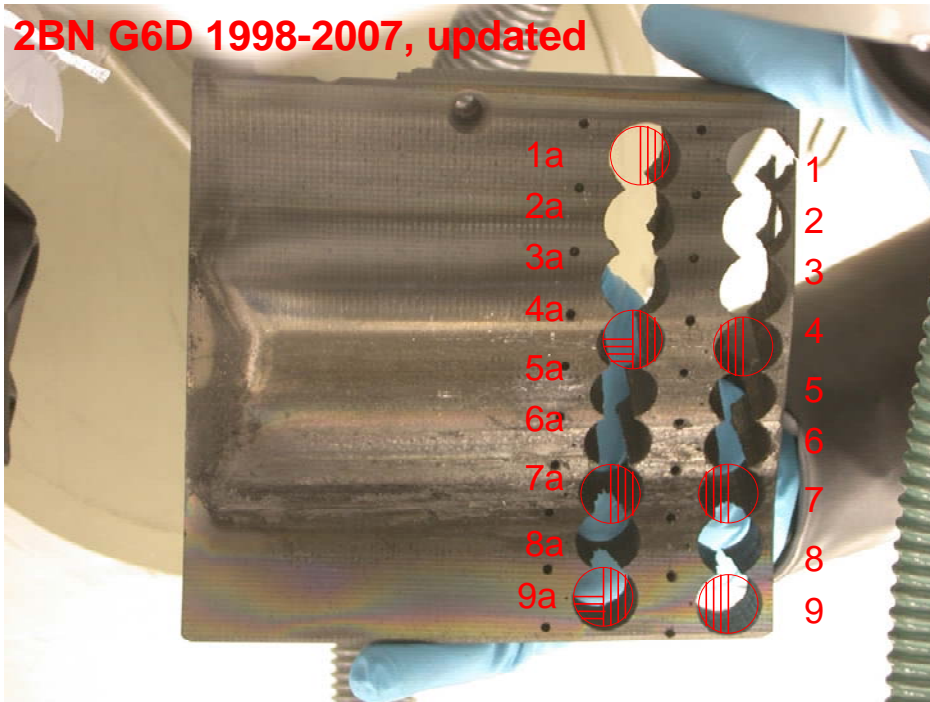
Standard samples were prepared in accordance with the concentration to be measured. To standards were prepared with the T/C ratio of 3,3 E-9 and 1,3 E-9 with an error of 6% each. The calculated errors contain the statistical error of counting (1%) and detection efficiency (3%), the error of the AIEA standard (3%), the error of weighting of standard solution (1%) and binding agent (2%) and the error of the amount of carbon in its composition (2%). The β^- activity of the 8.9×10^{-9} standard sample is less than 4Bq/cm².

4. Scientific description

AMS is a new, ultra-high sensitive and very complex atomic analyzing method. It was described in detail in the previous report. First, the samples for the AMS analyses have to be in solid state. This condition is required by ion source of the AMS facility that uses the sputtering process, by colliding accelerated ^{133}Cs ions on the target material to obtain the beam ions necessary for the AMS analyses. The samples are loaded in the ion source and then are collided by a ^{133}Cs accelerated ion beam, producing sputtered ions. The sputtered beam area on the target is about 2 mm². From all the scattered ions only the negative ions will be electrostatically extracted from the ion source.

The samples were cut from the diver tiles of JET. In Foto 1 are shown such cuts.





CONCLUSIONS

This report presents the scientific work performed for the first TASK of the project entitled: Tritium depth profile measurements of JET divertor tiles.

The performed tasks were the preparation of standard samples and preparation of samples from the divertor tiles of JET. Both tasks were fully accomplished. A two-piece set of standard samples for measuring T concentration depth profiling were chemical prepared, calibrated and tested experimentally. The entire AMS system is now ready to start in the next step the measuring the T concentration in protection tiles from JET.

PROGRESS REPORT 30.06.2010

Programul: CAPACITATI					Formular B	
Modul: Modulul III, Aria tematica PC7-EURATOM-Fuziune						
Titlul complet al Proiectului: ELECTRICAL, MAGNETIC AND MECHANICAL CHARACTERISATION OF RE 123 SUPERCONDUCTING CABLES AND TAPES (CARACTERIZAREA ELECTRICA, MAGNETICA SI MECANICA A BENZILOR SUPRACONDUCTOARE DE RE123)						
Document e suport	EFDA Task Agreement	Code: BS_SC	Notificati on	Code:		
	EFDA JET Task Agreement	Code:	JET Notificati on	Code:	JET Order 6.3 (OEP)	Code:

1. Introduction

The discovery of high temperature superconductivity (HTS) opened new perspectives in the area of high field magnets for fusion reactors. Moreover, the intrinsic characteristics of several HTS compounds, such as $\text{REBa}_2\text{Cu}_3\text{O}_7$ ($\text{RE} = \text{Y, Nd, Gd}$), are superior to Nb_3Sn . For example, the upper critical field, B_{C2} , of Nb_3Sn at 4.2 K is 23 T, while the upper critical field, B_{C2} , of YBCO at 77 K is greater than 35 T. Another advantage of using RE123 instead of NbTi or Nb_3Sn is the reduced refrigeration cost. Thus, by increasing the operating temperature from 4 K to 77 K the refrigeration costs are reduced by a factor of 10^4 .

During the last decade great progress has been registered in the field of YBCO based coated conductors fabrication. Thus, using the RABiTS technology, a long superconducting tapes up-to 10^3 m with a critical current greater than $1\text{MA}/\text{cm}^2$ at 77 K and zero magnetic are now available on the market. In order to applied the $\text{REBa}_2\text{Cu}_3\text{O}_7$ (RE123) superconducting tapes in the field of fusion reactor a fully characterization of the HTS superconducting conductors is necessary. This report presents the structural, morphological and electrical characterization of three superconducting coated conductors architectures: YBCO/ CeO_2 / NiO / Ni-V , YBCO/ CeO_2 / Ni-W and YBCO/ CeO_2 / YSZ / CeO_2 / Pd / Ni-W

2.Results

2.1 YBCO/ CeO_2 / NiO / Ni-V

Details about the surface oxidation epitaxy of the Ni-V substrate have been presented elsewhere [1]. The out-of-plane crystallographic alignment of the epitaxial YBCO/ CeO_2 / NiO / Ni-V structure, as determined by XRD ω -scans through the (002)Ni-V, (002)NiO, (002) CeO_2 and (005)YBCO peaks, is shown in Fig.1. The FWHM (Full Width Half Maximum) are 6° , 7° , 5.5° , and 8° , respectively. The in-plane alignment determined by the (113)YBCO, (111) CeO_2 , (111)NiO and (111)Ni-V pole figures revealed the presence of a (001)[100] cube texture for the Ni-V substrate. The epitaxial relationship of

YBCO/CeO₂/NiO/Ni-V multilayer structure is [100]YBCO//[110]CeO₂/[110]NiO/[100]Ni-W. The highest value obtained for the critical current density at 77K and zero magnetic field was 5.4×10^5 A/cm². This value is lower than that observed for YBCO epitaxially grown on (100) SrTiO₃. The J_c depression is probably correlated with the existence of poor coalescence zones close to the substrate grain boundaries. On the other hand, the presence of a-axis oriented grains, revealed by X-ray, causes high-angle grain boundaries which deteriorate the transport properties of the film. A magnetic field dependence of J_c at T=77K and 65K is shown in Fig. 2. The magnetic field, B, was applied parallel to the c-axis.

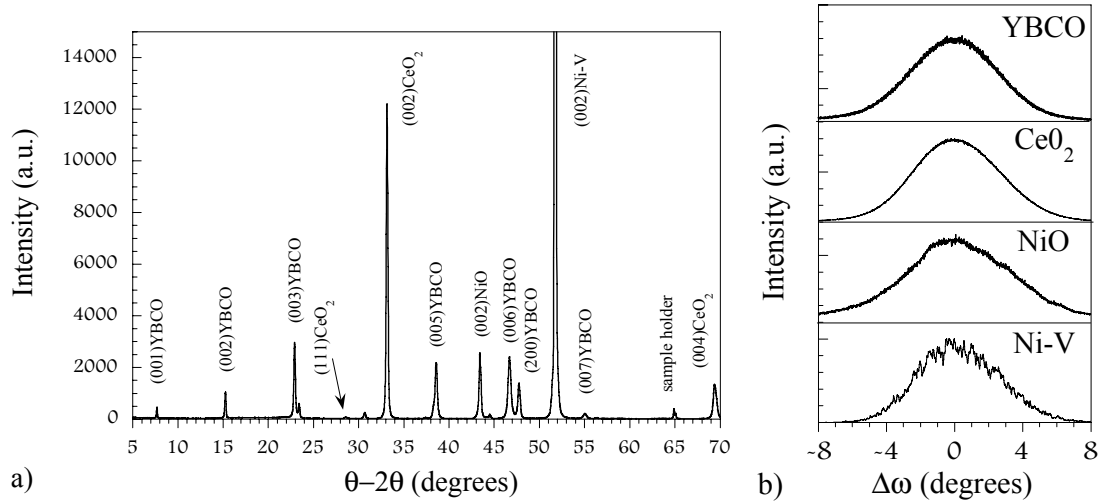


Figure1. (a) The X-ray diffraction θ - 2θ pattern of the YBCO/CeO₂/NiO/Ni-V architecture. (b) The ω -scans through the (002)Ni-V, (002)NiO, (002)CeO₂ and (005)YBCO peaks.

These measurements concern a sample with a $T_{cR=0}=87$ K. For comparison the same J_c vs B measurements for a 1 μ m thick YBCO film grown on (001) SrTiO₃ (STO) is also presented. The magnetic field behaviour of the J_c is very similar for both the YBCO film on cube textured Ni-V substrate and the YBCO film on (100) SrTiO₃. The existence of the plateau in the J_c vs B curve in the strong magnetic field (up to 12T) region demonstrates good in-plane and out-of-plane orientations of the YBCO film deposited on the Ni-V substrate. The weak-link behaviour in the limit of low field is more emphasized for the film on Ni-V with respect to the film grown on STO, indicating a greater fraction of weak-linked grains in the YBCO film deposited on Ni-V.

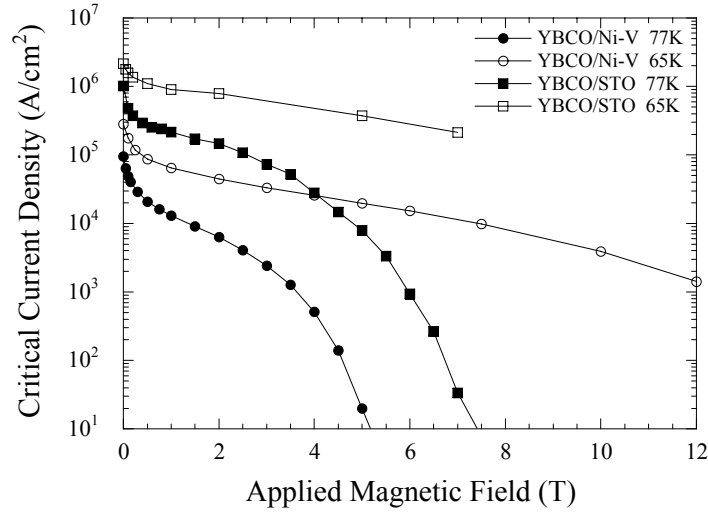


Figure 2. DC critical current density versus magnetic field measurements at $T=77K$ and $65K$ for the YBCO film on $CeO_2/NiO/Ni-V$ and for a YBCO film grown on $(100) SrTiO_3$.

2.2. YBCO/ CeO_2 /Ni-W ,

The θ - 2θ scan of the YBCO/ CeO_2 /Ni-W multilayer structure shows that both CeO_2 and YBCO layers exhibit a good c -axis orientation. Nevertheless, the presence of YBCO($h00$) peaks in the XRD spectra indicates that a small fraction of the grains are a -axis oriented. The ω -scans reveal a sharp out-of-plane texture with the FWHM of 5.8° , 5.5° and 5.6° for the (005)YBCO, (200) CeO_2 and

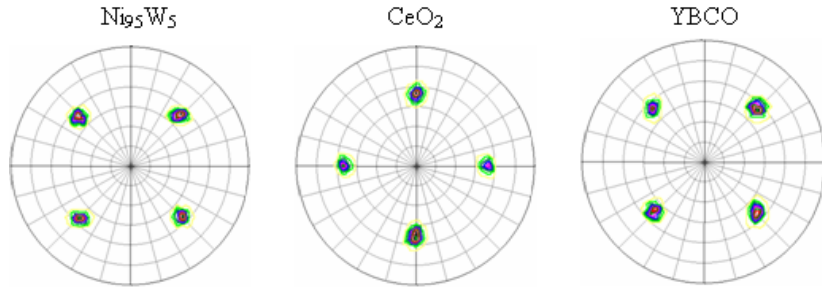


Figure 3. The Ni-W(111), CeO_2 (111) and YBCO(113) pole figure.

(200)Ni-W peaks, respectively. The FWHM values are very close, indicating a high degree of epitaxy for both CeO_2 and YBCO films. As shown in figure 3, the Ni-W(111), CeO_2 (111) and YBCO(113) pole figures demonstrate that the CeO_2 and YBCO layers are epitaxially grown with a single orientation. The epitaxial relationship of the YBCO/ CeO_2 /Ni-W multilayer structure is $[100]YBCO//[110]CeO_2//[100]Ni-W$. The ϕ -scans reveal an in-plane texture with the FWHM of 6.6° , 7.2° and 7° for (113)YBCO, (111) CeO_2 and (111)Ni-W, respectively.

The zero resistance critical temperature for the YBCO films is $\approx 88 K$ and the transition width is of about 1 K. The films exhibit a linear behaviour of the normal state resistance with the $R(300)/R(100)$ ratio of about 2.6, which suggests a high c -axis oriented film. The magnetic field dependence at 77K of the transport critical current density, J_c , for two YBCO films, 0.1 and 0.3 μm thick, grown epitaxially on single crystal substrate and

CeO₂/Ni-W template, respectively, is shown in figure 4. The highest J_c obtained so far is $\approx 1.2 \times 10^6$ A/cm². It should be noted that, up to 1 μ m thick films, no degradation of the J_c with film thickness was observed.

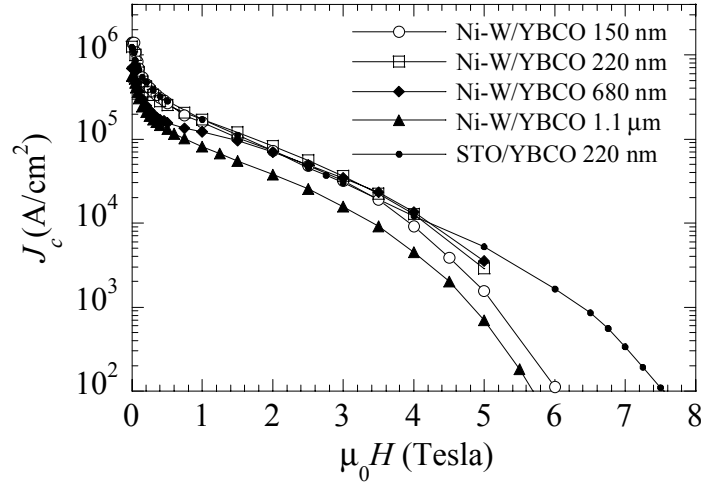


Figure 4. Critical current density vs. magnetic field for the YBCO film on CeO₂/Ni-W and on (100) SrTiO₃.

2.3. YBCO/CeO₂/YSZ/CeO₂/Pd/Ni-W

The details on the deposition and properties of the Pd seed layer are presented elsewhere [2]. Summarizing, the X-ray spectra have revealed that the Pd films are epitaxially grown at temperatures above 200 °C, with the relative intensities ratio $I(002)/(I(111)+I(002))$ ranging from 99.8% to 100%. Above 450 °C, a peak broadening in the high angle tail of the (002)Pd reflection is observable. This feature is related to the Pd-Ni interdiffusion. A sharpening up to about 60% with respect to the Ni-W substrate is reached at higher deposition temperatures. The φ -scans analyses on the (111)Pd and (111)Ni peaks reveal that the improvement of the Ni in-plane alignment induced by Pd is limited at about 18-20%.

Table 1.

Layer	Peak	FWHM
Ni-W	(002)	7.5°
Pd	(002)	2.7°
YSZ	(002)	3.5°
CeO ₂	(002)	3.1°
YBCO	(005)	2.7°

YBCO films and the standard CeO₂/YSZ/CeO₂ buffer layer structure have been grown on a Pd-buffered Ni-W by PLD [2]. The ω -scans in TD, are reported in table 2 for (005) YBCO, (002) CeO₂, (002) YSZ and (002) Ni-W. In table 2 the (002) ω -scans for the as deposited Pd film are also reported. As can be seen the FWHM drops from 7.5° of Ni-W to 2.7° of Pd, keeps constant through the oxide buffer layer structure and reaches a value of 2.7° in YBCO. Pole figures analyses reveal a single in-plane orientation with the epitaxy relationship [100]YBCO||[110]CeO₂||[110]YSZ||[100]Pd||[100]Ni-W. The FWHM values of the φ -scans for the (113)YBCO peak are of about 6°. Morphological analyses reveal that the YBCO films show a smooth and free of cracks surface, together with a good coalescence among the YBCO

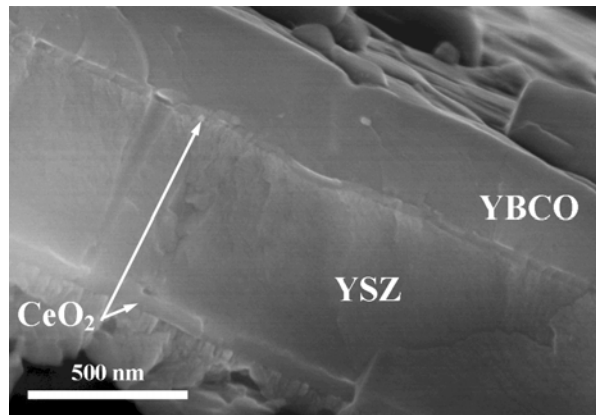


Figure 5. SEM cross-section of the YBCO film on CeO₂/YSZ/CeO₂ deposited on Pd-buffered Ni-W.

grains. Cross section analysis of fractured samples, figure 5, show that the whole buffer layer architecture and the YBCO film are dense and compact and the interface between each layer is clean and well defined. These results are remarkable, taking into account that, at YBCO deposition temperature, the interdiffusion between Pd and Ni-W is complete.

The zero resistance critical temperature for the YBCO film deposited on CeO₂/YSZ/CeO₂/Pd/Ni-W is about 88.5 K and the transition width is about 2 K. J_C measurements were performed on 2 mm wide as-deposited strip at 77 K and zero magnetic field. The J_C values obtained for some samples are listed on table 3, for YBCO films of two different thicknesses. J_C up to 2.1 MA/cm² is obtained for the 100 nm thick sample. As expected, the sharpening of the orientation distribution results in an improvement of the J_C value.

Table 3.

YBCO thickn ess (nm)	Pd (002) □- scan FWH M (°)	YBCO (005)□- scan FWHM (°)	YBCO (113) □- scan FWH M (°)	J_C (MA/c m ²)
280	8	6.3	6.7	0.75
280	3	3.2	6	1.35
100	3	3.1	6.1	2.1

3.References

- [1] T. Petrisor, V. Boffa, G. Celentano, L. Ciontea, F. Fabbri, V. Galuzzi, U. Gambardelle, A. Mancini, A. Ruffoloni, E. Varesi, "Epitaxial oxidation of Ni-V biaxially textured tapes", *Physica C* 377 (2002) 135-145
- [2] G. Celentano, V. Galluzzi1, A. Mancini1, A. Ruffoloni1, A. Vannozzi1, A. Augieri1, T. Petrisor, L. Ciontea, and U. Gambardella, , *Journal of Physics: Conference Series* **43** (2006) 158–161.

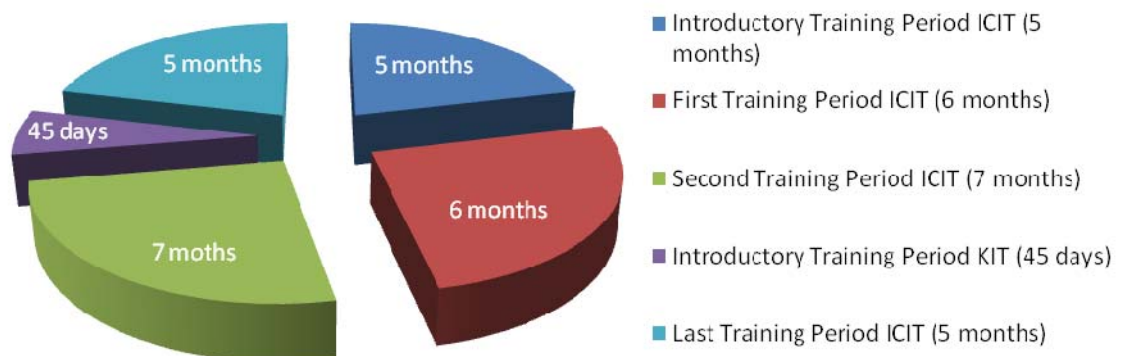
4. Published papers

- [1] Vannozzi, A., Thalmaier, Gy., Armenio, A. Angrisani, Augieri, A., Galluzzi, V., Mancini, A., Rufoloni, A., Petrisor, T., Celentano, G. *Development and characterization of cube-textured Ni-Cu-Co substrates for YBCO-coated conductors*, **Acta Materialia** **58(3)** pp 910-918 (2010)
- [2] Galluzzi, V., Augieri, A., Petrisor, T., Ciontea, L., Celentano, G., Mancini, A., Vannozzi, A., Angrisani, A.A., Rufoloni, A. *Deposition and characterization of YBCO films with BZO inclusions on single crystal substrate*, **Physica C** In Press, ISSN 09214534, (2010)

Periodic Report of MEdC/ICIT Trainee in Training Network
“Tritium Technologies for the Fusion Fuel Cycle”
- Annual Report 2010 -

MEdC/ICIT Trainee in TRI-TOFFY network - Work package No. 5, Experimental Pilot Plant for Tritium and Deuterium Separation, such planned:

Training Period Planned



- Introductory/accompanying training at ICIT
(duration: 5 months in total)

This scheduled objective has been already achieved in accordance with the Individual Development Plan and communicated into the last report to MEdC/EUROATOM

- Introductory/accompanying training at KIT
(duration: 45 days in total)

This scheduled objective has been already achieved in accordance with the Individual Development Plan.

- Research training at ICIT
(duration: 17 months)

This scheduled objective has been partial achieved in accordance with the Individual Development Plan and in the last report 6 months of first training period in ICIT have been communicated. In this report the second training period in ICIT of 6 months and the introductory training period at KIT of 45days will be communicated.

TOTAL: 22 months ICIT + 45 days KIT

Activity Report for Research training at ICIT and KIT

- THE ACTIVITY OF INTRODUCTORY TRAINING PERIOD AT KIT (FOR 45 DAYS)

- THE ACTIVITY OF SECOND TRAINING PERIOD AT ICIT (FOR 6 MONTHS)

1. Introduction to the existing systems at TLK

2. Experimental activities

2.1 Participation to tests of ICIT distillation packings on CD column in KIT

2.2 Involvement in test regarding determination of the minimum absorption rate in catalysts of activated charcoal

2.3 Participation to calibration tests of quadrupole mass spectrometer

3. Design activities

4. Participation to courses

5. Bibliography and references

1. Introduction to the existing systems at TLK

The introductory period at KIT had a major importance for a better understanding of the design and the functionality of WDS and ISS systems of TLK TRENTA. In this period at TLK-KIT I had also the opportunity to collect information regarding:

- the Tritium Transfer System (TTS) – controls the distribution of tritium to the experiments and other systems
- the Tritium Storage System (TLG) – stores the tritium that is not in actual use in the experiments or other systems
- the Tritium Cleaning System (CAPER) – removes impurities from gases containing hydrogen isotopes
- the Tritium Measurement Technique (TMT) – analyses the composition of gas samples
- the Isotope Separation System (ISS) – separates protium, deuterium and tritium from each other

Most of the information was about:

- CAPER (Tritium Cleaning System)

To obtain a decontamination factor of 100 million that is required for the gases exhausted from ITER, experimental work in TLK KIT has shown the need for three sequential and separate cleaning steps. According to the concept developed, first step is to separate the unconsumed deuterium and tritium in a front-end permeator. The next step is a chemical process, where tritium is removed from the impurities so that the tritium can be returned into the inner loop. The third and last step performs the final tritium decontamination of the exhaust gases. It is a newly developed process where the residual tritium attached to hydrocarbons is removed from it by isotopic exchange. All three steps are combined in the so-called CAPER process. The decontamination factor required by ITER is even exceeded by the CAPER process.

- TRENTA (Water Detritation and Cryogenic Distillation systems)

TRENTA facility has been conceived in stage approach, TRENTA 1 to TRENTA 4, in order to allow operation in quite closed loop with respect to tritium inventory and also to allow the investigation of key design and operation parameters of combined CECE (Combined Electrolytic Catalytic Exchange) used for the detritation of water and CD (Cryogenic Distillation) processes in similar conditions as envisaged for the ITER WDS-ISS.

TRENTA 4 was designed as a facility for tritium processing in closed loop within the system which consists of the combination of CECE and CD processes and the activities for completing the combination are on going at TLK (figure 1).

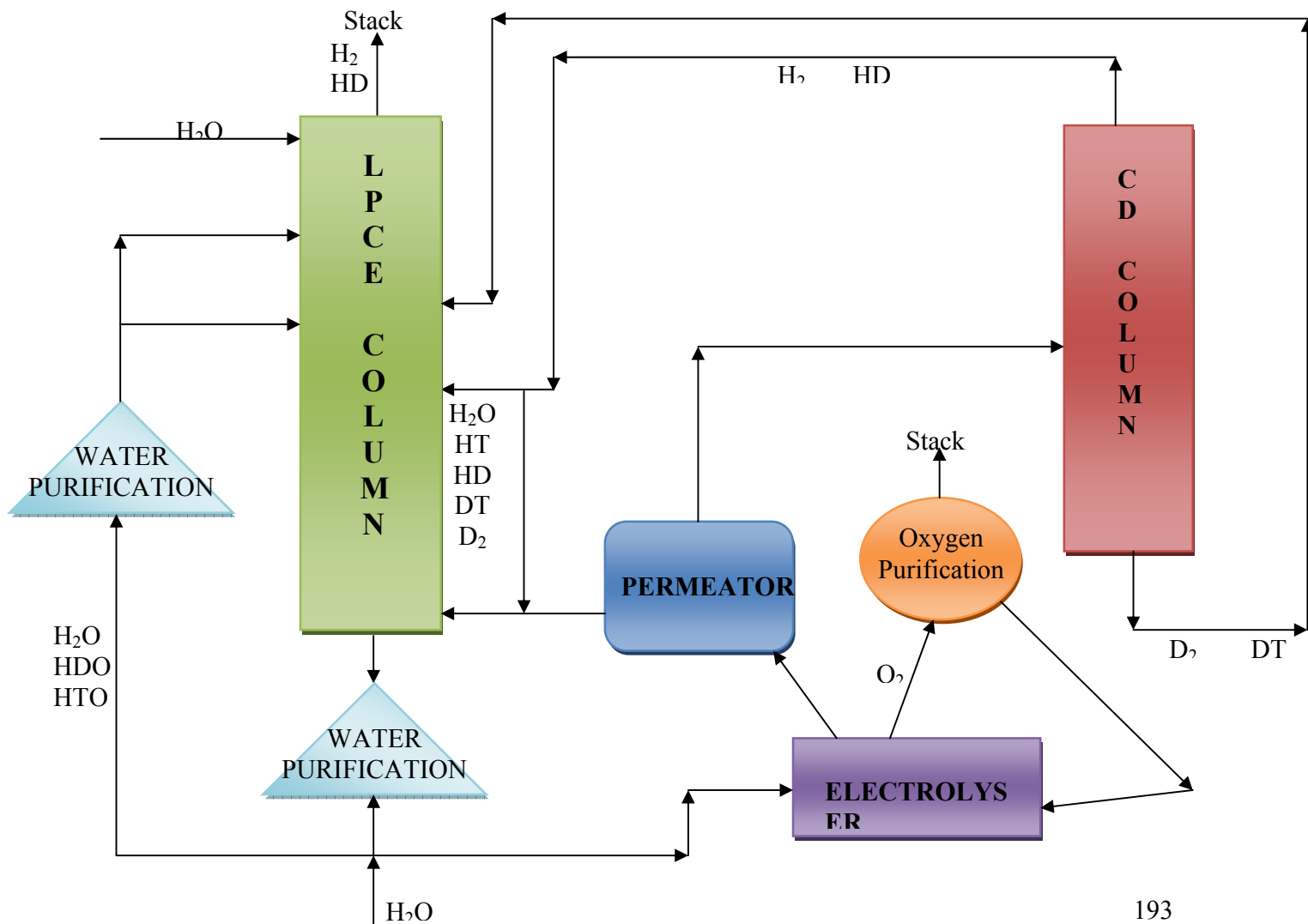


Figure1: TRENTA 4

The aim of these experiments is to obtain data for the design of the complete Water Detritation System (WDS) and Isotope Separation System (ISS) required ITER. The CECE technology is based on two solid polymer electrolyser cells with a total capacity of 2 m³/h of hydrogen production and an 8 meter long liquid phase catalytic exchange column (LPCE). First experiments with tritiated water have demonstrated the success of this concept. In parallel with the CECE process a cryogenic distillation plant has been installed. The major features of the cryodistillation system are a refrigerator with a maximum cooling power of 250 W, and a specially designed cold box.

From my study I realized that TRENTA 4 is an advance TRF (tritium removal facility), similar to the one in ICIT Ramnicu Valcea, the main difference represented by the use of CECE in detritation process of water.

2. Experimental activities

2.1 Participation to tests of ICIT distillation packings on CD column in KIT

I had the opportunity to participate to a test session regarding the ICIT packing (figure 2) on the CD column in KIT. Compared to the CD columns installed and tested at TRENTA4-pre before the CD column used for tests has a modified simpler design. In test we have determined the separation performance, expressed by the HETP (height of equivalent theoretical plate) and the liquid hold-up of the packings under total reflux conditions.

I was informed that the new column design was chosen to identify any constructional influence on the performance and the liquid hold-up on the packed sections. Therefore, the new CD column only consisted of a tube of 1200 mm length with an inner diameter of 50 mm (packable section) and two flanges for the connection to the injection unit (top) and the reboiler (bottom). No additional feeding lines, sampling lines or connections for TVO (temperature) sensors were along the column. The CD column with a total length of 1,20 m was filled with 23 packing units, resulting an effective packed length of 1,15 m. Knowing the used mixture of 30% D₂ , and 70% H₂ and also the packed volume (V_{pack}) of 0.002258 m³, the liquid hold-up of a packing (L_{pack}) (relation [1]) is expressed by the fluid load of packing (L_{fluid}) per unit of packed volume.

$$L_{pack} = L_{fluid} / V_{pack} \quad [1]$$

After subtraction of the liquid hold-up of the reboiler (L_{reb}), the liquid hold-up of the condenser (L_{con}) and the residual gas load (L_{gas}) of the CD system the fluid load (L_{fluid}) per packing could be determined, also knowing the total fluid inventory (Inv_{CD}) of the CD system(relation [2]).



Figure 2: ICIT packing

$$L_{fluid} = Inv_{CD} - (L_{reb} + L_{con} + L_{fluid}) \quad [2]$$

As final conclusion, the bottom and the top composition, at steady state, during total reflux condition, allows determining the separation performance over the packed length of the CD column. The separation performance is indicated by the HETP (height of equivalent theoretical plate) parameter. The HETP parameter is calculated (relation [3]) by dividing the length of the CD

column (l_{CD}) with the minimum number of theoretical plates for total reflux operation used to achieve the stated separation conditions (N_{min}).

$$HEPT = l_{CD} / N_{min} \quad [3]$$

Regarding the packed volume (V_{pack}) of the CD column applied with ICIT packing and the ITER reference for the liquid hold-up, a fluid load of packing (L_{fluid}) of 11,3 mol has to be achieved:

$$\begin{aligned} L_{fluid} &= Inv_{CD} - (L_{reb} + L_{con} + L_{fluid}) \\ L_{fluid} &= 11,3 \text{ mol} = 0.000290 \text{ m}^3 \text{ related to ITER reference of } 5000 \text{ mol} \cdot \text{m}^{-3} \\ L_{reb} &= 11,1 \text{ mol} = 0.000277 \text{ m}^3 \\ L_{con} &= 19,8 \text{ mol} = 0.000541 \text{ m}^3 \\ L_{gas} &= 4,2 \text{ mol} = 0.006625 \text{ m}^3 \end{aligned}$$

During this process I had the opportunity to become familiar with the operational process of the cryogenic distillation system and also gain knowledge about the calculation methods of the liquid hold-up of the packings.

2.2 Involvement in test regarding determination of the minimum absorption rate in catalysts of activated charcoal

I continued my research regarding catalyst characteristics and physical properties. After designing a 3D model of a absorption rate test bench in CATIA V5, I had the



Figure 3: Minimum Absorption Rate Determination Rig

opportunity to participate to the physical assembly of it and the tests with the activated charcoal as main probe for minimum absorption rate determination. For the experiments I've used H_2 , as gas to be absorbed at different temperature between 85 – 77 °K, into an absorbent like a activate charcoal with apparent density of 450 g/l and specific surface of 1115 m²/g. The total mass of the used charcoal was of 130 g. Knowing the mass and the apparent density I've determined the total volume of pores of the charcoal probe, comparing then with the volume of the container that holds the activated charcoal. I've made an input of three quantities (batches) of H_2 , the first had 5 bars pressure, the second had a

4 bars and the last one with a pressure of 3.5 bars. The vessel used to hold the H₂ inputs had a volume of 1400 cm³. For each input I've selected a temperature of absorption, choosing for the 5 bars input a temperature of 83.15 °K, for the 4 bars input a temperature of 78.65 °K and for the final input of 3.5 a temperature of 77 °K. I've also notice that absorption time has increased directly with the decrease of temperature. The density of H₂ has change at different input temperature in the charcoal absorber resulting a big variation in absorption time and absorbed quantity of H₂. After studying experimental database of thermodynamic proprieties of the H₂ at different pressures and temperatures I've chosen different values for each input of H₂ in the absorber. Practically I've observed that the first two H₂ inputs were totally absorbed, only the third one was partially absorbed meaning that the activated charcoal total volume and vessel volume of charcoal filling were fully occupied.

The final result concluded with different absorption levels for each input of H₂, regarding the temperature, pressure and time used for the input, the first batch giving a maximum absorption factor of 128.46 %, the second one a absorption factor of 65% and the last one with a minimum absorption rate of 47.30%. This values gave me the minimum guaranteed absorption rate of 80.25% of the activated charcoal probe.

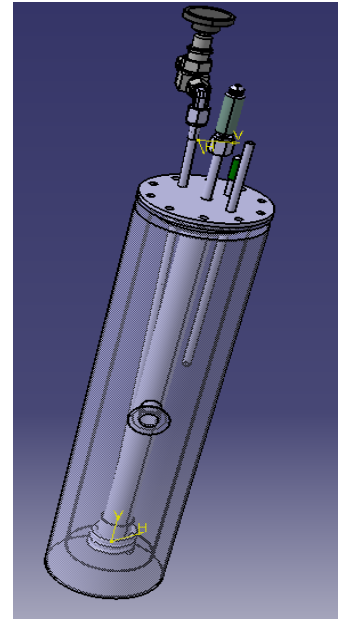


Figure 4.1: 3D model of

3. Design activities:

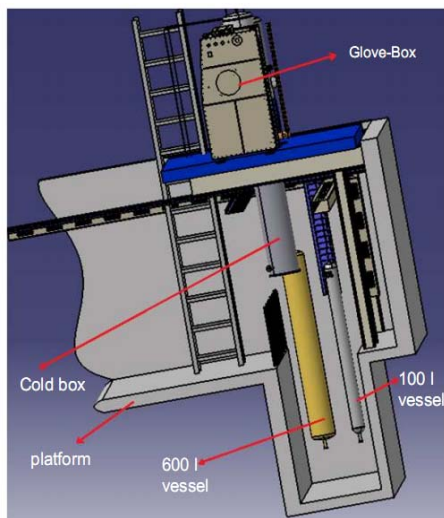


Figure 4: Isometric model of CD

Using again CATIA, I designed a 3D model of a caisson (figure 5) having as dimensional references a isometric model of the CD column platform were the caisson will be installed.

The main tasks, was to provide new safety designs for the caisson of the cryogenic distillation system, part of the TRF of KIT Karlsruhe. This construction of the caisson was proposed at KIT-TLK according to the required safety standards in cryogenic facilities in order to have a final barrier for tritium leaks from the vessel part of the TRF facility (0.6 m³ and 0.1 m³ ones). I've used the isometric model of the

CD Column platform (figure 4) for the

construction of the caisson (for height, length), and also real measurements in the location of construction.

According to "Technical Terms of Delivery and Acceptance of Glove Boxes and Similar Boxes for the Karlsruhe Tritium Laboratory" TLA No. 02 / 2009 this is a second shell, a component enclosing the first shell. Some of the construction requirements for the caisson were:

- The design solution should fulfill the nuclear safety regulation (after TLA No. 02/2007 – Technical Terms of

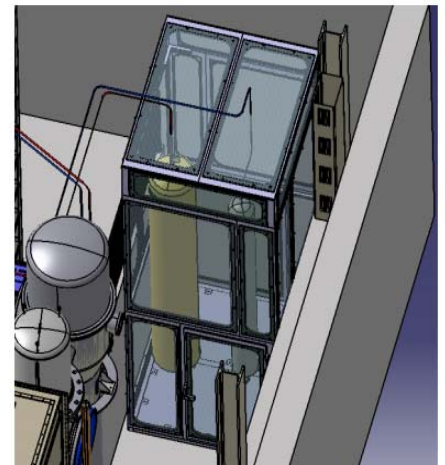


Figure 4: 3D model of proposed

Delivery and Acceptance of Glove Boxes and Similar Boxes for TLK);

- To have an easy access from the top of the vessel and also access to the connection parts of vessels;

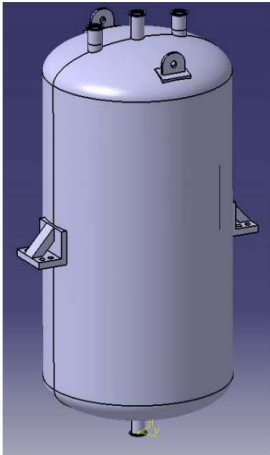


Figure 6: 3D model of the vessel

- To have enough free space for the installation of another 0.3 m^3 vessel;

To have low manufacture cost and to be easy to assemble;

For undesired leakages of tritium from installation at KIT-TLK, according to the required safety standards in cryogenic facilities a specified vessel of 0.3 m^3 volume for the secondary purge system was needed to be constructed also in the caisson with the other two vessels. I have made using CATIA V5, a 3D model of the vessel (figure 6) after a preliminary calculation of the vessel components.

The concept requirements were:

- To be done according to the required safety standards (ASME standards);

- Try to have a efficient construction solution for best quality, price and nuclear safety;

- Need of easy a positioning support that fits the caissons available space;

- To have the required volume of 0.3 m^3 ;

- Have the possibility to manufacture from standard market components (fittings(TU40K70-316), plates, end caps (DIN28011), etc.);

The conceptual design of the vessel was done according the german directive Vessel Directive 97/23/EG (according TÜV) standards:

- the material applied shall be austenitic steel with a material inspection certificate according to DIN 10204

- connections shall be made using standard flanges, preferably sealed with metals (VCR, no copper seal) or elastomers (CF, CF with Viton or Vespel) having a leak tightness of $=10^{-5} \text{ mbar} \cdot \text{l/s}$. Other important aspects considered:

- calculation of the needed volume;

- evaluation of the available space in the caissons including the other existing two vessels;

- estimation of positioning of the vessel in the available space;

- a market search for standard construction materials (fittings, end caps, etc);

- a standard calculation of size, tolerance measurements, volume, wall thickness and weld finishing of the vessel.

4. Participation to courses:

- “Membranes for Fusion Fuel” Course:

- Introduction to membranes and membrane reactors

- Introduction to the Pd/H system

- Pd-based membranes synthesis and characterization

- Modelling of Pd membrane reactors

- Process applications of Pd membrane reactors

- Pd-based membrane reactors applications at the European laboratories

- Advance CATIA course (4 days) consisting in:

- Equipment Arrangement;

- Piping Design;
- Piping Setup - ISOGEN

5. Bibliography and references

1. Romulus George Ana, Ion Cristescu, Lothar Dörr, Robert Michling, Stefan Welte, Werner Wurster – “Design and experimental activities in view of Water Detritiation–Isotopic Separation Systems combination in TRENTA facility”, Fusion Engineering and Design, 2009
2. Robert Michling – “Modification, Enhancement and Operation of a Water Detritiation Facility at the Tritium Laboratory Karlsruhe”, Elsevier Editorial System(tm) for Fusion, New York, Engineering and Design, 2008
3. Souers, P. Clark – “Hydrogen Properties for Fusion Energy”, University of California Press
4. Intern Document „TRENTA4-pre - Experiment CD19 / CD20”, TLK-KIT
5. Dr. Liang HU & Dr. Adeyinka A. Adeyiga - “ Carbon dioxide separation by phase enhanced gas-liquid Absorption”, School Of Engineering and Technology Hampton University, Hampton, 2000

Cuasi-coherent modes and the stationary state of
the Edge Localized Modes. Stationary parallel
dynamics and saturation of the filaments
generated in strong Kelvin-Helmholtz events in
the H-mode regime
BS-2, WP10-TRA-01-04 (L-H transition physics)
Detailed Report

1 Introduction

The precursors to the ELM event are due to the fact that the nonlinear tearing of the current sheet (coinciding with the vorticity layer) is not purely growing but also has a oscillatory part.

The basic fact in the ion-pressure driven instabilities in tokamak is that the parallel dynamics results from a balance where the electron collisions are essential. This represents the condition that must be invoked in the Hasegawa-Wakatani theory of drift-wave turbulence. When the temperature is high the collisionality is low and one expects that the parallel balance is not satisfactorily described as a dissipative mechanism. Frequently it is invoked the parallel Landau damping but the efficiency of this pseudo-dissipation model is problematic for short time scales as the ones that are implied in the Edge Localised Modes.

We propose to consider the transitory process of increase of the parallel current induced by the centrally advected vorticity in a Kelvin-Helmholtz event as constrained by the poloidal viscosity of neoclassical origin. This mechanism, the usual reason for the decay of poloidal rotation in plasma, is efficient due to the different drifts of electrons and ions in the radial direction, leading to currents that are subjected to resistive dissipation. We propose this mechanism as a source of force opposing the gradient of the parallel current. This will allow to balance in an efficient way the parallel dynamics and will give correct evaluation of the growth rates of the Edge Localised Modes.

2 Phenomenology of the parallel force balance during a transient ELM-like event

According to the model of Bulanov and Sasorov (and Trubnikov) the nonlinear tearing event that breaks up a layer of current and vorticity is purely growing due to the Chaplygin-gas behavior of the plasma, which consists of generation of quasi-singular structures, *i.e.* filaments. This behavior originates in the conservation of the toroidal invariants for electrons and ions, due to axisymmetry. In addition to this the evolution takes place in two-dimensions and there is no constraint along the symmetry direction (toroidal). In the case of drift wave perturbation however, the parallel dynamics of the electrons is constrained by the periodic variation of the electrostatic potential of the perturbation along the magnetic line. Then the electrons, which are very fast, can take a quasi-stationary distribution in this periodic potential by the balance of the pressure parallel gradient, the parallel electric field of the wave and the collisional force along the line. In the case of the nonlinear tearing of the layer we cannot invoke the parallel balance since our perturbation is essentially two dimensional and there is no periodic potential structure along the line. There is however a dynamics of the plasma along the line and this is connected with the formation of the vortex filaments. The layer of current is also a layer of vorticity and the filamentation of the current is accompanied by the formation of a vortex structure whose position coincides with that of the current filament. The event of filamentation of the current (described by the Chaplygin-gas with anomalous polytropic, or the “drop-on-ceil” instability) induces generation of local magnetic structure similar to a magnetic island, with magnetic field lines that have a local helical form around the axis of the filament. This induces the flow of plasma along the local helical magnetic field lines, a flow that has vortical nature. The conservation of the density leads to an increase of the particle velocity in the direction of the magnetic field. These processes:

1. current filamentation due to nonlinear tearing instability
2. formation of a vortex with an axis common with the current filament
3. increase of the flow of plasma along the axis

are combined in a synergetic way. The flow along the axis stabilises the vortex.

If we consider the filament and the coinciding vortex in the transient process along the magnetic field (the axis of the filamentation) we note that the plasma has to move through regions with different magnetic field, from the low-field side to the high-field side and so on. At first sight this seems in contradiction with the assumption of axisymmetry which is adopted for the conservation of the particle invariants. It is however a periodic effect, due to geometry, superposed over a basic axisymmetric structure of the magnetic field. The periodic variation of the magnetic field which results from the toroidality is small and acts as a perturbation on which one can average. On the other hand, the effect of this

periodic variation of the magnetic field along the line is important for the plasma flow. The magnetic pumping acts as a dissipative mechanism and produces a decay of the motion. In the case of poloidal plasma rotation the magnetic pumping associated with the motion of the plasma through regions of low and high field represents an efficient damping of the rotation, leading to its decay with a rate of the order of the inverse of the ion-ion collision time.

In our case, where the filamentation due to “drop-on-ceil” instability is purely growing, the increase of the flow along the line is a transient process. Plasma is suddenly pushed along the line due to the concentration of the density in the vortex and it has to traverse regions of different magnetic field. It is then subject to the magnetic pumping and the effect is a force that acts as a damping of the motion. This leads to a dynamic balance of the two contrary tendencies:

1. increase of parallel velocity of plasma associated with the concentration of density during filamentation and vortex formation
2. damping of the parallel motion due to the magnetic pumping effect

3 Current density filamentation following a KH event

It is known [1] that *the axial current ensures the stability of the magnetic tube.*

It should be underlined that the helical twist of the magnetic field lines depends on the filamentation of the current and this in turn is related with the instability of the Chaplygin gas. The paper **CurrentSheets Sudan** shows sheets of vorticity and sheets of current that coincide.

We have the polarization current as shown by **Horton** connected with the evolution of the vorticity. The divergence of the current of polarization is connected with a time variation of the vorticity

$$\nabla \cdot \mathbf{j}_p = -\frac{\rho}{B^2} \frac{d}{dt} \Delta \phi - \frac{\rho}{B^2} \frac{d}{dt} \left(\frac{\partial}{\partial t} \nabla_{\perp} \cdot \mathbf{A}_{\perp} \right)$$

where ρ is the density of plasma. For constant resistivity η we have the equation

$$\frac{\partial J}{\partial t} - \eta \nabla_{\perp}^2 J = -\nabla_{\parallel} \omega$$

where J is the parallel current. This means that the parallel current will increase in time via the parallel gradient of the vorticity, which is the *stretching* of the vortex tube just formed by the KH instability.

The variables are Ω (vorticity) and J_{\parallel} . These are the equations (**Ogino 1986**):

$$\begin{aligned} \frac{d\omega_{\parallel}}{dt} &= \frac{B^2}{\rho} \nabla_{\parallel} \left(\frac{j_{\parallel}}{B} \right) - \frac{2\mathbf{B} \cdot (\nabla p \times \nabla B)}{\rho B^2} + \frac{\mu}{\rho} \nabla^2 \omega_{\parallel} \\ \frac{\partial j_{\parallel}}{\partial t} &= \frac{1}{\mu_0} \nabla_{\parallel} (B \omega_{\parallel}) + \frac{\eta}{\mu_0} \nabla^2 j_{\parallel} \end{aligned}$$

When the pressure is uniform the second term vanishes. Assuming a form of the perturbation

$$\exp\left(\gamma t - \int k_{\parallel} z\right) J_0(k_{\perp} r)$$

for a highly conducting plasma one gets

$$j_{\parallel} = -\frac{k_{\parallel} B}{|k_{\parallel} B|} \left(\frac{\rho}{\mu_0}\right)^{1/2} \omega_{\parallel}$$

4 Parallel dynamics due to the force arising from magnetic pumping

The equation of evolution of the parallel plasma motion can be derived from the fluid momentum conservation equation:

$$m_i n_i \frac{\partial}{\partial t} \langle \mathbf{B} \cdot \mathbf{u}_i \rangle = - \langle \mathbf{B} \cdot \nabla \cdot \mathbf{\Pi}_i \rangle$$

where $\mathbf{\Pi}_i$ is the traceless part of the ion pressure tensor (the traceless stress tensor). The expression of the pressure balance on the surface

$$\frac{\nabla P_i}{n_i e} = \mathbf{E} + \mathbf{u}_i \times \mathbf{B}$$

then the perpendicular component of the plasma motion is

$$\mathbf{u}_{\perp} = \frac{\mathbf{B} \times \nabla P_i}{e n_i B^2} + \frac{\mathbf{B} \cdot \nabla \Phi}{B^2}$$

The total flow contains the parallel velocity and the form is

$$\mathbf{u} = u_{\parallel} \hat{\mathbf{n}} + \mathbf{u}_{\perp}$$

The components are

$$\begin{aligned} u_{\varphi\alpha} &= \frac{\mathbf{u}_{\alpha} \cdot \nabla \varphi}{|\nabla \varphi|} \\ &= u_{\parallel\alpha} \frac{B_{\varphi}}{B} - \frac{T_{\alpha}}{\Omega_{\alpha} m_{\alpha}} \frac{B_{\theta}}{B} \left(\frac{e\Phi'}{T_{\alpha}} + \frac{P'_{\alpha}}{P_{\alpha}} \right) \end{aligned} \quad (1)$$

and

$$\begin{aligned} u_{\theta\alpha} &= \frac{\mathbf{u}_{\alpha} \cdot \nabla \theta}{|\nabla \theta|} \\ &= u_{\parallel\alpha} \frac{B_{\theta}}{B} + \frac{T_{\alpha}}{\Omega_{\alpha} m_{\alpha}} \frac{B_{\varphi}}{B} \left(\frac{e\Phi'}{T_{\alpha}} + \frac{P'_{\alpha}}{P_{\alpha}} \right) \end{aligned} \quad (2)$$

The conservation of the toroidal angular momentum implies from Eq.(1) that a reduction of the parallel flow must be accompanied by a corresponding reduction of the radial gradients of the electric potential or the pressure. If the pressure gradient is constant, it results that a reduction of the parallel flow induce a reduction of the radial electric field (Stix says that the radial electric field existing initially is wiped out).

From the Eq.(2), it results that a reduction of the poloidal flow velocity $u_{\theta\alpha}$ induces a reduction of both the parallel flow velocity $u_{\parallel\alpha}$ and of the radial electric field. The one to be mainly affected is the term of electric field, since it contributes largely to the generation of $u_{\theta\alpha}$.

The expressions of the two component velocities also suggest the following observation. From Eq.(1) we see that if there is a reduction of the toroidal velocity (due to the non-conservation of the toroidal momentum, by magnetic pumping dissipation in the ripple modulations) is accompanied by a reduction of the parallel flow or an increase of the radial gradient of the electric potential, if this is positive. In general the plasma losses mainly the ions, by direct orbit loss or collisional expulsion from banana trajectories and the potential is negative, increasing towards the plasma edge. The electric field is negative, being oriented from the plasma border toward the centre. Then we can replace

$$\Phi' \rightarrow -E_r \rightarrow |E_r|$$

and we have

$$u_{\varphi\alpha} = u_{\parallel\alpha} \frac{B_\varphi}{B} - \frac{T_\alpha}{\Omega_\alpha m_\alpha} \frac{B_\theta}{B} \left(\frac{e|E_r|}{T_\alpha} + \frac{P'_\alpha}{P_\alpha} \right)$$

We can repeat the reasoning : a decay of the toroidal rotation (by ripple) can be obtained a decay of the parallel velocity or the increase of the magnitude of the radial electric field (when this one is oriented toward the plasma centre). But from the Eq.(2) it results that the magnitude of the radial electric field is reduced while the poloidal velocity decays (second term in (2)). Then the conclusion results that only the parallel velocity can be reduced in order to ensure the decay of the toroidal motion. The magnetic pumping associated with the presence of the ripple induces the reduction of the plasma parallel motion, *i.e.* it wipes out the disymmetry in the passing region of the parallel velocity space.

5 Relation between the time derivatives of the parallel and perpendicular velocities

Using the equations of motion for the two velocities where we neglect the Reynolds stress and the additional forces, we can eliminate the neoclassic F^{neo} we get

$$\frac{\partial u_{\parallel}}{\partial t} = - (1 + 2\hat{q}^2) \frac{B_\theta}{B_T} \frac{\partial u_{\perp}}{\partial t}$$

This shows that a change in the perpendicular velocity has only a small effect on the parallel velocity.

5.0.1 Asymptotic poloidal velocity

From momentum balance we obtain the equations for the time evolutions of the perpendicular and the parallel velocities:

$$nm(1 + 2\hat{q}^2) \frac{\partial u_{\perp}}{\partial t} = -F_{\perp}^R - F_{\perp}^R - F^{neo} - F_{\perp}^a \quad (3)$$

$$nm \frac{\partial u_{\parallel}}{\partial t} = \frac{B_{\theta}}{B_T} F^{neo} - F_{\parallel}^R - F_{\parallel}^a \quad (4)$$

where the forces with superscript R are due to the Reynolds stress in a turbulence and F^a are forces due to additional effects on rotation.

$$F^{neo} = -\frac{B_T}{B_0 B_{\theta}} \left\langle B^2 (\mathbf{B} \cdot \nabla) \frac{P_{\parallel} - P_{\perp}}{2B^2} \right\rangle$$

is the viscosity of the plasma when it is pushed along nonuniform magnetic field (magnetic pumping effect).

The additional forces are related to the ripple or to the atomic processes. The two components are

$$F_{\perp}^a = \left\langle \left[\frac{B_0 \nabla \psi \times \mathbf{B}}{2\pi R_0 B_{\theta} B^2} + \frac{B_T}{B_{\theta}} \left(\frac{B_0^2}{B^2} - 1 \right) \frac{\mathbf{B}}{B_0} \right] \cdot \mathbf{F}^a \right\rangle$$

$$F_{\parallel}^a = \left\langle \frac{\mathbf{B}}{B_0} \cdot \mathbf{F}^a \right\rangle$$

The neoclassical viscosity is

$$F^{neo} = -3\mu^{neo} \frac{B_T}{B_0^2} \left\langle \left(\frac{(\mathbf{B} \cdot \nabla) B}{B} \right)^2 \right\rangle \left(u_{\parallel} - \frac{B_T}{B_{\theta}} u_{\perp} - k_{\nu_*} \frac{1}{e B_{\theta}} \frac{dT_i}{dr} \right)$$

where the neoclassical viscosity coefficient is (for velocities which are much less than the sound velocity)

$$\mu^{neo} \approx R_0 q \frac{nm v_{th} \nu_*}{1 + \nu_*} \frac{1}{1 + \varepsilon^{3/2} \nu_*}$$

$$\nu_* = \nu \varepsilon^{3/2} \frac{q R}{v_{th}}$$

and ν is the ion collision frequency.

The coefficient k_{ν_*} describes the relative effect of the **parallel heat flux** on the longitudinal viscosity

$$\begin{aligned} k_{\nu_*} &= 1.17 & \text{for } \nu_* &\ll 1 \\ k_{\nu_*} &= -0.5 & \text{for } 1 &\ll \nu_* \ll \varepsilon^{-3/2} \\ k_{\nu_*} &= -2.1 & \text{for } \nu_* &\gg \varepsilon^{-3/2} \end{aligned}$$

The equilibrium value of the poloidal rotation

$$\begin{aligned} u_\theta &= -u^{neo} \\ &= -k_{\nu_*} \frac{1}{eB_T} \frac{dT_i}{dr} \left(\frac{L_n}{\rho_s c_s} \right) \end{aligned} \quad (5)$$

The equilibrium poloidal velocity is determined by the ion temperature gradient and it is

$$\begin{array}{ll} \text{ion diamagnetic direction} & \text{for } \nu_* > 1, \quad k_{\nu_*} < 0 \\ \text{electron diamagnetic direction} & \text{for } \nu_* < 1, \quad k_{\nu_*} > 0 \end{array}$$

6 Various approaches to the problem of decay by viscosity

6.0.2 Collisional regime (Stix)

The decay of the poloidal rotation in a low beta plasma is related to the motion of the plasma through the spatially-periodic magnetic field of the tokamak. This is the dissipative process of magnetic pumping and its effect is realized via the ion viscosity.

It is considered that at the initial moment a radial electric field exists in plasma. There is a poloidal rotation of plasma due to the interaction of this field with the confining magnetic field. Moving through this periodic magnetic field the drifts of the particles will create a radial electric current. This is because the drifts of the electrons and the ions are different in magnitude.

The drift kinetic equation is solved for the neoclassical distribution function in the first order in the neoclassical small parameter, δ . The radial current is obtained from the velocity space interagl of the particle radial drift, weighted by the first order distribution function.

The (magnetic surface averaged) radial current interacts with the confinement magnetic field and generates a torque which is the cause of the damping of the plasma rotation.

7 Model

7.1 The momentum balance in the toroidal rotation

The equilibrium of the plasma requires the determination of the various contributions to the momentum conservation equation.

The source of momentum for the rotation can be:

- a radial electric field, arising from the ambipolarity condition;
- a torque on plasma due to the ion-replacing current by which the plasma responds to the ion orbit loss mechanism;

The source of decay (the origin of the loss of momentum):

- collisional friction
- loss of momentum by charge exchange (energetic ions are replaced by low temperature ions);
- magnetic pumping due to the ripple modulation of the confining field

The first and the last contributions are collected together in the ion viscosity.

7.2 The drift-kinetic equation

The description of the ion viscosity starts by the determination of the distribution function of the ion component. One must solve the drift-kinetic equation obtained from the Boltzmann equation after gyroaveraging.

$$\begin{aligned}
& \frac{\partial \bar{f}}{\partial t} + \\
& \quad + (\mathbf{u} + \mathbf{v}_d + \mathbf{V}) \cdot \nabla \bar{f} \\
& \quad + \left\langle \frac{d\mu}{dt} \right\rangle \frac{\partial \bar{f}}{\partial \mu} \\
& \quad + w \frac{\partial \bar{f}}{\partial w} \\
& = 0
\end{aligned}$$

where

$$\begin{aligned}
\mathbf{v}_d = & \frac{\mathbf{F} \times \hat{\mathbf{n}}}{\Omega} + \\
& + \hat{\mathbf{n}} \frac{\mu B}{\Omega} \left(\frac{j_{\parallel}}{B} \right) \\
& + \frac{1}{\Omega} \hat{\mathbf{n}} \times (\mu \nabla B + u^2 (\hat{\mathbf{n}} \cdot \nabla) \hat{\mathbf{n}} \\
& \quad + \mathbf{u} \cdot \nabla \mathbf{V} + \mathbf{V} \cdot \nabla \mathbf{u})
\end{aligned}$$

The change in the particle energy

$$\begin{aligned}
\dot{w} = & \mathbf{F} \cdot (\mathbf{u} + \mathbf{v}_d) \\
& - \frac{\mu B}{\Omega} \hat{\mathbf{n}} \cdot \nabla \times \mathbf{F} \\
& - \mu B \nabla \cdot \mathbf{V} \\
& - (u^2 - \mu B) \hat{\mathbf{n}} \cdot \hat{\mathbf{n}} \cdot \nabla \mathbf{V} \\
& - \mu B u \hat{\mathbf{n}} \cdot \nabla \cdot \left(\frac{\pi}{p} \right) \\
& + \frac{2u}{\Omega} (\hat{\mathbf{e}}_n e_{n\parallel} + \hat{\mathbf{e}}_\perp e_{n\perp}) \cdot \left\{ -\mathbf{F} \times \hat{\mathbf{n}} \right. \\
& \quad (3\mu B - u^2) (\hat{\mathbf{n}} \times \nabla \hat{\mathbf{n}}) \\
& \quad \left. \frac{(\mu B - u^2)}{u} \frac{\hat{\mathbf{n}} \times (\mathbf{u} \cdot \nabla \mathbf{V} + \mathbf{V} \cdot \nabla \mathbf{u})}{u} \right\}
\end{aligned}$$

where π is the **magnetic viscosity part of the pressure tensor**

$$\begin{aligned}
\pi_{nn} &= -\pi_{\perp\perp} = -\frac{p}{\Omega} e_{n\perp} \\
\pi_{\parallel\parallel} &= 0 \\
\pi_{n\perp} &= \pi_{\perp n} = \frac{p}{2\Omega} (e_{nn} - e_{\perp\perp})
\end{aligned}$$

where \mathbf{e} is the **velocity stress tensor**

$$(\mathbf{e})_{\alpha\beta} = \frac{1}{2} \left(\hat{\mathbf{e}}_\alpha \cdot \hat{\mathbf{e}}_\beta \cdot \nabla \mathbf{V} + \hat{\mathbf{e}}_\beta \cdot \hat{\mathbf{e}}_\alpha \cdot \nabla \mathbf{V} - \frac{2}{3} \delta_{\alpha\beta} \nabla \cdot \mathbf{V} \right)$$

and

$$B \frac{d\mu}{dt} = \mu \frac{dB}{dt} - u \mathbf{s} \cdot \frac{d\hat{\mathbf{n}}}{dt} + \mathbf{F} \cdot \mathbf{s} - \mathbf{s} \cdot \mathbf{v} \cdot \nabla \mathbf{V}$$

The ion drift-kinetic equation

$$\begin{aligned}
& \frac{\partial \bar{f}}{\partial t} + (v_\parallel \hat{\mathbf{n}} + \mathbf{V}) \cdot \nabla \bar{f} - \\
& - [\mathbf{V} \cdot \nabla \mu B + \mu B (\nabla \cdot \mathbf{V} - \hat{\mathbf{n}} \hat{\mathbf{n}} : \nabla \mathbf{V})] \frac{\partial \bar{f}}{\partial \mu} + \\
& + \left(v_\parallel \frac{\hat{\mathbf{n}} \cdot \nabla \cdot \mathbf{P}}{nm_i} - \mu B \nabla \cdot \mathbf{V} - (v_\parallel^2 - \mu B) \hat{\mathbf{n}} \hat{\mathbf{n}} : \nabla \mathbf{V} \right) \frac{\partial \bar{f}}{\partial w} \\
& = C(\bar{f})
\end{aligned} \tag{6}$$

where the **ion STRESS tensor** is

$$\begin{aligned}
\mathbf{P} &\equiv \\
&= nT \mathbf{I} + \mathbf{\Pi} \\
&\simeq nT \mathbf{I} + \frac{3}{2} \pi_\parallel \left(\hat{\mathbf{n}} \hat{\mathbf{n}} - \frac{1}{3} \mathbf{I} \right)
\end{aligned}$$

and $\mathbf{\Pi}$ is the **ion VISCOSITY tensor**.

8 Assambling the contributions: Magnetic pumping in ripple

8.1 Magnetic pumping

8.1.1 Particle motion in ripple

The equation

$$\ddot{z} = -\frac{\mu}{m} \frac{\partial B}{\partial z}$$

where: z is the distance measured on the line of magnetic field;

$$\mu = \frac{mv_{\perp}^2}{2B}$$

and the magnetic field is

$$B = B_0 + B_1 \exp\left(-\frac{z^2}{a^2}\right)$$

Then

$$\frac{1}{2} \frac{d}{dt} (\dot{z})^2 = -\frac{\mu B_1}{m} \frac{d}{dt} \left[\exp\left(-\frac{z^2}{a^2}\right) \right]$$

with the result

$$V(z) = V_0 - \lambda \frac{\mu B/m}{V_0} \exp\left(-\frac{z^2}{a^2}\right)$$

for the small ripple magnetic modulation

$$\lambda = \frac{B_1}{B}$$

One can see that at $z \rightarrow \pm\infty$ the velocity is the same: there is no change in the energy. The reason is: it is necessary to have

- collisions (see for exemple Stix 73)
- or other dissipative mechanism, like the time variation of the magnetic field

The mechanism of decay of the poloidal rotation in tokamak is the viscosity associated to the magnetic pumping. Similarly, there is a magnetic pumping in the ripple modulation.

The energy which can be thermalized in one collision time by magnetic pumping is approximately

$$\frac{1}{6} |\lambda|^2 \left(\frac{3}{2} nT \right)$$

This can be large compared with the kinetic energy of rotation. The modulation of the magnetic field is of the order

$$\lambda \sim \frac{r}{R} \equiv \varepsilon$$

8.1.2 Particular ion populations

Collisionless ions in ripple-modulated magnetic field:

$$m\ddot{l}_{\parallel} = -\mu \frac{\partial B}{\partial l_{\parallel}}$$

with a magnetic field of the form

$$B = B_0 (1 - \varepsilon \cos \theta - \delta \cos (N\varphi))$$

$$\frac{dv_{\parallel}}{dt} = \frac{v_{\perp}^2}{2} \left(\frac{\varepsilon}{qR} \sin \theta \pm \frac{\delta N}{R} \right)$$

(Yushmanov estimate): Time difference between transit in the ripple sector of the upper tip *vs.* the transit in the lower sector:

$$\begin{aligned} \Delta t &= \sqrt{\frac{R/N}{\frac{dv_{\parallel}}{dt}}} \\ &= \frac{\delta R}{Nv} \left(\frac{qN}{\varepsilon \sin \theta} \right)^{3/2} \end{aligned}$$

approximately

$$\Delta t \sim 10^{-5} \text{ (sec)}$$

The radial drift of the particles

$$\begin{aligned} \Delta r &= v_{Dr} \Delta t \\ &= \frac{1}{\Omega_i} \frac{v_{\perp}^2/2 + v_{\parallel}^2}{R} \Delta t \\ &\sim 10^{-2} \text{ (m)} \end{aligned}$$

where $v_{Dr} \sim 10^3 \text{ (m/sec)}$.

The time of bounce on the banana

$$\begin{aligned} \tau_{bounce} &= \frac{qR}{\sqrt{\varepsilon}} \frac{1}{v} \\ &= 3 \cdot 10^{-5} \text{ (sec)} \end{aligned}$$

The toroidal precessional drift

$$\begin{aligned} v_{\varphi} &= \frac{v_{thi}^2}{R\Omega_{\theta i}} \\ &= 3 \cdot 10^4 \text{ (m/sec)} \end{aligned}$$

The time of toroidal motion by precession in a ripple sector

$$\begin{aligned} \tau_{\varphi} &= \frac{l_{\varphi}}{v_{\varphi}} \\ &= 10^{-5} \text{ (sec)} \end{aligned}$$

Total radial drift during the precessional motion of the (bouncing) particle: cumulated radial shifts

$$\begin{aligned}\Delta r^{total} &= \Delta r \frac{\tau_\varphi}{\tau_{bounce}} \\ &\sim 3 \text{ (cm)}\end{aligned}$$

8.1.3 Estimation of the threshold for the plasma rotation

Power lost by magnetic pumping We shall assume the following values for the geometry and plasma

$$\lambda = \frac{r}{R} \equiv \varepsilon = 0.3$$

$$n = 10^{20} \text{ (m}^{-3}\text{)}, \quad T = 10 \text{ (KeV)}, \quad B_T = 3 \text{ (T)}$$

The energy which is thermalized at every **collision time** τ_{ii} by the *magnetic pumping* in every unit volume

$$\begin{aligned}\delta E_\tau &= \frac{1}{6} |\lambda|^2 \left(\frac{3}{2} n T \right) \\ &= 4 \cdot 10^3 \text{ (J/m}^3\text{)}\end{aligned}$$

Let us consider a plasma rotation velocity (in the poloidal direction) representing a fraction α from the thermal ion velocity

$$\alpha = \frac{v^{rotation}}{v_{thi}}$$

Then, the number of “collision times” in the time interval necessary for a rotation with the velocity $v^{rotation}$ is

$$\begin{aligned}N &= \frac{\tau_{rotation}}{\tau_{ii}} \\ &= \frac{2\pi a}{\alpha v_{thi}} \frac{1}{\tau_{ii}}\end{aligned}$$

This has sense only if $N > 1$ which puts a inferior bound to $\alpha > \alpha_0 \sim 0.0024$. Here

$$\begin{aligned}\nu_{ii} &= 3.42 \cdot 10^{-5} \frac{n}{T^{3/2}} [Z] \\ &\simeq 4 \cdot 10^3 \text{ (sec}^{-1}\text{)} \\ N &= \frac{10^{-2}}{\alpha}\end{aligned}$$

The energy lost by magnetic pumping in a plasma volume:

$$\begin{aligned}\Delta E &= N \cdot \delta E_t \cdot Vol \\ &= \frac{10^{-2}}{\alpha} 4 \cdot 10^3 (\delta r \text{ (} 2\pi a \text{)} (2\pi R))\end{aligned}$$

The work done by the $\mathbf{j} \times \mathbf{B}$ force Consider ions extracted from the plasma. They generate a radial electric current j_r which interacting with the magnetic field will produce a force. The volume density of this force

$$\mathbf{f} \left(\frac{N}{m^3} \right) = \mathbf{j} \left(\frac{A}{m^2} \right) \times \mathbf{B} \ (T)$$

Then the force in the plasma volume Vol will be

$$F_\theta = j_r B_T \cdot Vol$$

The work done by this force to rotate the plasma is

$$L_\theta^{work} = F_\theta \cdot dl_\theta \ (Joule)$$

$$L_\theta^{work} = I_r \cdot B_T \cdot (\delta r \ (2\pi a))$$

Comparison The factor

$$\eta = \frac{\Delta E}{L_\theta^{work}}$$

should be less than 1 in order the rotation to be possible.

$$\eta \sim \frac{10^3}{\alpha I_r} < 1$$

For the velocity of the order of the asymptotic poloidal velocity (which remains after the decay of any initial rotation),

$$I_r > 10^3 \ (A)$$

Fraction of particles involved in the generation of j_r Suppose that a fraction β of the total density of particles n_0 is involved in the loss process. Every time there is a collision at the collision frequency ν_{ii} , the ion from this subset of particles will be lost to the border. The total current arising from a volume of plasma of width $\delta r = a/10$ is

$$\begin{aligned} I_r &= e\beta n_0 \nu_{ii} (\delta r \ (2\pi r) \ (2\pi R)) \\ &\simeq 1.6 \cdot 10^5 \beta \end{aligned}$$

This yields the following limitation for β :

$$\beta > 0.006$$

9 Conclusion

The parallel dynamics during the transient filamentation of the current and vorticity sheet at the tokamak edge is the result of a balance between the increased flow along the line and the damping of the motion *magnetic pumping*. This provides the basis for an explanation of the oscillatory precursors of the ELMs: before the filamentation becomes purely growing, the damping from magnetic pumping compensates periodically the increase in the parallel current and the flow due to the vorticity concentration.

References

- [1] Helical Kink Twisted Magnetic Linton
- [2] F. Spineanu, M. Vlad, “Filamentation of a strongly sheared rotation layer”, Transport Task Force Meeting, JET, Culham, September 2009.

National Research and Development Institute for Cryogenics and Isotopic Technologies
National Institute for Laser, Plasma and Radiation Physics

SCIENTIFIC REPORT

To the Contract 1EU/08/08.2008

January-June 2010

Project BS-7: Upgrade of the JET Gamma-Ray Diagnostics

Project leader: M. Curuia

EFDA-JET Task Agreement: JW6-TA-EP2-GRC-04

Specific Objective

Upgrade of the JET gamma-ray cameras – neutron attenuators (code KN3-NA)

*Marian Curuia⁽¹⁾, Mihai Anghel⁽¹⁾, Teddy Craciunescu⁽²⁾, Elena David⁽¹⁾, Mihaela Gherendi⁽²⁾,
Sorin Soare⁽¹⁾, Vasile Zoita⁽²⁾*

⁽¹⁾ National Research and Development Institute for Cryogenics and Isotopic Technologies, Rm. Valcea

⁽²⁾ National Institute for Laser, Plasma and Radiation Physics, Magurele, Bucharest

June 2010 milestones:

A. Report on the non-nuclear (in-house) test

B. Preparation of radiation tests on the neutron attenuator prototype. Preliminary results.

CONTENTS

Summary

A. Report on the non-nuclear (in-house) test

A.1. Introduction

A.2. Structure of the KN3-NA Assembly

A.2.1 Horizontal camera neutron attenuator

A.2.2 Vertical camera neutron attenuator

A.2.3 Steering and Control System

A.3. KN3-NA Assembly in-house tests

A.3.1 Mechanical tests

A.3.2 Pneumatic tests

A.3.3 Electrical tests

A.3.4 Hydraulic tests

A.4. Conclusions

B. Preparation of radiation tests on the neutron attenuator prototype. Preliminary results

B.1 Introduction

B.2 Methods

B.3 Experiments and results

B.4 Conclusions

B.5 Acknowledgement

Reference

Summary

The JET gamma-ray cameras neutron attenuator assembly (KN3-NA) consists of three main parts: horizontal camera neutron attenuator (KN3-NA-HC), vertical camera neutron attenuator (KN3-NA-VC) and steering and control system (used to move the attenuators from parking to working position and vice-versa). The steering and control system permanently connects the KN3 NA system with CODAS (Command and Data Acquisition System). All components of the KN3-NA assembly were assembled on the KN3-NA test stand. The KN3-NA test stand is a 1:1 scale replica of the JET structures on which the KN3 neutron attenuators are to be installed. All in house tests were carried out on the KN3-NA system installed on the test stand. The tests (mechanical, electrical, hydraulic and pneumatic) were performed according to the KN3-NA Test Procedure (Annex 2) and manufacturing drawings.

The next step for the validation of the KN3-NA system consists in radiation tests. These tests are started already with a preparation phase and preliminary results were obtained and reported here. The radiation tests are performed by using the PF-1000 plasma-focus device at Institute of Plasma and Laser Micro fusion IPPLM Warsaw.

A. Report on the non-nuclear (in-house) test

A.1. Introduction

The manufactured KN3 components and sub-assemblies, individually checked, were installed on the test stand prior to the full system testing.

Depending upon the requirements the attenuators are to be moved in or out of the KN3 detector line of sight. The attenuators are steered by pneumatic drives using a local controller based in a cubicle in J1D mezzanine, KN3 area, with movements initiated by diagnostics Responsible Officer and monitored by CODAS.

The operation of the neutron KN3 attenuators assembly was tested before delivery to JET. The in-house tests were carried out on a test stand specifically designed for this purpose. The in-house tests addressed all the functions of the neutron attenuators assembly except for the

radiation functions. The radiation tests will be carried out somewhere else (Association EURATOM-IPPLM), using the vertical camera neutron attenuator prototype.

A2. Structure of the KN3-NA Assembly

KN3-NA assembly consists of the following main parts: neutrons attenuator for horizontal camera (HC-NA), neutrons attenuator for vertical camera (VC-NA) and steering and control system.

A.2.1 Horizontal camera neutron attenuator

The horizontal camera neutron attenuator functions as neutron filter when is in working position (in the plane determined by the gamma-ray detectors lines of sight), figure 2.1. To move the attenuator casing in and out the detector line of sight, a steering and control system is used. The structure of the steering and control system is the same both for HC NA and VC NA.

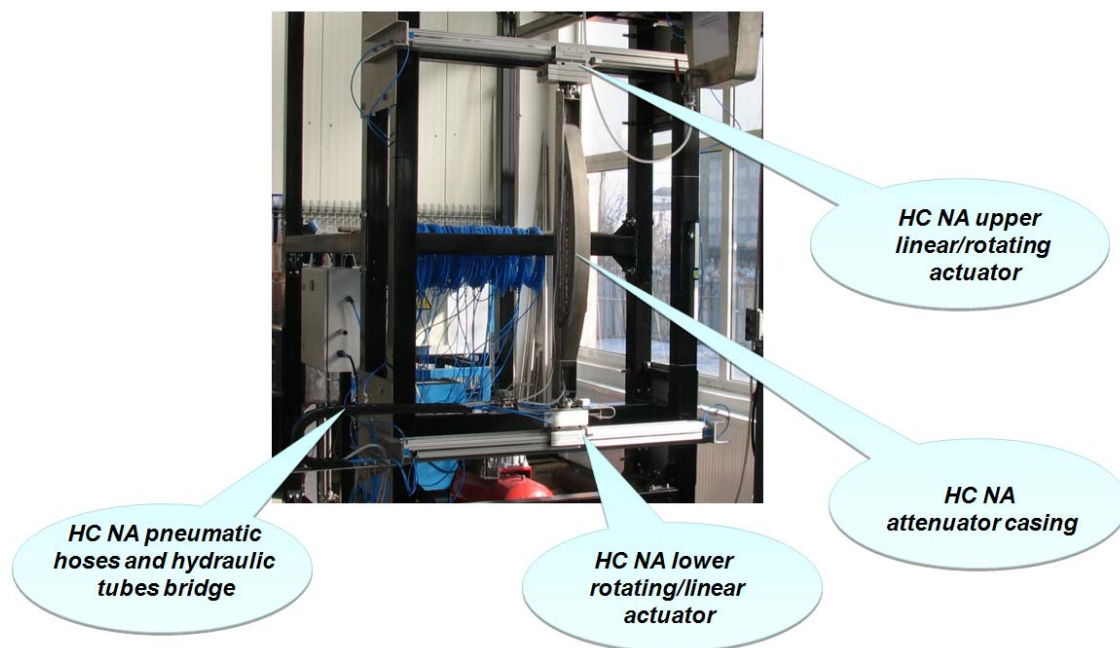


Figure 2.1 Installed HC-NA

A pneumatic system consisting of two linear and two rotating actuator is used to move the attenuator casing between the two fixed positions: working and parking positions. The components required for actuators command: flow control valves, pneumatic-electric convertors

and block valves are placed into a cubical (called Electro-Pneumatic Cubicle). Between pneumatic system and Electro-pneumatic Cubicle are 25 m pneumatic hoses. The electrical parts are placed into a 19" 4U rack cubicle (called PLC Cubicle). Between PLC Cubicle and Electro-Pneumatic Cubicle is a 50 m long electrical connection. The pneumatic part is supplied with pressurized air provided by an air compressor. Figure 2.1 shows the installed HC-NA and figure 2.2 presents details of the lower actuators.

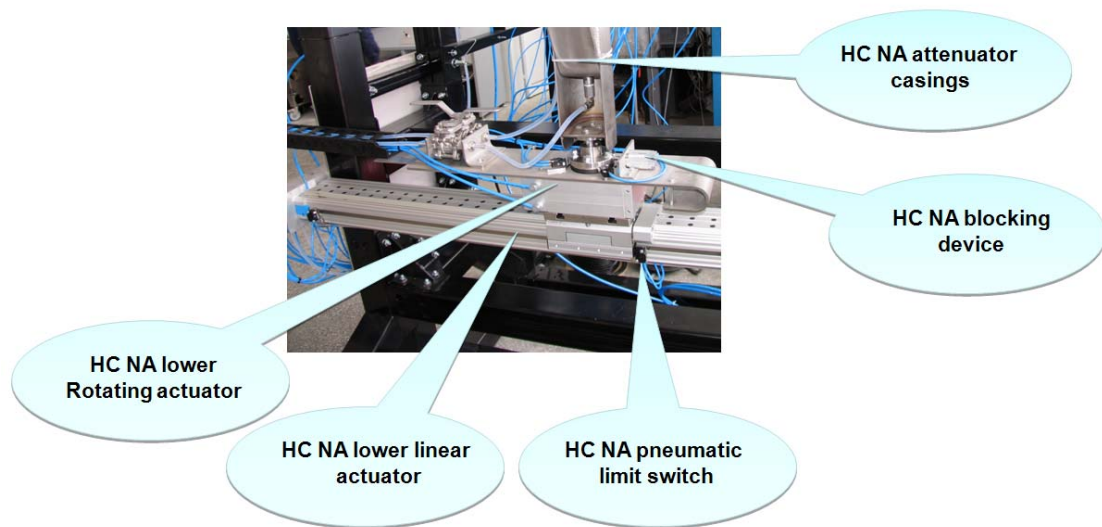


Figure 2.2 HC-NA Lower actuators

A.2.2 Vertical camera neutron attenuator

The vertical camera neutron attenuator (VC-NA) is also mounted on the KN3-NA Test Stand by means of the KS3 middle frame replica. To move in and out of the working location the attenuator is translated 100 mm by the steering and control electro-pneumatic system. Pneumatic linear drives perform the required actions while pneumatic limit switches confirm their completion. The pneumatics is fed from the pressurized air compressor. KN3-NA vertical camera assembly is shown in figure 2.3.



Figure 2.3 VC-NA mounted on the test stand

A.2.3 Steering and control system

The Programmable Logic Controller (PLC) together with the power supply, the main switch, the emergency stop switch, the main fuse, the push-buttons are placed into a standard 19"x4U rack case (figure 6.5), called LUC-1/PLC Cubicle. The electrical connection between PLC Cubicle and Electro-Pneumatic Cubicle was done using two 32 ways plug-in cable connectors and 50 m/32 wires automation cable. In figure 2.4 is presented a general view with LUC 1 and LUC 2 on test stand.

All the pneumatic components are placed into a 500x500x210 (mm) RITTAL industrial case, called LUC-2/Electro-Pneumatic Cubicle. The air pressure is measured by means a manometer placed on the front panel of the cubicle. The Electro-Pneumatic Cubicle figure 2.4 will be wall mounted in J1D. For an easy installation Electro-Pneumatic Cubicle was fitted with push-in connectors both for inlet and outlet.

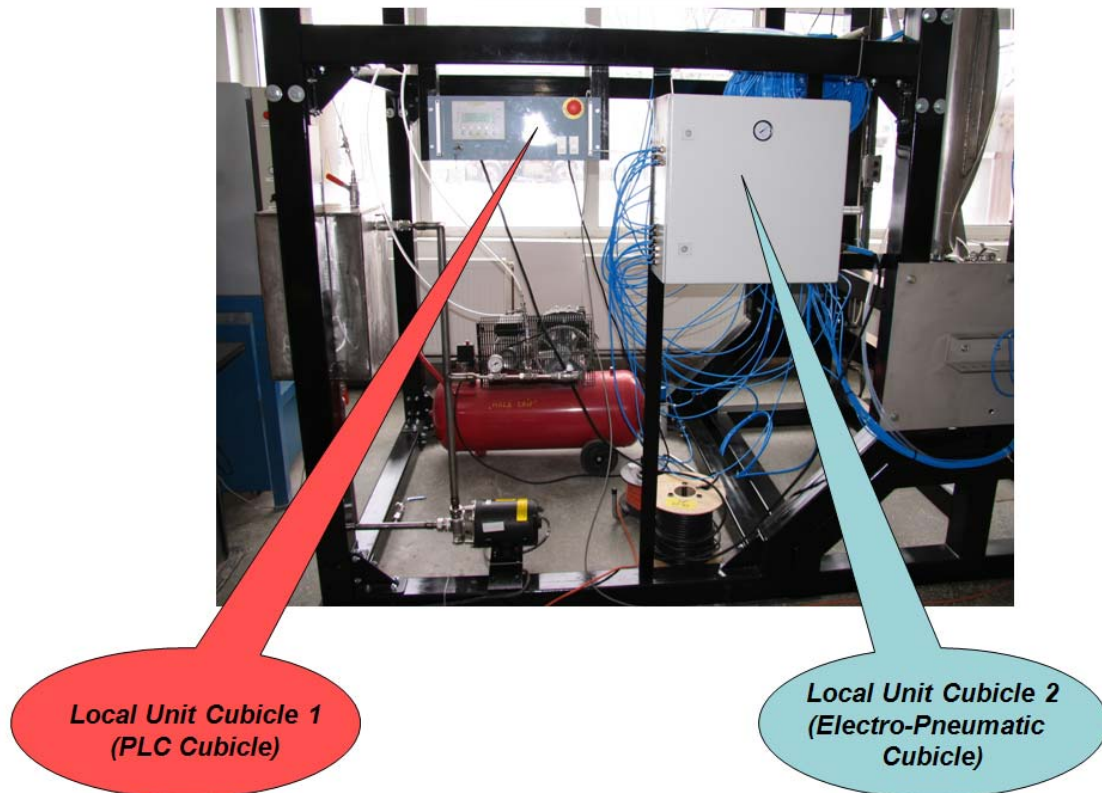


Figure 2.4 LUC 1 and LUC 2 mounted on the test stand.

A.3. KN3-NA Assembly in-house tests

The KN3-NA assembly in house testing started at the beginning of 2010 after the water circuit was completed. The bloc diagram of the KN3 NA system used for in house tests is presented in figure 3.1. The full assembly was tested until middle of June when it was dismantled and prepared for delivery at JET. During this prolonged testing period more than 300 cycles were performed. The results were positive and conclusive: all assemblies and sub-assemblies performed as expected. This was confirmed at the end of the inspection of JOC and CSU representatives. During the inspection the operation of the full system was witnessed and the documentation was checked. After the inspection the approval for delivery was given .

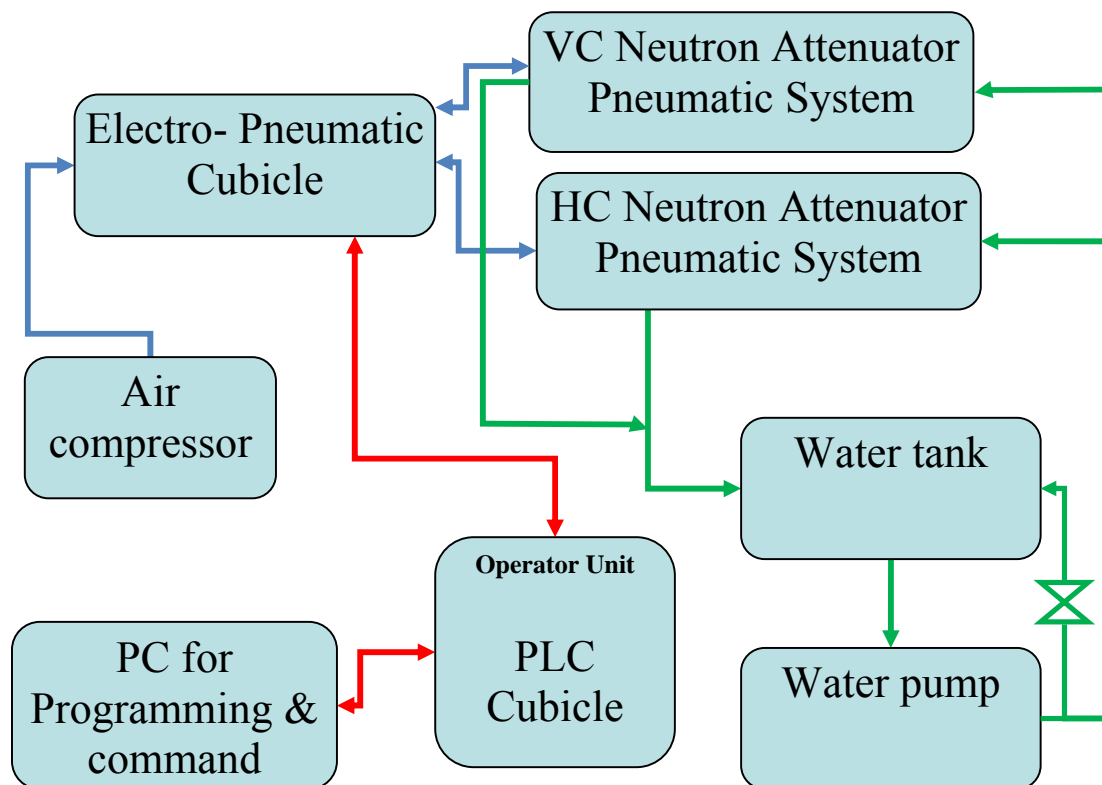


Figure 3.1 Bloc diagram of the in-house test stand

A.3.1 Mechanical tests

According to the manufacturing drawings the following were checked: the dimensions of the test stand structure, clearance between neutron attenuator and mounting structure, attenuators positions (parking/working the detector line of sight position). Taking into account that the stroke of actuators is smaller than the length of the linear actuator, the working position of attenuators were checked and the limiter positions and pneumatic limit switches were fixed, both for horizontal camera neutron attenuator, figure 3.2, and for vertical camera neutron attenuator, figure 3.3

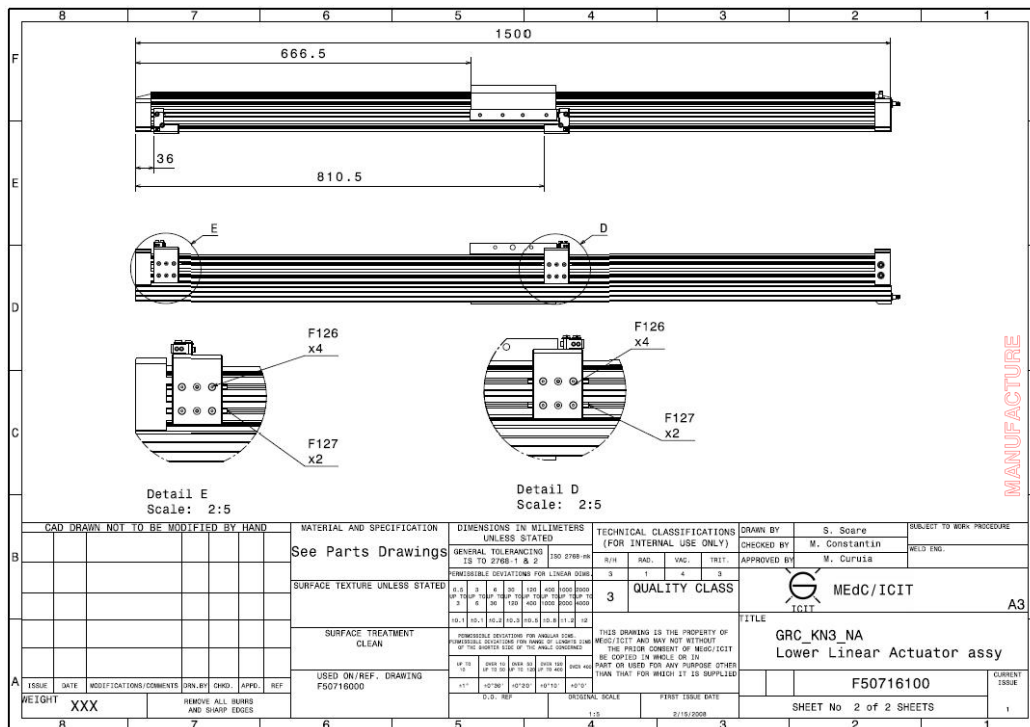


Figure 3.2 Limiter positions for horizontal camera neutron attenuators

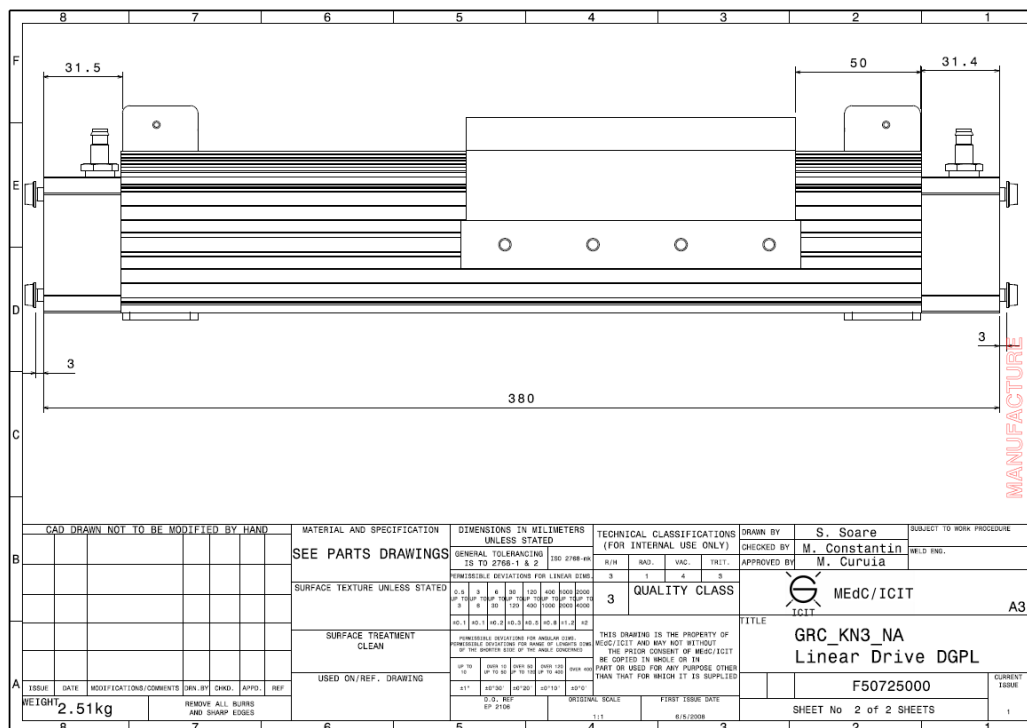


Figure 3.3 Limiter positions for vertical camera neutron attenuators

3.2 Pneumatic tests

An air compressor was used to provide the pressurized air for actuators supply (linear and rotating) figure 3.4. The compressor was fitted with a regulator filter which allows the pressure adjustment according to the system requirements and in the same time retains impurities from air. A second regulator filter was placed inside the electro-pneumatic cubicle. It was used (according to the technical specifications of the KN3-NA system) to adjust the pressure at the following values: 5, 6, 7 bars. All pneumatic tests were carried out for each of these values.

After the KN3-NA pneumatic circuit was pressurized, a leakage check was performed using the manometer fitted on the Electro-pneumatic cubicle. No leakage being recorded, the next step was to manually command each actuator, to check if the pneumatic limit switches work properly and to adjust the translation or rotation speed using the vacuum control valves. The block diagram (figure 3.5) shows the main steps sequence.

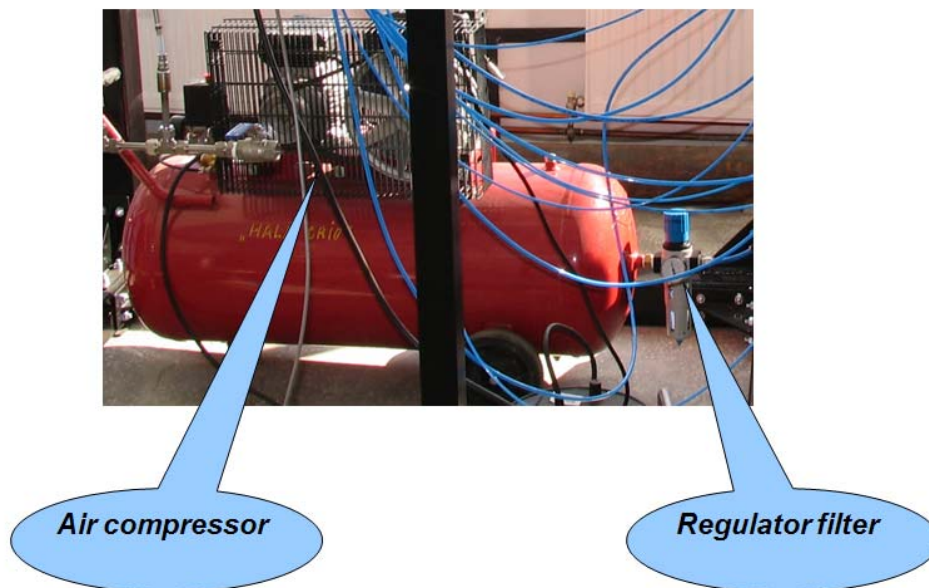


Figure 3.4 Compressor for test stand supply

During the pneumatic tests, special attention was paid to clamping unit (KU) and pneumatic limit switches (PLS). The role of clamping unit is to lock the attenuator either in working or in parking position thus preventing any movement not requested via PLC. PLS provide information about attenuator's position, information which is used by PLC.

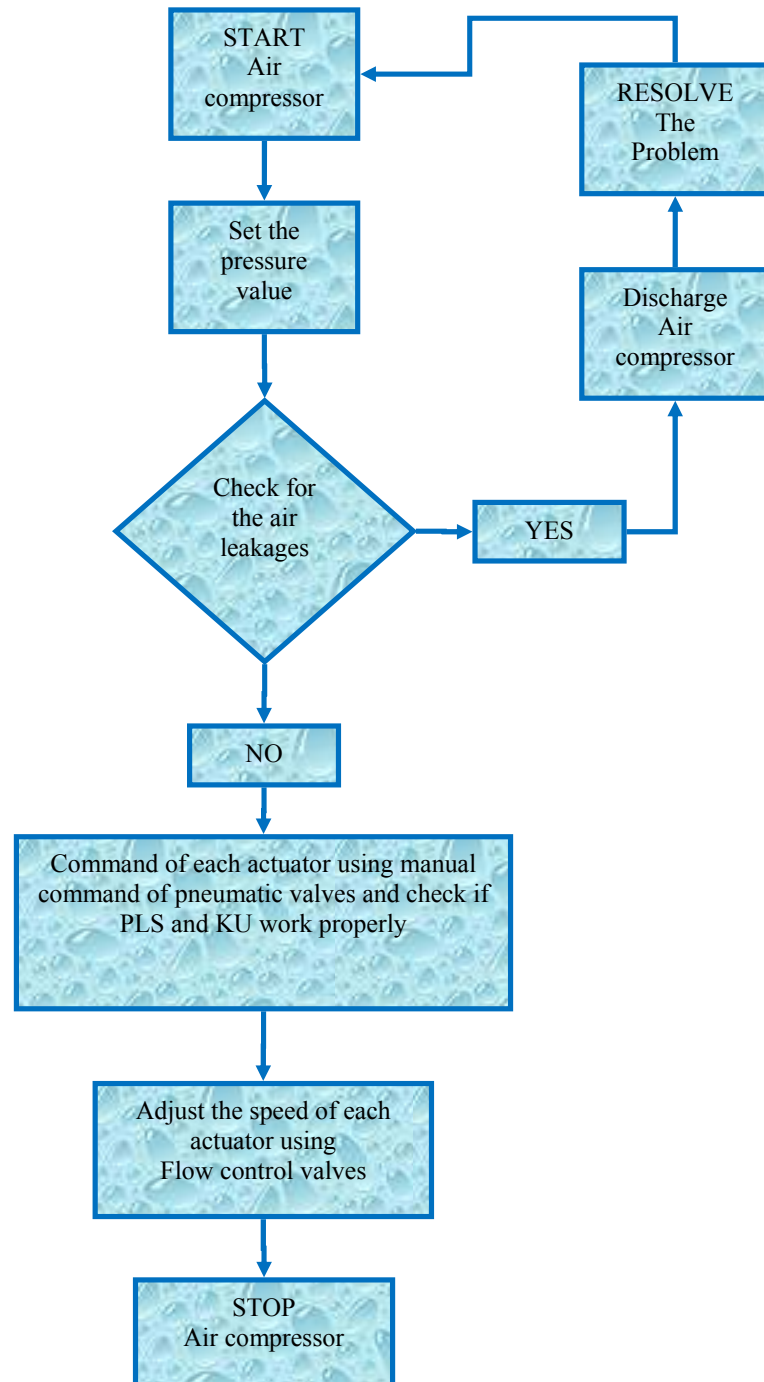


Figure 3.5 Block diagram of pneumatic tests

A.3.3 Electrical tests

From the electrical point of view, the PLC Cubicle represents the most important part of the steering and control system so that the electrical tests were focused on this cubicle. By means of PLC the KN3 neutron attenuators can be locally commanded and monitored by CODAS. This is in accordance with Responsible Officer requirements. To avoid any unauthorized commands, the PLC Cubicle was fitted with a key lock, figure 3.6. The movements can only be requested locally and will be monitored by CODAS Nevertheless the PLC can be commanded remotely by means of Ethernet connection, and this feature was tested also.

A.3.3.1 KN3-NA Assembly - local commands

The movements were initiated using the Operator Unit (OU). On OU were displayed information regarding: pressure status, camera positions for horizontal and vertical and event messages (pressure fails and attenuators displacement timeout).



Figure 3.6 PLC Cubicle- Operator Unit (OU)

The system was tested at different pressure values: 5; 6 and 7 bars. For each pressure value, 100 cycles (attenuator from parking to working location and return) were carried out. In the table 3.1 are presented the displacement time mean values. These mean values were obtained for the lowest speed of actuators which provide a smooth movement.

Tab. 3.1

Displacement time for HC (s)						
Working pressure (bar)	PL to WL			WL to PL		
5	48	48	48	46	47	46.5
6	47	47	47	46	46	46
7	46	47	46.5	46	45	45.5

Displacement time for VC (s)						
Working pressure (bar)	PL to WL			WL to PL		
5	7	7	7	10	10	10
6	7	7	7	8	8	8
7	7	7	7	8	7	7.5

A.3.3.2 KN3-NA Assembly remotely commanded

The entire assembly has been tested using remote commands via CODAS interface test. The main page of the CODAS interface test is shown in figure 3.7. From this page can be displayed all variables, fig. 3.8.

Hydra-Central - Windows Internet Explorer

http://localhost/metacentral

File Edit View Favorites Tools Help

Google Search Share Sidewiki Check AutoFill

Convert Select Web Search Bookmarks Settings Messenger Mail MySpace News

Favorites Suggested Sites Web Slice Gallery

Hydra-Central

Navigate Hydra:

Level3 System	Functions
overview	overview overview document, as used by dotJET
meta	central Start page for browsing, uses two frames navigation this page
festo	Black box commands
	monitor
	log
	control
	node
	namespace description read write
	state-variables (6) read -
	Parameter (6) read write
	PLC commands
	show all variables all 12 variables sorted by ID
Current Variable Configuration XML configuration, for future use when definition was changed	
create new state-variable/parameter	

Overview

Overview

Version 1.2

TimeStamp 20/06/2010 - 23:10:12

Host

Namespace	Name	Value
DOT/Runtime	Total Memory	7MB
DOT/Runtime	Free Memory	3MB
DOT/Runtime	Used Memory	57%
DOT/Runtime	Threads	5
DOT/System Variables	java.vendor	Sun Microsystems Inc.
DOT/System Variables	org.osgi.bundles.defaultStartLevel	4
DOT/System Variables	sun.java.launcher	SUN_STANDARD
DOT/System Variables	org.osgi.supports.framework.extension	true
DOT/System Variables	sun.management.compiler	HotSpot Client Compiler
DOT/System Variables	org.framework.beginningstartlevel	1
DOT/System Variables	os.name	Windows XP
DOT/System Variables	sun.boot.class.path	C:\Program Files\Java\jre6\lib\resources.jar;C:\Program

Done

Figure 3.7 CODAS interface – main page

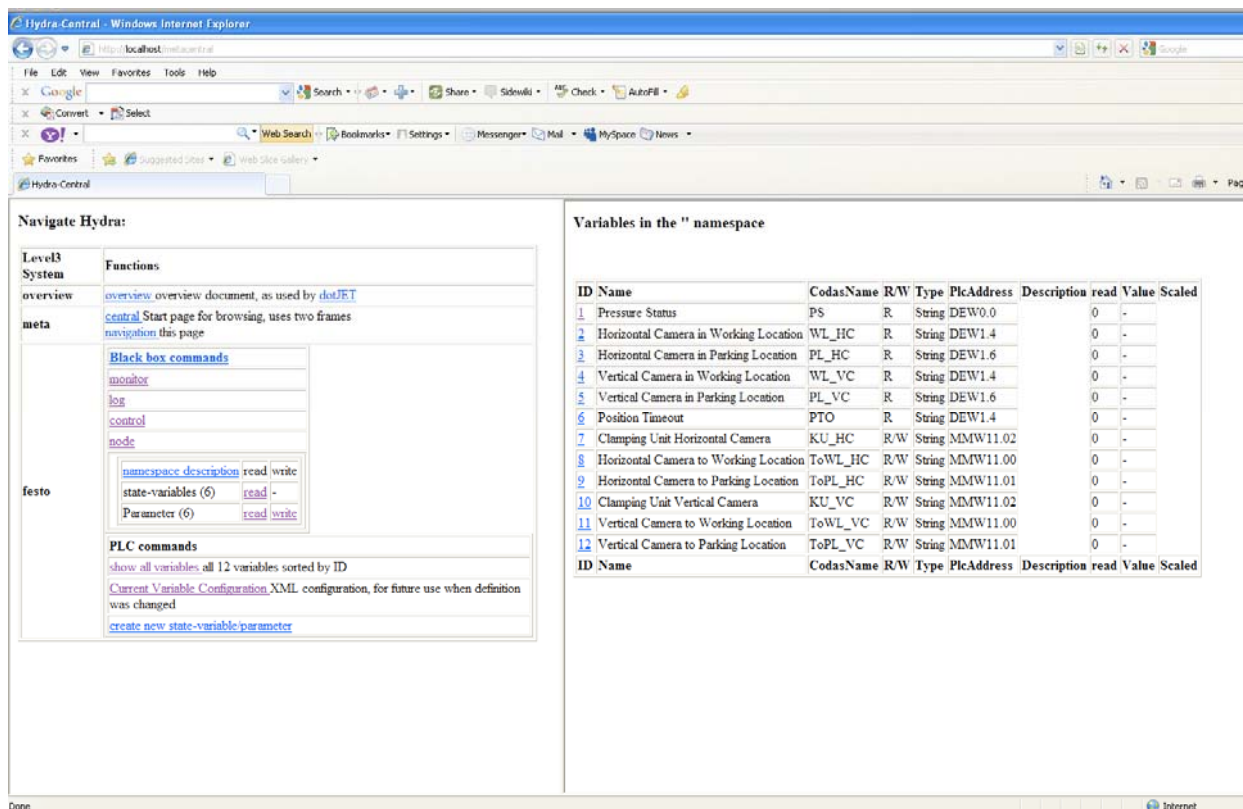


Figure 3.8 CODAS interface - variables

All variables are grouped in: state-variables (read only) and parameters (read/write).

These are the following:

- KU_HC - Clamping Unit Horizontal Camera (1-ON; 0-OFF)
- KU_VC - Clamping Unit Vertical Camera (1-ON; 0-OFF);
- ToWL_HC - Horizontal Camera to Working Location (1-ON; 0-OFF) ;
- ToPL_HC - Horizontal Camera to Parking Location (1-ON; 0-OFF);
- ToWL_VC - Vertical Camera to Working Location (1-ON; 0-OFF);
- ToPL_VC - Vertical Camera to Parking Location (1-ON; 0-OFF);
- PS - Pressure Status (1-OK; 0-Failed);
- WL_HC - Horizontal Camera in Working Location (1-ON; 0-OFF);
- PL_HC - Horizontal Camera in Parking Location (1-ON; 0-OFF);
- WL_VC - Vertical Camera in Working Location (1-ON; 0-OFF);
- PL_VC - Vertical Camera in Parking Location (1-ON; 0-OFF);
- PTO - Position Timeout (1-OK; 0-Failed).

The state-variables provide the most important information for the system: pressure status, positions for attenuators (both for vertical and horizontal camera) and displacement timeout (when it happens), fig. 3.9.

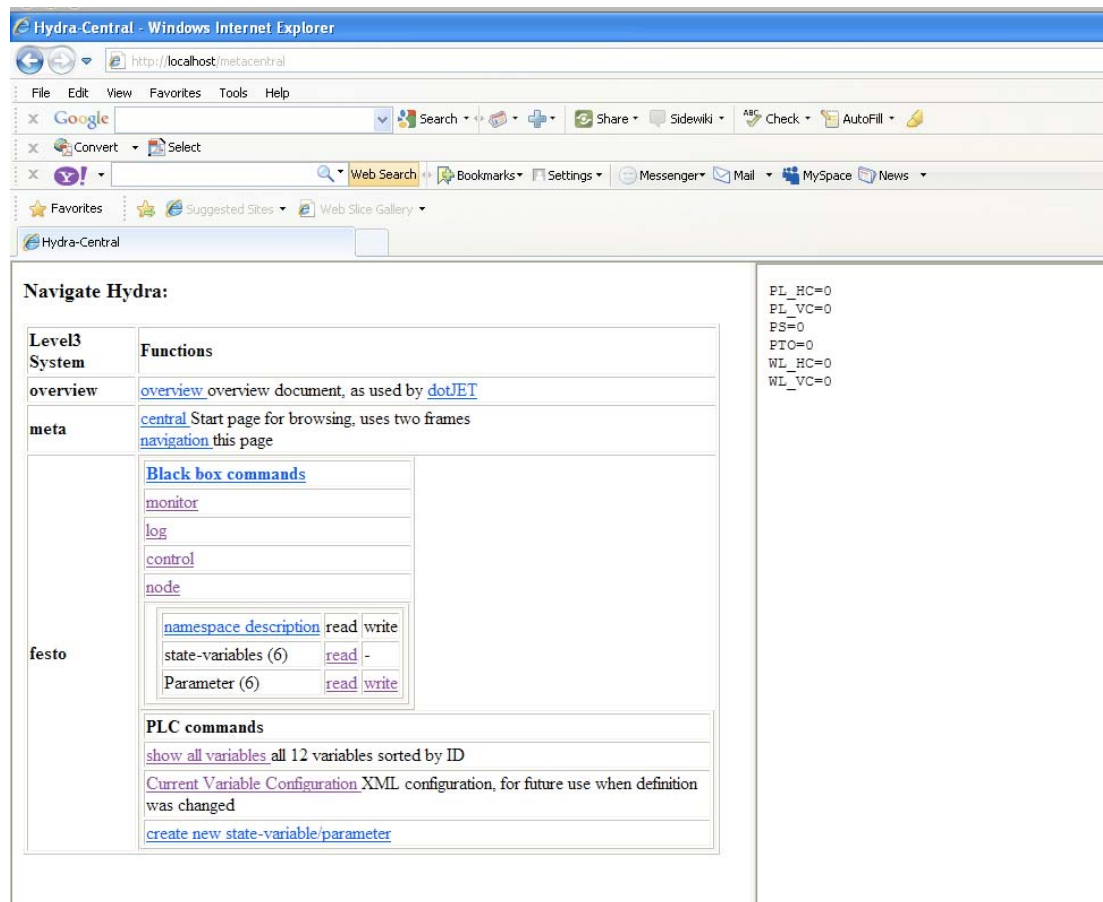


Figure 3.9 CODAS interface- system status

To submit parameter values to move one attenuator, for example, from working/parking location to parking/working location is used the following window, fig. 3.10.

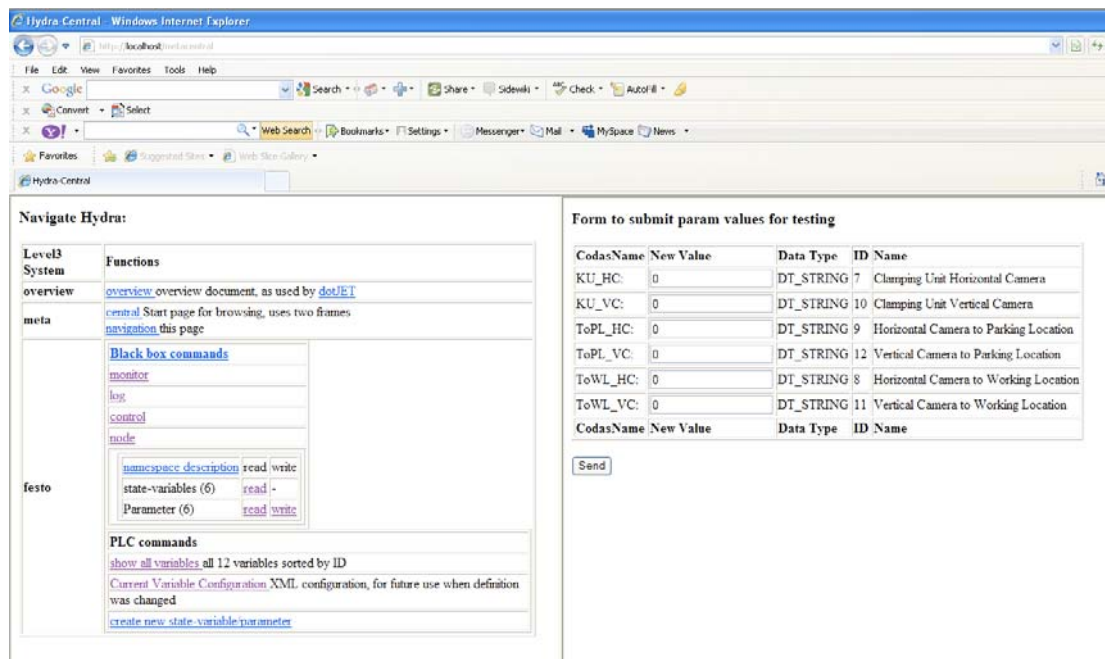


Figure 3.10 CODAS interface parameters sending

After the submitting of parameters in another window are displayed the sent values, fig. 3.11.

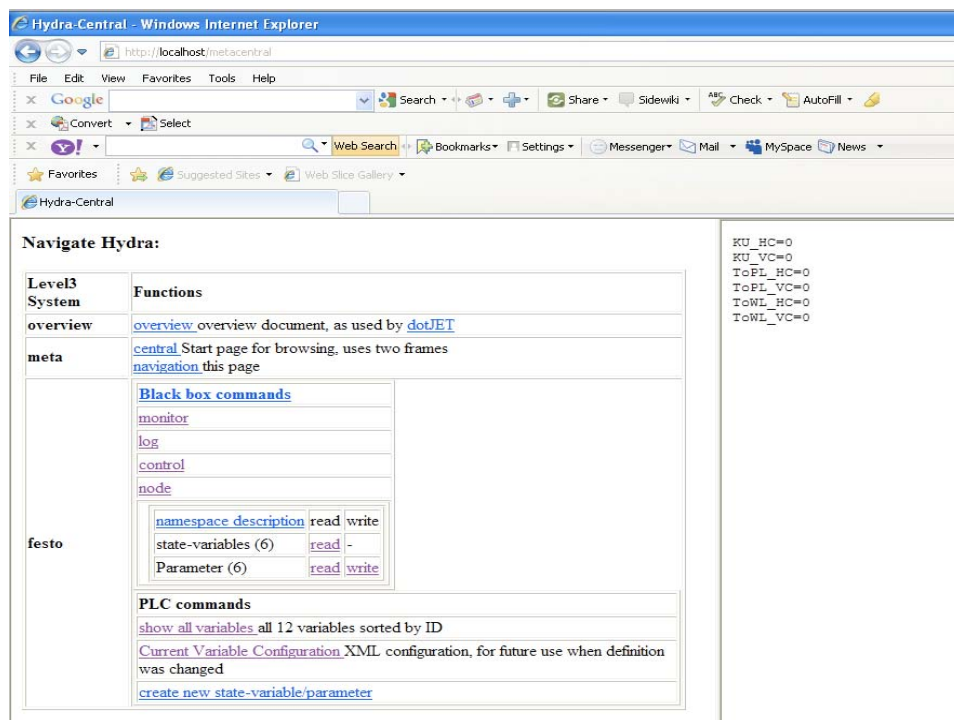


Figure 3.11 CODAS interface displayed value of the parameters

3.4 Hydraulic tests

After installation at JET the attenuators will be connected at the 5 bars demineralised cooling water network. To simulate the same working conditions, a hydraulic system consisting of a water pump and a circulation system was manufactured and installed, figure 3.6. All components of the hydraulic system, including the pump and water tank were made of stainless steel (316). During the whole testing period the attenuators were permanently filled with ultra-pure water and operated at 5 bars.

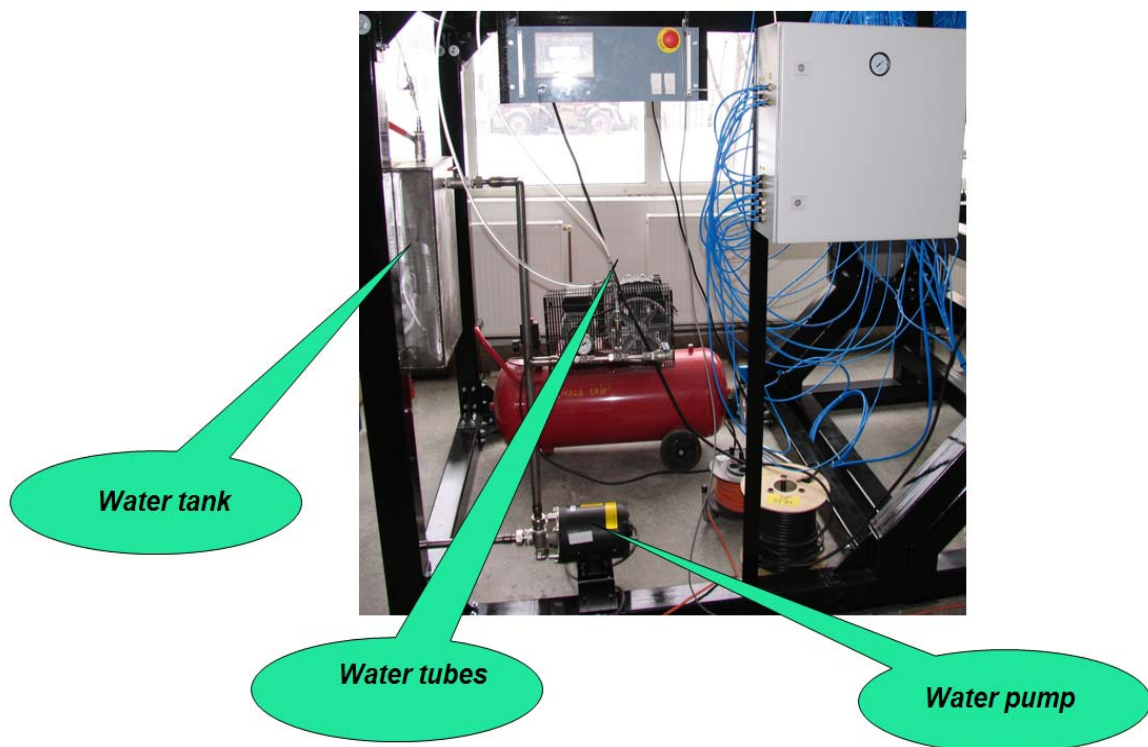


Figure 3.6 the water system used for in house test

A.4. Conclusions

The KN3-NA Assembly was tested over a period of five months and more than 300 tests were performed. All tests (mechanical, pneumatic, electrical and hydraulic) showed good results and safe operation. According to the technical specifications the tests were carried out at the following pressure values: 5; 6 and 7 bars. A visit of JOC and CSU representatives was made on 30th April 2010, when the system function was witnessed. As a result of this visit an approval for delivery to JET of the system was given.

B. Preparation of radiation tests on the neutron attenuator prototype. Preliminary results

B.1 Introduction

The JET KN3 gamma-ray cameras diagnostics system has already provided valuable information on the fast ion evolution in JET plasmas. Gamma-ray diagnostics at JET (gamma-ray spectrometry [1] and imaging [2]) have provided some of the most interesting results in experiments such as those of the TTE campaign [3]. The applicability of gamma-ray imaging diagnostics to high power deuterium pulses and to deuterium-tritium discharges is strongly dependent of the fulfilment of rather strict requirements for the control of the neutron and gamma-ray radiation fields. Therefore a coherent set of upgrades was therefore considered indispensable to extend the JET gamma-ray diagnostic capabilities and to improve the measurements in order to better support the experimental programme. One of these objectives consists in the design, construction and testing of neutrons attenuators for the vertical and horizontal cameras of the KN3 gamma-ray imaging diagnostics. This diagnostics upgrade should make possible gamma-ray imaging measurements in high power deuterium JET pulses, and eventually in deuterium-tritium discharges.

Design solutions based on water neutron attenuators have been developed for the KN3 Gamma-Ray Cameras (the KN3-NA diagnostics upgrade) [4]. At the present moment all the components of the KN3-NA assembly have been manufactured and tested on a on test stand which is an exact replica of the KN3 horizontal camera neutron attenuator assembly and partially replicates the installation configuration for the KN3 vertical attenuator installation configuration. Mechanical, electrical, pneumatic and hydraulic tests were performed.

The next step for the validation of the KN3-NA system consists in radiation tests. These tests are started already with a preparation phase and preliminary results were obtained and reported here. The radiation tests are performed by using the PF-1000 plasma-focus device at Institute of Plasma and Laser Microfusion IPPLM Warsaw.

B.2 Methods

As it is not possible to test the attenuators at their final location, using the KN3 detectors, an independent setup was planned in order to get experimental info on the neutron field. This setup

includes the use of other detectors than those of the KN3 diagnostics. The experiments have to be compared with MCNP calculations, done for this test configuration. The obtained information will be used for the interpretation of the actual KN3-NA system working on the tokamak plasma source.

Initially it was planned to perform the tests at JET site, using a point neutron source (Cf-252), placed at the focal point and one additional side position (see Fig. 1). This configuration allows the measurement of integrated neutron flux and also of neutron energy distribution behind the attenuators.

However due to the specific operations schedule during JET shutdown it was not possible to allow enough time for the experiments. Therefore, the test experiment plan was changed. The new location, where the experiments already started, is the Institute of Plasma Physics and Laser Microfusion, Warsaw, Poland. The neutron source is provided by the Plasma-Focus PF1000 device. This is the largest dense magnetised plasma facility in the world and in the same time, the main plasma installation of the International Centre for Dense Magnetised Centre. The main electromagnetic parameters are given in Table 1. Other characteristic information is provided in Fig. 2.

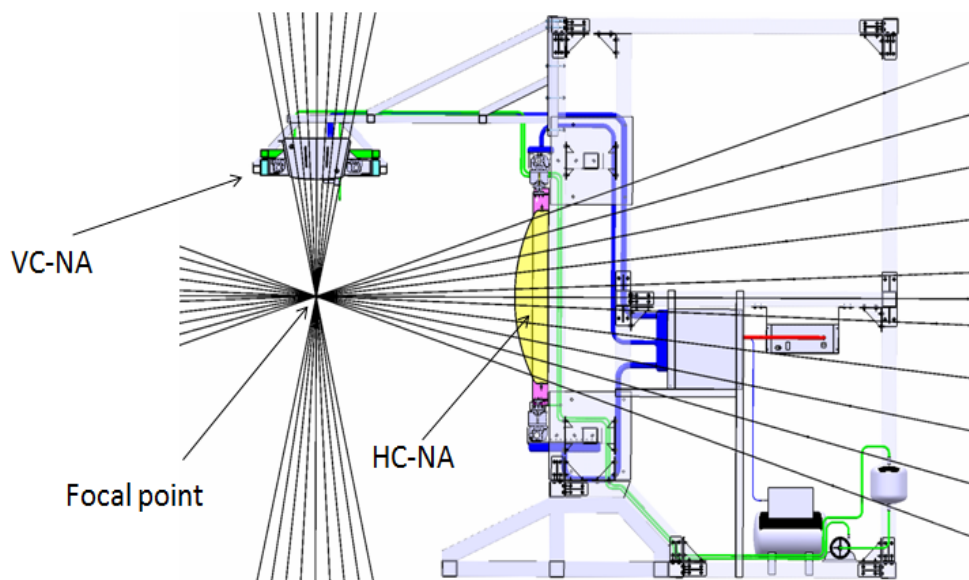
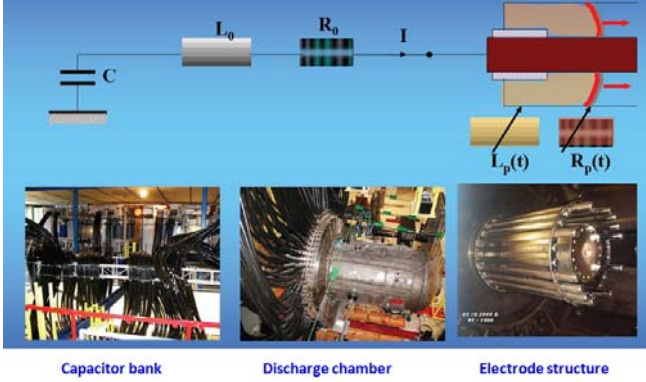
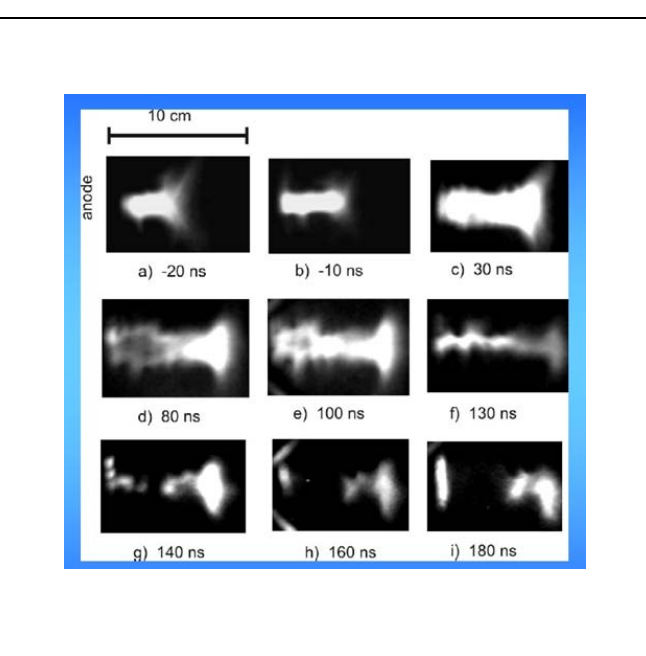


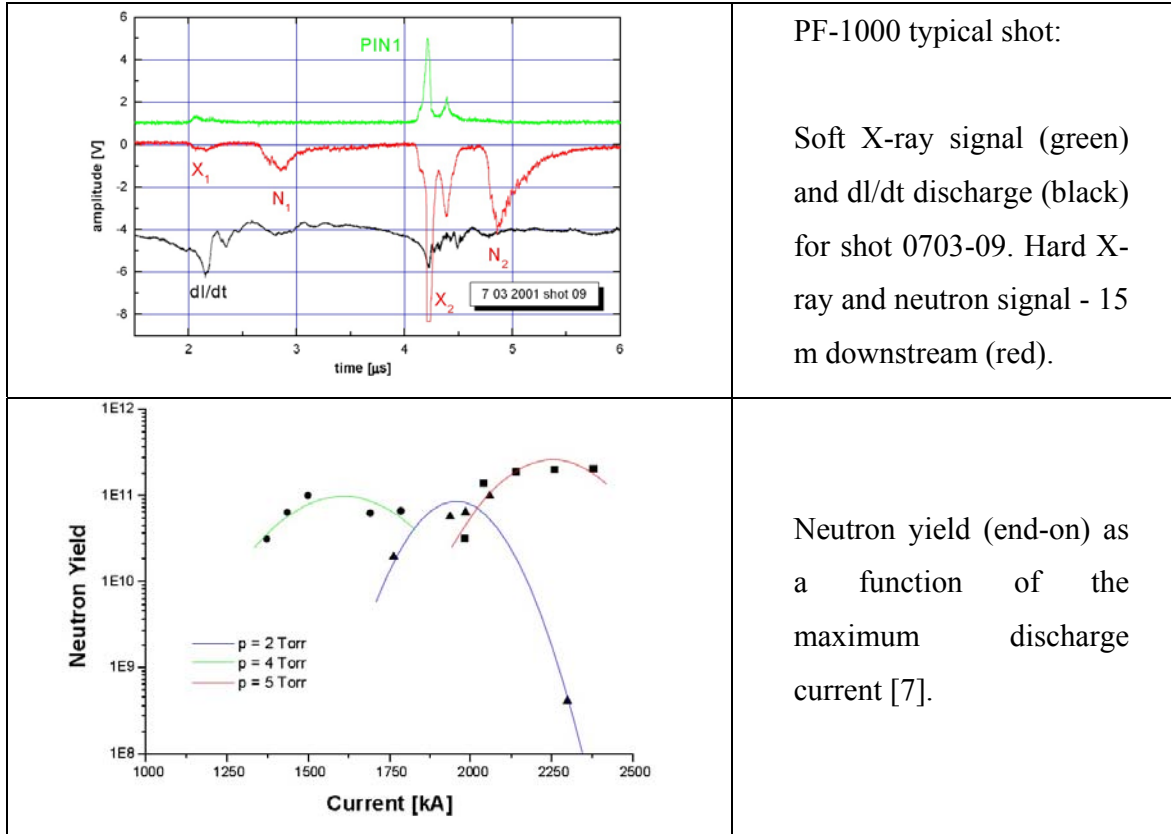
Figure 1 - Initial test configuration

Table 1 - Main electromagnetic parameters of PF-1000 [5]

Capacitor bank charging voltage:	20-40 kV
Capacitor bank stored energy:	266 - 1064 kJ
Current rise-time:	6 μ s
Peak current:	1.3 - 2.5 MA

Table 2 – PF-1000 description.

 <p>Capacitor bank Discharge chamber Electrode structure</p>	<p>PF equivalent discharge circuit [6]</p>
	<p>XUV frames [6] - exposure time 2 ns, window 200-300 eV+above 600 ev</p> <p>a-c: pinch Ø 1-2 cm d: first expansion e-f: second pinch g-i: explosion, dense structure without zipped-effect dense spherical structure</p>



In order to measure the transfer function of attenuator, the neutron field was measured using super-heated fluid detectors, SHFFD's (also known as "bubble detectors"). SHFD are suspensions of metastable droplets which readily vaporize into bubbles when they are nucleated by radiation interactions [8]. The active detecting medium is in the form of microscopic (20-50 μm) droplets suspended within an elastic polymer. The phenomenon of neutron detection by a SHFD is a mixture of nuclear interactions (neutron collisions with nuclei of the active medium), thermodynamic behavior of the detecting medium (the super-heated fluid), and the mechanical response of the elastic polymer. If sufficient energy is transferred from the colliding neutron to the nucleus of one of the elements in the composition of the active medium, the recoil nucleus will initiate the generation of a vapor embryo of sub-micron dimensions. Under proper conditions (that depend on the thermodynamics of the active medium) the vapor embryo will lead to the vaporization of the super-heated droplet with the subsequent expansion into a macroscopic (0.2 – 0.5 mm) bubble. The SHFD's have a threshold-type energy response with the threshold energy depending on droplet composition, detector operating temperature, detector operating pressure. For a standard bubble detector like the BD-PND type, the energy response is approximately flat

within the range 0.3-10 MeV. Using detectors with different energy thresholds, a bubble detector spectrometer (BDS) is obtained. The BDS covers a broad energy range (0.01 – 20 MeV) and provides six energy thresholds in that range (Fig. 2). Therefore the SHFD detectors were used for measuring the neutron fluence and also to determine the energetic spectrum. Based on this data the shielding and filtering effect of the KN3 attenuators will be evaluated.

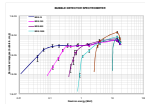


*Figure 2 – BDS neutron
energy response*

As the experiments provide a large amount of experimental data, it was necessary to develop a software package in order to ensure an automatic counting of the bubbles in each detector with enough precision and allowing fast data processing. The software implements a sequence of image processing techniques which are briefly presented here. First an automatic threshold is performed in order to isolate in the image the bubble structure. The automatic threshold is performed by the clustering method. This technique sorts the histogram of the image within a discrete number of classes corresponding to the number of phases perceived in an image. The gray values are determined, and a barycenter is determined for each class. This process repeats until it is obtained a value that represents the centre of mass for each phase or class. Very small particles, which do not correspond to neutron detection, are removed by using an image opening function followed by dilation. This operation does not significantly alter the area and shape of particles because erosion and dilation are dual transformations, in which borders removed by the erosion process are restored during dilation. Filling holes and smooth right angles along the edges of particles is performed prior to evaluate particle parameters. Pixels are added to the image in a neighbourhood that matches a template specified by the structuring element. A 4-connectivity

structure element proved to be an optimum choice for this kind of images. The Heywood circularity factor [9-10] is used in order to classify the particles in the image.

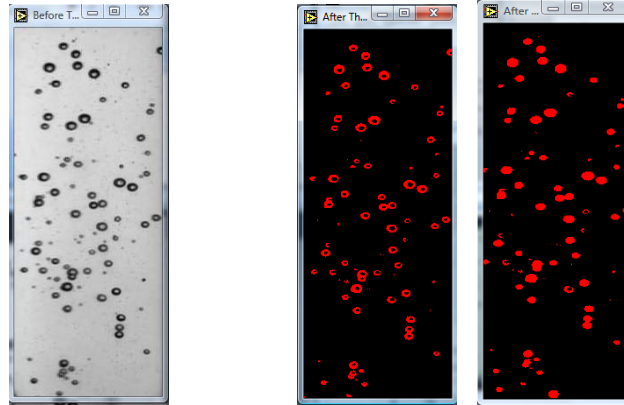
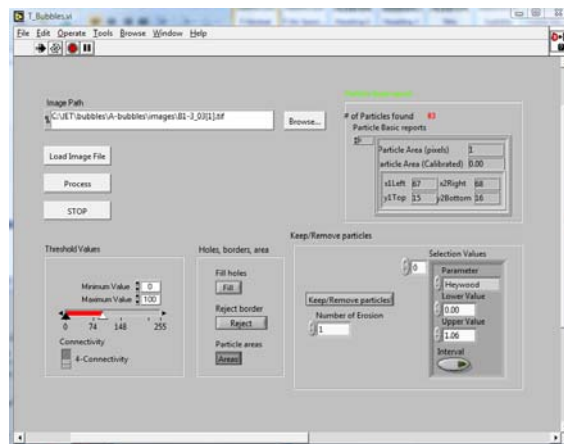


Figure 3 – Illustration of the image processing sequence for bubble detector counting: recorded image of bubbles (left), image after thresholding and opening-dilation process (middle) and image after filling holes and smooth right angles (right).



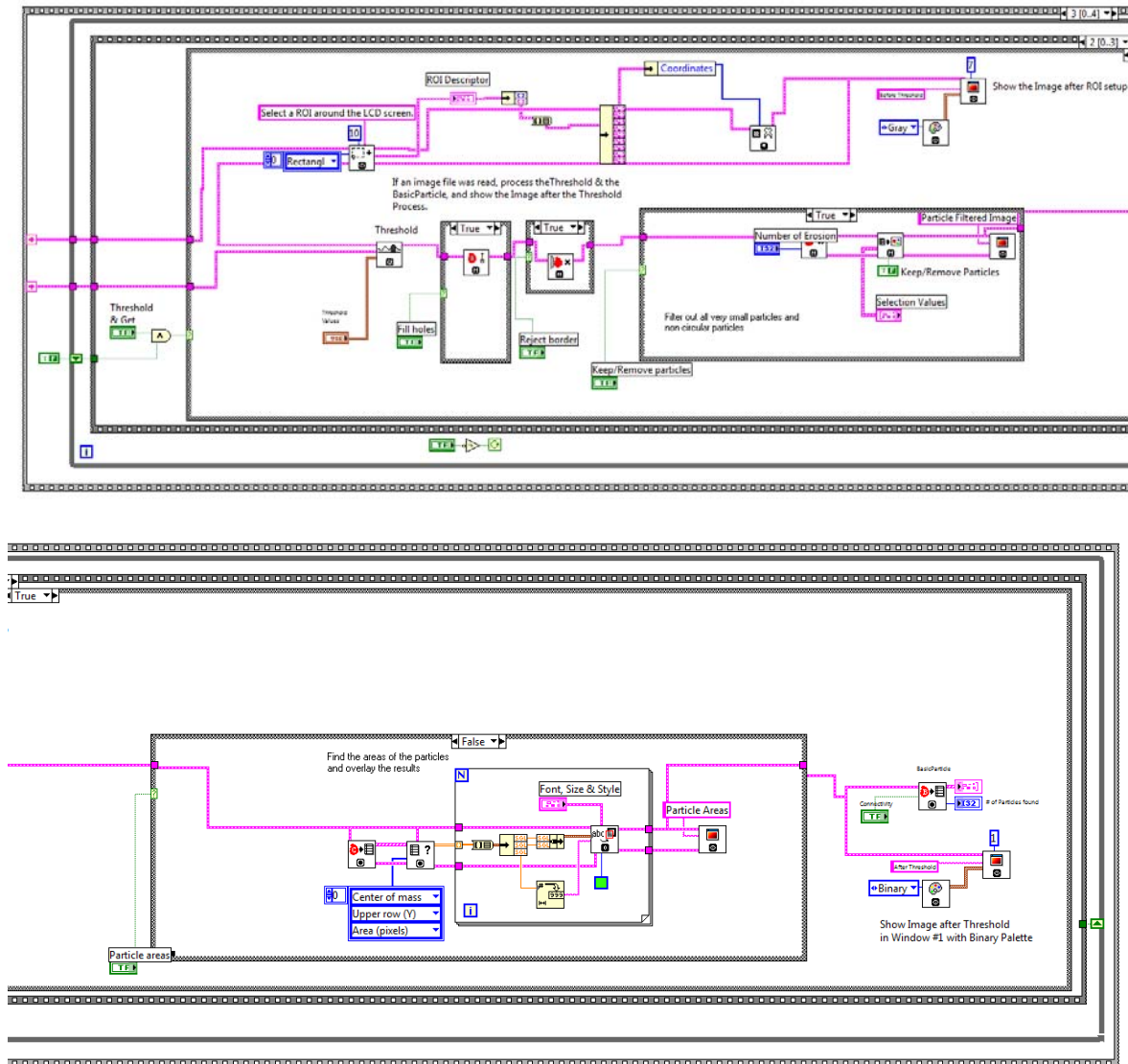


Figure 4 – Labview/IMAQ-Vision implementation of the image processing sequence.

The Heywood factor is defined as the ratio of a particle perimeter to the perimeter of the circle with the same area. The closer the shape of a particle is to a disk, the closer the Heywood circularity factor to 1. For our images we found that a value in the range [0.94-1.06] will ensure a correct detection of the particles. An illustration of the results of the image processing sequence is given in Fig. 3. The image processing sequence was implemented using IMAQ Vision for Labview software package (<http://www.ni.com/vision/>) – see Fig. 4.

B.3 Experiments and Results

First experiments were performed taking into the assumption that the neutron source can be approximated with a point source: the source was estimated from XUV diagnostics (Table 2 [6]) to have a cylinder shape (2 cm diameter, 5 cm length) and the direction from the point source is perpendicular to the detectors plane (see Fig. 5). The source-detector distance is of the order of 2-4 meters (depending on the necessary detection efficiency). It was also assumed that neutron scattering can be neglected. However, experiments proved clearly that one of the assumptions is not fulfilled. The ratio between neutron fluencies without and with attenuator has a value far from the predicted one (Fig. 6).

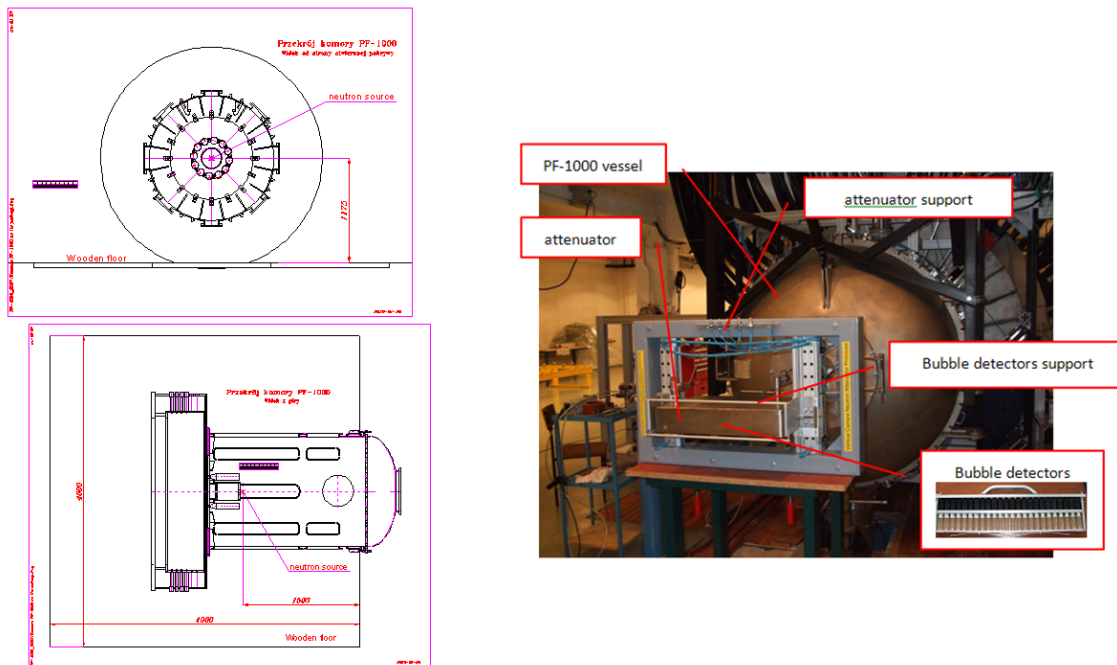


Figure 5 – Experimental configuration #1

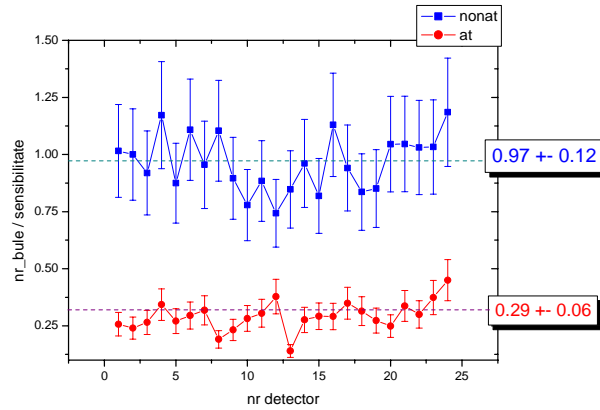


Figure 6 – Neutron fluences in experimental configuration #1

Therefore extensive experiments were performed for the determination of the of the neutron field characteristics of PF-1000 device. Neutron spectra were recorded, using the detectors with different energy thresholds (BDS bubble detector spectrometer), in the same experimental configuration (Fig. 7). It can be observed that even without attenuator, the spectrum has a strong component in the low energy range ($E < 0.1$ MeV). This suggests that neutron scattering has a strong influence on measurements concerning the attenuation factor. Surrounding structures create a low-energy neutron field with intensity (fluence) comparable with the fast neutron field.

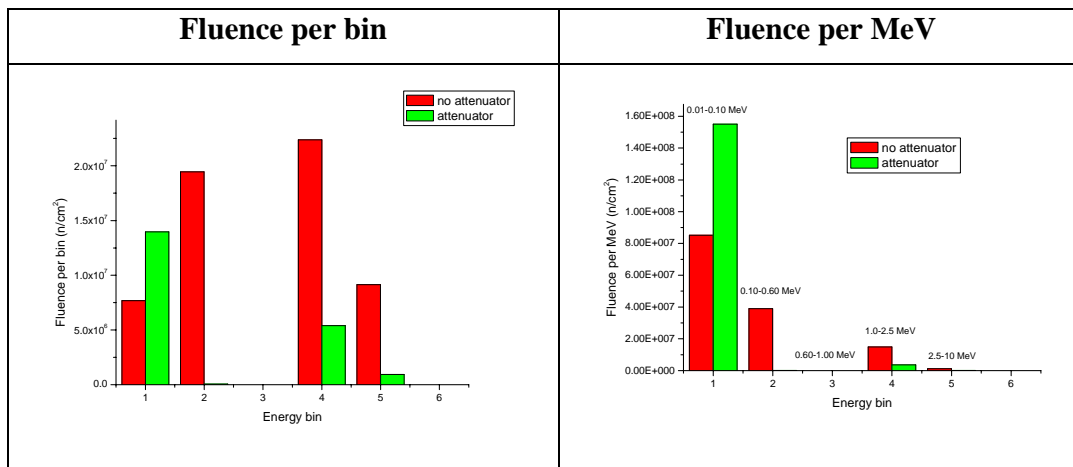


Figure 7 – Neutron spectra obtained in experimental configuration #1

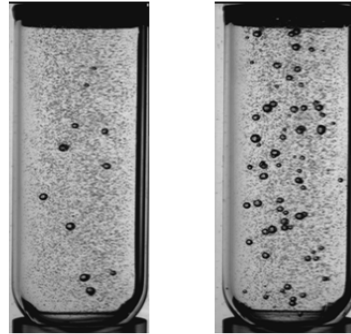
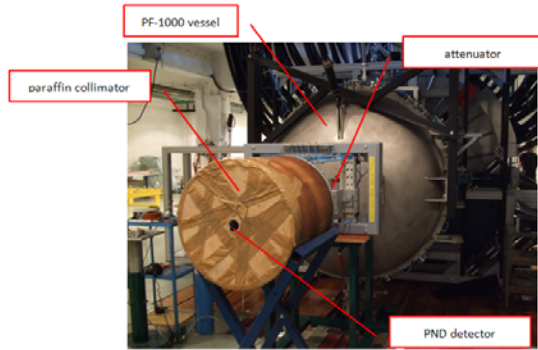


Figure 8 – Experimental configuration #2

Figure 9 – Representative results obtained in configuration #2 with attenuator (left) and without (right).

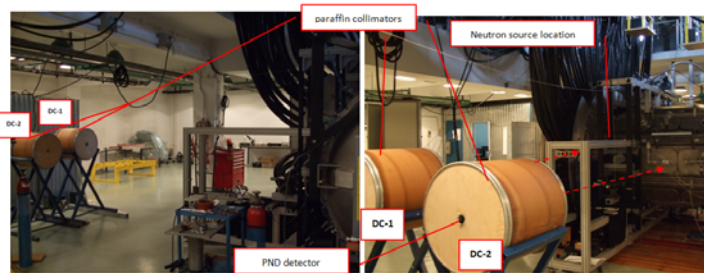
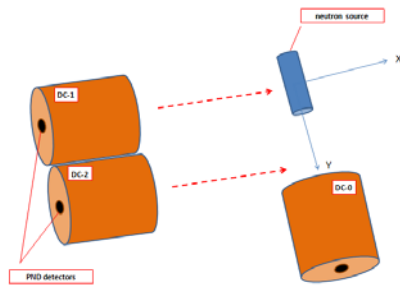


Figure 10 – Experimental configuration #3

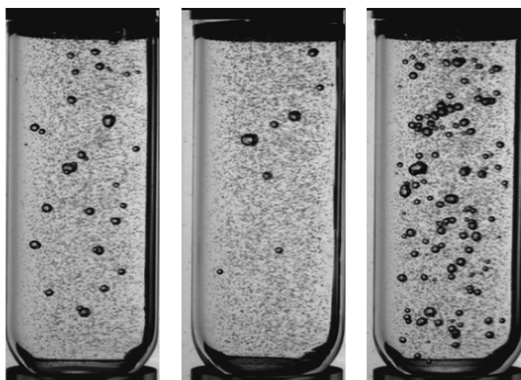


Figure 11 - Representative results obtained in configuration #3: DC-1 (left), DC-2 (middle) and DC-0 (right).

This conclusion is supported also by the results obtained using the experimental configuration #2 (Fig. 8). Representative detector exposure is illustrated in Fig. 9. PND detectors were placed inside a paraffin collimator. It ensures shielding for detectors. The ratio between neutron fluencies without and with attenuator has an improved value of ~ 15 . However this value proves that the shielding provided by the paraffin collimator is only a partial one.

Several experiments were performed also in order to test point-source hypothesis. Experimental configuration #3 (Fig. 10) was used. Two paraffin collimators with PND detectors – DC-1 and DC-2 – were placed at 90° in respect with the reference position determined by the axis of collimator DC-0 used also in configuration #2. DC-0 looks at the neutron source along the axis of the cylinder and DC-1 looks on the perpendicular direction. The axis of DC-2 is located at ~ 1 m from the axis of DC-1. Its role is to get information on the axial extent of neutron source. The results of the measurement (Fig. 11) are compatible with the assumption of a very long cylindrical shape of the neutron source. The number of bubbles recorded at DC-0 approximately 3 times greater than the number recorded at DC-1. The ratio between the number of bubbles recorded at DC-1 and DC-2, which has a value of ~ 4 give an idea about the extension of the neutron sources.

B.4 Conclusion

The preliminary experiments revealed that high neutron scattering characterize the neighbourhood of the PF-1000 device, which represents a serious problem for the determination of the transfer function of the KN2-NA attenuator. Neutron source size is also a parameter which must be controlled. Further experiments will be performed in order to find an optimum experimental setup. New spectrometric detectors (BDS), with increased efficiency will be purchased and used for determining the attenuation factor. The neutron field will be characterized in order to find a location with a negligible scattering background. If not enough, shielding options will be taken into account in order to establish an optimal configuration for the determination of the transfer function of the KN3-NA neutron attenuator. Finally, the results will be compared with MCNP calculations performed for PF-1000 experimental setup.

B.5 Acknowledgement

The reported work includes contributions from Marian Curuia (ICSI Rm-Valcea) and the following people outside the EUATOM-MEdC Association: Marek Scholz, Marian Paduch, Sławomir Jednorog, Rafał Prokopowicz (EURATOM-IPPLM< Warsaw, Poland).

References

- [1]V.G. Kiptily , F.E. Cecil, O.N. Jarvis , M.J. Mantsinen, S.E. Sharapov, L. Bertalot, S. Conroy, L.C. Ingesson, T. Johnson, K.D. Lawson, S. Popovichev, *γ -ray diagnostics of energetic ions in JET*, Nucl. Fusion 42(2002)999.
- [2]O.N. Jarvis, J Adams, P.J.A. Howarth, F.B. Marcus, E. Righi, G.J. Sadler, D.F.H. Start, P. Van Belle, C.D. Warrick, N. Watkins, *Gamma ray emission profile measurements from JET ICRF-heated discharges*, Nucl. Fusion, 36(1996) 1513.
- [3]V. G. Kiptily, Yu. F. Baranov, R. Barnsley, L. Bertalot, N. C. Hawkes, A. Murari, S. Popovichev, S. E. Sharapov, D. Stork, V. Yavorskij, *First Gamma-Ray Measurements of Fusion Alpha Particles in JET Trace Tritium Experiments*, Phys. Rev. Lett. 93(2004)115001.
- [4]V. Zoita, M. Anghel, T. Craciunescu, M. Curuia, T. Edlington, M. Gherendi, V. Kiptily, K. Kneupner, I. Lengar, A. Murari, A. Pantea, P. Prior, S. Soare, S. Sanders, B. Syme, I. Tiseanu. Design of the JET upgraded gamma-ray cameras. Fus. Eng. Des. 84(2009)2052.
- [5]H. Schmidt et al., "Review of Recent Experiments with the Megajoule PF-1000 Plasma Focus Device", Physica Scripta. Vol. 66, 168, 2002.
- [6]M. Scholz et al., "Recent Results of MJ Plasma-Focus Experiment". 6th Dense Z-Pinch Symposium, Oxford, 2005.
- [7]P. Kubes, "Fast deuterons and neutrons in Plasma Focus discharge", 34th EPS Conference on Plasma Phys. Warsaw, Vol.31F, P-1.017 (2007).

- [8]M. Gherendi, V. Kiptily, V. Zoita, S. Conroy, T. Edlington, D. Falie, A. Murari, A. Pantea, S. Popovichev, M. Santala, S. Soare “Super-heated fluid detectors for neutron measurements at JET”, J. Optoelectronics Advanced Mat., 10 (2008) 2092-2094.
- [9]H. Heywood, Particle shape coefficients, Journal of the Imperial College Chemical Society, 8(1954)15.
- [10]R M Carter, Y Yan, Measurement of particle shape using digital imaging techniques, Journal of Physics: Conference Series 15 (2005) 177.

SCIENTIFIC AND TECHNICAL REPORT

Contract Number: 1-EU-8-BM-1-/1.03.2010

Project title: Transmission and Backscattering Mössbauer Spectroscopy Studies of the Short Range Order, Structure and Magnetic Properties in α -Fe and Binary Fe-Cr Model-Alloys.

Phase No. 1: *First round Mössbauer measurements. Dead line: June 30th 2010*

Room temperature transmission Mössbauer measurements on α -Fe (powder and foil) and on Fe-Cr powder alloys obtained by ball milling; thermal treatments of the Fe-Cr powder alloys; data computing and analysis of magnetic properties. All Mössbauer measurements will be preceded by X-ray diffraction analyses (XRD).

CONTENTS

	Page
I. Title.....	1
II. Contents and objectives.....	2
III. Report abstract.....	2-4
IV. Introduction	5-6
V. Room temperature XRD, transmission Mössbauer measurements and computer analyses of structural and magnetic properties on α -Fe powder and foil.....	6-12
VI. Room temperature XRD, transmission Mössbauer measurements and computer analyses of structural and magnetic properties on Fe-Cr powder alloys obtained by ball milling.....	12-23
VII. Thermal treatments of the Fe-Cr powder alloys.....	23-26
VIII. Conclusions.....	26-28
IX. References... ..	28-29
X. Next period working plan.....	29-30

General objectives

This project aims to contribute to the achievement of the following one or more issues in Fe-Cr based alloys (potential candidates for blanket structures in fusion reactors) and α -Fe materials by means of Mössbauer spectroscopy: investigation of local structure and short range order, study of magnetic properties ‘via’ hyperfine magnetic fields in correlation with Cr concentration in the samples. The obtained results will be used for a more general and important issue: to realise if Mössbauer spectroscopy can be used to improve the technology for obtaining FeCr based alloys (in particular prepared via ball milling route) in view of applications for fusion reactors.

Objectives of present report

A comparative Mössbauer study α -Fe/FeCr based materials will allow us a better understanding of the peculiarities of FeCr based alloys obtained by mechanochemical route. The characteristic Mössbauer parameters like hyperfine magnetic fields will be investigated in order to find out correlations with Cr concentration in the system as well as with theoretical calculation of the probabilities for the iron substitution by Cr in the

investigated FeCr based alloys. It is expected also to obtain information regarding the sample homogeneity, a key parameter when we discuss about the applications in blanket structures for reactors.

Report abstract

α -Fe samples in powder or foils as well as some FeCr based alloys obtained by planetary milling were investigated by means of XRD and transmission Mössbauer spectroscopy at room temperature. In addition, thermally treated FeCr samples (at 760 °C under vacuum conditions) were studied by Mössbauer spectroscopy.

In the case of α -Fe, from the studied X-ray diffractograms (XRD), one can infer that all samples of α -Fe powder and foils present the same cubic bcc structure. Rietveld refinements revealed practically very close values of lattice parameters proving the high purity of the investigated samples. Room temperature (RT) transmission Mössbauer spectra display similar six line patterns characteristic for bcc α -Fe structure. The difference between powders and foils of are given by the intensities of the lines 2 and 5 due to the preferential alignment of the nuclear magnetic moments in the foil samples.

FeCrY and FeCrTiY samples prepared in Portugal (our EFDA collaborators at IST Portugal, group of Professor Jose Brito Correia) by ball milling route under argon atmosphere, for 18 hours at 450 rot / min were analysed by XRD and (RT) Mössbauer spectroscopy. It was found that XRD cannot be used for a reliable phase analysis because of the isostructural behaviour of α -Fe and α -Cr and the effects of very large line width in the case of nano scaled particles. However, Rietveld refinements were used to obtain the lattice parameters and particle size (Scherrer equation). A particle dimension close to 10 nm was obtained for both samples.

Mössbauer spectroscopy investigations revealed a FeCr alloy structure, being able to evidence the hyperfine field distribution given by the Cr, and Ti atoms substituting iron in the studied systems. The presence or contribution of high radius Y atoms cannot be directly evidenced by Mössbauer spectroscopy at least for such small amount of yttrium in the system. The calculation of the binomial probabilities to find Cr atoms in the first four coordination spheres around Mössbauer Fe atoms agrees well with the obtained magnetic field distribution given by Mössbauer spectra fitting within a distribution model.

From the mean magnetic field values given by Mössbauer spectra fitting, the atomic Cr concentration in the studied FeCr based alloys was determined and compared with the

nominal known concentration. A very good concordance was found. That means all the initial Cr atoms are in the FeCr alloy structure. From the resulted distributions of magnetic fields it results that in the samples there are *Fe rich regions and Cr rich regions*, that means the samples are inhomogeneous. This behaviour was ascribed to a rather low ball milling time of only 18 hours, at 450 rot / min.

FeCrY and FeCrTiY nanopowder samples were thermally treated at 760 °C, in vacuum.

Magnetic field distributions obtained for treated samples reveals the presence of iron rich and Cr rich regions in the sample. Moreover the evaluation of the Cr content in both FeCrY and FeCrTiY, of approximately 9% instead of ~ 15% in the untreated samples evidences a Cr atoms rejection process during thermal treatment. Based on the presented results and of the exiting literature in the field of FeCr alloys one can infer that Mössbauer spectroscopy is a powerful instrument for the investigation that can be used to improve the elaboration technology of FeCr based materials for fusion reactors.

Introduction

Chromium ferritic/martensitic steels are potential candidates for blanket structural materials in future fusion reactors [1]. Their use for this application requires a careful assessment of their mechanical stability under high energy neutron irradiation [2]. Thus, their chemical composition and thermo-mechanical treatments have been optimized over decades of experimental investigations to resist the expected unfriendly conditions [3]. It was established that the magnetic properties and electrical resistivity depends strongly on Cr content of the binary alloys. For fusion reactor steels, the chromium content is around 10 %. Phase stability of the Fe-Cr system is an essential topic, as the formation of chromium-rich ' α' ' precipitates triggers hardening and embrittlement of ferritic/martensitic steels under neutron irradiation. The peculiarity of the Fe-Cr system is the existence of a wide miscibility gap in the phase diagram where both Fe and Cr are insoluble at room temperature (RT). The chemical arrangement of the atoms in the alloy can either be *random* or exhibit *clustering* among similar atoms [4], according to the preparation method and further heating treatment. Beyond that, the Fe-Cr system is characterised by rich non-equilibrium behaviour.

In the last decade many advanced techniques were applied in order to investigate the relationship structure – physico-chemical properties of Fe-Cr alloys, *inter alia* Mössbauer spectroscopy. This is a versatile technique that can be used to provide information in many areas of science such as Physics, Chemistry, Biology and Metallurgy. It can give very precise information about the chemical, structural, magnetic and time-dependent properties of a material. Key to the success of the technique is the discovery of recoilless gamma ray emission and absorption, now referred to as the 'Mössbauer Effect' (Nobel Prize in Physics in 1961).

Generally, in physical metallurgy, Mössbauer spectroscopy technique has been applied mainly for: 1) monitoring the effect of deliberate modification of the metal by processing, either at the pre-treatment stage; 2) monitoring changes in the metal not caused deliberately, i.e. the side-effects of processing (e.g. reactor steels, and phase transformation during intensive plastic deformation); 3) obtaining information to enable fundamental understanding of metals and alloys (the formation of intermetallic phases in industrial alloys, the influence of metal ions on iron oxide rusts and the study of quasi-

crystalline alloys etc). The information gained has helped the improvement of properties, the monitoring of changes in structures, as well as the development of fundamental understanding of metals and alloys. Mössbauer spectroscopy has been also used to investigate the degree of intermixing of Fe and Cr in solid solutions and amorphous Fe-Cr phases [5, 6].

It is the aim of this project to investigate the local structure in correlation with magnetic properties and to study the short range order in α -Fe materials and some Fe-Cr based alloys obtained by ball milling (potential candidates for blanket structures in fusion reactors).

In agreement with the working plan of the contract (*First round Mössbauer measurements; dead line: June 30th 2010*), this report will present:

- A. Room temperature XRD, transmission Mössbauer measurements and computer analyses of structural and magnetic properties on α -Fe powder and foil;
 - B. Room temperature XRD, transmission Mössbauer measurements and computer analyses of structural and magnetic properties on Fe-Cr powder alloys obtained by ball milling;
 - C. Thermal treatments of the Fe-Cr powder alloys.
- A. Room temperature XRD, transmission Mössbauer measurements and computer analyses of structural and magnetic properties on α -Fe powder and foil**

α -Iron powders from Riedel de Hæn and Merck (both of purity higher than 99.5 %) as well as α -Iron foil were selected for XRD and Mössbauer analyses.

A.1 X-ray diffraction data

Iron crystallizes in the bcc structure (S.G. No. 229) below 912 °C and under low pressure. The lattice parameter according to ICSD is $a = 2.8660 \text{ Å}$. This phase orders in the ferromagnetic mode at relatively high temperature of 770 °C and the magnetically ordered iron having bcc structure is called α -Fe (Figure 1).

Bruker Advance D8 X-ray diffractometer (with $\text{Cu-K}\alpha$ radiation without monochromator) was utilized to record the XRD patterns of our α -Fe samples (Figure 2).

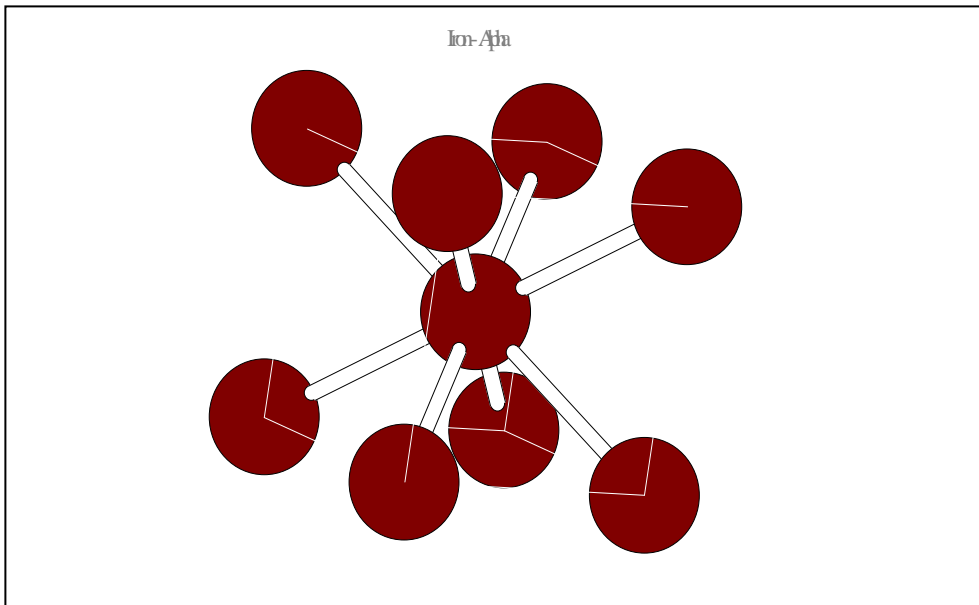


Figure 1. Bcc structure of α -Fe.



Figure 2. Bruker Advance D8 X-ray diffractometer.

In Figure 3, XRD patterns of Riedel de H  en and Merck α -Iron powders are presented.

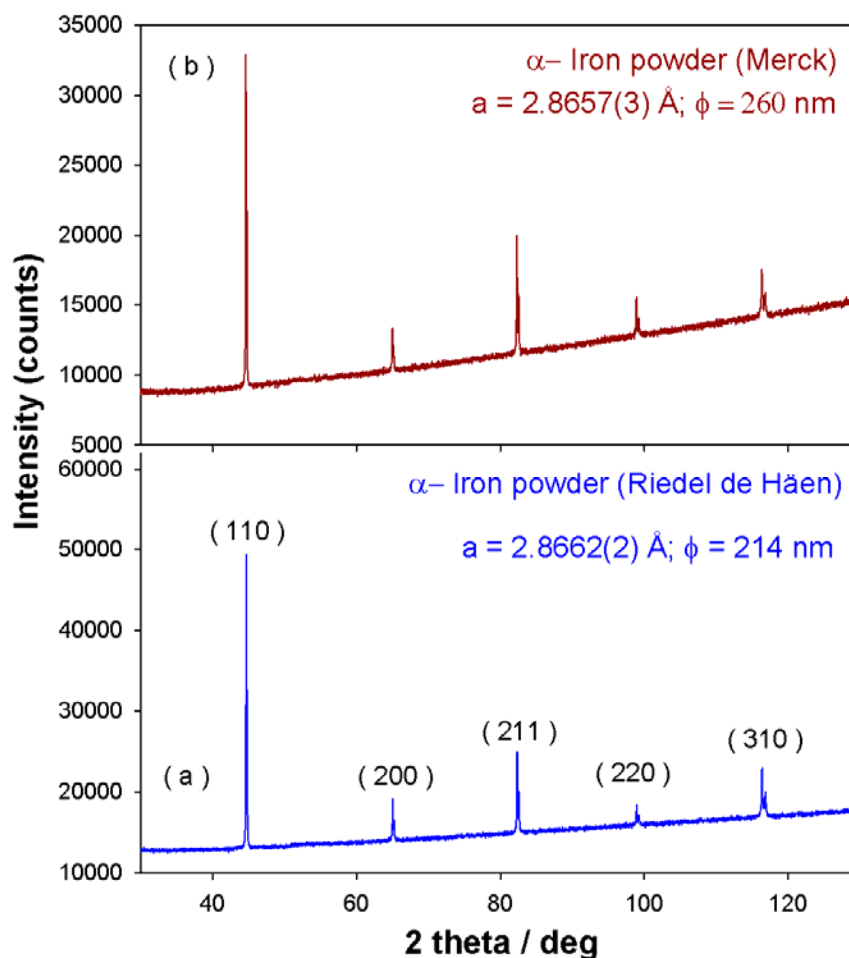


Figure 3. XRD patterns of ‘Riedel de H  en’ and ‘Merck’ α -Iron powders.

The typical α -Fe pattern of can be seen in both cases. The lattice parameters **a** given by Rietveld refinements of XRD patterns are practically the same in the limit of the experimental errors, and very close to the ISCD value of 2.8660   . This behaviour could be an argument for the high purity of the investigated samples.

The XRD pattern of the α -Fe foil (the standard for velocity calibration on Fe^{57} M  ssbauer spectroscopy) is depicted in Figure 4. One can remark the disappearance of the main line (110); this effect can be ascribed to effect of the rolling procedure to obtain thin iron foil as requested for M  ssbauer spectroscopy absorbers.

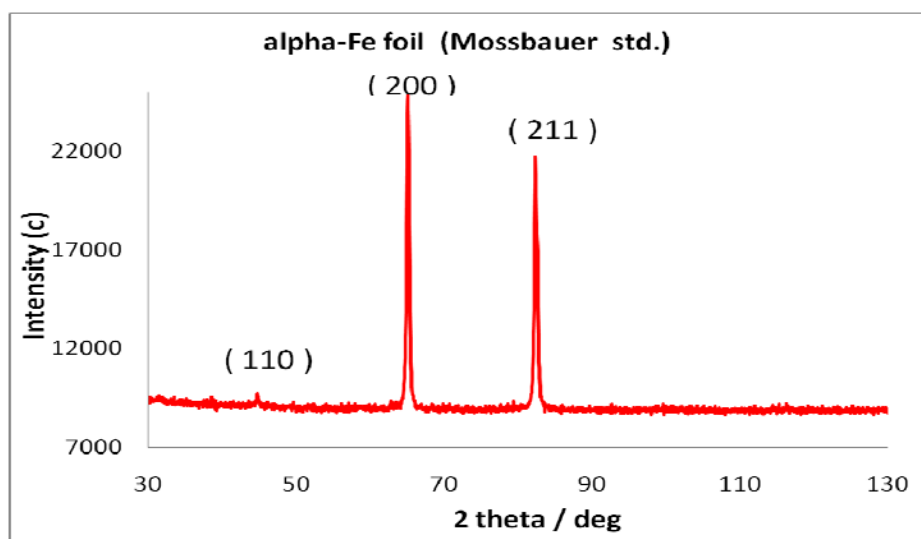


Figure 4. XRD pattern of α -Iron foil.

A.2 Transmission Mössbauer spectroscopy data on α -Fe samples

Mössbauer spectra of the α -Fe samples were recorded at room temperature by means of Promeda (Israel) type standard spectrometer with a WissEL (Germany) acquisition interface (Figure 5a). A 25 mCi Co/Rh source was used in a velocity range of ± 10 mm/s. Helium liquid temperature Mössbauer investigations (to be presented in December 2010) will be performed on a See Co (USA) close cycle cryostat (Figure 5b).



(a)



(b)

Figure 5. Laboratory Mössbauer spectrometers: a) Promeda spectrometer; b) See Co spectrometer.

Figure 6 shows the Mössbauer spectra of the analysed sample. All spectra exhibit a typical six lines magnetic hyperfine pattern characteristic for α -Fe.

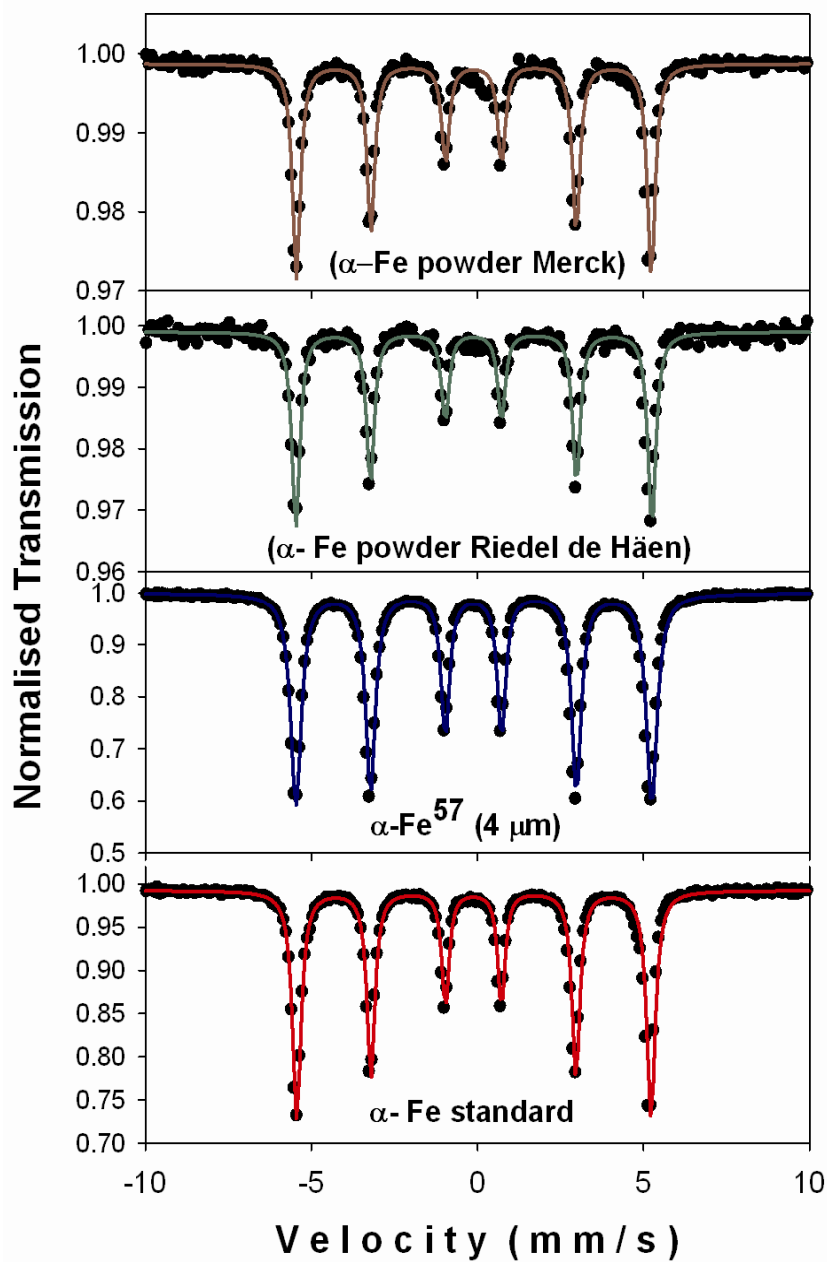


Figure 6. Mössbauer spectra of α -Fe powders and foils together with the computer fit (continuous lines).

In the case of foils we have in fact the spectra commonly used for calibration channel-velocity. Very thin absorbers were prepared (5 mg Fe/cm^2) from iron powder samples in

order to obtain line widths as narrow as possible. The fit parameters in the approximation of Lorentizan line are summarized in the table 1.

Table 1. Mössbauer fit parameters for the α -Iron samples.

Sample	H (T)	IS* (mm/s)	QS (mm/s)	Γ (mm/s)	3:2x:1 2x=
α - Fe powder Merck	33.02	-0.036	0.005	0.282	2.32
α - Fe powder (Riedel de Häen)	33.12	-0.039	0.009	0.285	2.28
α - Fe ⁵⁷ foil (4 μ m)	33.10	-0.039	0.000	0.386	2.52
α - Fe standard	32.96	-0.038	0.009	0.309	2.28
Errors	± 0.04	± 0.002	± 0.004	± 0.003	± 0.01

*IS relative to α -Fe

For all samples the resulted hyperfine magnetic field at the iron nucleus is close to 33.0 T. This behaviour is due to the fact that pure iron is extremely soft magnet with the easy axis of magnetization oriented along one of the principal axes of the chemical unit cell. Therefore, the internal hyperfine field on the iron nucleus is almost entirely due to the *Fermi contact term**, as dipolar fields cancel exactly for the pure iron, while the orbital contribution is almost quenched in the metallic environment of iron and for the 3d magnetic shell [7]. Magnetic moments are well localized in iron [8] and the electric field gradient vanishes on the iron nuclei due to the cubic symmetry. These arguments support the values of the fit parameters (table 1) obtained for α -Fe samples in powder or foils. The observed changes in the intensity from powder to foil are due to the deviation from the ratio 3:2:1 in the case of ideal polycrystalline powder [9, 10] to 3:

$(4\sin^2\theta)/(1+\cos^2\theta) : 1$ where θ is the angle between the Mössbauer gamma-ray and the nuclear spin moment. The stronger effect is evident in the case of a very thin α -Fe⁵⁷ foil. The very narrow line widths support the hypothesis of unique position of iron in the cubic α -Fe lattice. In contradistinction with the XRD patterns which are different from powder to foil, our Mössbauer spectra are similar because the magnetic hyperfine field in α -Fe is given by Fermi contact interaction.

B. Room temperature XRD, transmission Mössbauer measurements and computer analyses of structural and magnetic properties on Fe-Cr powder alloys obtained by ball milling.

B0. Sample preparation by planetary milling

Two samples of FeCr like alloys, FeCrY and FeCrTiY (courtesy of Prof. Jose Brito Correia - IST Portugal) were considered for Mössbauer investigations. The FeCr alloys were prepared by ball milling in argon atmosphere, at 400 rot/min for 18 hours, using planetary mill Retsch PM100MA with Stainless steel vials. The target composition was: 85.2%Fe-14.1%Cr-0.3%Y-0.3%Ti. One of the bunches milling charge was constituted by 17.16g of Fe, 2.82 g of Cr and 0.02g of Y; the other was constituted by: 17.05 g of Fe, 2.82 g of Cr, 0.06 Y and 0.07 g of Ti.

B1. X-ray diffraction data on FeCrY and FeCrTiY obtained by planetary ball milling

According to the equilibrium Fe-Cr phase diagram the disordered bcc solid solution (α phase) exists at temperatures above the spinodal decomposition line. The chromium XRD pattern is very similar to that of α -Fe ($a = 2.8660 \text{ \AA}$) because it crystallize similarly in a bcc structure (S.G. No. 229) with lattice parameter $a = 2.8839 \text{ \AA}$. The difference in their lattice parameters is only 0.62%. The diffraction technique becomes obviously unfavourable when two elemental powders possess nearly identical lattice constants in the same crystallographic structure and result in a homogeneous solid solution.

XRD patterns of both FeCrY and FeCrTiY samples are depicted in figures 7 and 8. Rietveld refinements of the XRD patterns (figure 8a) support the α -Fe structure with very large line width indicating the presence of nanoscaled particles of the order of 10 nm. The cubic lattice parameters for both samples are indicated in the figures 7 and 8. An increase of the lattice parameters with respect α -Fe ($a = 2.8660 \text{ \AA}$) can be observed for

both samples, supporting the presence of Cr, Y and respectively Ti in the bcc structure of iron.

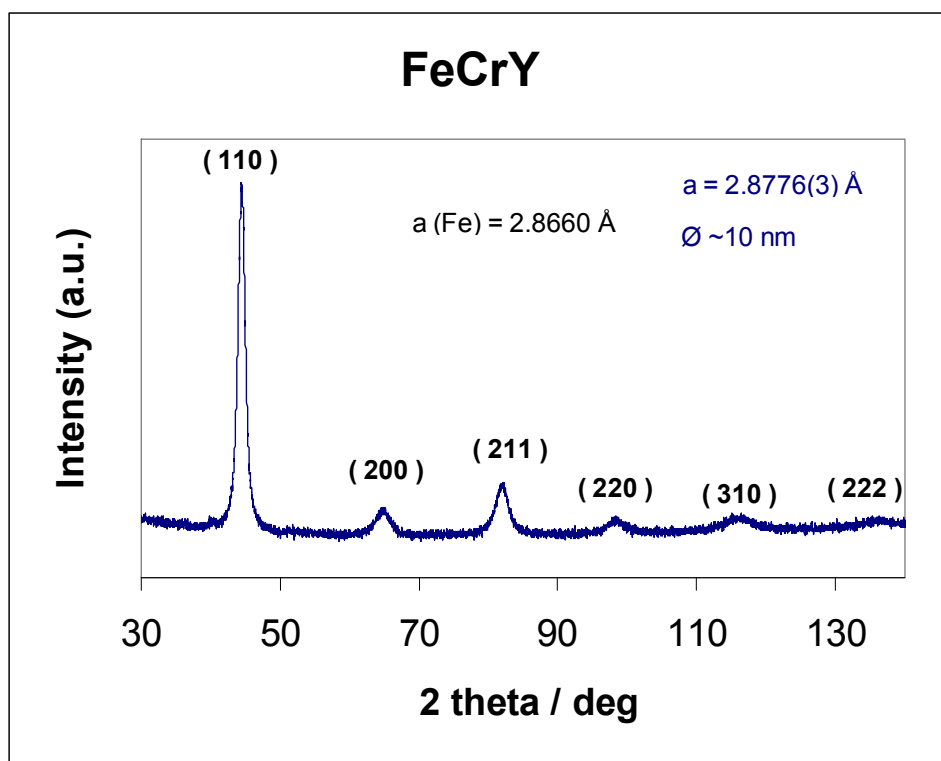


Figure 7. XRD pattern of the sample FeCrY, together with hkl indexes for α -Fe.

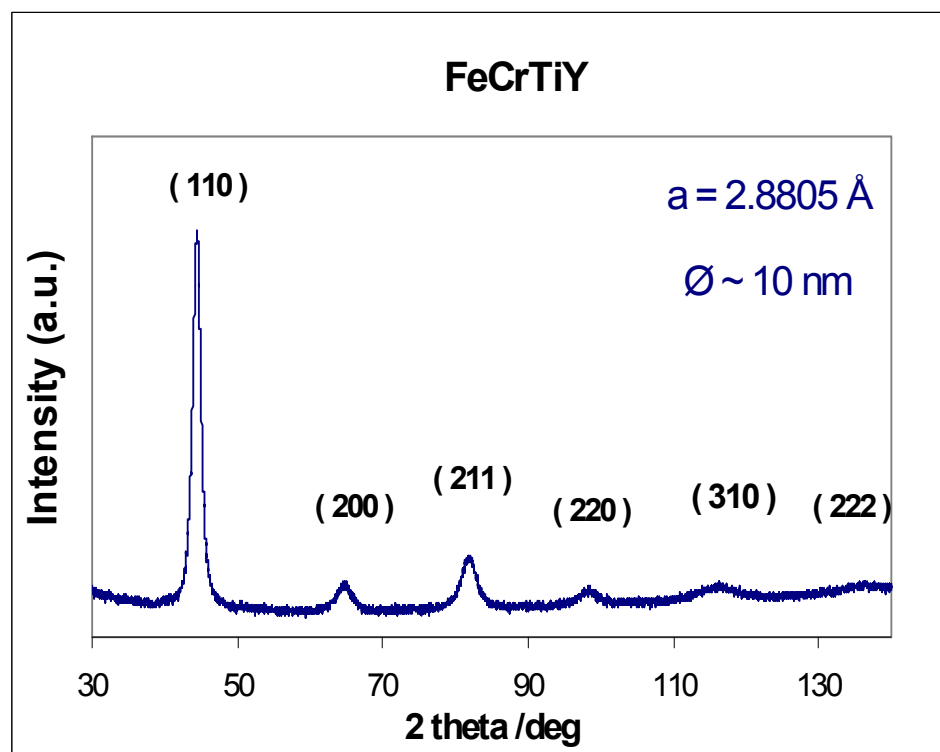


Figure 8. XRD pattern of the sample FeCrTiY, together with hkl indexes for α -Fe.

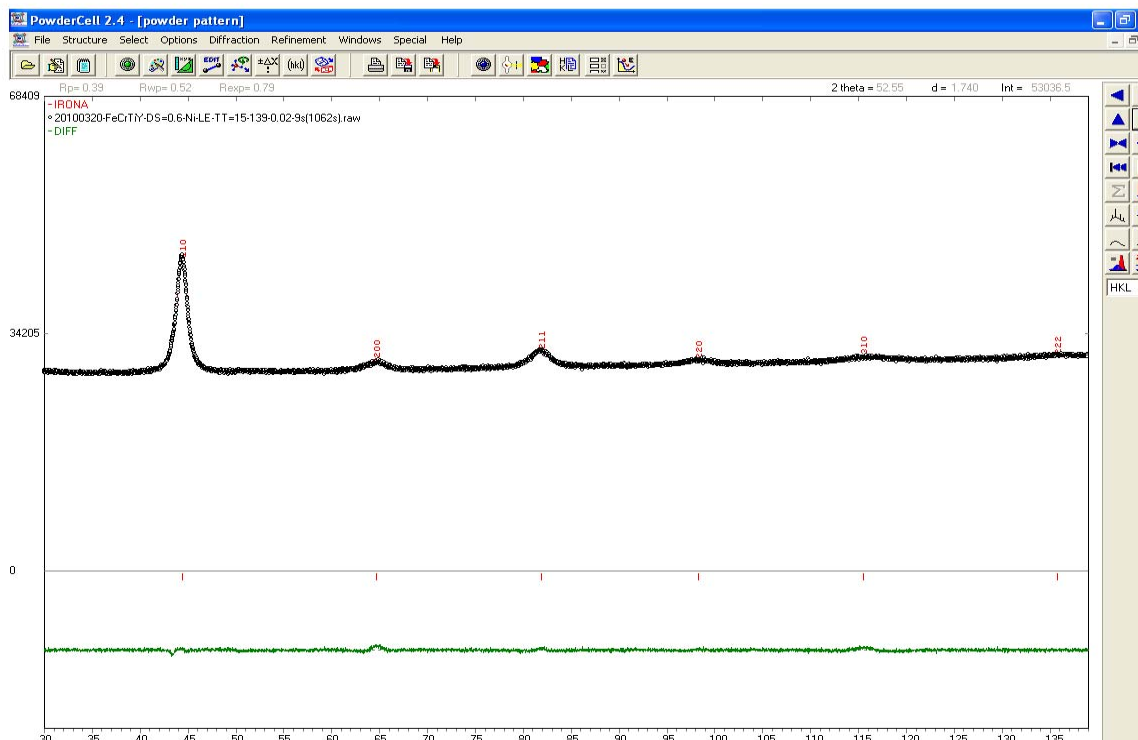


Figure 8a. Rietveld refinement of FeCrTiY sample starting with α -Fe lattice parameters

However, some interesting comments regarding the refinement of XRD patterns of these two samples have to be presented. In the hypothesis that FeCrY or FeCrTiY alloys are not formed after 18 hours of milling, a refinement starting with α -Fe and Cr lattices was performed (figure 9a and 9b). The fit parameters were practically the same with the case when only α -Fe lattice and corresponding substitution elements Cr, Y, Ti were considered (figure 8a). Moreover the same good fit was obtained considering the Cr, Y or Ti occupation factors in the structure or simply α -Fe lattice. All these results can be attributed to the very large line width characteristic for nanoscaled particles that make questionable the refinement of XRD patterns. Though the diffraction lines of the respective elements can be resolved in the starting powders, line broadening owing to the accumulation of strains and defects in the course of the ball milling makes it almost impossible to track the structural change any further.

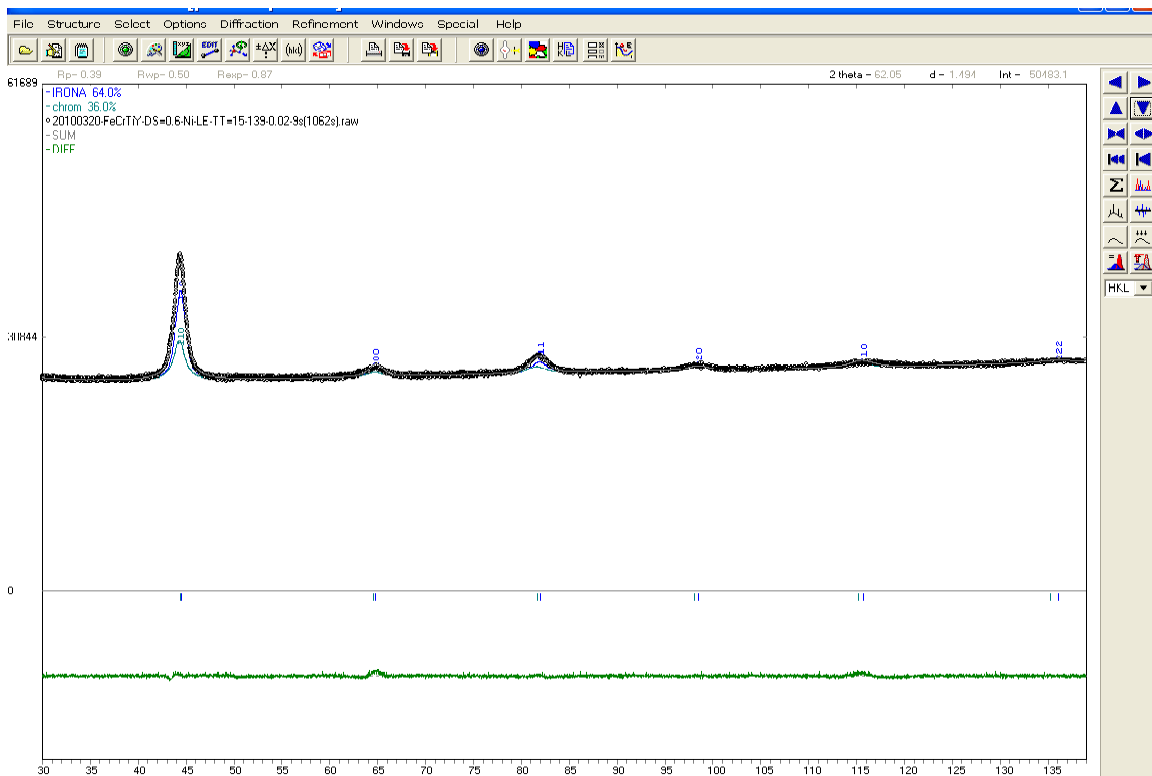


Figure 9a. Rietveld refinement of Ferity sample starting with α -Fe and α -Cr lattice parameters.

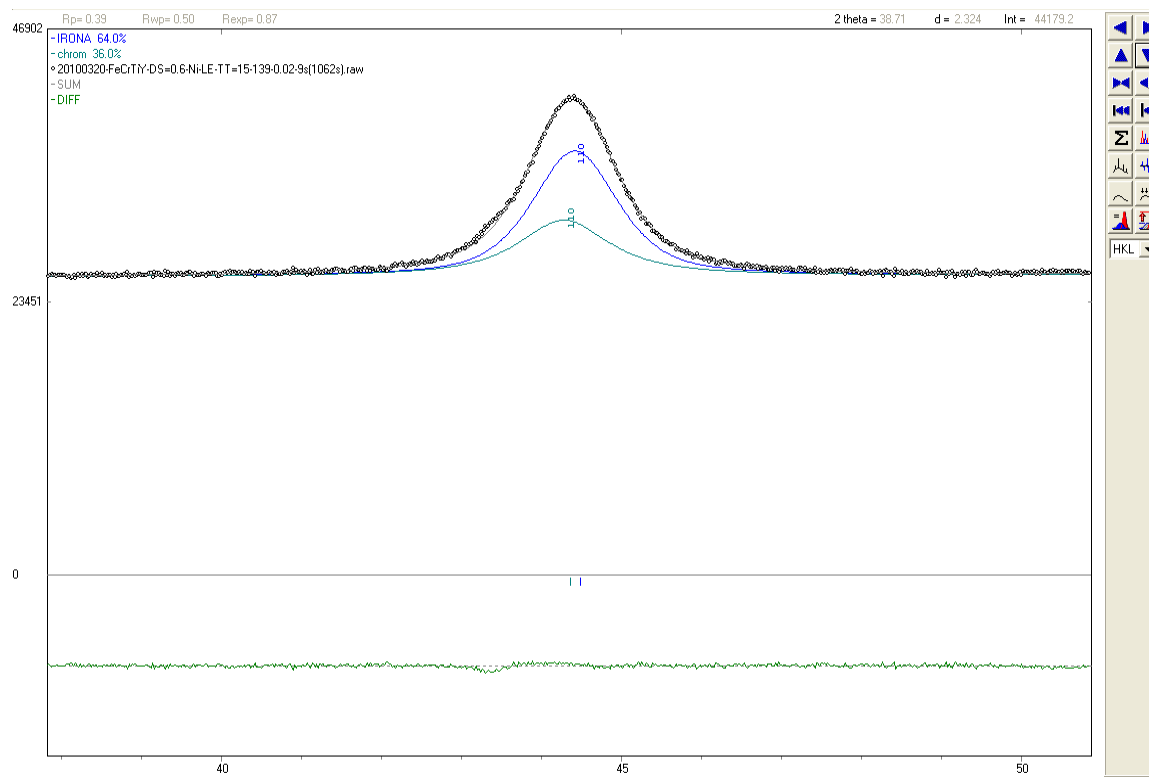


Figure 9b. Rietveld refinement of FeCrTiY sample starting with α -Fe and α -Cr lattice parameters. Details on the main line $\langle 110 \rangle$.

Some complementary methods are required for phase identification and characterization of the studied systems. Due to the relevant presence of iron in our samples the Mössbauer spectroscopy was applied in order to obtain more accurate information about the FeCrYT_i system under mechanical activation.

B2. Transmission Mössbauer spectroscopy data on FeCrY and FeCrTiY obtained by planetary ball milling.

Many metallic *non-magnetic impurities* could be dissolved in the α -Fe on the regular iron sites leading to the binary alloys of the random order [11]. Such impurities do not affect significantly lattice dynamics providing they are sufficiently diluted. They do not generate significant electric field gradients as well due to the effective screening by the conduction band. They could lead to some residual dipolar hyperfine fields on iron nuclei, by these fields are negligible in comparison with the Fermi contact fields. Due to the fact that the system remains highly metallic and cubic no orbital terms are created on iron atoms. Magnetism here is due to the 3d electrons of iron, the latter being sufficiently close to the Fermi surface of the conduction band in order to quench orbital terms. The ferromagnetism of α -Fe is preserved as well for sufficiently diluted impurities. The presence of solute atoms evidently perturbs the hyperfine field characteristic to pure iron. The Mössbauer spectrum for dilute polycrystalline ion alloys was shown to be a superposition of many six line subspectra, each with hyperfine magnetic fields (H) and isomer shift (IS) determined by the near neighbour and next near neighbour dopant concentration [12]. A good approximation is to assume a *random distribution* of solute atoms on substitutional lattice sites, at least for very dilute alloys. It is important however to know which subspectrum is associated with which atomic configuration. The most practical assumption in this context is that the magnetic *hyperfine field is isotropic* i.e. that magnetic field H is determined only by the distance of the solute atom from the iron atom under discussion.

The magnetic properties of Fe and Cr are quite different from each other. α - Iron is ferromagnetic below 770 °C, while Cr is nonmagnetic at room temperature. The α -phase Fe_{100-x}Cr_x alloy, which can be obtained by quenching from temperatures above the spinodal decomposition line, exhibits ferromagnetism in the Cr concentration range 0<x<70, while those with x>76 exhibit mictomagnetism at low temperatures [13]. The Curie- temperature in the α -phase initially increases but begins to decrease with further

increase in the Cr concentration. The magnetic moment almost linearly decreases with increasing the Cr concentration in conformity with the Slater-Pauling curve. This strong dependence of magnetic properties on the Chromium concentration make possible to extract valuable information on the mechanical alloying process in this system. Moreover, the local structure around Fe atoms can be deduced by analyzing the Fe⁵⁷ Mössbauer spectra.

Room temperature Mössbauer spectra of FeCrY and FeCrTiY (figures 10 and 11) exhibit six line patterns significantly modified from the six well-defined resonance lines characteristic of ferromagnetic α -Fe.

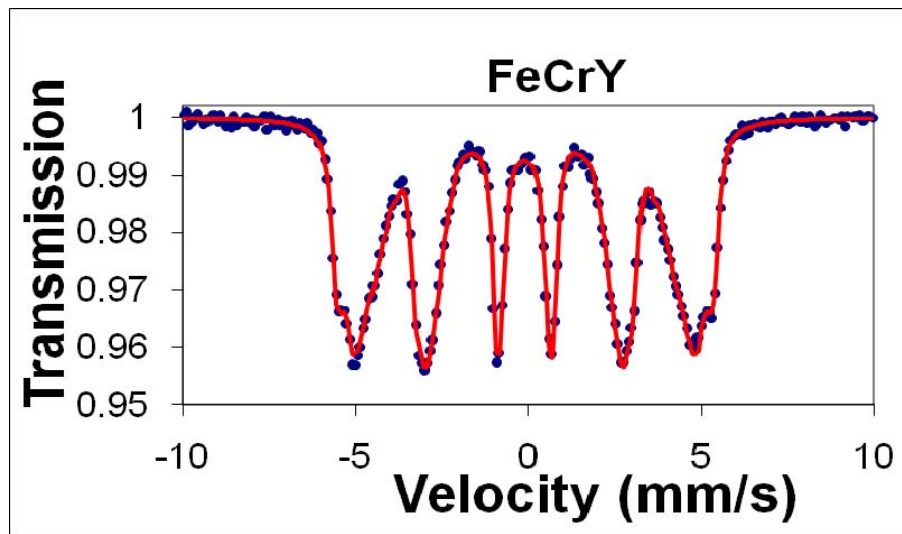


Figure 10. Mössbauer spectrum of the sample FeCrY.

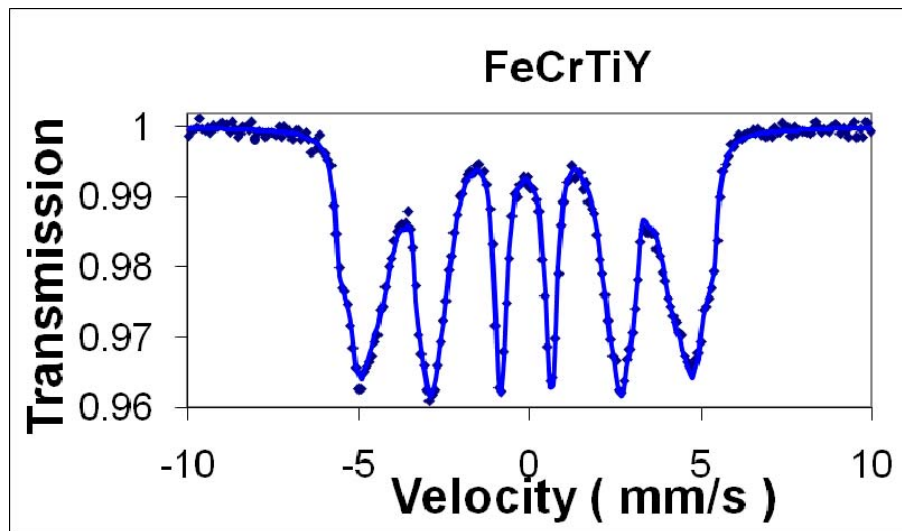


Figure 1. Mössbauer spectrum of the sample FeCrTiY.

This behaviour suggests that we are dealing with solid solution due to replacement of iron atoms by nonmagnetic Cr atom as well as by Y and respectively Ti atoms. The best fit (continuous lines in figures 10 and 11) with the experimental spectra for our samples was obtained assuming a hyperfine magnetic field distribution. A computer program based on Hesse-Ruebartsch model [14] for magnetic field distributions was used. Figure 11a and 12a show room temperature distribution probabilities $P(H)$ versus hyperfine magnetic fields at the iron nucleus in FeCrY and FeCrTiY respectively.

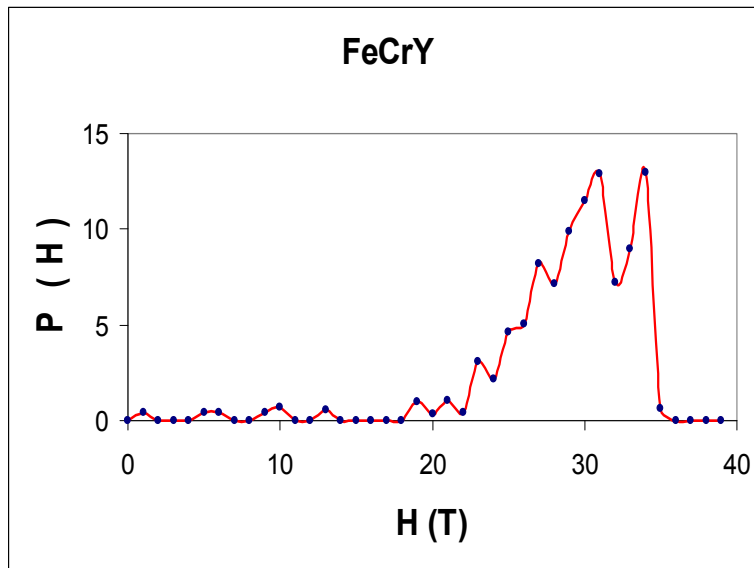


Figure 11a. RT distribution probabilities $P(H)$ versus hyperfine magnetic field for the sample FeCrY.

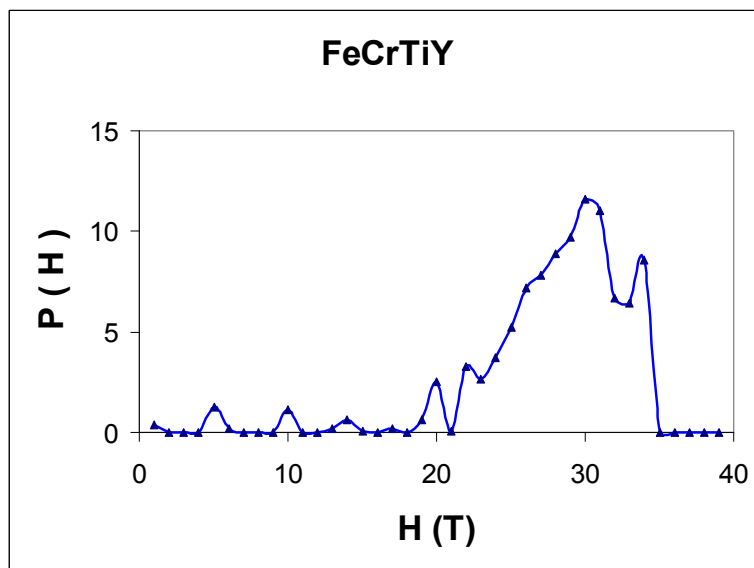


Figure 12a. RT distribution probabilities $P(H)$ versus hyperfine magnetic field for the sample FeCrTiY.

In figures 11b and 12b a tentative to deconvolute the $P(H)$ in Gaussians is depicted.

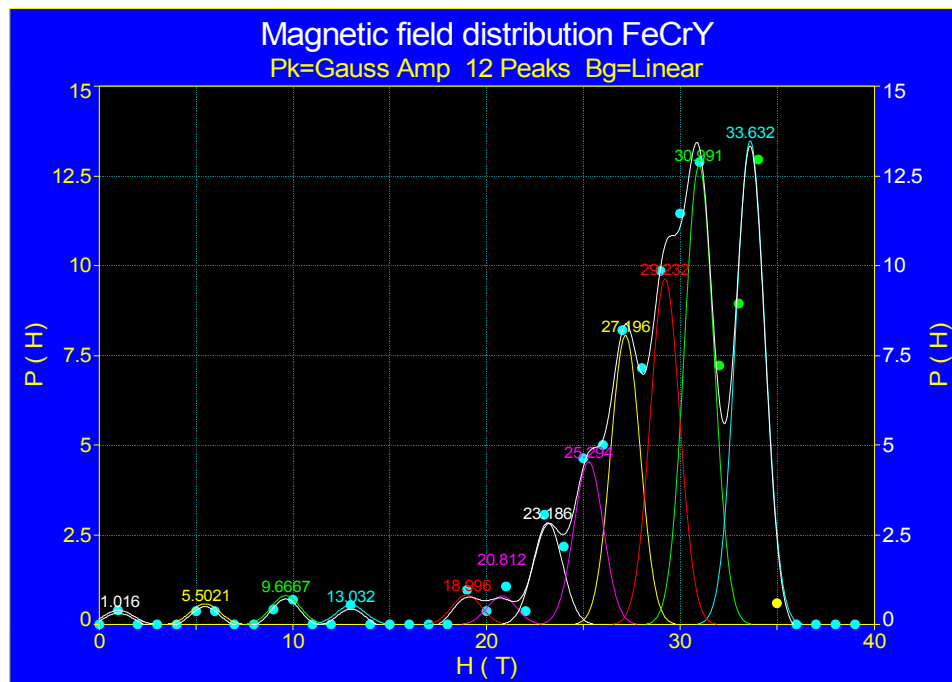


Figure 11b. Gaussian deconvolution of $P(H)$ distribution for FeCrY sample.

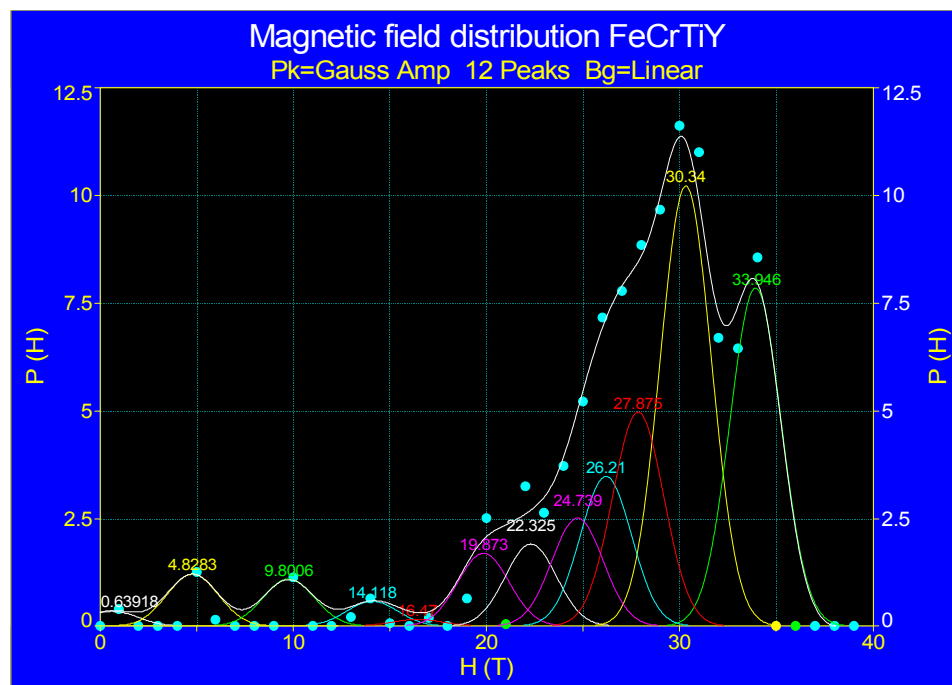


Figure 12b. Gaussian deconvolution of $P(H)$ distribution for FeCrTiY sample.

The main fit parameters for both samples are listed in table 2.

Table 2. RT Mössbauer fit parameters obtained with a magnetic field distribution model. 'IS' is the isomer Shift, ΔEQ is the quadrupolar splitting and $\langle B \rangle$ is the average magnetic field.

Sample	IS* (mm/s)	EQ (mm/s)	$\langle B \rangle$ (T)
FeCrY	-0.011 ± 0.0012	0.013 ± 0.002	28.91 ± 0.05
FeCrTiY	-0.010 ± 0.0017	0.018 ± 0.0034	27.85 ± 0.05
	*(relative to α -Fe)		

The mean hyperfine magnetic field is lower when titanium was added in the sample as expected. The average hyperfine field is calculated considering the magnetic contribution and using the formula:

$$\langle H \rangle = \sum P_i H_i / \sum P_i \quad (1)$$

where $\langle H \rangle$ is the hyperfine magnetic field of the subspectrum i and P_i its relative fraction. For various Fe–Cr magnetic alloys, a linear relation between the magnetic field H and Cr content was given by H. Kuwano [15]:

$$H = 33.07 - 26.58c \quad (2)$$

where c stand for the Cr concentration. The average hyperfine field for the magnetic component yields Cr content in bcc matrix of about 15.1% which is close to the calculated Cr concentration of about 15%. *Therefore Mössbauer spectroscopy could be an useful instrument to determine the Cr concentration in FeCr alloys, with rather good confidence.*

The resulted field distributions for our samples are not Gaussian curves that should indicate a random distribution of Cr, Y and Ti in created alloy. One can remark a peak at 33.8T (FeCrY) and respectively 33.6T (FeCrTiY), well separated from the others at much lower magnetic field values. Taking into account the characteristic magnetic

hyperfine field of α -Fe of $\sim 33.3\text{T}$, we can infer the presence of iron rich and respectively Cr rich regions in our samples. This result agrees well with the results of Fischer [16] and Kuwano [17].

It has been reported that Fe atoms, which possess Cr atoms as the nearest neighbour, exhibit a smaller hyperfine field than that of pure Fe, and its reduction rate per Cr atom is about 30 kOe [18]. We have a drop in the mean magnetic field value of ~ 44 kOe for FeCrY and of ~ 55 kOe in the case of FeCrTiY.

For a better understanding of these effects it is necessary to go more deeply inside the FeCr structure. In Figure 13a a three dimensional structure around Mössbauer iron atom (in red colour) is represented up to the 4th metallic ions shells.

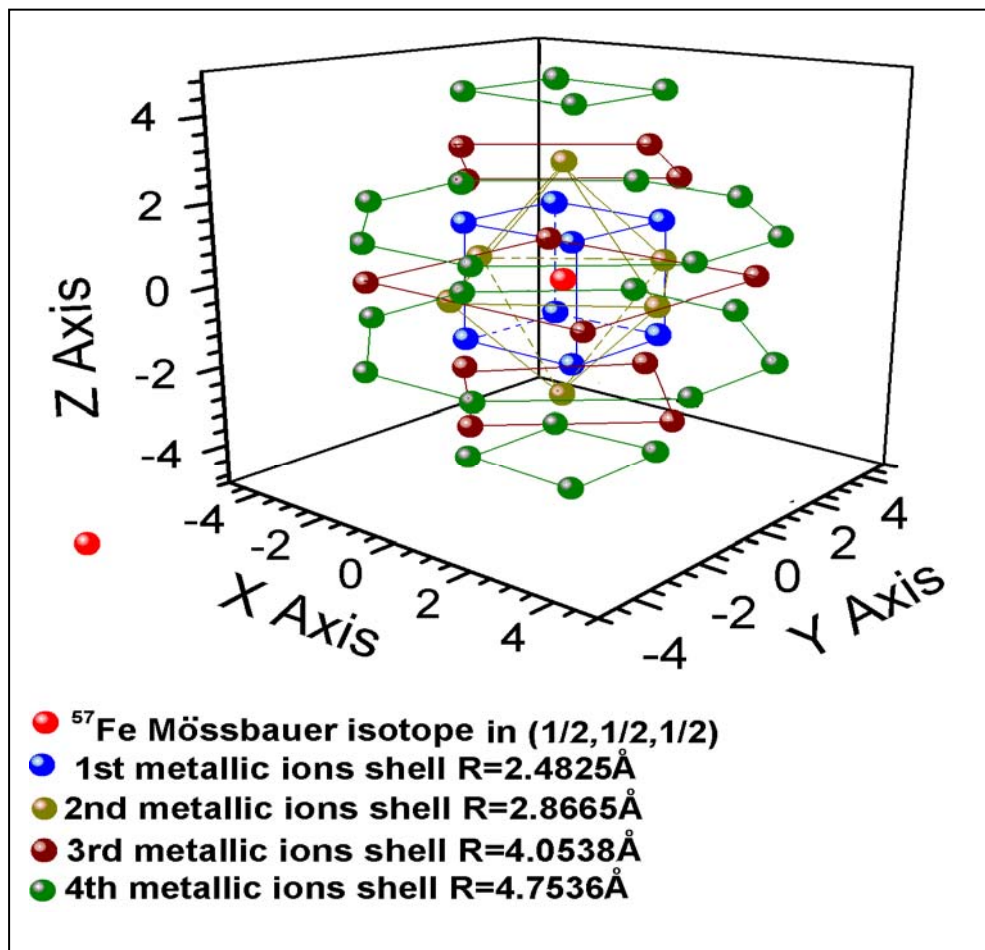


Figure 13a. Local environment around ^{57}Fe Mössbauer isotope in α -FeCr.

The first and the second metallic surroundings are cubic and octahedral ones. The third and the fourth metallic shells contain 12 and respectively 24 neighbours, arranged in parallel planes along Z axis. Probability calculations regarding the substitution of iron atoms by Cr atoms,

versus Cr molar concentration x , (for the first four relevant coordination spheres around the central Mössbauer iron atom), are depicted in Figure 13b.

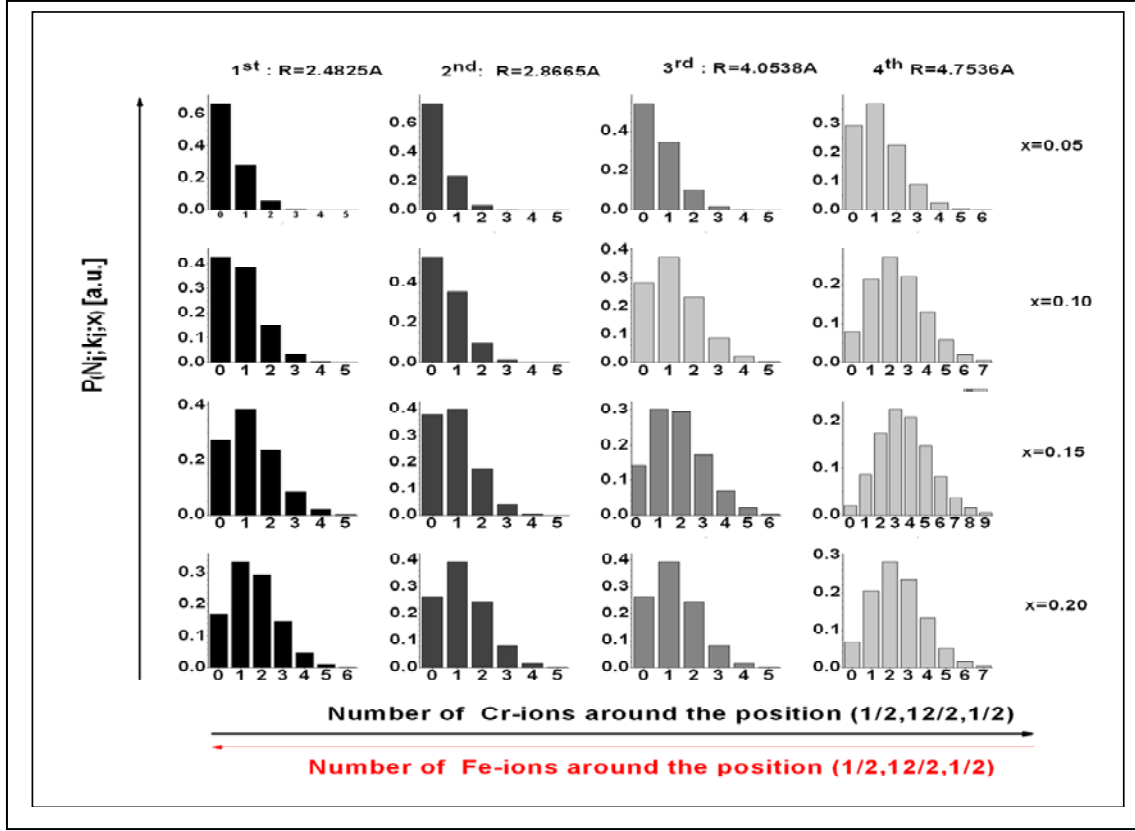


Figure 13b. The binomial probability $P(x; N_j, k_j)$ of the Fe substitution by Cr in the 1st, 2nd, 3rd or 4th vicinity of α -Fe structure where x is the Cr concentration. The asymmetry of the histograms decreases with increasing of x and N_j .

The binomial probability to occupy position k_j from all the N_j positions that belong to the j shell was calculated with the following equation:

$$P(x; N_j, k_j) = \binom{N_j}{k_j} x^{k_j} (1-x)^{N_j-k_j} \quad (3)$$

At $x=0.15$ one can observe that in all four coordination spheres approximately 12-14 Cr atoms have a significant probability to substitute for iron in the bcc lattice of α -Fe, in rather good agreement with the number of relevant magnetic fields in the distribution for the investigated samples (the observed magnetic field distributions in our samples are induced mainly by the Cr atoms because of the prevailing abundance in the studied systems, of about 15%).

C. Thermal treatments of the Fe-Cr powder alloys

The samples FeCrY and FeCrTiY obtained by planetary milling were thermally treated at 760 °C for 2 hours in order to study the phase transformations. The treatments were performed under vacuum in order to avoid oxidations processes. The room temperature Mössbauer spectrum of the sample FeCrY after thermal treatment is depicted in figure 14. The general shape suggests the presence of a magnetic field distribution in the sample. The fit with magnetic field distribution model gives the distribution presented in figures 15a and 15b.

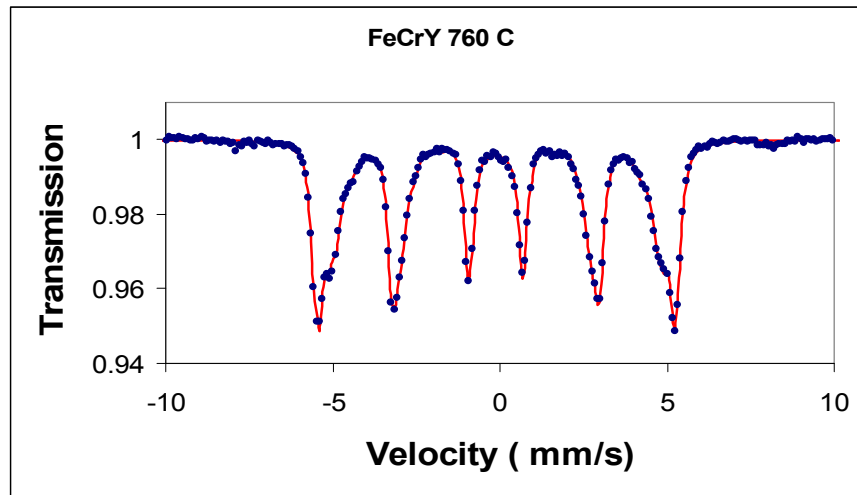


Figure 14. RT Mössbauer spectrum of the sample FeCrY after thermal treatment.

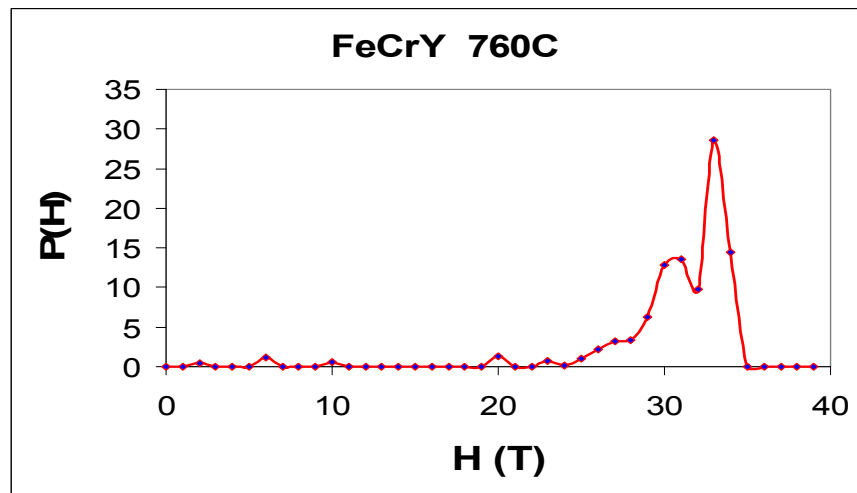


Figure 15a. RT distribution probabilities $P(H)$ of hyperfine magnetic fields for the sample FeCrY after thermal treatment at 760 °C/ 2hours.

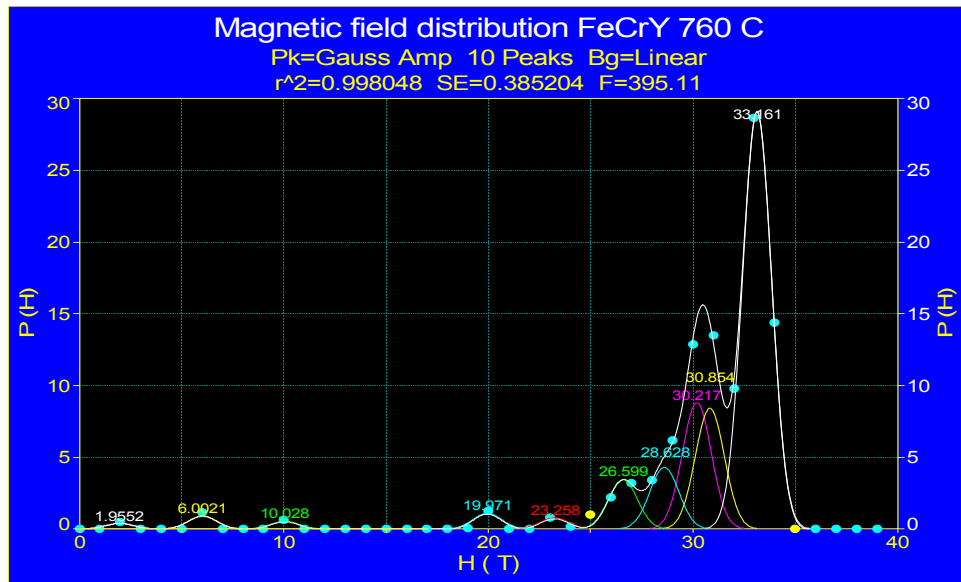


Figure 15b Gaussian deconvolution of P (H) distribution for FeCrY sample thermal treatment at 760 °C/ 2hours.

Room temperature Mössbauer spectrum of the sample FeCrTiY after thermal treatment at 760 °C and the corresponding hyperfine field distribution are depicted in figures 16 and 17a, b.

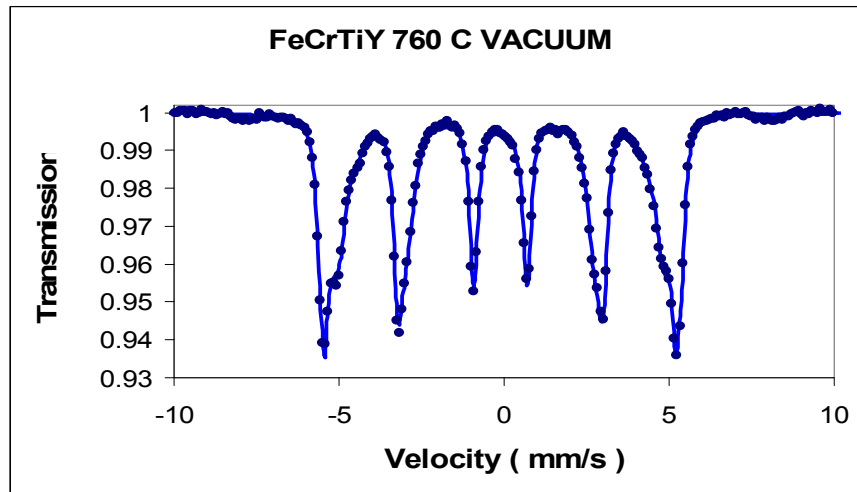


Figure 16. RT Mössbauer spectrum of the sample FeCrTiY after thermal treatment at 760 °C/ 2 hours.

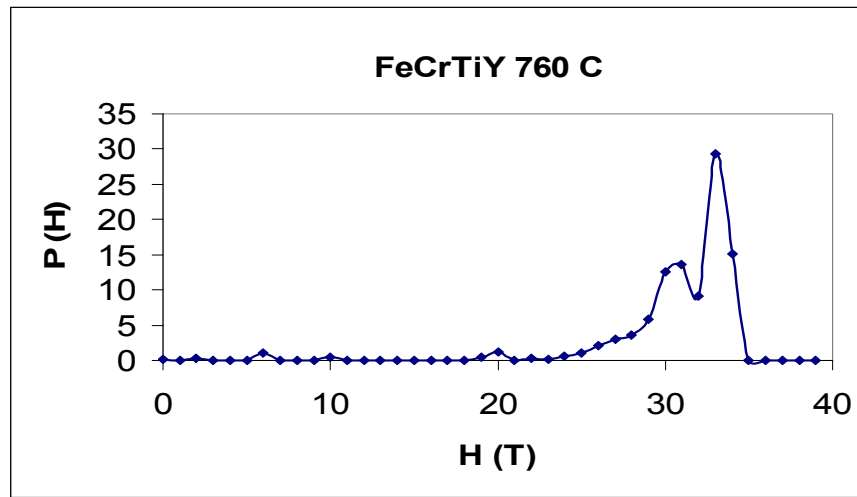


Figure 17a. RT distribution probabilities $P(H)$ versus hyperfine magnetic field for the sample FeCrTiY after thermal treatment at 760 °C/ 2hours.

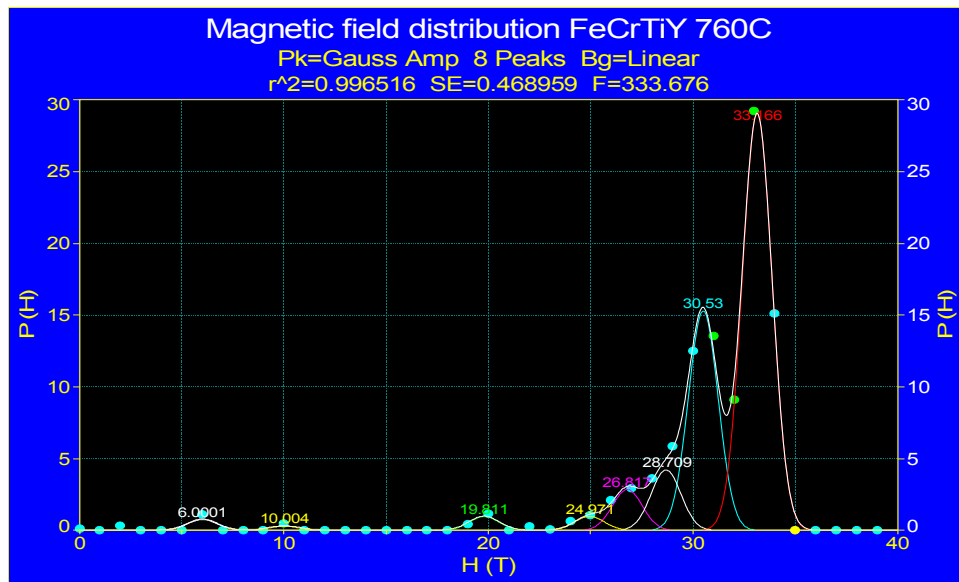


Figure 17b. Gaussian deconvolution of $P(H)$ distribution for FeCrTiY sample thermal treatment at 760 °C/ 2hours.

From the behaviour of the magnetic field distributions we can infer the existence of rich iron region and rich Cr regions. In comparison with the untreated samples the Cr rich regions are less abundant. The dominant peak in the distribution belongs to α - Iron that reach a 30 % of probability. Table 3 shows the fit parameters for both samples after thermal treatment. The mean magnetic field values for the treated samples are: 30.63 T for FeCrY sample and 30.71 T for FeCrTiY sample. Considering the relation (2) for the

calculation of chromium concentration knowing the mean magnetic field one obtain $c \approx 9\%$. Therefore we can infer a reject process of Cr atoms from the FeCr structure during the thermal treatment at 760 °C.

Table 3. RT Mössbauer fit parameters obtained with a magnetic field distribution model for thermally treated FeCrY and FeCrTiY at 760 °C.

Sample	IS* (mm/s)	EQ (mm/s)	<H> (T)
FeCrY 760 °C	-0.005 ± 0.0013	0.009 ± 0.002	30.63 ± 0.05
FeCrTiY 760 °C	-0.005 ± 0.0014	0.007 ± 0.004	30.71 ± 0.05
	*(relative to α -Fe)		

Conclusions

α -Fe samples in powder or foils as well as two samples FeCrY and FeCrTiY obtained by planetary milling in argon atmosphere were investigated by means of XRD and transmission Mössbauer spectroscopy at room temperature. In addition, thermally treated FeCrY and FeCrTiY samples (at 760 °C under vacuum conditions) were studied by Mössbauer spectroscopy.

α -Fe based samples

- From the studied X-ray diffractograms, one can infer that all samples of α -Fe powder and foils present the same cubic bcc structure.
- Rietveld refinements revealed very close values of lattice parameters proving the high purity of the investigated samples.
- RT transmission Mössbauer spectra display similar six line patterns characteristic for bcc α -Fe structure. The difference between powders and foils of are given by

the intensities of the lines 2 and 5 due to the alignment of the nuclear magnetic moments in the foil samples.

FeCrY and FeCrTiY samples at room temperature

- It was evidenced that XRD cannot be used for a reliable phase analysis because of the isostructural behaviour of α -Fe and α -Cr and the effects of very large line width in the case of nano scaled particles. However, Rietveld refinements were used to obtain the lattice parameters and particle size (Scherrer equation). A particle dimension close to 10 nm was obtained for both samples.
- Mössbauer spectroscopy investigations revealed a FeCr alloy structure, being able to evidence the hyperfine field distribution given by the Cr, and Ti atoms substituting iron in the studied systems. The presence or contribution of high radius Y atoms cannot be directly evidenced by Mössbauer spectroscopy at least for such small amount of yttrium in the system.
- From the mean magnetic field values given by Mössbauer spectra fitting, the atomic Cr concentration in the studied FeCr based alloys was determined and compared with the nominal known concentration. A very good concordance was found. That means all the initial Cr atoms are in the FeCr alloy structure.
- The calculation of the binomial probabilities to find Cr atoms in the first four coordination spheres around Mössbauer Fe atoms agrees well with the obtained magnetic field distribution given by Mössbauer spectra fitting within a distribution model.
- From the resulted distributions of magnetic fields it results that in the samples there are *iron rich regions and Cr rich regions*, that means the samples are *inhomogeneous*. This behaviour could be ascribed to a rather low ball milling time of only 18 hours, at 450 rot / min. We expect that a superior milling time will produce a much more homogeneous sample. This statement is very important because can help to improve the process of the synthesis of the FeCr based alloys for specific applications. Cr rich regions are unwanted because triggers hardening and embrittlement of ferritic/martensitic steels under neutron irradiation.

FeCrY and FeCrTiY samples after thermal treatment at 760 °C, in vacuum.

- Magnetic field distributions obtained for treated samples reveals the presence of iron rich and Cr rich regions in the sample. Moreover the evaluation of the Cr content in both FeCrY and FeCrTiY, of approximately 9% instead of ~ 15% in the untreated samples evidences a Cr atoms rejection process during thermal treatment. Much more samples should be analysed in order to conclude this effect might be associated with the mecanochemical route for the preparation of fine particle FeCr based alloys. On the other hand, the problem of the influence of Cr on the average field is complex and a comparison of results obtained by various authors is difficult due to different routes used to prepare the samples.
- Based on the presented results and of the exiting literature in the field of FeCr alloys one can infer that Mössbauer spectroscopy is a powerful instrument for the investigation of iron based alloys. Mössbauer data can help improving the synthesis technology giving unique information on the structure and interactions in the system.

One can conclude that all the tasks of the period Mars 1st – June 30th are fully achieved. Based on the presented results and considering the very challenging Mössbauer equipments available in the Institute, our research group can be considered for the future topics regarding the characterization of FeCr based alloys in correlation with the elaboration technologies, for fusion reactors applications.

References

- [1] R. L. Klueh, D.R. Harries, High-Chromium Ferritic and Martensitic Steels for Nuclear Applications, ASTM, 2001.
- [2] K. Ehrlich, Fus. Eng Des. 71, 56-57 (2001).
- [3] M. Matijasevic, A. Almazouzi, Journal of Nuclear Materials 377,147–154 (2008).
- [4] S. Dubiel, C. Sauer, W. Zinn, Phys. Rev. B 30, 6285 (1984).
- [5] B. F. O Costa, S. M. Dubiel and J. Cie’slak, J. Phys.: Condens. Matter 18, 3263–3276 (2006)

- [6] F.Z. Bentayeb, S. Alleg, B. Bouzabata, J.M. Greneche, JMMM 288, 282–296 (2005)
- [7] A. Balachowski, Vol. 114 (2008) *ACTA PHYSICA POLONICA A*, 117, 6 (2008).
- [8] A.H. Morrish, *Physical Principles of Magnetism*, Wiley-IEEE, New York 2001.
- [9] N.N. Greenwood, T.C. Gibb, *Mössbauer spectroscopy*, Chapman and Hall Ltd. London (1971).
- [10] D. Barb, *Efectul Mössbauer si Aplicatiile sale*, Ed. Academiei Bucuresti 1972; *Grundlagen und Anwendungen der MosbauerSpektroskopie*, Berlin 1980.
- [11] J. Cieslak, S.M. Dubiel, *J. Alloys Comp.* 350, 17 (2003).
- [12]. G.K. Werthaim, V. Jaccarino, J.H. Wernik, D.N.E. Buchanan, *Phys. Rev. Lett.*, 12, 24 (1964).
- [13] C. Bansal, T. Kumaran, S. J. Campbell, and G. L. Whittle, *Phys. Rev. B* 44, 7111 (1991).
- [14] J. Hesse and A. Rübartsch, *J. Phys. E: Sci. Instruments* 7, 352-532 (1974).
- [15] H. Kuwano, *Trans. Jpn. Inst. Met.* 26 473 (1985).
- [16] R.M. Fischer, E.J. Dulis, K.G. Carroll, *Trans. AIME* 197,690 (1953).
- [17] H. Kuwano, Y. Hamaguchi, *J. Nucl. Mater. B*, 1071, 155-157 (1988).
- [18] S. M. Dubiel and J. Zukrowski, *J. Magn. Magn. Mater.* 23, 214 (1981).

—•—

In agreement with the working plan of the Contract, for the period 1st July – 15th December 2010 the following activities are scheduled:

- **Second round Mössbauer measurements. Dead line: December 15th, 2010**
- Room temperature transmission Mössbauer measurements on Fe-Cr powder alloys obtained by ball milling, after thermal treatments. (*This point was already presented in the present report; in case EFDA partners could provide us other interesting FeCr samples, we shall consider them for Mössbauer investigations*).
- Liquid helium temperature transmission Mössbauer measurements on Fe-Cr powder alloys obtained by ball milling (*measurements already started in the laboratory*).

- Backscattering Mössbauer spectroscopy studies by Conversion electron Mössbauer spectroscopy (CEMS) measurements and Conversion X-ray Mössbauer spectroscopy (CXMS) measurements on relevant samples.
- Data computing and analysis of short range order (SRO), local structure and magnetic properties.

Dr. Lucian Diamandescu

National Institute of Physics, Bucharest, Romania

Project:

FUNCTIONAL GRADIENT W-STEEL MATERIALS BY UNCONVENTIONAL CO-SINTERING ROUTES

< MAT-WWAlloys-01-01 >

First stage: April-June 2010:

Process parameters and preparation routes for W-Fe FGM

Report content

- Main lines of the project and scientific content
- First stage main lines
- Summary of the work performed
- Main scientific and technical results
- Conclusions and future steps
- References
- Summary of the report (Romanian)

Main lines of the project and scientific content

The development of the DEMO fusion reactor is a priority of the EU. In this frame the construction of the reactor structure is a complex and fast evolving domain. This includes joining, machining, fabrication process development, and mock-up testing on the basis of the current He cooled divertor design. Thus identification of fabrication related material issues and implications for tungsten materials development are important. In general, W is going to be used as armor material while Eurofer is going to be used as structural material, with the expectation that ODS steels will replace Eurofer in various parts of the structure in the future. Development of functional gradient materials (FGM) for the transition from W to Eurofer steel, using co-sintering of property gradient alloys with low or reduced activity is a key issue in this work.

The main goal for this year is to realize W-steel FGM. Thus different proportions of W-steel powders will be mixed (and/or mechanical alloyed) by ball milling. About 40 samples with 4 to 10 layers of these powders will be sintered by different routes using unconventional sintering like spark plasma, hot press or microwave. The composition and microstructure of the materials will be evaluated by SEM and EDX. Other properties like specific heat (DSC, TG-DTA), thermal transport (Laser Flash technique) and electrical transport will be investigated at temperatures up to or above 1000 C.

First stage main lines

In the first stage the **process parameters and preparation routes for W-Fe FGM** will be obtained experimentally aiming to obtain solid and mechanical consistent samples.

Summary of the work performed

In this first stage of the project FGM W-Fe cylindrical samples with 10-20 mm diameters and 1-10 mm heights have been sintered at different temperatures and applied pressures. The samples were realized by spark plasma sintering (SPS) or classical sintering starting with mixtures of Fe and W powders in 1:0, 1:1, 1:2, 1:3 atomic proportions, placed in up to 7 different layers with thickness from 0.2 to 5 mm. A typical specimen is depicted in figure 1



Fig.1 Typical W-Fe FGM specimen, realized by SPS at 1120 C and 80 MPa in Ar.

SEM and EDX investigations have been performed for all the samples, aiming to investigate the influence of layer thickness and compositions as well as the role of different sintering temperatures and pressures and process optimisation. Important results were obtained concerning the effects of different thermal and electrical conductivities of W and Fe in SPS process, the oxygen influence on sintering process and the diffusion of Fe and W in final materials. Finally the results are also a test of our equipments capabilities.

Main scientific and technical results

Fe spherical powder with grain sizes from 1-4 μm and W powders 0.5-10 μm have been mixed by ball milling at low energy in 1:0, 1:1, 1:2, 1:3 atomic proportions. The start materials SEM pictures are shown in figure 2.

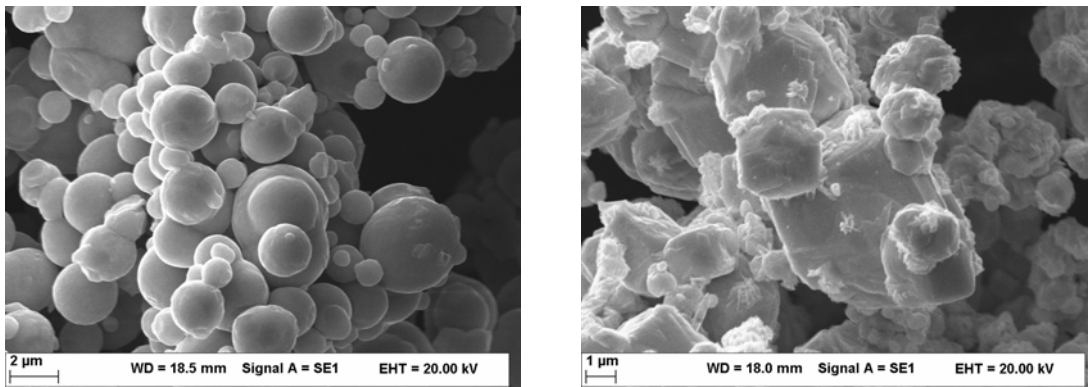


Fig. 2. Fe start powder (left) and W start powder (right)

The different shapes of the Fe and W grains allowed us to visually monitor the sintering effect in final materials. From this powder mixtures up to 7 different layers have been placed in graphite mold and sintered at 980-1450 C, 0-100 Mpa in Ar or air by SPS. Analysis of SEM and EDX results showed that Fe diffusion in W is higher than W diffusion in Fe. This result can be clearly deduced from the EDX specific metal profiles as shown in figure 3.

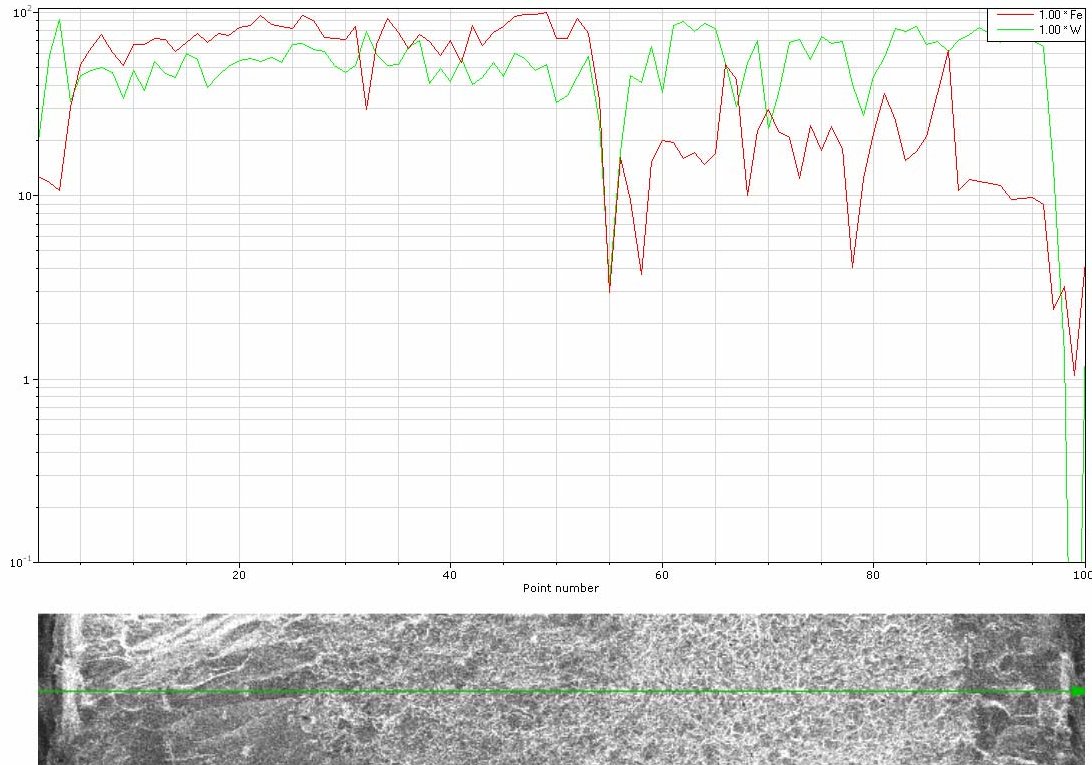


Fig 3. A 0.5 mm zone at the border of 1:1 FeW to W (each about 0.25 mm) in a sample produced by SPS at 1450 C in Ar at about 50 Mpa. Left zone FeW (Fe = red), note the slight decrease of Fe content. Right zone W, note about 15% Fe content.

The Fe diffusion can be seen in the entire W rich zone, up to the sample edge. A quantitative EDX analysis at this edge confirms presence of Fe and also a higher oxygen content at this edge compared to the Fe rich edge. The result of this analysis is shown in figure 3.

One should also notice the relatively high C content in the material. This is due to the C migration from the graphite mold.

From this results some important improvement for sample preparation have been inferred and will be used during the next stages of the project.

- ▶ the powder manipulation should be performed only in protective or reducing atmosphere.
- ▶ a BN coating of the graphite mold might be useful to reduce the C diffusion in the sample
- ▶ using a metallic W plate at the W rich sample edge will lead toward a 100% W zone.

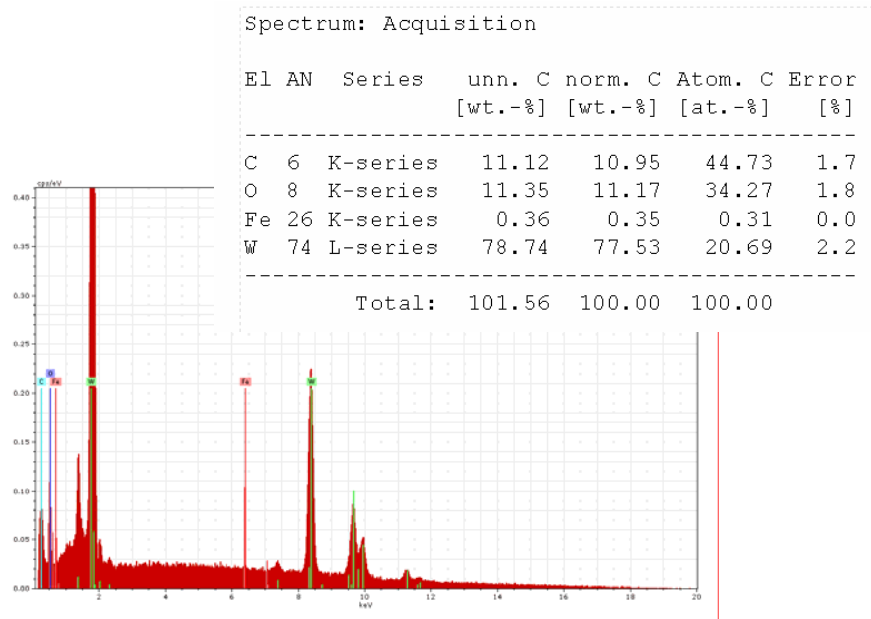


Fig 3. EDX spectrum and analysis results at the W rich edge of the sample

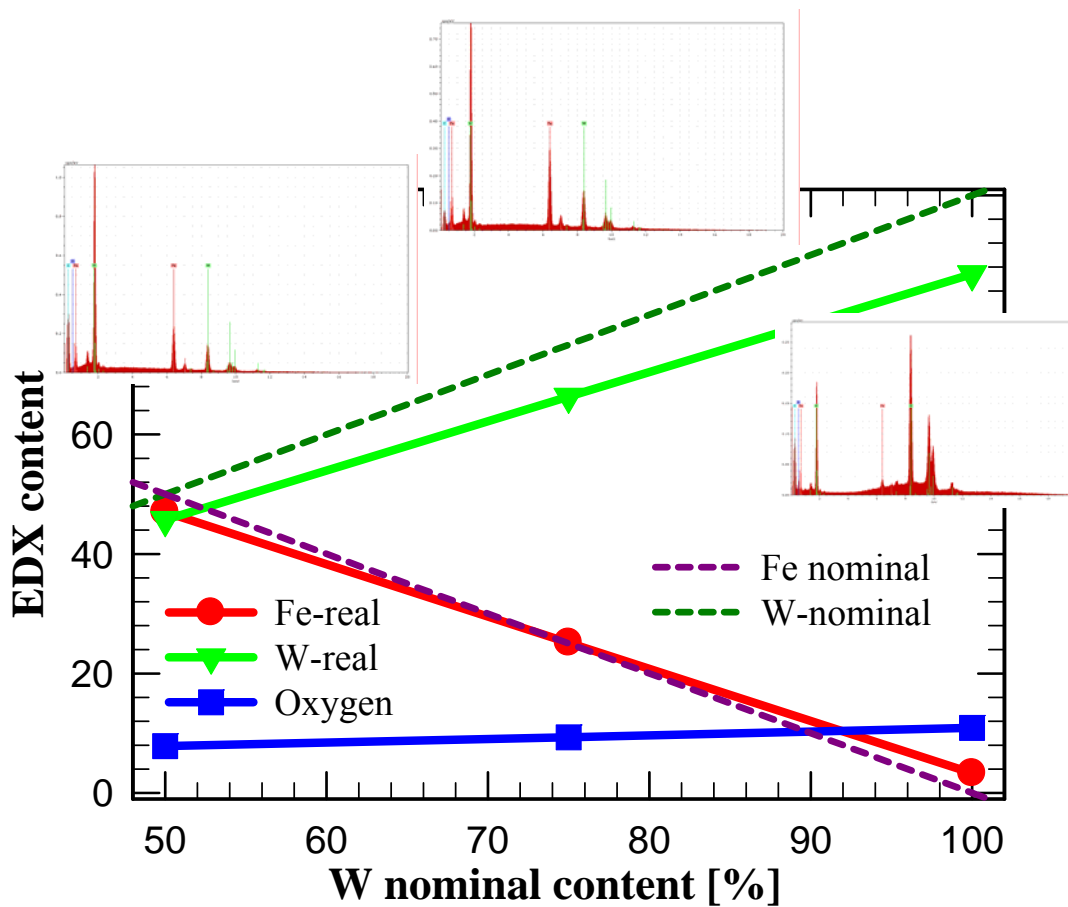


Fig 4. Oxygen content along a Fe-W FGM sample (SPS at 1450 C in Ar, at about 50 MPa powder manipulation in air)

As mentioned before, we have noticed the presence of O in the samples and the oxidation effect is important to the strength of the samples. Thus EDX spectra have been recorded in different zones of the samples. A typical result is plotted in figure 4.

The quality of the Fe-W FGMs can be estimated from the sample morphology. Thus SEM pictures have been recorded from different areas in the section of the samples. Some typical results and improvement possibilities are presented below.

Sintering of Fe-FeW-W gradient material at 1120 C

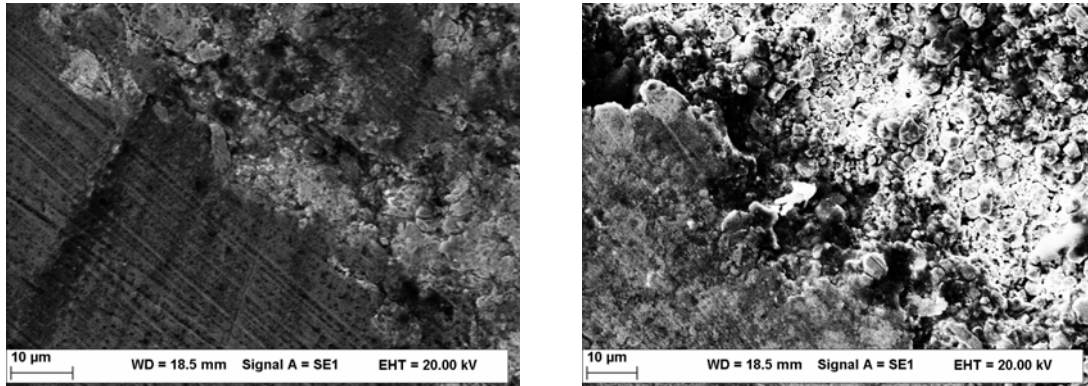


Fig. 5. SEM results for a FGM obtained by SPS at 1120 C in Ar, at about 80 Mpa, section cut with a diamond saw. Left (Fe 100%) - (Fe 50% W 50%) interface, right (Fe 50% W 50%) – (W 100%) interface

In figure 5 SEM results for a FGM obtained by SPS at 1120 C in Ar, at about 80 Mpa, are shown for different layer interfaces. One can observe a generally sharp change in the sample morphology. Thus we concluded that more layers are necessary for a proper gradient and also a decrease of layer thickness is needed. Comparison with other results and the literature brought the conclusion that 1100 C is the lowest temperature possible for effective sintering of powders with μm grain size

Sintering of Fe-Fe₂W-FeW₂-W gradient material at 980 C

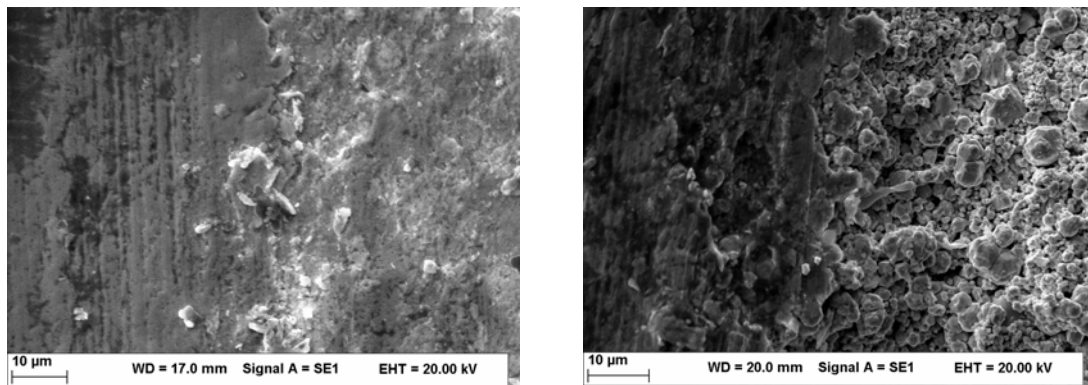


Fig. 6. SEM results for a FGM obtained by SPS at 980 C in Ar, at about 80 Mpa, section cut with a diamond saw. Left (Fe 100%) - (Fe 75% W 25%) interface, right (Fe 25% W 75%) – (W 100%) interface.

In figure 6 SEM results for a FGM obtained by SPS at 980 C in Ar, at about 80 MPa, are shown for different layer interfaces. A sharp change can be observed at 100%-

75% interface, but a better gradient appears in the sample middle sections. Thus one can draw the conclusion that more layers and thinner toward sample edges are necessary. Concerning the work temperature a lower contraction was recorded, pointing to the necessity of a higher sintering temperature.

Sintering of Fe-FeW-W gradient material at 1450 C

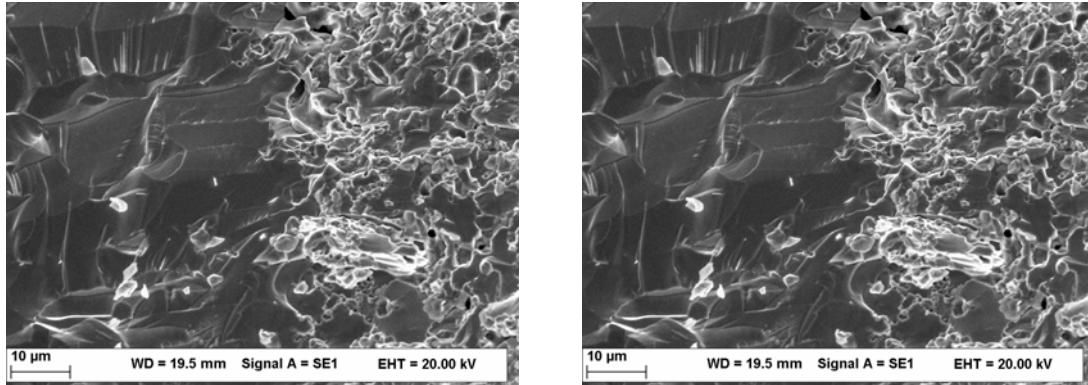


Fig. 7. SEM results for a FGM obtained by SPS at 1450 C in Ar, at about 50 Mpa, in a fracture section. Left (Fe 100%) - (Fe 50% W 50%) interface, right (Fe 50% W 50%) – (W 100%) interface

In figure 7 SEM results for a FGM obtained by SPS at 1450 C in Ar, at about 50 MPa, are shown for different layer interfaces. One can observe a melting process result in the Fe rich area. This melting can be explained by the lower thermal and electrical conductivity of the Fe compared to W at high temperature. The former induces a longer time necessary for the dissipation of the accumulated heat while the later produces an enhanced Joule heating of the sample in this area. Thus a decrease of the sintering temperature might be necessary to avoid partial sample melting. On the other hand, as shown in figure 8, a very good sintering was observed in the Fe-W mixture area with a general compaction of the sample toward 100%.

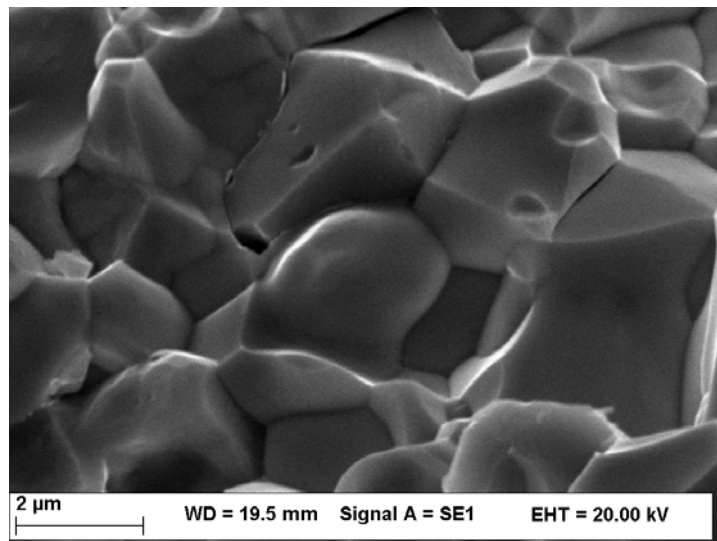


Fig. 8. An almost perfect sintering of the Fe-W mixture obtained by SPS at 1450 C.

Conclusions and future steps

The investigation of process parameters and preparation routes for W-Fe FGM was performed in this stage shows that sintering of samples 10-20 mm diameter, 1-10 mm height with 0.2-5 mm thick layers is possible at 1100-1400 C with moderate pressures. For an apparent morphologic gradient 2-4 thin layers toward each margin composition are necessary.

EDX and SEM results show that Fe diffuses more in W than W in Fe. Also we observed that oxygen is more present in W rich layers. Thus we conclude the necessity of powder manipulation in protecting atmosphere.

Since both thermal and electrical conductivity of Fe are lower than those of W the temperature must be lower in Fe rich zones. Slightly lower sintering temperatures or an improved design of the molds is important to avoid partial melting of the sample.

Using these results, in the second stage the sintering process will be optimised for different W-steel FGM and the properties of the resulting materials will be analyzed and compared to the requirements of the DEMO design.

The present results will contribute to the development of material science and advanced materials for DEMO. The information and know-how obtained will be a start point for further work concerning property gradient joint between W-Eurosteel by unconventional co-sintering.

References

- R.M. German, Z.A. Munir. Metallurgical Transactions A, **7A** (1976) 1873.
- G. Prahbu, A. Chakraborty, B. Sarma, Int Journal of Refractory Metals & Hard Metals; **27** (2009) 545.
- Y. Kawakami, F. Tamai, T. Otsu, K. Takashima, M. Otsu, Solid State Phenomena; **127** (2007) 179.
- H. Wang, Z. Zak Fang, Kyu Sup Hwang, H. Zhang, D. Siddle, Int Journal of Refractory Metals & Hard Metals; **28** (2010) 312.

Summary of the report (Romanian)

In cadrul acestei etape au fost realizate probe de materiale cu gradient functional (FGM) din pulberi de W si Fe prin sinterizare asistata de camp electric sau clasica. Au fost obtinute specimene cilindrice cu diametre de 10-20 mm si inaltime de 1-10 mm la temperaturi cuprinse intre 980 si 1450 C sub influenta unor presiuni moderate (sub 100 MPa). Probele contin 3-7 straturi de amestec de pulberi de Fe si W in proportii atomice 1:0, 1:1, 1:2, 1:3 cu grosimi intre 0.2 si 5 mm.

Investigatii prin SEM si EDX au fost realizate pentru a monitoriza influenta grosimii si compozitiei straturilor, precum si efectul diferitilor parametri de sinterizare in vederea optimizarii procesului. Rezultate importante au fost obtinute privind efectul conductibilitatii termice si electrice diferite in cazul Fe si W, influenta O in procesul de sinterizare precum si difuzia relativa a Fe si W in matrice. Rezultatele constituie si un test pentru posibilitatile echipamentelor utilizate, succesul obtinut asigurand trecerea in cadrul fazei urmatoare la producerea de FGM pe baza de W si oțeluri speciale.

SECTIUNEA 1

RAPORTUL STIINTIFIC SI TEHNIC

FAZA DE EXECUTIE NR. 1.

CU TITLUL:

**ANALIZA MICRO SI NANO-STRUCTURALA PRIN T.E.M., X-EDS, E.E.L.S.,
XRD SI SPECTROSCOPIE MOESSBAUER A MATERIALELOR REZULTATE
IN FAZELE DE PROCESARE TEHNOLOGICA PENTRU OBTINEREA
OTELURILOR FERITICE TIP O.D.S. (O.D.S.F.S.) SI A
ALIAJELOR DE W TIP O.D.S.**

- ☐ **RST – raport stiintific si tehnic in extenso**
- ☐ **PVAI – proces verbal de avizare interna**
- ☐ **PVRLP – procese verbale de receptie a
lucrarilor de la parteneri***
- ☐ **PF – protocol de finalizare(numai pentru faza
finala)**

* forma si continutul se stabilesc de catre conducatorul proiectului, tinand seama de cele continute in PVAI

REPORT on PROGRESS

**Stage of research performed in the frame of the
contract nr. 1EU-8 / 01.03.2010**

entitled

**MICRO AND NANO-STRUCTURAL ANALYSIS BY T.E.M., X-EDS,
E.E.L.S., XRD AND MOESSBAUER SPECTROSCOPY OF THE
PROCESSED MATERIALS IN VARIOUS TECHNOLOGICAL
STAGES OF O.D.S. FERRITIC STEELS (O.D.S.F.S.) AND O.D.S. W-
ALLOYS ELABORATION**

**concerning the following activities mentioned in the
EFDA WP10-MAT-ODSFS task agreement**

WP10-MAT-ODSFS-01-01/MEdC/BS

WP10-MAT-WWALLOY-01-01/MEdC/BS

**P.I. Dr. Corneliu Sarbu
project responsible**

**Natl. Inst. for Mater. Physics
Magurele-Bucharest, Romania**

June 2010

CONTENT

General and partial objectives	pag-4
Abstract	pag-5
Results of the research performed until June 30th	
The materials. The instruments	pag-6
The XRD results	pag-7
The X-EDS microanalysis results obtained by TEM and SEM	pag-9
The experimental X-EDS data acquired from the two MA fabricated powder alloys	pag-12
 The Moessbauer spectroscopy results	pag-20
The classical TEM results	pag-22
The HRTEM results	pag-23
About the applicability of EELS method	pag-24
Conclusions	pag-26
Bibliography	pag-27
Annex 1-RST	pag-28

GENERAL OBJECTIVES

The reported research aims at matching the two following general objectives:

(i) Developing the present generation of nano-structured ODSFS by optimising the chemical composition and determining a set of parameters for the Mechanical Alloying (MA) process and the subsequent Thermal-Mechanical Treatments (TMT), aimed at reproducing the main microstructure features identified as responsible for the high strength and the limited loss of fracture toughness after irradiation. The optimisation will concentrate on chemical composition of the 14Cr-Y-W-Ti (14YWT) type.

(iii) Developing an optimised generation of nano-structured & nano-grained ODSFS. The ODS ferritic steel is a driving system and the aim is the fabrication of ODS ferritic steels with improved plasticity. The nano-grain sized 14YTW alloys will be produced on the laboratory scale using (i) High Energy Ball Milling (HEBM), (ii) consolidation, i. e. extrusion and/or spark plasma sintering, and (iii) thermo-mechanical treatment (TMT). The effect of hot extrusion parameters on microstructure and mechanical behaviour will be characterised to select the best fabrication route for an optimised strength-ductility relation. The microstructure is expected to be characterized using transmission electron microscopy (TEM), atom probe tomography (APT), and related methods.

PRESENT STAGE OBJECTIVES HAVING JUNE 30 AS DEADLINE

According to the contract, the partial objectives assumed for the first round of analysis (deadline June 30, 2010) are:

- a) analysis of a powder of mechanically alloyed alpha-Fe with Y₂O₃
- b) analysis of a powder of mechanically alloyed alpha-Fe with Ti and Y₂O₃
- c) analysis of consolidated samples (if supplied in due time by the foreign partner) obtained from these powders;
- d) analysis of final ODSFS samples (if supplied in due time by the partner), obtained by extrusion from the consolidated materials;

We have to pointed out that, according to the contract, our work of analysis is highly dependent on the supply of samples by our foreign partner.

Not all the above mentioned *objectives proposed for the 1-st round of research (deadline June 30)* were accomplished till end of June 2010, because of the delay in the supply of samples from our partner. Therefore, until June 30-th only the *partial objectives labelled above as (a) and (b) are accomplished*.

The contract stipulation (see Section B-4) referring to this foreseen situation is mentioning that: “if necessary, the analysis of samples supplied with delay by our Portuguese partner will be extended beyond June 30, 2010”.

ABSTRACT

A couple of powders fabricated by the Mechanical Alloying (MA) procedure was studied. These powders are intended to be used as starting materials in subsequent procedures leading to an ODS steels (ODSFS).

The informations we will supply to the powders producer are important for the setting of MA process parameters, which has a technological importance.

We drew the general conclusion that there is a clear inhomogeneity of the elemental composition of the powders, which means that the MA parameters should be modified.

RESULTS OF THE RESEARCH PERFORMED UNTIL JUNE 30th

The materials. The instruments

We have investigated 2 samples of mechanically alloyed (M.A.) powders, intended to have the following elemental composition:

Fe-Cr-Y-Ti (labelled as sample-1)

Fe-Cr-Y (labelled as sample-2)

which were kindly supplied by Dr. Jose Brito-Correia from the Association IST, i.e. Instituto Superior Tecnico (Universidade Tecnico de Lisboa), Lisbon, Portugal.

The samples were prepared by mechanical alloying (MA) starting with pure elements, according to the already reported recipe: Fe (99%, 44 μm), Cr (99.95%, particle size < 25 μm), Y (99.9%, median particle size 500 μm) and Ti (99.9%, particle size < 105 μm). The milling was done in stainless milling media, at 400 rpm for 18 hours, in a planetary mill model Retsch PM100MA. One of the batch milling charge was constituted of 17.16 g Fe, 2.82 g Cr and 0.02 g Y. The other batch milling charge was: 17.05 g Fe, 2.82 g Cr, 0.06 g Y and 0.07 g Ti.

The target composition in view to result for MA of powders was:

85.2wt%Fe-14.1wt%Cr-0.3wt%Y-(0.3wt%Ti)

The dissolution of Y₂O₃ in the Fe-Cr solid solution during MA was previously communicated [1] in the litterature.

The instruments used for micro and nano-characterization are:

(1) X-ray diffractometer Bruker D8 Advance, in Bragg-Brentano configuration, working with filtered Cu-K α radiation. The powder diffractograms were acquired by setting high quality parameters: angular steps of 0.02deg and dwell times of 8s/step and 9s/step.

(2) analytical TEM electron microscope model JEM-200CX-TEMSCAN, generating an electron beam of maximum 200kV. It is equipped with an attachment allowing the work in SEM mode besides TEM mode. It is equipped also with an X-EDS spectrometer model EDS2004 made by IXRF Systems Inc., 15715 Brookford Drive, Houston, Texas. It operates with a detector mounted in high position, i.e. working at a takeoff angle of 72deg., which is favourable because the sample has not to be tilted away from horizontal in order to acquire a good quality spectrum. In the TEM mode of operation (at 40, 80, 120, 160 and 200 kV) the electron beam cannot be focussed as microbeam, which means that the focussed beam can analyse only

particles as a whole which frequently includes also some of its surroundings. In the SEM mode of operation the achievable focussing is that of micrometers diameter.

The main advantage offered by this instrument is that it can work in SEM mode at much higher accelerating voltages than in dedicated SEM microscopes. These highly focussed energetic beams can penetrate and generate X-rays from very deep levels inside the material.

(3) dedicated SEM microscope model Zeiss EVO, with a maximum acceleration voltage of 30kV. It is equipped with a Bruker made X-EDS spectrometer.

(4) analytical (HR)TEM electron microscope made by FEI, model Tecnai™ G-2 F-30 S-TWIN, operated at 300kV. This instrument is able to generate very finely focussed electron beams (up to nanometer size diameters). It is equipped with an X-EDS spectrometer made by EDAX, the detector being positioned at low level (detector angle 14.6deg), which means that it can work when shifted very close to the sample (at 11.8mm). This is allowing a very good collection of the X radiation.

The XRD results

The high quality X-ray diffractograms generated by the 2 samples and acquired in angular steps of 0.02° and with a dwell time per step of 9s are looking very similar, as shown in Fig-1.

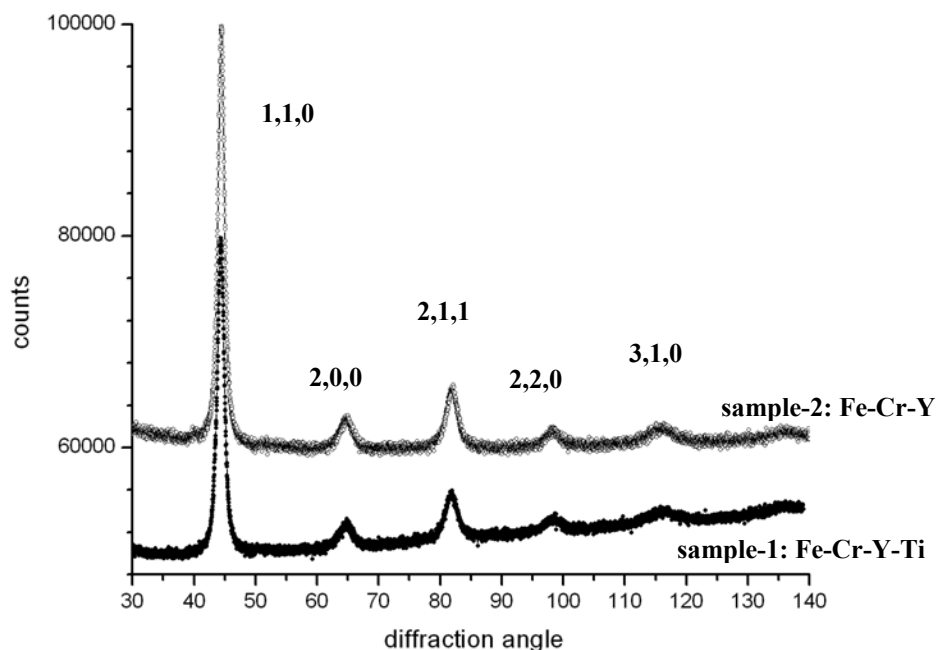


FIG-1

The peaks pattern of the 2 samples corresponds very well to the cubic b.c.c. crystallographic structure (Im-3m, SG 229) and can be indexed as shown. It is to be noticed that the diffraction lines are largely broadened, the FWHM of peaks being almost the same in both diffractograms.

The Powder Diffraction Files (PDF) database used for matching the 2 diffractograms has shown best fit for both with the PDF-file nr. 00-034-0396. This is the reference for the matrix (solid solution of Fe and Cr) of the 434L ferritic stainless steel. This very good fit is demonstrated in FIG-2.

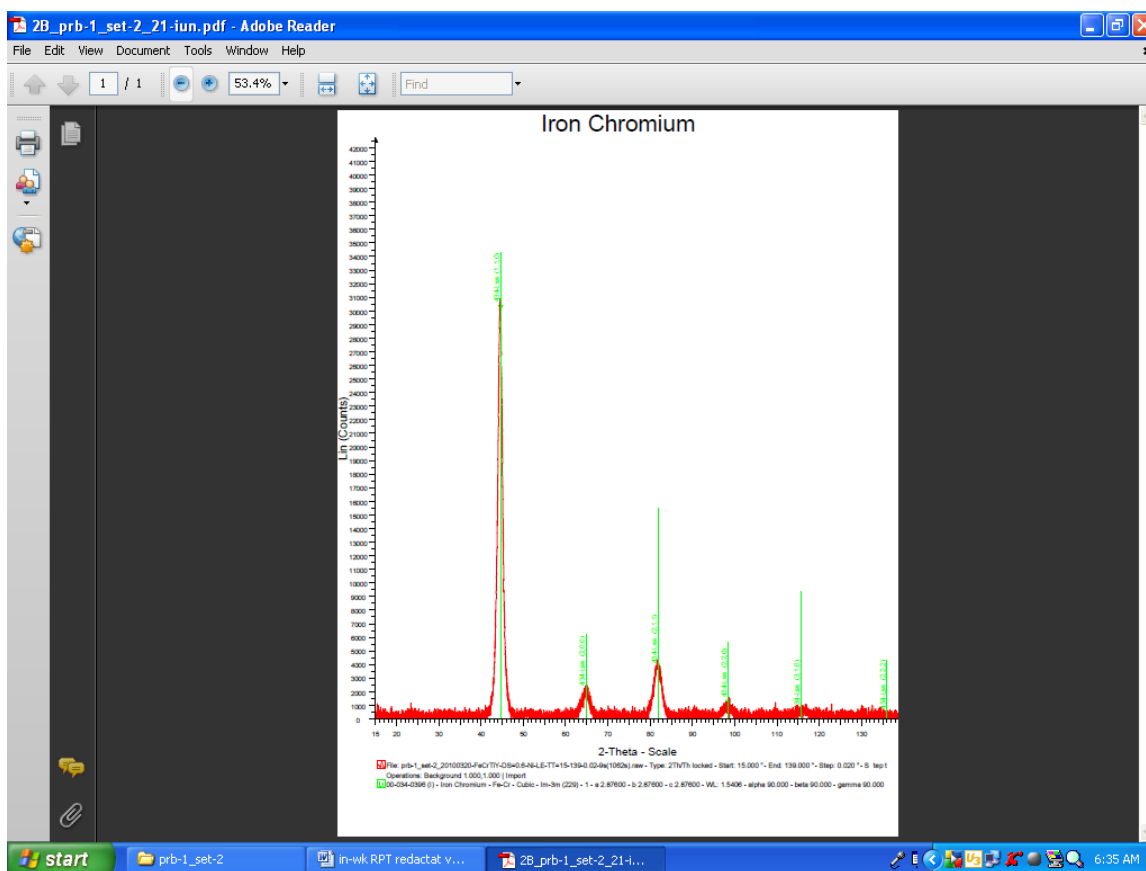


FIG-2

A worse fit occurs with the PDF-file nr. 03-065-7775 which is the reference of another b.c.c. structure of a Cr-Fe solid solution labelled as Cr1.07Cr18.93. A comparison of the different quality of the two fits can be best revealed by looking at the strongest reflexion (1,1,0), as shown in FIG-3 (a) and (b). FIG-3(a) proves that the fit with the b.c.c. structure (Im-3m, SG 229, matrix of 434L steel, lattice constant 0.2876nm) is better than the fit (see FIG-3(b)) with the similar structure of Cr1.07Fe18.93 (having a lattice constant of 0.2869nm). The same fitting quality is valid for all the peaks of the experimental diffractograms.

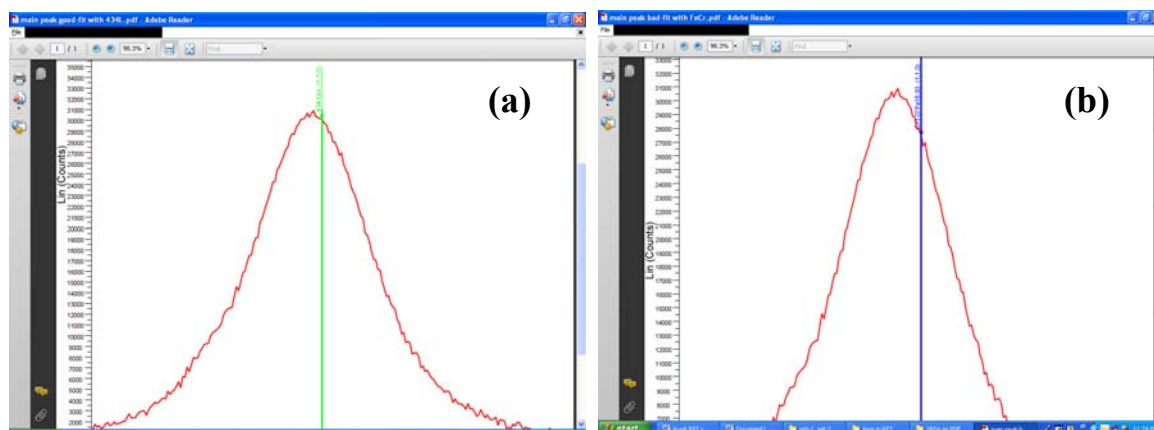


FIG-3

The application of Scherrer formula to the strongest (1,1,0) reflection peak, after manually measuring the FWHM, leads to the value of less than 10nm (about 8 nm) of the average dimension of the crystallites present in both samples. We have no reason to consider any *strong* influence of mechanical stress on the crystallites, as long as the sample is a powder and therefore this average value is taken as being due only to particles dimensions statistic distribution. The experimentally determined average value of about 8nm is confirmed also by the inspection of the TEM images. A Rietveld fit of the same two experimental diffractograms led to a value, averaged over the whole diffractogram, very close to 8nm.

The data provided by TEM and SAED (i.e. selected area electron diffraction) led us to the conclusion that there is no observable *amorphous component* in the two materials.

CONCLUSION. The XRD study of the two powders fabricated by MA by starting with pure powders of Fe, Cr, Yttria and Ti shows (a) that a solid solution is formed, with a crystalline structure very close to that of the ferritic matrix of the 434L steel, and (b) that the alloys powders are of nanometric size, with an average size value of about 8nm. No amorphous component is to be supposed as present in the two materials.

The X-EDS microanalysis results by TEM and SEM

The X-EDS test analysis of a pure Yttria sample

It is well known that stray X radiation is always present when X-EDS analysis is performed in the TEM mode. That is due to the X-ray fluorescence

induced in the materials surrounding the sample. In order to identify the stray X radiation specific to the JEM-200-CX microscope, the most intensively used for performing the X-EDS analysis of our samples, a standard sample was prepared from powder of pure Yttria (Y_2O_3) on substrate of carbon thin film.

The X-EDS spectra acquired in SEM mode from the standard Yttria sample are shown in FIG-4 for the analysis performed at 200kV and in FIG-5 for that performed at 40kV. The choice of the two values of accelerating voltages (40kV and 200kV) was driven by the fact that all the subsequent analysis of particles in the 2 samples of interest was done with electron beams with energy of either 200keV or 40keV. A rich counting statistics of 100K counts was acquired for both accelerating voltages. It is to be pointed out that in SEM mode the electron beams have the finest diameter of focussing and the lowest rate of stray radiation generation. It was selected a platelike particle of the pure Yttria particle, semi-transparent to the 200kV beam, but too thick for being transparent for the 40kV beam.

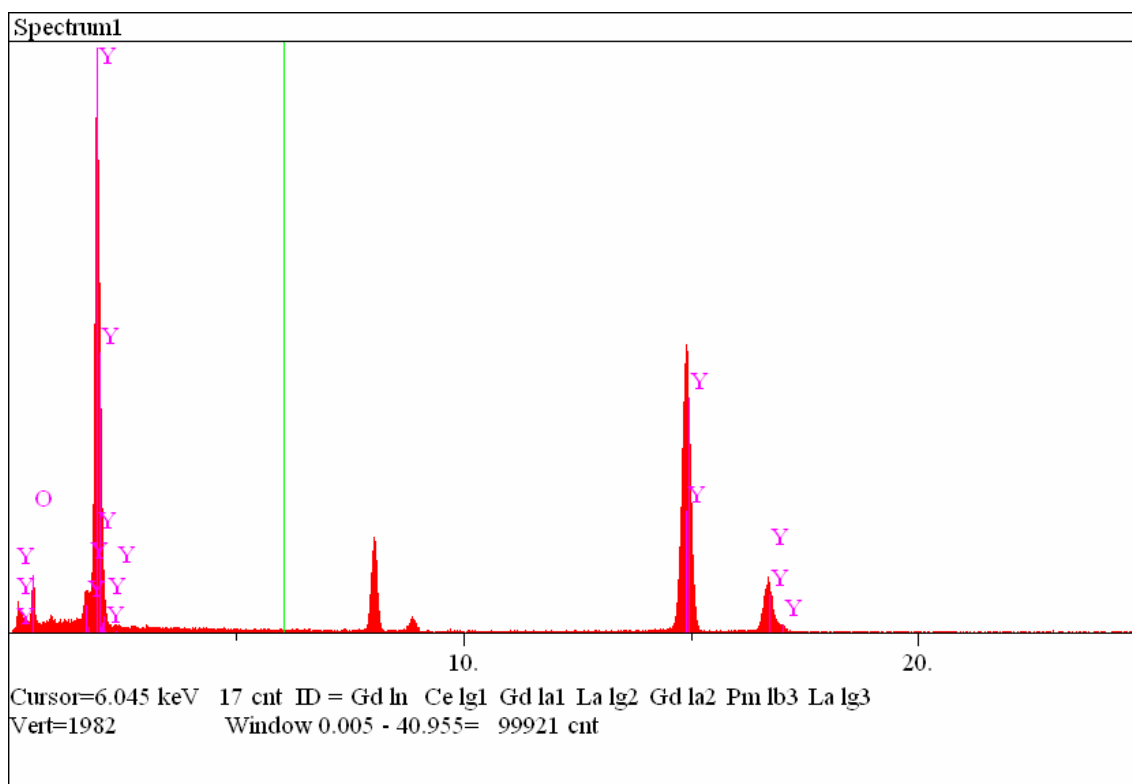


FIG-4(A). X-EDS entire spectrum of 100K counts, acquired from a platelike particle of pure Y_2O_3 .

In FIG-5(B) is shown that the only stray radiation present in the spectrum is that generated by Cu, which is a familiar and permanent presence in any X-EDS spectrum acquired in a transmission electron microscope. In FIG-5(C) is shown the spectrum shape in the energy range from 0 to the energy specific to the main Cu peak. The spectrum shape in this range is showing only the presence of a pure

background counting. This one should be the shape to be observed when no impurity or elements in minor quantity are present in the analysed particle. It can be considered as a reference shape.

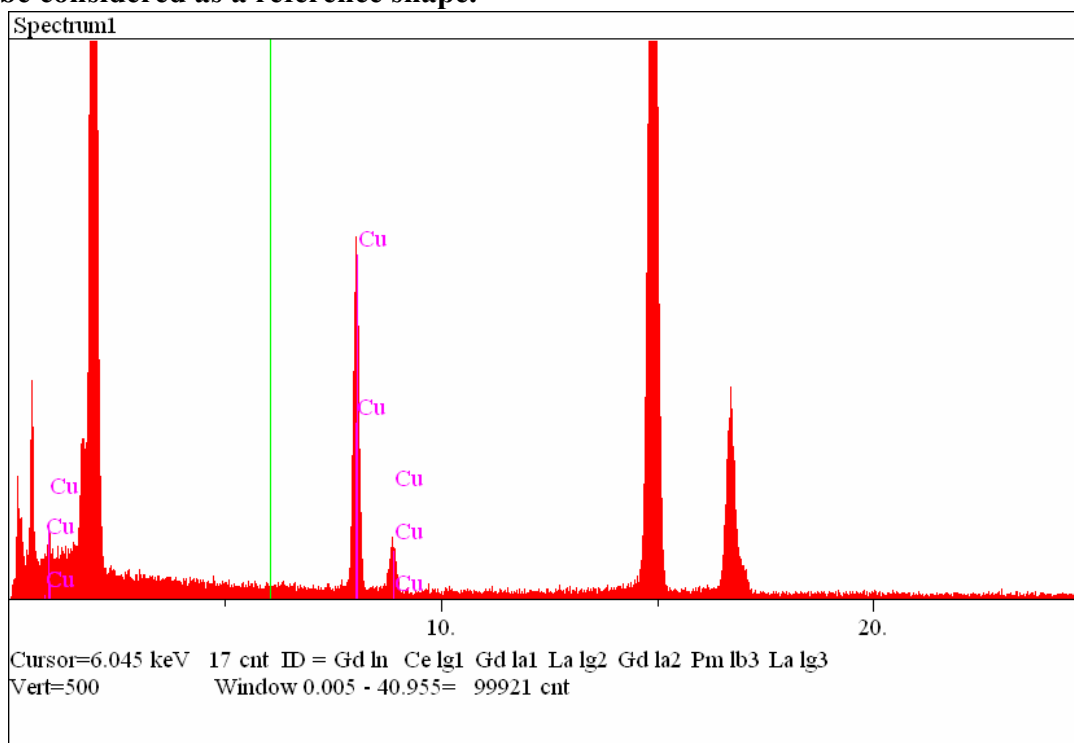


FIG-4(B) shows that in our reference X-EDS spectrum the only stray radiation is that normal for an acquisition in TEM, generated by Cu

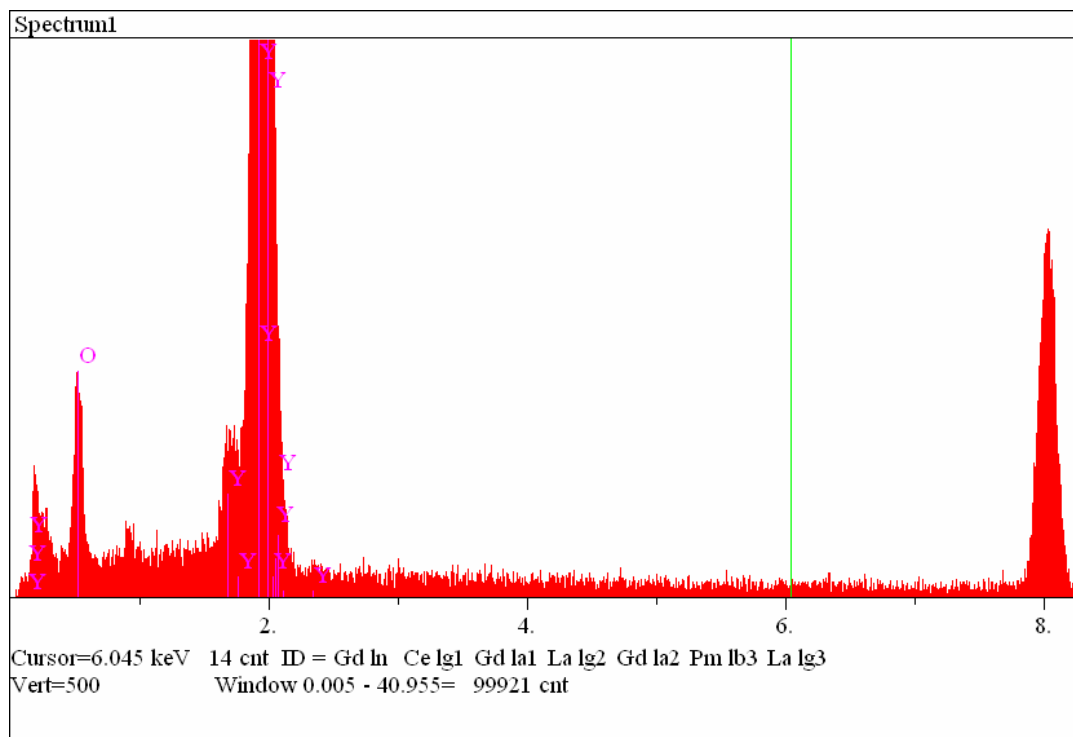


FIG-4(C) shows the normal shape of background in the energy range from 0 to 8keV

CONCLUSION. Except for Cu, no other stray radiation should be detected in the X-EDS spectra as generated by the structural materials of the TEM we used.

The experimental X-EDS data acquired from the two powder alloys fabricated by MA

Careful X-EDS analysis of a total of 26 particles in the two samples was performed in the following two manners:

(a) in TEM by focussing the beam and statically directing it either to illuminate an entire single particle (including a small area of its surroundings) or only a small fraction of an entire particle area (including a small area of its surroundings). The accelerating voltage was always of 200kV when performing analysis in this mode.

(b) in TEM, but putting the electron beam under the control of the SEM device, which means that it is strongly focussed to a diameter of micrometers, i.e. by using a much finer beam than in TEM mode. The accelerating voltage was either of 40kV, or of 200kV and the beam was either statically focussed on a point of the particle, or scanned over a very small area of the particle.

The results are collected in Table-1 for sample-1 and in Table-2 for sample-2. In these tables are mentioned also some features which are important for understanding the particular mode in which a particle was analysed, as are:

(a) whether the analysis was done on a single point (on-point) or by scanning a selected area;

(b) how many counts were accumulated in the spectrum and how long lasted the analysis;

(c) whether the particle is thick or semi-transparent or transparent to the electron beam;

(d) which kind of correction was used for the quantitation;

(e) comments about the quantification accuracy;

(f) comments about the visibility of the Yttrium-L peaks in the spectrum;

TABLE-1 (concerning Ti-containing sample-1, besides Y)

Particle label	SEM or TEM kV e-beam	Total counts (livetime)	Composition wt%	Observations
p-1 very thick particle	TEM 200kV whole particle	~356K 500s	Ti 8.010 \pm 2.037 Cr 6.770 \pm 1.544 Fe 15.342 \pm 2.082 Y 69.878 \pm 17.519	consistent O peak detected; Si, S peaks visible; Y peak not clearly visible; moderate error of the Y

	illuminated			quantification
p-2 thin layer of disperesed material	"	~27K 300s	Ti 1.501 \pm 0.621 Cr 8.653 \pm 1.154 Fe 65.567 \pm 3.631 Y 24.280 \pm 13.858	consistent O peak detected; Y peak not clearly visible high error of the Y quantification
p-3	"	100K 500s	Ti 1.822 \pm 0.180 Cr 8.190 \pm 0.298 Fe 84.159 \pm 1.280 Y 5.830 \pm 2.383	consistent O peak detected; Si peak clearly visible; Y peak hardly visible; high error of the Y quantification
p-4	"	41.2K 500s	Ti 1.458 \pm 0.202 Cr 8.514 \pm 0.380 Fe 84.053 \pm 1.606 Y 5.975 \pm 3.028	Mn, Zn low peaks present; Y peak not visible; Si very low amount, peak visible; Ti peak not visible; high error of the Y quantification
p-5 very thin platelike particle	"	41.7K 500s	thin film correction Ti 5.510 \pm 2.321 Cr 2.320 \pm 0.988 Fe 62.482 \pm 25.637 Y 29.688 \pm 23.013	huge O peak; no other elements detected; Y peak hardly visible high error of the Y quantification
p-6			-	The X-EDS spectrum was strongly distorted because of the much too high rate of radiation to be processed by the detector
p-7	"	25.6K 500s	Ti 7.461 \pm 4.409 Cr 6.047 \pm 3.242 Fe 8.289 \pm 3.321 Y 78.204 \pm 37.470	huge Si peak; O peak very high; Y peak hardly visible; high error of the Y quantification
p-8 thin large transparent platelike particle complex of several single crystals, as shown in the SAED	TEM 200kV two separate areas were analysed	on area-1 147K on area-2 290K	on area-1, applying the thin-film correction Ti 14.472 \pm 5.994 Cr 15.850 \pm 6.258 Fe 47.231 \pm 10.994 Y 22.448 \pm 11.575 on area-2, applying thin film correction Ti 11.083 \pm 3.177 Cr 7.979 \pm 2.301 Fe 15.247 \pm 2.871 Y 65.691 \pm 23.326	obvious composition inhomogeneity of the single crystalline parts moderate and high error in the Y quantification
p-9 thick particle,	SEM 40kV micro-beam	500s about 25K	Ti 1.832 \pm 0.279 Cr 9.145 \pm 0.490 Fe 81.349 \pm 1.915	very high error of the Y quantification

first in a group of 3	focussed on-point		Y 7.675 \pm 4.086	
p-10 thick particle, second in idem	"	500s ~90K	Ti 1.715 \pm not-registered Cr 9.055 \pm idem Fe 85.566 \pm ibidem Y 3.664 \pm ibid	An error occurred in the registration of the quantification error value for Y
p-11 thick particle, 3rd in ibidem	"	500s ~90K	Ti 1.553 \pm not-registered Cr 9.227 \pm idem Fe 85.292 \pm ibidem Y 3.928 \pm ibid	idem
group-of-particles-p-12	SEM 40kV micro-beam scanning on selected area	500s ~40K	Ti 1.574 \pm 0.191 Cr 9.016 \pm 0.360 Fe 87.106 \pm 1.570 Y 2.304 \pm 1.809	high error of the Y quantification
group-of-particles-p-13	"	500s ~30K	Ti 1.711 \pm 0.247 Cr 8.892 \pm 0.442 Fe 86.126 \pm 1.890 Y 3.618 \pm 2.747	high error of the Y quantification
group-of-particles-p-14	"	500s ~50K	Ti 1.505 \pm 0.161 Cr 10.060 \pm 0.401 Fe 87.740 \pm 1.571 Y 0.695 \pm 0.286	
p-26 thick particle	SEM 200kV micro-beam scanning a selected area	900K 963s	Ti 1.697 \pm 0.038 Cr 8.499 \pm 0.066 Fe 85.870 \pm 0.287 Y 3.934 \pm 0.437	a very small Y-peak is clearly visible Fe, Cr, Ti but also visible Si, S, Zn, Ca very low error of Y quantification
p-26 same particle explored on-point	SEM 40kV on-point	500K 1585s	Ti 2.016 \pm 0.080 Cr 9.120 \pm 0.135 Fe 83.360 \pm 0.547 Y 5.504 \pm 0.985	idem

TABLE-2 (concerning sample-2, that should not contain Ti)

Particle label	SEM or TEM kV e-beam	Total counts (livetime)	Composition wt%	Observations
p-15	TEM 200kV smallest beam	500K 3387s	Ti 1.372 \pm 0.045 Cr 8.656 \pm 0.084 Fe 88.407 \pm 0.394 Y 2.159 \pm 0.442	in X-EDS spectrum Y-peak is visible highest precision of Y

	focussed on particle			quantitation
same p-15 particle analysed with a different beam intensity & up to 700K counts in spectrum	"	700K 3145s	Ti 1.388 \pm 0.042 Cr 7.974 \pm 0.078 Fe 88.984 \pm 0.372 Y 1.654 \pm 0.364	Y-peaks hardly visible high precision of Y quantitation
p-16 this is an Yttria particle	"	350K 2321s	ZAF correction O 0.000 \pm 0.000 Y 100.000 \pm 0.925 Thin film corr. O 10.684 \pm 0.303 Y 89.316 \pm 0.826	oxide quantification cannot be done correctly
p-17 it is a transparent agglomerate of nano-crystals as seen in its bright field t.e.m. image	"	500K 1699s	Thin film correct. Ti 1.625 \pm 0.079 Cr 14.172 \pm 0.233 Fe 83.982 \pm 0.576 Y 0.221 \pm 0.045	Ti-peak is high & visible Si, Mo & Ca peaks are present high precision of Y quantitation
p-18	"	500K 1718s	Thin film corr. should be the best Ti 1.515 \pm 0.050 Cr 14.399 \pm 0.155 Fe 83.807 \pm 0.380 Y 0.278 \pm 0.033	huge amount of Si detected much less amounts of Mo, Ca, Al detected high precision of Y quantitation
p-19 thick particle	"	500K 891s & 900K 1415s	For 500K counts ZAF corr. only Ti 1.351 \pm 0.043 Cr 8.376 \pm 0.083 Fe 87.847 \pm 0.380 Y 2.426 \pm 0.451 For 900K counts ZAF corr. only Ti 1.353 \pm 0.032 Cr 8.194 \pm 0.061 Fe 88.652 \pm 0.286 Y 1.801 \pm 0.291	Y peak clearly visible Very low amount of Si and Ca Ti-peak high high precision of Y quantitation
p-20 this is not an	"	50K time not		A lot of Mo & Zn presence detected

alloy particle		recorded		no Fe, Cr, Ti, Si visible a bit of Ca
p-21 semi-transparent to electron beam	"	75K 1517s	Thin-film corr. Ti 2.265 \pm 0.538 Cr 14.481 \pm 1.357 Fe 79.859 \pm 3.242 Y 3.395 \pm 1.021	Fe, Cr, Si high Ti not visible low precision of Y quantitation
p-22 very thick particle	"	100K ?s counter error & 280K 2470s	For 100K Ti 1.526 \pm 0.128 Cr 8.043 \pm 0.228 Fe 86.953 \pm 1.037 Y 3.478 \pm 1.484 & For 280K Ti 1.391 \pm 0.143 Cr 8.933 \pm 0.281 Fe 72.265 \pm 0.965 Y 17.410 \pm 3.118	Fe, Cr, Ti high Y hardly visible Low and medium precision of Y quantitation
p-23 very thick	"	500K 1607s	ZAF correction Ti 1.392 \pm 0.052 Cr 8.186 \pm 0.099 Fe 86.867 \pm 0.445 Y 3.555 \pm 0.644	Ti peak high low peaks of Si & Ca Y presence visible only in the background subtracted spectrum
p-24 thin transparent particle which seems to be Yttrium oxide	"	100K 878s	Quantification considering only Y & O O 0.000 \pm 0.000 Y 100.000 \pm 1.996 excluding O Ti 0.209 \pm 0.043 Cr 0.078 \pm 0.020 Fe 0.076 \pm 0.016 Y 99.636 \pm 1.989	
p-25 semi-transparent	"	200K 2671s	Thin film corr. Ti 1.734 \pm 0.129 Cr 13.336 \pm 0.357 Fe 84.48 \pm 0.916 Y 0.441 \pm 0.101 & ZAF correction Ti 1.709 \pm 0.127 Cr 7.935 \pm 0.213 Fe 81.424 \pm 0.882 Y 8.932 \pm 2.046	High amount of Si Low amount of Ti Y peak not visible good precision of Y quantitation

DISCUSSION of X-EDS results

In spite of the frequent mention in Table-1 and Table-2 that the Y peak is not visible in the experimentally acquired spectra, there are reasons to accept the existence of Y in the samples.

(a) the Y series-L of peaks are energetically very close to the Si-K peak and Si is frequently detected as clearly present in the sample. The Si peak origin is not clear, but it cannot result as an artefact due to the microscope, as proven by the pure Yttria spectrum shown above, where no Si peak is visible. The Y series of L-peaks could be in most cases obstructed by the neighbouring Si-K peak. That could be an explanation for the quantification results supplied by the spectrum processing software in spite of the lack of clear visibility of the Y peak and for the very high error in the Y quantification. The quantitative data supplied by the software in spite of the lack of clear visibility of Y peak shows that the assessment of Y presence in the corresponding particles is doubtful but not excluded de plano.

For an example of the frequently observed shape of X-EDS spectra in the energy range where Si-K and Y series-L peaks are not clearly visible see FIG-5(A). The quantitative data supplied by the quantification software are based in most cases on the kind of spectra shown in FIGS-5(A)&(B).

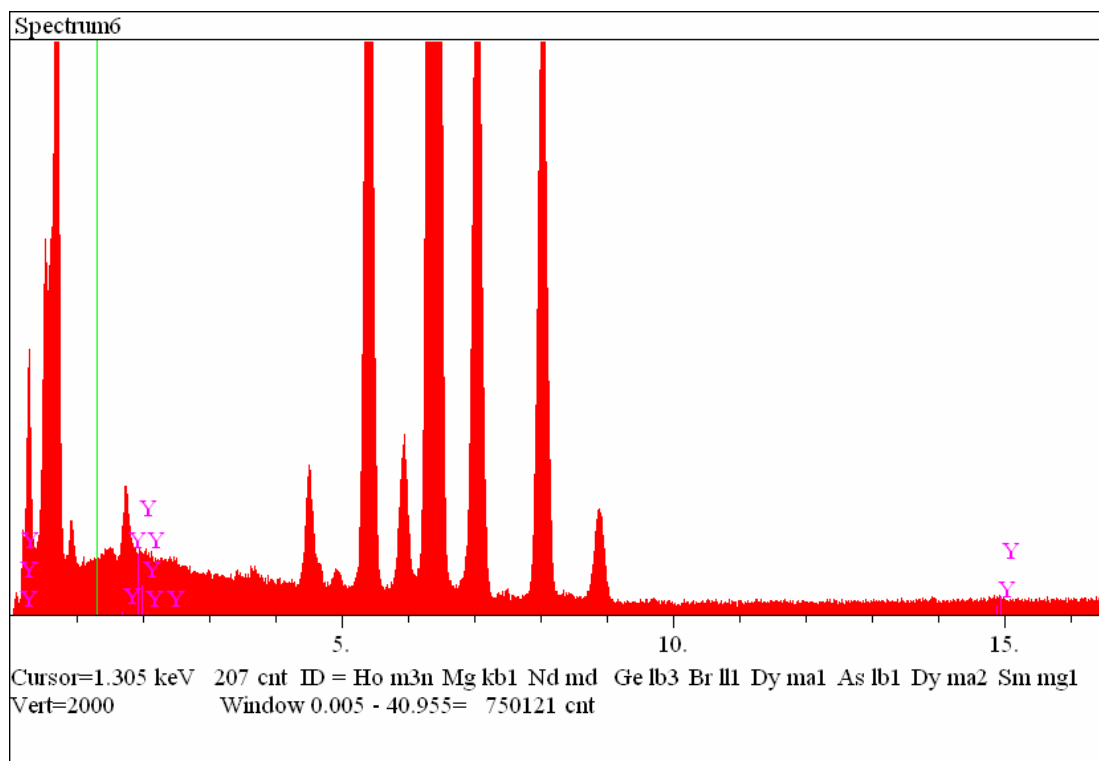


Fig-5(A) Spectrum contains an accumulation of 750K counts

After background subtraction, the quantification software generates a shape model of the peaks to be quantified, as shown in FIG-5(B), finally assessing on this ground a wt% to the required elements. The resulting quantification error for Y is high in these circumstances.

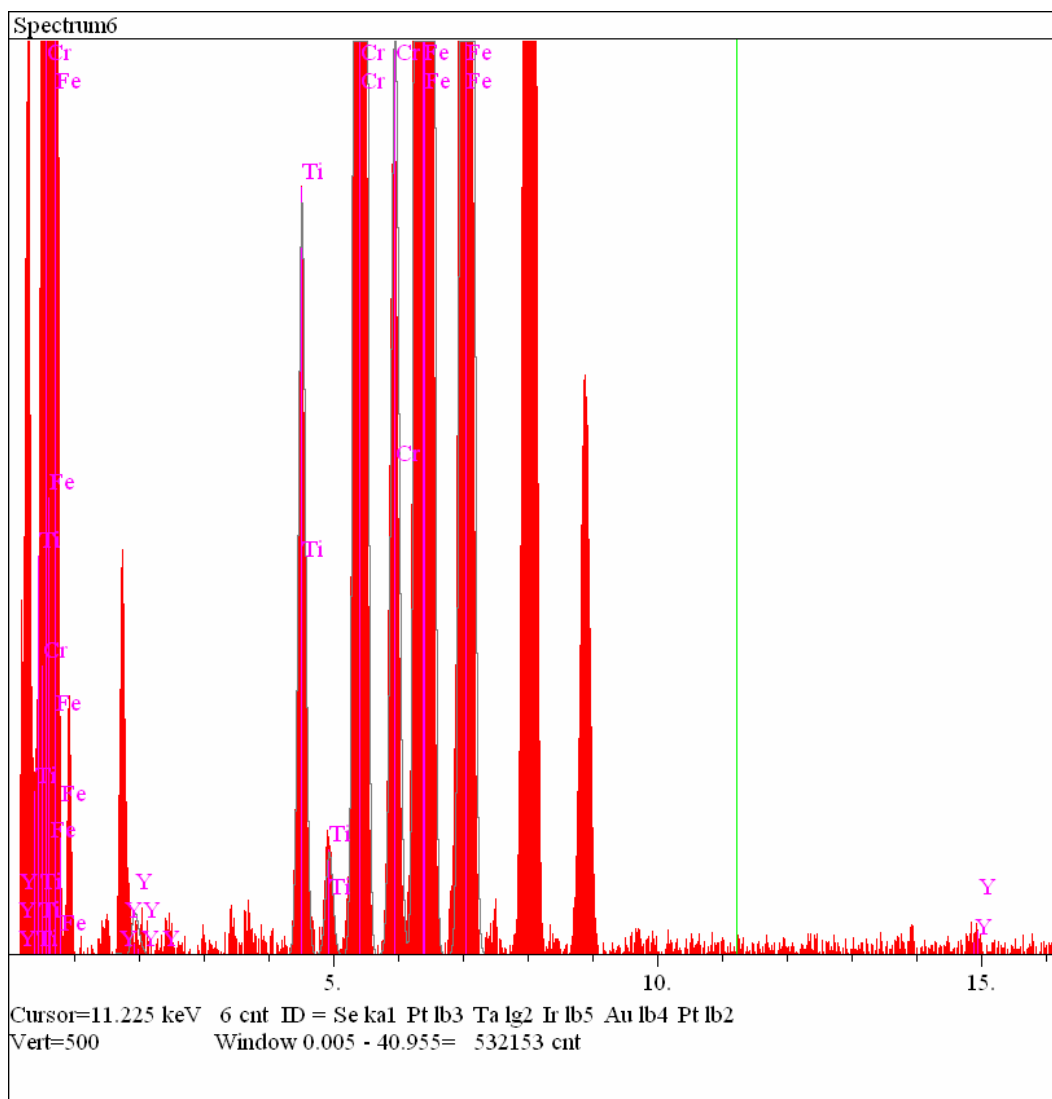


Fig-5(B) The software modelling of the quantified elements peaks. Here the presence of Y is undoubted due to the visibility of its peaks around the 15keV energy value and in spite of the low visibility of its peaks in the energy range around 2keV

(b) in few cases the Y peak presence in the spectrum is clearly visible, in spite of the presence of Si-K peak next to and preceding it and of a S-K peak following it, as shown in FIG-6(A). In these circumstances the quantification error for Y is much

lower. It is based on background subtracted spectra and modelled peaks as shown in FIG-6(B), which are looking similar to those already shown in FIG-5(B).

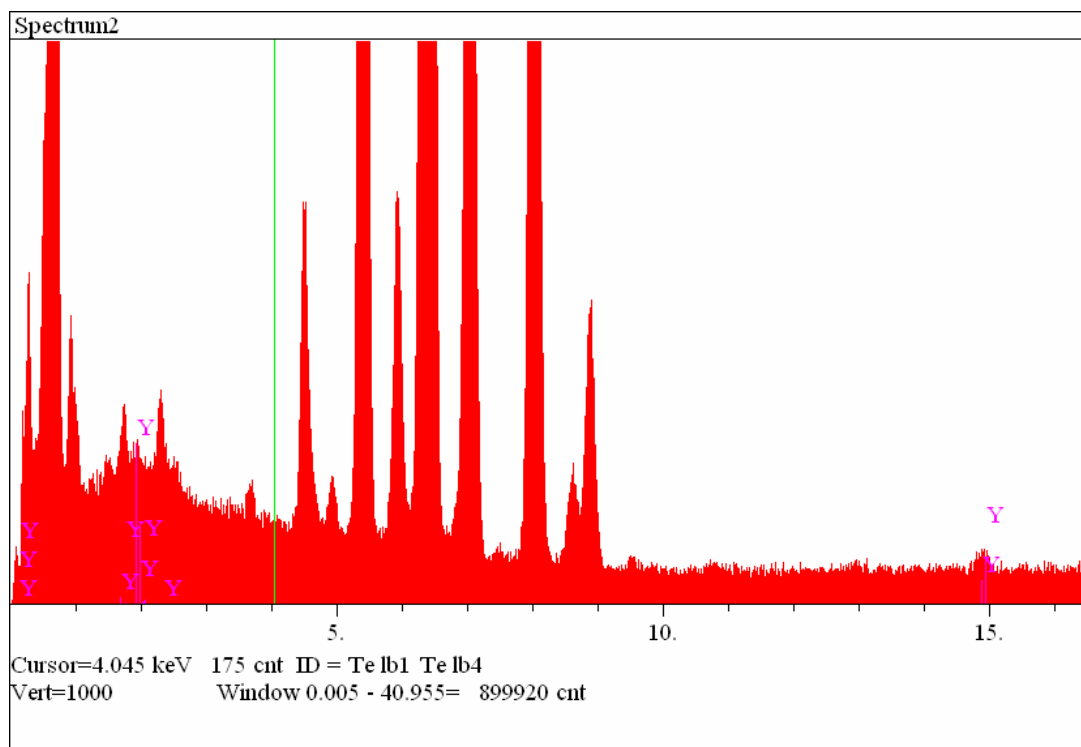


Fig-6(A). Spectrum contains 900K counts

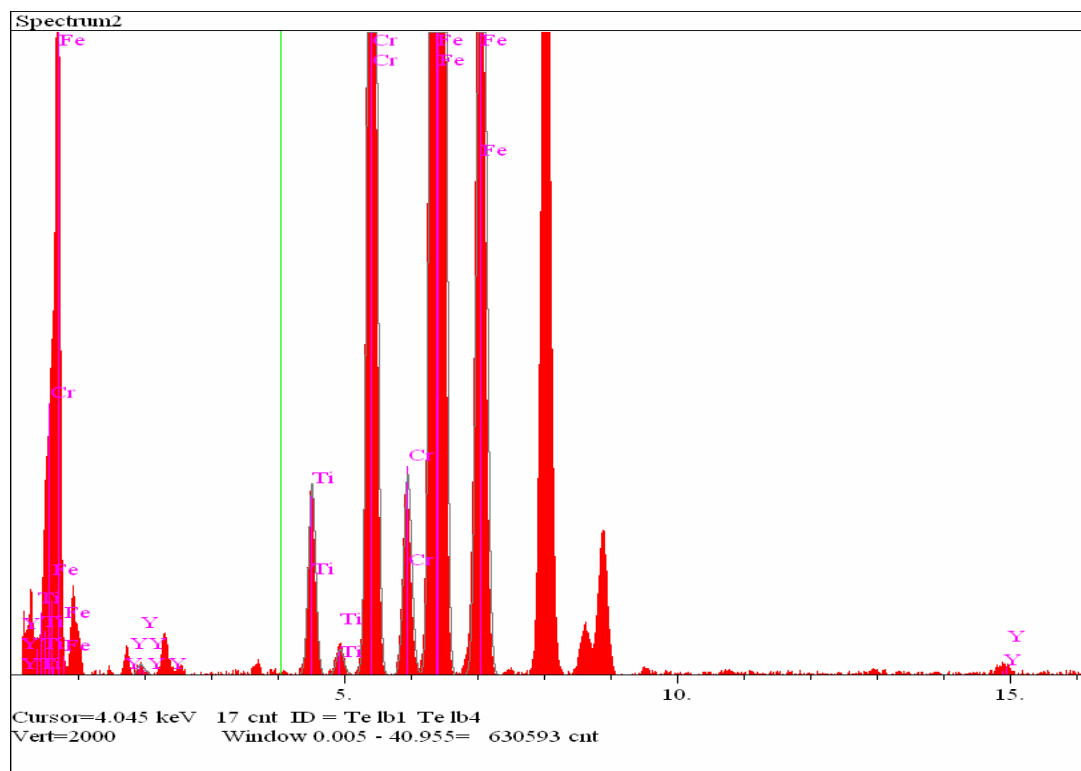


Fig-6(B)

(c) a few particles were detected (p-16 and p-24 in Table-2; p-1, p-2 and p-8 in Table-1 are containing high amounts of Y also) as containing a huge amount of Y, besides O. It is to be supposed that these are Yttria particles which were not dissolved into the Fe-Cr matrix.

Final conclusions concerning the X-EDS results

(a) The Y content is not uniformly distributed in the alloy particles. This is supported also by the observation that there are Yttria particles not dissolved into the Fe-Cr matrix.

(b) Ti is present almost overall, even in sample-2 which is supposed not to contain this element.

(c) a few particles were detected which contain impurities. The presence of Si is observed in most cases.

The Moessbauer spectroscopy results

The Moessbauer spectra obtained from the two alloy samples are shown in next FIG-7 and FIG-8. The comparison of each of these two spectra with the spectrum of pure alpha-Fe shown in FIG-9 is evidencing a clear distortion of the alpha-Fe crystal lattice. This is mainly due to the formation of Fe-Cr solid solution during the MA process and on a much more reduced scale to the penetration in the Fe-Cr solid solution crystal b.c.c. type lattice of other foreign atoms.

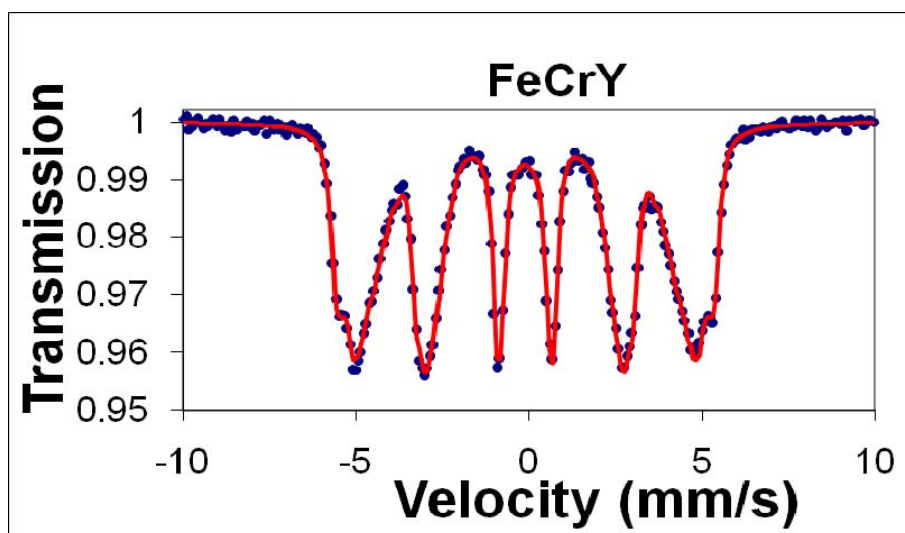


FIG-7

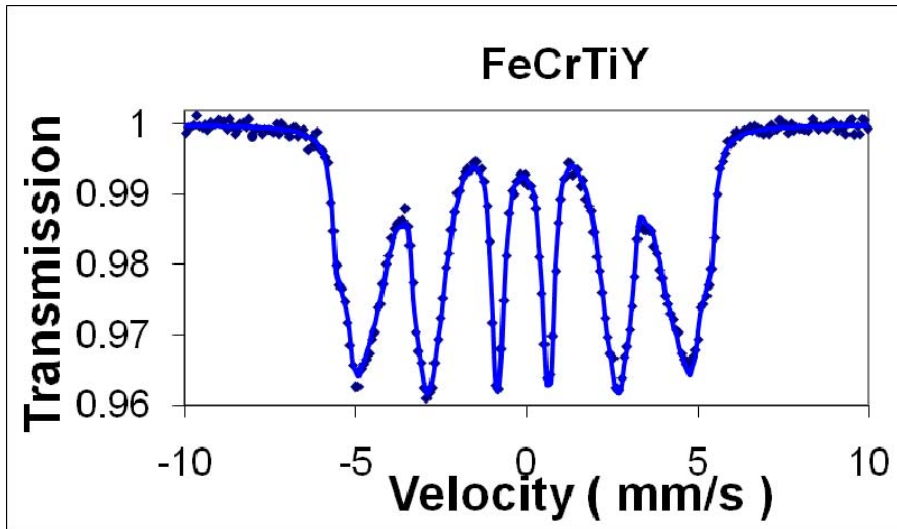


FIG-8

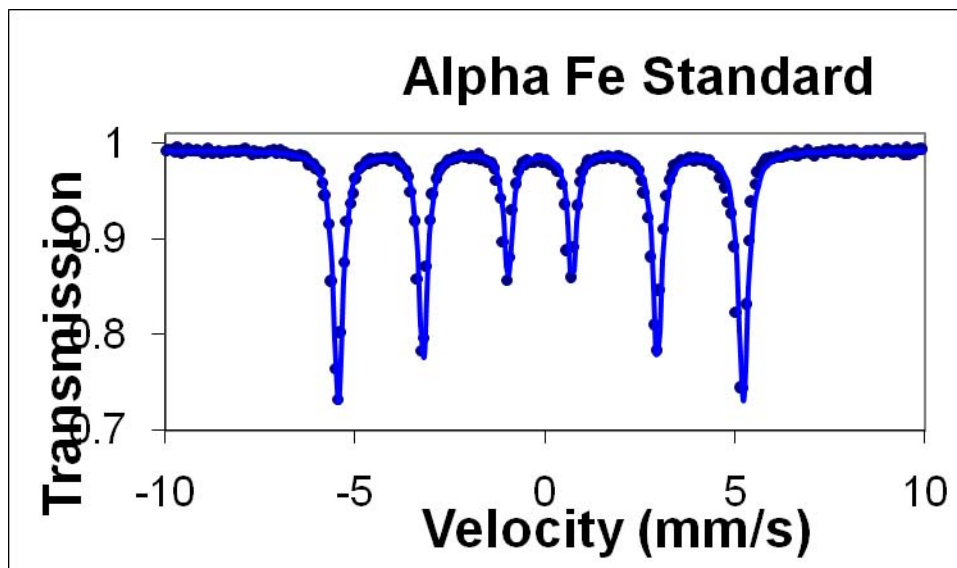


FIG-9

It is to be noticed the high similarity of the two Moessbauer spectra shown in Fig-7 and Fig-8. This is an evidence for that the crystall lattice formed by MA alloying in the two samples are perfectly similar.

The Moessbauer spectroscopy cannot detect which are the foreign atoms, others than Cr that did penetrate the crystal lattice. It can only estimate that, on average, the amount of Cr in the b.c.c. solid solution Fe-Cr is about 15%

The classical TEM results

The classical TEM was used for getting images of the crystallites which are responsible for the distortion of XRD peaks discussed above. By means of dark-field imaging it was assessed that the powder particles are agglomerations of both very small crystals and much bigger ones. To illustrate this aspect we show in FIG-10 an image revealing the very small crystallites and in FIG-11 an image revealing an agglomeration made up from much larger crystallites. These images are typical for both analysed powder alloys. Images from FIG-11 are self-explanatory.

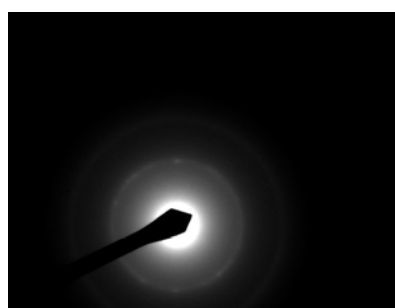
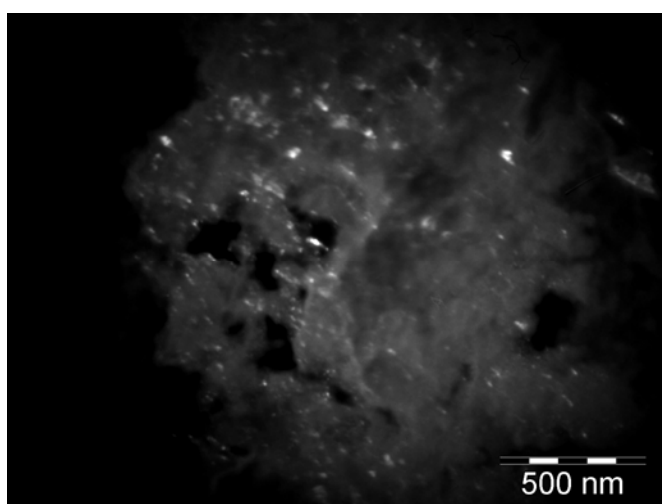


Fig-10. Dark field image and its corresponding electron diffraction pattern

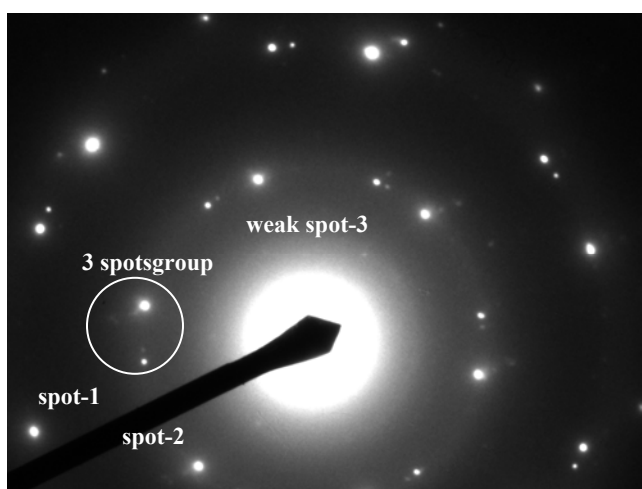


Fig-11(A)

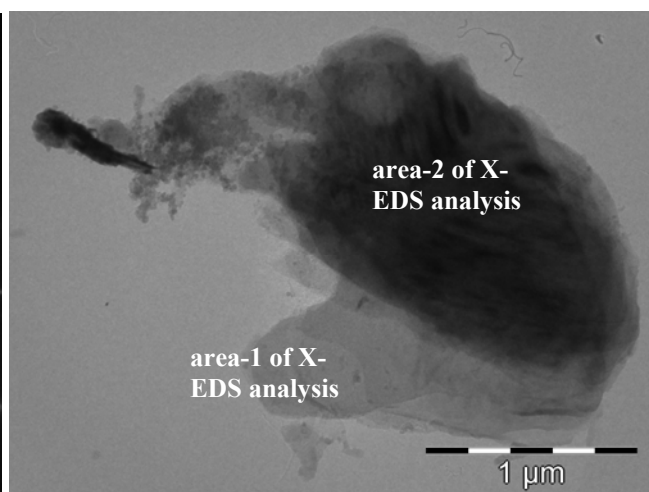
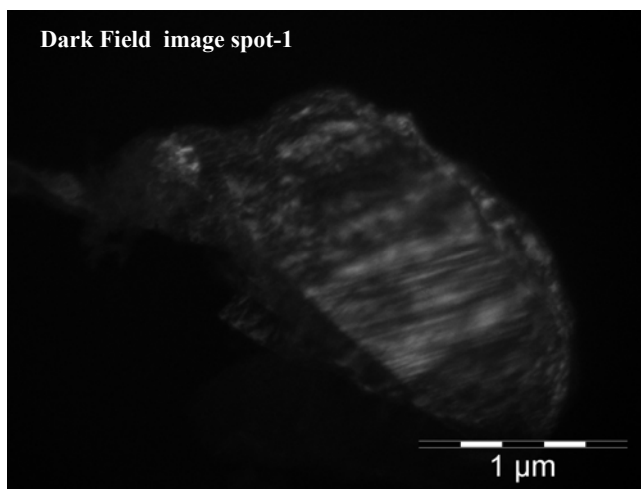
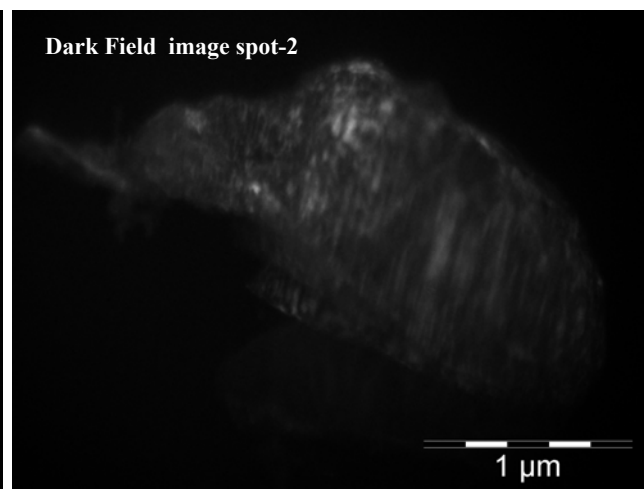
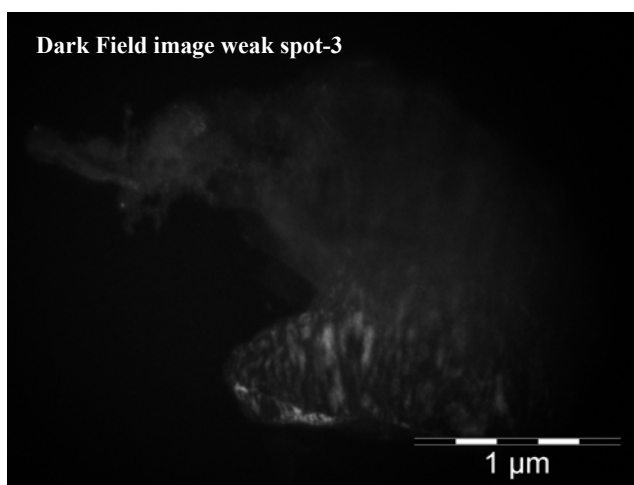
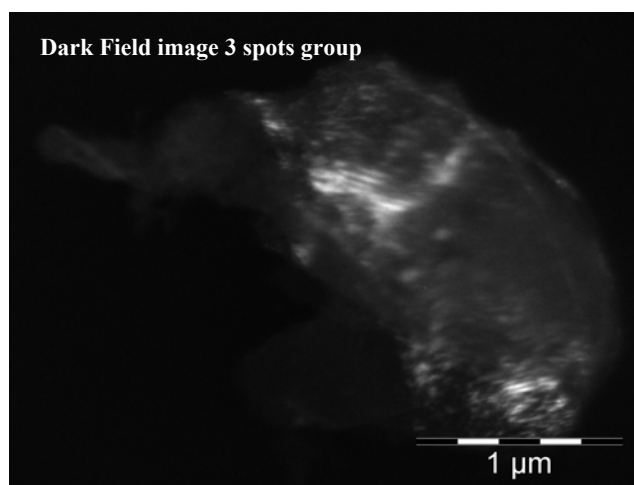


Fig-11(B)

**Fig-11(C)****Fig-11(D)****Fig-11(E)****Fig-11(F)**

The HRTEM results

The HRTEM technique confirms the results already obtained by means of other methods. In FIG-12 is shown a HR bright field image on which it can be measured the dimensions of the smallest particles in the powders.

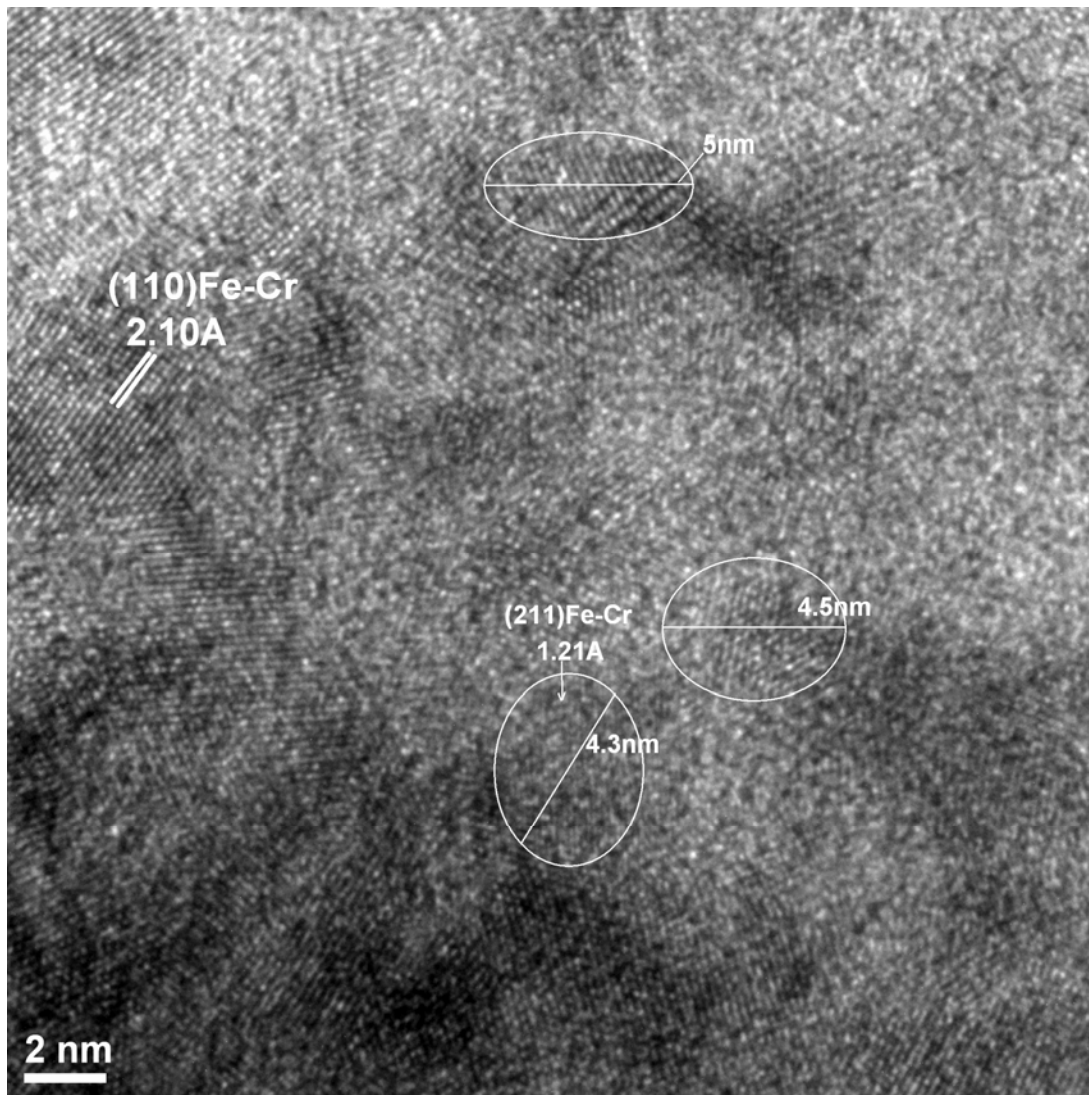


Fig-12 HRTEM image of smallest particles observed in sample-1

About the applicability of EELS method

It was made an attempt to get EELS spectra from the particles of the two samples. Because of the thickness of supporting carbon film, the spectra were of a low quality and did not allow any valuable observations. In these circumstances, it is hopeless to get energy filtered images, for which the thickness demands are even more strict than for getting EELS spectra.

We hope to be able in the future to find a method of samples preparation allowing to get EELS spectra and energy filtered images.

CONCLUSIONS

The main conclusion of our research is that there is a clear inhomogeneity of the elemental composition of the MA prepared powders aiming at a content of Fe-Cr-Y and Fe-Cr-Y-Ti.

There are impurities all over the two samples, which could affect the final material to be produced by consolidation and hot extrusion.

The crystallites composing the two samples are of a nanosize distribution, a fact that was aimed by the powders producer.

The penetration of Y in the Fe-Cr b.c.c. nano and micro-crystals is not yet uniform, which rises the problem for the powders manufacturer of modifying the parameters of MA process.

The methods we used for characterization of the two powder samples can give satisfactory results.

BIBLIOGRAPHY

- [1] M.J.Alinger et al., *J.Nucl.Mater.*, 323-333 (2004) 382-386.

Indicatori de realizare a fazei (conform specificului fiecarui program/proiect)

Denumirea indicatorilor	Numar/ Mii Ron	
	Planificat	Realizat
1. Investiții noi în infrastructura CDI		
2. Gradul mediu de utilizare a echipamentelor CDI	15%	15%
3. Număr de entități susținute pentru creșterea capacității de ofertare a serviciilor de experiment		
4. Număr de reviste finanțate, din care - Co-editate internațional - Indexate ISI - Incluse în alte baze de date internaționale recunoscute		
5. Cărți, atlase, dicționare și alte produse cu caracter științific publicate anual, în țară și în străinătate		
6. Număr de conferințe organizate, din care internaționale		
7. Număr de expoziții finanțate		
8. Valoarea investiției în infrastructură și servicii de comunicații		
9. Ponderea cercetătorilor care au acces la resursele de informare on- line	100%	100%
10. Număr de reviste dedicate popularizării științei		
11. Număr de proiecte de comunicare știință-societate		
12. Număr de proiecte de studii prospective		
13. Număr de proiecte de pregătire a unor participări la programe internaționale		
14. Număr de participări în proiecte internaționale	1	1
15. Valoarea apelurilor tematice comune lansate		

Scientific Report

To the Contract 1EU-3/11.08.2008
For the period 04.01.2010 – 30.06.2010

Sub-Project BS-6: Sheath properties and related phenomena of the plasma wall interaction in magnetised plasmas. Application to ITER

Authors: V. Anita, C. Agheorghiesei, S. Costea, C. Costin, G. Popa, L. Sirghi, M. L. Solomon

Subject: Plasma diagnostics

Specific Objective: Characterisation of Pilot-PSI plasma beam by electrical methods (different types of probes, electrostatic analysers, etc)

Multi-channel analyzer measurements

Plasma beam diagnostic for Pilot-PSI (at FOM, The Netherlands) continues in 2010 through multi-channel analyser (MCA) measurements at the target, by monitoring the time-space (2D) distribution of edge plasma parameters (floating potential, electron/ion flux, energy distribution), characterising the plasma that reaches the target. The experiments are performed within EFDA PWI Task Force (WP10-PWI-04-04/BS).

The experimental data obtained in November 2009 on the 2D distributions of the plasma current reaching the grounded target and the floating potential at the target surface have been further analyzed. Besides the results already reported in 2009, new remarks came out. Floating potential distribution has a good radial symmetry while current distribution presents angular inhomogeneity at higher radii (see Fig.1). The density of the electric current received by the grounded collectors increased strongly with the magnetic field strength (from $\sim 64 \text{ A/cm}^2$ at 0.4 T to $\sim 575 \text{ A/cm}^2$ at 0.8 T in the centre of the plasma column). The negative values of the measured currents are related to the electron dominated current received by the grounded collectors. The measured floating potential ranges between $\sim 0 \text{ V}$ at the side of the beam and -70 V at 0.4 T up to -165 V at 0.8 T in the centre of the plasma column. An increase of the total discharge current was observed to decrease the floating potential at the target.

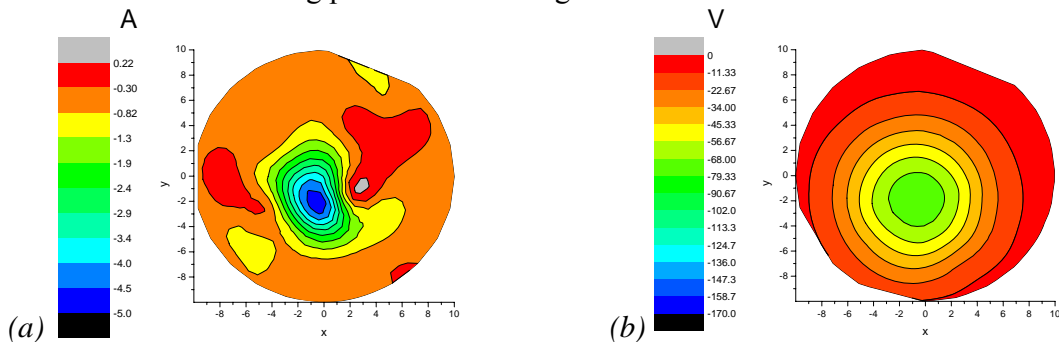


*Fig.1. Example of 2D current (a) and floating potential (b) distributions at the target surface
($B = 0.8 \text{ T}$, discharge current $I = 100 \text{ A}$)*

In order to improve the measurements, a new design of the analyzer has been created this year. While in the former design the collectors were placed behind the channels drilled in the front plate, the new analyzer has the collectors introduced in the channels of the front plate, so that the surface of both the front plate and collectors to be in the same plane, all directly exposed to the plasma (Fig.2). This new design improves the equivalence of the analyzer with a compact target in order to better investigate the interaction plasma-target. Carbon, tungsten and titanium have been used as materials for the front plate.



Fig.2. New design of the analyzer with 61 collectors

Design and manufacturing of a 3-grid analyzer

Measurements of ion energy at the interface of plasma with a solid target are extremely important because the ions are the dominant factor determining interaction of plasma with the target surface. Our approach for such measurements is to use an electrostatic analyzer with 3 grids (Fig.3): a separation grid to reject plasma electrons, an ion energy controlling grid, and a secondary electron emission suppression grid. All analyzer components are encapsulated in a Faraday cup mounted in the centre of Pilot-PSI target. A data acquisition and grid biasing system using a NI PXI-4123 board controlled by home-made LabView software will be used to take I-V characteristics in snapshots of about 150 ms during plasma beam confinement (2-4 s).

The electrostatic analyzer was already built and in the second semester of 2010 it will be tested and used in order to obtain information on ion energies flowing to the central point of the carbon target (floating and/or grounded). Thomson scattering will be simultaneously used to obtain information on plasma density.



Fig.3. Electrostatic analyzer with 3 grids

Specific Objective: Plasma diagnostic in the Scrape-off Layer (SOL) of COMPASS tokamak by electrical methods (different types of probes)

Continuing the collaboration of the two Associations (started in 2005 on CASTOR tokamak), a short-term mission was programmed in March 2010 at the new tokamak facility (COMPASS) at IPP Prague, Czech Republic. One key element in our future collaboration is the description of SOL plasma by electrical diagnostics.

Design the diagnostic system based on electrostatic probes

We started to design a manipulator with changeable head that will serve as support for different types of probes. It will be installed on a port placed on the bottom of the vessel, probably one of the two ports existing between the magnetic coils 12 and 13. Thus, the probes will be positioned between divertor tiles. The manipulator will provide 2 movements for the probes: translation on 2-3 cm and rotation. The changeable head will hold several probes at the same time. The new device will be built and used for diagnostics in 2011.

Planning the next measurements campaign

The future campaign for probe measurements will use the actual diagnostic system already installed in the tokamak: divertor array probes and a reciprocated probe for SOL investigations. It is programmed between August 18th and September 16th, 2010. Current-voltage characteristics will be acquired on these probes in order to investigate edge-plasma parameters.

Subject: Theory and modelling

Specific objective: Development of a 2D PIC-MCC model for magnetised plasma devices (application to Pilot-PSI)

The PIC-MCC simulation code (PLUAIC) was adjusted to study plasma parameters in front of a solid surface, with direct application to Pilot-PSI target:

- different boundary conditions were tested for the target of Pilot-PSI device (several surface processes were considered as secondary electron emission, absorption and reflection of the charged particles);
- the influence of different collisional processes as well as the target bias on energy distribution function of the charged particles has been investigated;
- the code has been parallelized using MPI and POSIX Threads. The parallelisation method was applied to the module that moves the charged particles in a time step (including collisions) while electric field module is solved on a single computing machine.

Publications

- [1] M. L. Solomon, V. Anita, C. Costin, I. Mihaila, L. Sirghi, G. Popa, M. J. van de Pol, R. S. Al, G. J. van Rooij, J. Rapp, "2D distributions of current and floating potential at the target surface in Pilot-PSI", *37th European Physical Society (EPS) Conference on Plasma Physics*, 21-25 June 2010, Dublin, Ireland (poster presentation)
- [2] M. L. Solomon, V. Anita, C. Costin, I. Mihaila, L. Sirghi, G. Popa, M. J. van de Pol, G. J. van Rooij, J. Rapp, "Current and floating potential distributions measured by a multi-probe system at the end plate surface in Pilot-PSI", *15th International Conference on Plasma Physics and Applications (CPPA)*, Iasi, Romania, 1-4 July 2010 (poster presentation P6-07)
- [3] M. L. Solomon, V. Anita, C. Costin, I. Mihaila, G. Popa, H. J. van der Meiden, R. S. Al, M. van de Pol, G. J. van Rooij, J. Rapp, "Multi-channel analyzer investigations of ion flux at the target surface in Pilot-PSI", *Contrib. Plasma Phys.* (2010) (in print)

